DETERMINATION OF DARK MATTER MASS AT LEPTON COLLIDERS
AND
EXPERIMENTAL STUDIES IN TWO DIMENSIONAL TURBULENCE

by

Stefanus

B. E. Computer Engineering, NTU, Singapore, 2003

M. S. Physics, University of Pittsburgh, 2010

Submitted to the Graduate Faculty of
the Kenneth P. Dietrich School of Arts and Sciences in partial fulfillment
of the requirements for the degree of

Doctor of Philosophy

University of Pittsburgh

2014

UNIVERSITY OF PITTSBURGH

DEPARTMENT OF PHYSICS AND ASTRONOMY

This dissertation was presented

by

Stefanus

It was defended on

June 4th 2014

and approved by

Tao Han, Professor, Department of Physics and Astronomy

Walter Isaac Goldburg, Professor Emeritus, Department of Physics and Astronomy

Vittorio Paolone, Associate Professor, Department of Physics and Astronomy

Ayres Freitas, Assistant Professor, Department of Physics and Astronomy

Rob Coalson, Professor, Department of Chemistry

Dissertation Director: Tao Han, Professor, Department of Physics and Astronomy

DETERMINATION OF DARK MATTER MASS AT LEPTON COLLIDERS
AND
EXPERIMENTAL STUDIES IN TWO DIMENSIONAL TURBULENCE

Stefanus, PhD

University of Pittsburgh, 2014

In Ch. 1 - 5 we present a study of antler decay in determining dark matter mass. It was shown that the cusps and endpoints in some kinematic distributions of the antler decay at the LHC can probe the masses of the parity-odd missing energy particles as well as the intermediate particles. We extend this study into the high energy e^+e^- (or more generally lepton) linear collider, which will provide unambiguous center of mass frame and energy. We found new and more powerful cusp structures of new kinematic observables, possible only at the International Linear Collider (ILC). As a benchmark scenario, we study $e^+e^- \to \tilde{l}^+\tilde{l}^- \to l^+l^-\tilde{\chi}_1^0\tilde{\chi}_1^0$ and $e^+e^- \to \tilde{\chi}_1^+\tilde{\chi}_1^- \to j\,j\,j\,j\,\tilde{\chi}_1^0\tilde{\chi}_1^0$ in the framework of the Minimal Supersymmetric Standard Model.

Ch. 6 presents a new way to characterize turbulence through a search for conformal invariance in vorticity isolines of two-dimensional compressible turbulence. The conformal invariance theory being tested here is related to the behavior of equilibrium systems near a critical point. This theory is associated with the work of Löwner, Schramm and others and is usually referred to as Schramm-Löwner Evolution (SLE). The system was exposed to several tests of SLE.

In Ch. 7 we introduce a photon correlation method for measuring components of the shear rate tensor in a turbulent soap film. The technique yields the mean shear rate $\overline{s}$, its standard deviation σ, and a simple mathematical transform of the probability density function $P(s)$ of the shear rate itself.

Ch. 8 presents a computer algebra package to automatically generate particle physics Lagrangians based on group symmetries input by the user.

TABLE OF CONTENTS

LIST OF TABLES

LIST OF FIGURES

PREFACE

This thesis is dedicated to all DOTA 2 fans out there, road to #TI4 ! On a more serious note, I would like to thank my advisor, Dr. Han, for taking me in as his student in 2011 and for all his financial support during the past three years. Many thanks to our beloved postdoc Neil Christensen who has been very patient in guiding me through the different projects. Lastly, a very big and warm hug to “Dr. G”, as I always call him, for all of his kindness in giving me advice, time, food and most amazingly for putting my interests ahead of his. He might be the last of the species of professors who exemplify the motto “Professors should work for their students” (a statement in his own words), it was an epic blessing for me to know him.

And if an American (by some random fluctuations) happens to read this thesis, Singapore is **NOT** in China!

1.0 INTRODUCTION

With the monumental discovery of the Higgs boson at the LHC [1], all of the fundamental particles in the Standard Model (SM) have been discovered. The SM as an effective field theory can be valid up to a very high scale. Nevertheless, there are strong indications that the SM is incomplete and that there are particle physics phenomena that cannot be accounted for within the SM. Among them, the discovery and characterization of the dark matter particle may be one of the most pressing issues.

The existence of dark matter has been well established through several observations. Notably, they are galactic velocity rotation curves [2, 3, 4, 5], weak and strong gravitational lensing [6, 7], Big Bang nucleosynthesis [8], the cosmic microwave background [9] and the bullet cluster [10]. A few of these evidences will be discussed in more detail below.

Galactic rotation curves are the first and oldest evidence of the existence of dark matter. These curves refer to the rotation speed of stars at the rim of galaxies. It was observed that these stars possess higher speed than that allowed by Newtonian dynamics. That is, given the total visible mass in the galaxy, the gravitational pull generated will not be sufficient to induce centripetal acceleration needed to keep the stars bound to the galaxy. Therefore there must be invisible matter that keep the stars from flying off.

The gravitational lensing evidence refers to the fact that we observe more lensing of faraway galaxies than that is allowed by the visible matter between us and those astronomical objects (assuming unmodified general relativity). Thus, there must be extra invisible mass that bend the light rays coming from those distant galaxies.

Bullet clusters consists of collisions between two clusters of galaxies. Gravitational lensing of background object produced by these clusters show that there are more mass than what is visible through x ray observation. Since the extra mass is invisible, it has to be dark, *i.e.*

electromagnetically non interacting.

From observations done so far, we know that dark matter is electrically neutral, non-baryonic and composes roughly 83% of the matter and 23% of the energy of the universe. There are many possibilities for dark matter [12], however, weakly interacting massive particles (WIMPs) are very popular because they are generated in many theories beyond the Standard Model which are designed to solve other problems. These theories often contain a new discrete symmetry which removes unobserved baryon and/or lepton number violating processes such as proton decay. Under this discrete symmetry, Standard Model particles are even while the new particles are odd. As a result, since all interactions preserve the discrete symmetry, an even number of new particles must be involved in any reaction.

Assuming WIMP dark matter, there are three types of observations of dark matter particles. They are indirect, direct and collider searches, see Fig. 1. In indirect detections, we observe the visible products of WIMP annihilations as WIMP particles usually annihilate into three types of visible particles, gamma rays, neutrinos, and positrons. For direct detections, we want to see the effect of WIMP collision with nucleons by measuring the recoil of the nucleons where recently there have been recent statistically inconclusive but tantalizing excesses in measurements of the weak scattering of WIMP off normal matter [11]. If confirmed, these observations will confirm that at least some of the dark matter is weakly interacting, lending further solidifying the idea of WIMP as dark matter. Our focus in this article is the production of WIMPs at earth based colliders. As all three types of detections are just different aspects of the same feynman diagram, see Fig. 1, to convincingly establish a DM candidate, it is ultimately important to reach consistency between indirect, direct searches and collider signals for the common parameters of mass, spin and coupling strength.

A further evidence for WIMPs is the observed relic abundance of cold dark matter. In the early universe, dark matter particles were in thermal equilibrium along with everything else. As the universe expanded and cooled, the separation between dark matter particles became too great for efficient annihilation and the dark matter particles froze out to form the relic dark matter density. Amazingly, theories beyond the SM predict roughly the right relic density. This is often called the WIMP miracle. To get the relic abundance right, a

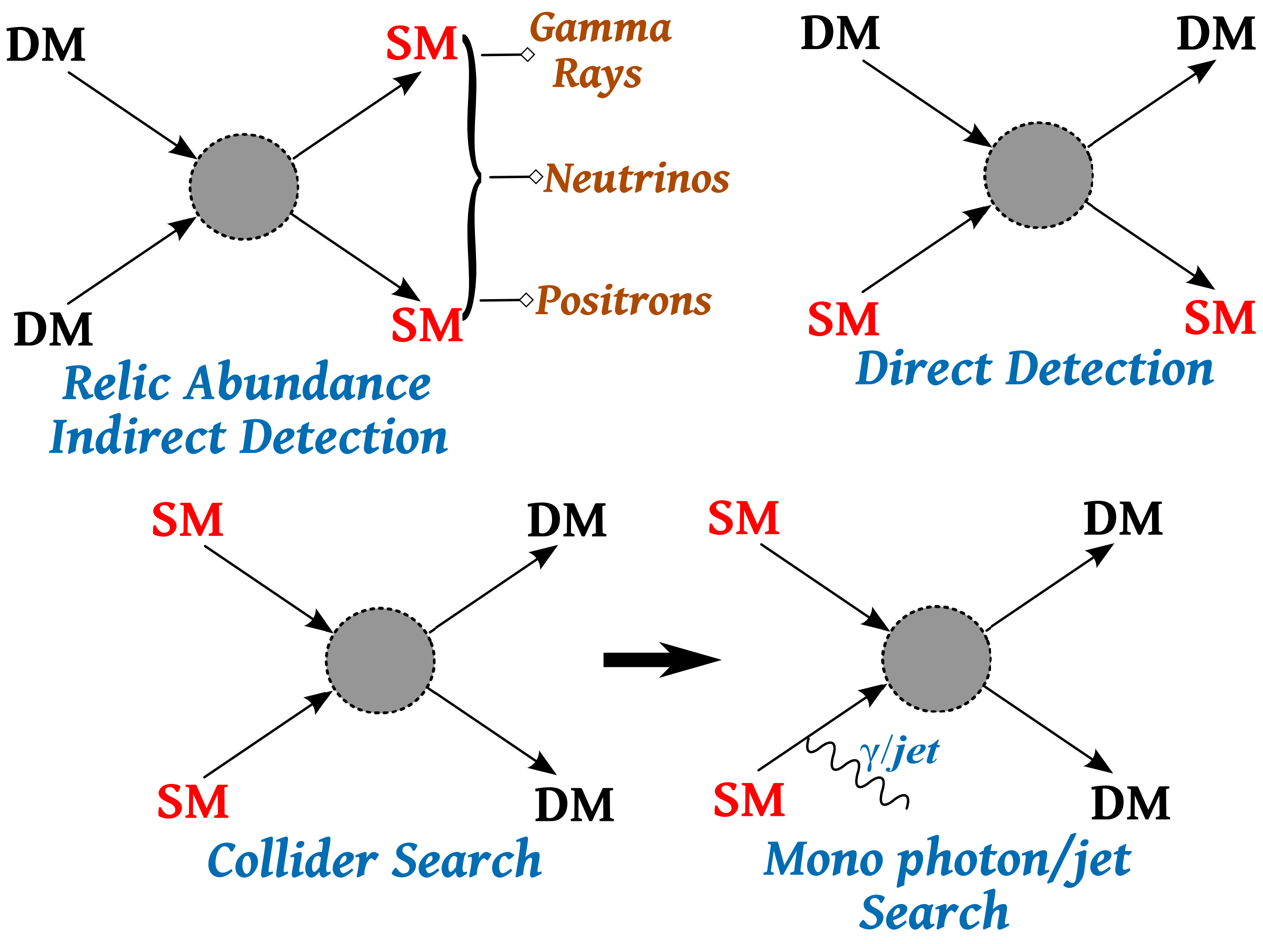

Figure 1: Feynman diagrams of the three types of searches of WIMP dark matter. Here DM stands for Dark Matter (WIMP) particles and SM Standard Model particles. All of them are equivalent since one diagram is nothing but a rotated version of another, *e.g.* the direct search diagram (top right) is just the indirect search diagram (top left) rotated 90 degrees clockwise. Besides enabling indirect detection by the visible particles they produce, annihilations of WIMPs (top left) are responsible for the relic abundance of WIMPs we observe today. Collider searches (bottom left) usually require some identifier (bottom right) since WIMPs do not react electromagnetically and hence pass through detectors, a common identifier is a photon or gluon (which decays into jets).

WIMP mass is roughly

$$M_{\text{WIMP}} \lesssim \frac{g^2}{0.3}\, 1.8 \text{ TeV}, \tag{1.1}$$

which miraculously coincides with the new physics scale expected based on the "naturalness" argument for electroweak physics. Therefore, there is a high hope that the search for a dark matter particle may be intimately related to the discovery of TeV scale new physics.

If their mass is not too great, it is likely WIMPs will appear in pairs at collider experiments such as the Large Hadron Collider (LHC) or future lepton colliders. If any pair of parity odd particles are produced, they will cascade decay down to the lightest parity odd particle, which is a stable dark matter candidate. Since they are nonbaryonic and electrically neutral, however, they will not react with the detectors and will, therefore, be very hard to detect. One common way to know whether WIMPs are produced during a collision is to use an identifier such as mono photon/jet, see Fig. 1, and finding out if there is missing momenta by balancing the initial and final momenta of all visible particles involved in the collision. Any missing momenta signify that there are invisible particles generated. As a result, it is very difficult to measure the properties of WIMPs, such as their mass and spin.

One conventional technique to measure WIMP mass is to use the end-point energy of the photon to measure the masses of the WIMPs in the event where there is nothing else produced by the collision except for a single photon [13]. Another past attempt in measuring WIMP mass is the measurement the endpoints of the energies of visible particles emitted in cascade decays [14, 15, 16, 17, 18, 19, 20, 21]. Recently, it was pointed out that if the cascade decays form an "antler" diagram, there are other kinematic cusps and endpoints which can be used [22].

In this article, we analyze the potential of antler cusps and endpoints at lepton (e^+e^-) colliders. Since the collision frame corresponds with the lab frame, we know the center of mass energy and, consequently, the full missing momentum. This allows the antler cusps and endpoints to be applied in the absence of a resonant particle at the beginning of the antler diagram. It also allows the construction of the invariant missing mass, which we show, also has kinematic cusps and endpoints related to the mass of the WIMPs. Our analysis includes the effects of cuts, initial state radiation (ISR), beamstrahlung and detector smearing on these observables. We also compare the antler cusps and endpoints to photon energy method and the visible energy endpoint method and show that it does much better than the former and as good as the latter. In this way, it gives further handles for the mass, increasing the significance of the measurement.

Although there are multiple models beyond the SM that contain WIMPs, we will concentrate on the MSSM and consider the scenario where the lightest neutralino is the Lightest Supersymmetric Particle (LSP) and, therefore, stable. We will consider the pair production of sleptons (charginos) which then decay to visible leptons (W bosons) and the LSP ($e^+e^- \to \tilde{l}^+(\tilde{\chi}_1^+)\tilde{l}^-(\tilde{\chi}_1^-) \to l^+(W^+)\, l^-(W^-)\chi_1^0\chi_1^0$). However, the qualitative features certainly apply to other WIMP scenarios.

1.1 A BRIEF REVIEW OF THE STANDARD MODEL

The Standard Model of particle physics, also known as the Glashow-Weinberg-Salam model, is the most complete and successfully tested physical theory of the subatomic particles, with the last piece of the puzzle, the Higgs particle, discovered recently at the LHC in 2012.

It describes the building blocks of (visible) matter using six leptons (electrons, muons, taus, neutrinos and their anti particles), six quarks (and their anti particles), gauge bosons, which are force carriers and finally the Higgs boson.

It is a gauge theory with gauge group SU(3)×SU(2)×U(1), complemented with spontaneous symmetry breaking and Yukawa couplings for mass generation of the gauge bosons and the fermions respectively. It has three sectors: the gauge and Higgs sector, the lepton sector and the quark sector. Each of these three sectors [23] will be briefly described in the following sub sections (with the emphasis on the mass generation mechanism). This discussion follows closely to that of [23].

The main purpose of this review is to show that spontaneous symmetry breaking does not generate any mass for the neutrinos (assuming there is no right handed neutrino), which is the only dark matter candidate in the Standard Model. Therefore, an extension of the Standard Model is needed to accommodate massive dark matter particles, hence our choice of Supersymmetry for this project, which will be discussed in the next section.

1.1.1 Gauge and Higgs Sector

The fields (or particles) in SM are represented under the gauge group by $(1, 2, -\frac{1}{2}) \oplus (1, 1, +1) \oplus (3, 2, +\frac{1}{6}) \oplus (\overline{3}, 1, -\frac{2}{3}) \oplus (\overline{3}, 1, +\frac{1}{3})$. The first number in each bracket is the representation of the SU(3), the second of SU(2) and the last of U(1).

The spontaneous electroweak symmetry breaking (Higgs mechanism) breaks the SU(2)×U(1) group down to a U(1), which is the gauge group of electromagnetism. Since the SU(3) is unbroken, the SU(3) gauge bosons (gluons) stay massless.

The Higgs field is represented by a complex scalar field $\phi(x)$ under the representation $(1, 2, -\frac{1}{2})$, the SU(2) components of which are given by $\phi(x) = \begin{pmatrix} \phi_1(x) + i\phi_2(x) \\ \phi_3(x) + i\phi_4(x) \end{pmatrix}$ with $\phi_{1,2,3,4}(x)$ all real.

Since the Standard Model is based on gauge theory, the SM Lagrangian has to be gauge invariant. This requirement necessitates the use of covariant derivatives and singlet interaction terms.

The coupling of the Higgs field with the gauge bosons are given through the covariant derivative as

$$D_\mu \phi = \partial_\mu \phi - i(g_2 A^a_\mu T^a + g_1 B_\mu Y)\phi \tag{1.2}$$

where A^a_μ is the gauge boson for the SU(2), B_μ the gauge boson for the U(1), $T^a = \frac{1}{2}\sigma^a$ the generators of the SU(2) gauge group, σ^a the Pauli matrices and Y the hyper charge of the U(1) gauge group. As we can see, ϕ does not couple to the gluons since it is under the singlet $(\mathbf{1}, 2, -\frac{1}{2})$ representation of SU(3).

Expanding the covariant derivative in matrix form, we get

$$D_\mu \phi = \partial_\mu \phi - \frac{i}{2} \begin{pmatrix} g_2 A^3_\mu - g_1 B_\mu & g_2(A^1_\mu - iA^2_\mu) \\ g_2(A^1_\mu + iA^2_\mu & -g_2 A^3_\mu - g_1 B_\mu \end{pmatrix} \phi. \tag{1.3}$$

This covariant derivative of the Higgs is the exact coupling that is responsible for generating masses for the (SU(2)) W and Z bosons. To achieve this, the Higgs field needs to acquire a vacuum expectation value (VEV), $\frac{1}{\sqrt{2}}v = \langle\phi\rangle$. Once the VEV is acquired, we can Taylor expand ϕ around v (in unitary gauge),

$$\phi(x) = \frac{1}{\sqrt{2}}\begin{pmatrix} v + H(x) \\ 0 \end{pmatrix}. \tag{1.4}$$

Through the kinetic term of the Higgs field, given by $D^\mu\phi(D_\mu\phi)^\dagger$, the expansion of ϕ around its VEV v gives us the following mass matrix for the gauge bosons,

$$\frac{1}{8}v^2(1\ 0)\begin{pmatrix} g_2A^3_\mu - g_1B_\mu & g_2(A^1_\mu - iA^2_\mu) \\ g_2(A^1_\mu + iA^2_\mu & -g_2A^3_\mu - g_1B_\mu \end{pmatrix}^2\begin{pmatrix} 1 \\ 0 \end{pmatrix}. \tag{1.5}$$

Diagonalizing this mass matrix by introducing the Weinberg angle θ_W and defining the W, Z bosons and A (photon) as

$$\begin{aligned} \theta_W &\equiv \tan^{-1}\left(\tfrac{g1}{g2}\right) \\ W^\pm_\mu &\equiv \tfrac{1}{\sqrt{2}}(A^1_\mu \mp iA^2_\mu) \\ Z_\mu &\equiv \cos(\theta_W)A^3_\mu - \sin(\theta_W)B_\mu \\ A_\mu &\equiv \sin(\theta_W)A^3_\mu + \cos(\theta_W)B_\mu \end{aligned} \tag{1.6}$$

yields the following diagonal mass matrix

$$\begin{aligned} &\tfrac{1}{8}g_2^2v^2(1\ 0)\begin{pmatrix} \frac{1}{\cos(\theta_W)}Z_\mu & \sqrt{2}W^+_\mu \\ \sqrt{2}W^-_\mu & \frac{1}{\cos(\theta_W)}A_\mu \end{pmatrix}^2\begin{pmatrix} 1 \\ 0 \end{pmatrix} \\ = \ & M_W^2W^{+\mu}W^-_\mu + \tfrac{1}{2}M_Z^2Z^\mu Z_\mu \end{aligned} \tag{1.7}$$

with $M_W = \frac{g_2v}{2}$ and $M_Z = \frac{g_2v}{2\cos(\theta_W)}$.

Here we see that while both W and Z bosons acquire mass, the photon A remains massless, this is the heart of the Weinberg-Salam model. The mass generation of the leptons is done through Yukawa coupling, which will be reviewed next.

1.1.2 Lepton Sector

The Standard Model accommodates three families of leptons (electron, mu, tau and their respective neutrinos). Each family of leptons is represented by left-handed Weyl (2-component) fields l and $\overline{e}$ under the representation of $(1, 2, -\frac{1}{2})$ and $(1, 1, +1)$ respectively, *i.e.*

$l(x) = \left(\begin{array}{c} \nu(x) \\ e(x) \end{array} \right)$ and $\overline{e}(x) = \overline{e}(x)$.

For now, we can think of $\nu(x)$ as a left handed neutrino field, $e(x)$ as a left handed electron field and $\overline{e}^{\dagger}(x)$ as a right handed electron field.

The complex representation of l is needed because the Standard Model has to incorporate parity violation for weak interactions. Choosing a complex representation means that the left handed l and the right handed $l^{\dagger}$ are in ***different*** representations of the gauge group, and since parity transformation changes a left handed Weyl field to a right handed one (and vice versa), the Lagrangian density containing l and $l^{\dagger}$ is automatically parity violating.

Both l and $\overline{e}$ couple to the gauge bosons through the covariant derivative in their kinetic terms given by

$$il^{\dagger}\overline{\sigma}^{\mu}(D_{\mu}l) + i\overline{e}^{\dagger}\overline{\sigma}^{\mu}(D_{\mu}\overline{e}) \tag{1.8}$$

where $\overline{\sigma}^{\mu} \equiv (I, -\vec{\sigma})$ with $\vec{\sigma}$ being a three dimensional vector of Pauli matrices.

After symmetry breaking and diagonalization of the mass matrix of the gauge bosons, this kinetic term gives the coupling of the leptons to the weak currents.

Forming a singlet using only l and $\overline{e}$ under their chosen representations alone is impossible, making a mass term non existent. However, the Higgs field $\phi(x)$ introduced in the previous section can be combined with both l and $\overline{e}$ to form a singlet under SU(2) × U(1), given by

$$y\epsilon^{ij}\phi_i l_j \overline{e} + (y\epsilon^{ij}\phi_i l_j \overline{e})^{\dagger}. \tag{1.9}$$

Expanding the Higgs field around its VEV (in unitary gauge) yields

$$\frac{y}{\sqrt{2}}(H(x) + v)(l_2\overline{e} + (l_2\overline{e})^{\dagger}) = \frac{y}{\sqrt{2}}(H(x) + v)(e\overline{e} + \overline{e}^{\dagger}e^{\dagger}). \tag{1.10}$$

By defining a 4-component Dirac field for the lepton $\psi_e(x) \equiv \left(\begin{array}{c} e(x) \\ \overline{e}^{\dagger}(x) \end{array} \right)$ we get a lepton mass term of the form $\left(\frac{yv}{\sqrt{2}}\right)\overline{\psi}_e\psi_e$, where $\overline{\psi}_e = \psi_e^{\dagger}\gamma^0$. We can easily read off the mass of the lepton to be $M_e = \frac{vy}{\sqrt{2}}$ while the neutrino $\nu = l_1$ remains massless. The mass generation for the other two families of leptons are produced in the same way.

As a side note, a more general Yukawa coupling for the leptons can be written as $y_{IJ}\epsilon^{ij}\phi_i l_{jI}\overline{e}_J$ where I and J are the family index. In this case y_{IJ} is a 3×3 matrix and has to be diagonalized to obtain mass eigenstates of the leptons. The diagonalization of y_{IJ} has the potential of mixing different families of leptons, but since the neutrinos are massless we can always redefine the mass eigenstates of the neutrinos while leaving the massive leptons in tact.

1.1.3 Quark Sector

The quark mass generation mechanism follows closely from their lepton counterpart. So far there are only six observed flavors of quarks grouped in three families. Each family of quarks is represented by three left handed Weyl fields, q, $\overline{u}$, $\overline{d}$ under the representations $(3, 2, +\frac{1}{6})$, $(\overline{3}, 1, -\frac{2}{3})$, $(\overline{3}, 1, +\frac{1}{3})$ respectively, where the SU(2) components are
$q(x) = \left(\begin{array}{c} u(x) \\ d(x) \end{array}\right)$, $\overline{u}(x) = \overline{u}(x)$ and $\overline{d}(x) = \overline{d}(x)$. (Since the Higgs does not break SU(3), its components are not shown). We can think of u as a left handed up quark and d as a left handed down quark.

As with the leptons, the quarks are under complex representations, producing a chiral (parity violating) Lagrangian. As usual, the quarks couple to the gauge bosons through the covariant derivative but since they are not singlet under SU(3), they couple to the W, Z bosons, photons and also the gluons.

Yukawa coupling is also needed to generate mass because no singlet combination can be formed using the above mentioned representations alone. The Higgs field $\phi(x)$ is needed to form a singlet combination, which is

$$y'\phi_i^\dagger q^i \overline{u} + y''\epsilon^{ij}\phi_i q_j \overline{d} + (y'\phi_i^\dagger q^i \overline{u} + y''\epsilon^{ij}\phi_i q_j \overline{d})^\dagger. \tag{1.11}$$

Taylor expanding the Higgs field in unitary gauge gives

$$\begin{aligned} & \tfrac{1}{\sqrt{2}}y'(v+H)q_1\overline{u} + \tfrac{1}{\sqrt{2}}y''(v+H)q_2\overline{d} + (\tfrac{1}{\sqrt{2}}y'(v+H)q_1\overline{u} + \tfrac{1}{\sqrt{2}}y''(v+H)q_2\overline{d})^\dagger \\ = \; & \tfrac{1}{\sqrt{2}}y'(v+H)(u\overline{u} + \overline{u}^\dagger u^\dagger) + \tfrac{1}{\sqrt{2}}y''(v+H)(d\overline{d} + \overline{d}^\dagger d^\dagger). \end{aligned} \tag{1.12}$$

Defining 4-component Dirac Fields $\psi_u \equiv \begin{pmatrix} u \\ \overline{u}^\dagger \end{pmatrix}$ and $\psi_d \equiv \begin{pmatrix} d \\ \overline{d}^\dagger \end{pmatrix}$, we get $\frac{1}{\sqrt{2}}y'(v+H)\overline{\psi}_u\psi_u + \frac{1}{\sqrt{2}}y''(v+H)\overline{\psi}_d\psi_d$, where we can easily read off the masses of the up and down quarks, they are $M_u = \frac{y'v}{\sqrt{2}}$ and $M_d = \frac{y''v}{\sqrt{2}}$ respectively. Notice that both up and down quarks acquire mass while in the lepton case the neutrino remains massless.

We now generalize the Yukawa coupling to include all three families of quarks, $y'_{IJ}\phi_i^\dagger q_I^i \overline{u}_J + y''_{IJ}\epsilon^{ij}\phi_i q_I^i \overline{d}_J + (y'_{IJ}\phi_i^\dagger q_I^i \overline{u}_J + y''_{IJ}\epsilon^{ij}\phi_i q_I^i \overline{d}_J)^\dagger$, where I, J are family indices.

The y'_{IJ} and y''_{IJ} are now 3 × 3 matrices. In this case, the mass eigenstates of the quarks are obtained by diagonalizing both Yukawa matrices. To do this we introduce unitary transformations, $u_I \rightarrow U_{IJ}u_J$, $\overline{u}_I \rightarrow \overline{U}_{IJ}u_J$, $d_I \rightarrow D_{IJ}d_J$, $\overline{d}_I \rightarrow \overline{D}_{IJ}\overline{d}_J$. We choose U, $\overline{U}$, D, $\overline{D}$, such that $U^T y' \overline{U}$ and $D^T y'' \overline{D}$ are both diagonal and real. Note that these unitary transformations leave the kinetic terms of the quarks invariant. They, however, change the couplings of the quarks to the W bosons by a CKM (Cabibbo-Kobayashi-Maskawa) matrix (V_{CKM}) given by the product of unitary transformations above which is

$$V_{\text{CKM}} \equiv \overline{U}D. \tag{1.13}$$

1.1.4 Dark Matter in the Standard Model

Dark matter is known to not interact strongly or electromagnetically, and as can be seen from the previous three subsections, the only candidate for Dark Matter (DM) particle in the Standard Model is the neutrino. Since the neutrinos are exactly massless in SM, they are relativistic (so called hot dark matter).

There has been evidences that hot dark matter is constrained to only a tiny fraction of the mass density of the universe. Thus a cold dark matter is needed to explain our current cosmological observations [24]. Furthermore, even though neutrinos were recently found to have mass, the lower bound on the mass of cold dark matter at roughly 2 keV [24] still puts them as hot dark matter.

There are several candidates for cold dark matter including primordial black holes, axions and gravitinos but in this article, we will focus solely on the Lightest Supersymmetric Particle (LSP) of Minimal Supersymmetric Standard Model (MSSM) as dark matter. This choice merely serves as an example of how the antler scheme works in detecting dark matter at particle colliders and not as an advocate of what dark matter really is.

1.2 A PEDESTRIAN LOOK AT SUPERSYMMETRY

Supersymmetry (SUSY) was initially introduced as a symmetry in String theory [25]. Nowadays however, it is the most popular extension of the Standard Model. One particular nice feature of SUSY is that it tames the fine tuning required in the Higgs radiative correction due to the cancellation between bosonic and fermionic loops. It also has, as an added bonus, candidates for cold dark matter, especially WIMPs.

It is interesting to note that SUSY does not unify known particles (or forces), instead it adds a superpartner to each known particle in the Standard Model.

The following discussion reviews the basics of SUSY and it follows closely that of [26]. Supersymmetry is an inherently rich subject, the following discussion focuses only on the basics and the mechanism that enables SUSY to provide a cold dark matter candidate.

1.2.1 Supersymmetry Basics

The choice of 2-component Weyl fields in the previous subsections was a judicious one as a segway to Supersymmetry. The main idea of Supersymmetry is to extend Poincaré symmetry by adding generators that act like spinors.

1.2.1.1 A Brief Review of Poincaré Algebra Poincaré group is a symmetry group that contains both Lorentz transformations (boosts and rotations) and translations.

The Lorentz group has six generators, three for boosts (K_i) and three for rotations(J_i). The generators' algebra is given by

$$\begin{aligned} [J_i, J_j] &= i\epsilon_{ijk} J_k \\ [K_i, K_j] &= -i\epsilon_{ijk} K_k \\ [J_i, K_j] &= i\epsilon_{ijk} K_k \end{aligned} \tag{1.14}$$

They are commonly expressed in terms of $J_j^{\pm} = \frac{1}{2}(J_j \pm iK_j)$ with the algebra

$$\begin{aligned} [J_i^{\pm}, J_j^{\pm}] &= i\epsilon_{ijk} J_k^{\pm} \\ [J_i^{\pm}, J_j^{\mp}] &= 0 \end{aligned} \tag{1.15}$$

The merit of rewriting the generators in terms of $J^{\pm}$ is that it is now easy to see that the Lorentz group is made up of two SU(2)'s, which is equivalent to SL(2,C) (the group of complex two by two matrices with determinant ±1). In fact, spinors (which will be used heavily in the following sections) are a basic representation of SL(2,C). This is why a spinor ψ_α and its conjugate (usually denoted by a dot on top of the component index) $\overline{\psi}_{\dot\alpha} = (\psi_\alpha)^\dagger$ are in two *different* representations.

To complete the Poincaré group we add the translation generator (P_μ). The full Poincaré algebra then reads

$$\begin{aligned} [P_\mu, P_\nu] &= 0 \\ [M_{\mu\nu}, M_{\rho\sigma}] &= ig_{\nu\rho} M_{\mu\sigma} - ig_{\mu\rho} M_{\nu\sigma} - ig_{\nu\sigma} M_{\mu\rho} + ig_{\mu\sigma} M_{\nu\rho} \\ [M_{\mu\nu}, P_\rho] &= -ig_{\rho\mu} P_\nu + ig_{\rho\nu} P_\mu \end{aligned} \tag{1.16}$$

where $M_{\mu\nu}$ is anti symmetric and $M_{0i} = K_i, M_{ij} = \epsilon_{ijk} J_k$. The last commutation relation is needed to make sure that the algebra closes (which roughly means that the commutations of P_μ and $M_{\mu\nu}$ results in P_μ and $M_{\mu\nu}$).

1.2.1.2 Supersymmetric Algebra The main idea of Supersymmetry is to add Supersymmetric generators to the Poincaré group denoted by Q_α^I and $\overline{Q}_{\dot\alpha}^I$, where $\alpha, \dot\alpha$ are the spinor indices. The index I indicates that there can be more than one pair of new generators. The new generators are spinorial objects, *i.e.* they are in the $(\frac{1}{2}, 0)$ and $(0, \frac{1}{2})$ representations of the Lorentz group respectively. As such, they anti commute among themselves although they have to commute with translations. The additional algebra is then given by

$$\begin{aligned}
[P_\mu, Q^I_\alpha] &= 0 \\
[P_\mu, Q^I_{\dot\alpha}] &= 0 \\
[M_{\mu\nu}, Q^I_\alpha] &= i(\sigma_{\mu\nu})_\alpha{}^\beta Q^I_\beta \\
[M_{\mu\nu}, Q^{I\dot\alpha}] &= i(\overline{\sigma}_{\mu\nu})^{\dot\alpha}{}_{\dot\beta}\overline{Q}^{I\dot\beta} \\
\{Q^I_\alpha, Q^J_{\dot\beta}\} &= 2\sigma_{\alpha\dot\beta}P_\mu\delta^{IJ} \\
\{Q^I_\alpha, Q^J_\beta\} &= \epsilon_{\alpha\beta}Z^{IJ} \\
\{\overline{Q}^I_{\dot\alpha}, \overline{Q}^J_{\dot\beta}\} &= \epsilon_{\dot\alpha\dot\beta}Z^{IJ}
\end{aligned} \tag{1.17}$$

where $(\sigma_{\mu\nu})_\alpha{}^\beta$ and $(\overline{\sigma}_{\mu\nu})^{\dot\alpha}{}_{\dot\beta}$ are the Lorentz group generators for Q^I_α and $\overline{Q}^{I\dot\beta}$, Z^{IJ} are the (anti commuting) central charges (they are automatically zero if there is only one pair of Supersymmetric generators). The anti commutation relations are needed to make sure that the algebra closes.

To illustrate what Supersymmetric generators do, take $\mu = 1$ and $\nu = 2$ for example, for which the algebra then reads

$$\begin{aligned}
[J_3, Q^I_1] &= \tfrac{1}{2}Q^I_1 \\
[J_3, \overline{Q}^{I1}] &= \tfrac{1}{2}\overline{Q}^{I1} \\
[J_3, Q^I_2] &= -\tfrac{1}{2}Q^I_2 \\
[J_3, \overline{Q}^{I2}] &= -\tfrac{1}{2}\overline{Q}^{I2}
\end{aligned} \tag{1.18}$$

which means that the (spinor components of the) Q^I_α and $\overline{Q}^I_{\dot\alpha}$ acting on a particle state changes the spin by a half unit. In short, Supersymmetry is a symmetry that relates bosons to fermions and vice versa.

It is important to note that in this article we will only deal with *one* pair of spinorial generators, $I = 1$.

We will now state the properties of Supersymmetric algebra without derivation, for detailed explanation please see [26]. First, the irreducible representation of Supersymmetric algebra (called a supermultiplet) represents multiple particles and it contains the same number of fermionic and bosonic degrees of freedom. Second, both bosons and fermions in the same supermultiplet have the same mass. Lastly, Supersymmetric states have energy greater than or equal to zero.

As an example, consider a massless supermultiplet. In this case, there will be only two states, a fermion and a boson. They are usually organized into chiral multiplets containing spin 0 and spin $\frac{1}{2}$ and a vector multiplet containing spin $\frac{1}{2}$ and spin 1.

1.2.1.3 Superspace and Superfields

In order to construct a Supersymmetric Lagrangian, it is most convenient to use the formalism of Superspace and Superfields.

The idea of superspace is very similar to the Supersymmetric algebra. It is an extension of the normal space time by the inclusion of (anti commuting) spinorial superspace coordinates θ_α and $\overline{\theta}_{\dot{\alpha}}$ (much like the same way we add anti commuting generators to Poincaré algebra). The complete superspace coordinates are then $(x^\mu, \theta_\alpha, \overline{\theta}_{\dot{\alpha}})$.

It is interesting to note that for anti commuting (Grassmanian) numbers, integral operations are always defined to be integral from $-\infty$ to ∞. In addition, a derivative operation is the same as an integral operation.

A superfield is then defined to be a function of the superspace with the restriction that it should have the same number of fermionic and bosonic degrees of freedom as discussed earlier. A (scalar) superfield is thus (all spinor indices suppressed)

$$\begin{aligned} S(x,\theta,\overline{\theta}) &= f(x) + \theta\psi(x) + \overline{\theta}\overline{\chi}(x) + \theta\theta m(x) + \overline{\theta\theta}n(x) + \theta\sigma^\mu\overline{\theta}v_\mu(x) \\ &\quad +\theta\theta\overline{\theta\lambda}(x) + \overline{\theta\theta}\theta\rho(x) + \overline{\theta\theta}\theta\theta d(x). \end{aligned} \tag{1.19}$$

Since θ's ($\overline{\theta}$'s) are anti commuting, there are at most only two powers of θ ($\overline{\theta}$).

The Supersymmetric generators then produce an infinitesimal transformation in $S(x,\theta,\overline{\theta})$ defined as

$$(1 + i\epsilon Q + i\overline{\epsilon}\overline{Q})S(x^\mu, \theta^\alpha, \overline{\theta}^{\dot{\beta}}) = S(x^\mu - i\epsilon\sigma^\mu\overline{\theta} + i\epsilon\sigma^\mu\overline{\epsilon}, \theta^\alpha + \epsilon^\alpha, \overline{\theta}^{\dot{\beta}} + \overline{\epsilon}^{\dot{\beta}}) \tag{1.20}$$

from which we can read off

$$\begin{aligned} Q_\alpha &= -i\tfrac{\partial}{\partial\theta^\alpha} - \sigma^\mu_{\alpha\dot{\beta}}\overline{\theta}^{\dot{\beta}}\partial_\mu \\ \overline{Q}_{\dot{\alpha}} &= i\tfrac{\partial}{\partial\overline{\theta}^{\dot{\alpha}}} + \theta^\beta\overline{\sigma}^\mu_{\beta\dot{\alpha}}\partial_\mu \end{aligned} \tag{1.21}$$

where $\frac{\partial}{\partial\theta^\alpha}$ and $\frac{\partial}{\partial\overline{\theta}^{\dot{\alpha}}}$ are also taken to be anti commuting.

To construct a Lagrangian, one needs a derivative. In this case it has to be a Supersymmetric covariant derivative (acting on a superfield it returns a superfield), *i.e.* it anti commutes with the Q's:

$$\begin{aligned}\{D_\alpha, Q_\beta\} = \{D_\alpha, \overline{Q}_{\dot\beta}\} = \{\overline{D}_{\dot\alpha}, Q_\beta\} &= \{\overline{D}_{\dot\alpha}, \overline{Q}_{\dot\beta}\} = \{D_\alpha, D_\beta\} = \{\overline{D}_{\dot\alpha}, \overline{D}_{\dot\beta}\} = 0 \\ \{D_\alpha, \overline{D}_{\dot\beta}\} &= 2i\sigma^\mu_{\alpha\dot\beta}\partial_\mu\end{aligned} \tag{1.22}$$

with $\overline{D}_{\dot\alpha} = (D_\alpha)^\dagger$, the D's are also anti commuting spinorial objects. The last three anti commutations are there to make sure that the algebra closes.

Thus, the covariant derivative is defined to be

$$\begin{aligned}D_\alpha &= \tfrac{\partial}{\partial\theta^\alpha} + i\sigma^\mu_{\alpha\dot\beta}\overline{\theta}^{\dot\beta}\partial_\mu \\ \overline{D}_{\dot\alpha} &= \tfrac{\partial}{\partial\overline{\theta}^{\dot\alpha}} + i\theta^\beta\overline{\sigma}^\mu_{\beta\dot\alpha}\partial_\mu\end{aligned} \tag{1.23}$$

As currently stated, $S(x^\mu, \theta^\alpha, \overline{\theta}^{\dot\beta})$ has too many degrees of freedom to be a scalar superfield. This only means that S is a reducible representation. To reduce the number of degrees of freedom we should impose a supersymmetric invariant constraint.

A constraint of the form

$$\begin{aligned}\overline{D}_{\dot\alpha}\phi &= 0 \\ D_\alpha\overline{\phi} &= 0\end{aligned} \tag{1.24}$$

defines a chiral (anti chiral) ϕ ($\overline{\phi}$) superfield. Note that since $D_\alpha\overline{\theta} = \overline{D}_{\dot\alpha}\theta = 0$, ϕ ($\overline{\phi}$) is more conveniently expressed in terms of $y^\mu = x^\mu + i\theta\sigma^\mu\overline{\theta}$, where $D_\alpha\overline{y}^\mu = \overline{D}_{\dot\alpha}y^\mu = 0$. The chiral superfield $\phi(y, \theta)$ is then given by

$$\phi(y, \theta) = z(y) + \sqrt{2}\theta\psi(y) - \theta\theta f(y). \tag{1.25}$$

The chiral superfield $\phi(y, \theta)$ now has the correct number degrees of freedom for an irreducible representation, two real degrees of freedom from the complex scalar $z(y)$, two helicities of the fermion $\psi(y)$, plus an auxiliary field $f(y)$ to account for the off shell degrees of freedom of the fermion (a Weyl field has two *complex* components → four real degrees of freedom) [27].

Under Supersymmetric generators, the chiral superfield transforms as

$$\begin{aligned} \delta\phi(y,\theta) &\equiv (i\epsilon Q + i\overline{\epsilon}\overline{Q})\phi(y,\theta) \\ &= \sqrt{(2)}\epsilon\psi + \sqrt{2}\theta(\sqrt{2}i\sigma^{\mu}\overline{\epsilon}\partial_{\mu}z - \sqrt{2}\epsilon f) + \theta\theta(i\sqrt{2}\overline{\epsilon}\overline{\sigma}^{\mu}\partial_{\mu}\psi) \end{aligned} \tag{1.26}$$

We can then easily read off the transformation of the component fields

$$\begin{aligned} \delta z &= \sqrt{2}\epsilon\psi \\ \delta\psi &= \sqrt{2}i\sigma^{\mu}\overline{\epsilon}\partial_{\mu}z - \sqrt{2}\epsilon f \\ \delta f &= i\sqrt{2}\overline{\epsilon}\overline{\sigma}^{\mu}\partial_{\mu}\psi \end{aligned} \tag{1.27}$$

It corroborates the result shown previously that a Supersymmetric transformation changes a boson to a fermion and a fermion to a boson and it also confirms the need of an auxiliary field to account for the off shell degrees of freedom of the fermion field.

We now turn to the subject of the inclusion of gauge symmetry in Supersymmetry. For this purpose we need a vector superfield, defined as e^V, where $V \equiv 2gV^aT^a$, T^a the generators of the gauge group in the adjoint representation and g the gauge coupling strength.

The matrix valued Supersymmetrically irreducible vector superfield (in Wess-Zumino supergauge) is given by

$$V_{WZ}(x,\theta,\overline{\theta}) = \theta\sigma^{\mu}\overline{\theta}v_{\mu}(x) + i\theta\theta\overline{\theta}\overline{\lambda}(x) - i\overline{\theta}\overline{\theta}\theta\lambda(x) + \frac{1}{2}\theta\theta\overline{\theta}\overline{\theta}D(x) \tag{1.28}$$

where $v_{\mu} = 2gv_{\mu}^{a}T^{a}, \lambda = 2g\lambda^{a}T^{a}$, and $D = 2gD^{a}T^{a}$. Here, v_{μ} is the gauge boson while λ is its superpartner, usually dubbed the gauginos.

It is easy to check that $V^n = 0$ for $n > 2$ and thus

$$e^V = 1 + V + \frac{1}{2}V^2. \tag{1.29}$$

The gauge transformation of e^V is given by $e^V \rightarrow e^{-i\Lambda^{\dagger}}e^Ve^{i\Lambda}$ where Λ is a chiral superfield.

1.2.1.4 Supersymmetric Lagrangian We are now in a position to build a Supersymmetric and gauge invariant Lagrangian. The only change we need is that the chiral superfield ϕ now takes a representation R of the gauge group G and transforms as $\phi^i \to (e^{i2g\Lambda})^i_j \phi^j$.

The Supersymmetric and gauge invariant kinetic term of the chiral superfield is now given by $\mathcal{L}_{kin} = \int d^2\theta d^2\overline{\theta}\ \phi^\dagger e^V \phi$. The integral $\int d^2\theta d^2\overline{\theta}$ means that we only need the term proportional to $\theta\theta\overline{\theta\theta}$ (usually called the D-term) in $\phi^\dagger e^V \phi$, which is given by

$$\phi^\dagger e^V \phi \to (D_\mu z)^\dagger D^\mu z - i\overline{\psi}\overline{\sigma}^\mu D_\mu \psi + f^\dagger f + \frac{1}{2} z^\dagger D z + \frac{i}{\sqrt{2}} z^\dagger \lambda \psi - \frac{i}{\sqrt{2}} \overline{\psi\lambda} z \tag{1.30}$$

where here D_μ is only the gauge covariant derivative (not the Supersymmetric covariant derivative), $D_\mu = \partial_\mu - igv^a_\mu T^a$, v^a_μ is a component field of the vector superfield V but now T^a is in the same representation R of ϕ.

The Supersymmetric potential (superpotential) for the chiral superfield is given by the observation that $\int d^2\theta d^2\overline{\theta}\ \delta^2(\overline{\theta}) F(\phi) = \int d^2\theta F(\phi)$ is also invariant under Supersymmetry. From this definition, it is clear that the only part of $F(\phi)$ that contributes to the integral is the one proportional to $\theta\theta$. Thus $F(\phi)$ has to be a function of only ϕ and not its conjugate $\phi^\dagger$, *i.e.* $F(\phi)$ has to be a holomorphic function of ϕ [27]. This Supersymmetrically invariant term in the superfield is conventionally called the F-term. Hence we can take the superpotential $W(\phi)$ to be any holomorphic function of ϕ.

The full Lagrangian for ϕ is then given by

$$\begin{aligned} \mathcal{L}_{chiral} &= \int d^2\theta d^2\overline{\theta}\ ((D_\mu z)^\dagger D^\mu z - i\overline{\psi}\overline{\sigma}^\mu D_\mu \psi + f^\dagger f + \tfrac{1}{2} z^\dagger D z + \tfrac{i}{\sqrt{2}} z^\dagger \lambda \psi - \tfrac{i}{\sqrt{2}} \overline{\psi\lambda} z) \\ &\quad + \int d^2\theta\ W(\phi) + \int d^2\overline{\theta} W^\dagger(\phi). \end{aligned} \tag{1.31}$$

To construct the kinetic term for the vector superfield we need

$$\begin{aligned} W_\alpha &= -\tfrac{1}{4}\overline{DD}(e^{-V} D_\alpha e^V) \\ \overline{W}_{\dot{\alpha}} &= \tfrac{1}{4} DD(e^{-V} \overline{D}_{\dot{\alpha}} e^V) \end{aligned} \tag{1.32}$$

Turning to Wess-Zumino supergauge and Taylor expanding e^V we get

$$\begin{aligned} W_\alpha &= -\tfrac{1}{4}\overline{DD} D_\alpha V + \tfrac{1}{8}\overline{DD}[V, D_\alpha V] \\ W_\alpha &= -i\lambda_\alpha(y) + \theta_\alpha D(y) + i(\sigma^{\mu\nu}\theta)_\alpha F_{\mu\nu}(y) + \theta\theta(\sigma^\mu D_\mu \overline{\lambda}(y))_\alpha \end{aligned} \tag{1.33}$$

where $F_{\mu\nu} = \partial_\mu v_\nu - \partial_\nu v_\mu - ig[v_\mu, v_\nu]$ is the field strength tensor for the component field v_μ and D_μ the gauge covariant derivative.

The Lagrangian for the vector superfield is conventionally defined as

$$\begin{aligned} \mathcal{L}_{gauge} &= \tfrac{1}{32\pi}\mathrm{Im}(\tau \textstyle\int d^2\theta \ \mathrm{Tr}(W^\alpha W_\alpha)) \\ &= \mathrm{Tr}(-\tfrac{1}{4}F^{\mu\nu}F_{\mu\nu} - i\lambda\sigma^\mu D_\mu\overline{\lambda} + \tfrac{1}{2}D^2) + \tfrac{\Theta}{64\pi^2}g^2\epsilon^{\mu\nu\rho\sigma}\mathrm{Tr}(F_{\mu\nu}F_{\rho\sigma}) \end{aligned} \tag{1.34}$$

where $\tau \equiv \frac{\Theta}{2\pi} + \frac{4\pi i}{g^2}$, Θ is the CP violating angle.

However, if there is a U(1) gauge group, the D-term of V (gD) contributes as well, making the complete Lagrangian

$$\mathcal{L}_{gauge} = \frac{1}{32\pi}\mathrm{Im}(\tau \int d^2\theta \mathrm{Tr}(W^\alpha W_\alpha)) + gD. \tag{1.35}$$

1.2.2 Softly Breaking Supersymmetry

As mentioned earlier, particles and their superpartners have the same mass if Supersymmetry is an exact symmetry. The fact that these superpartners have not been observed in *any* experiment conducted to date means that Supersymmetry has to be broken such that the superpartners have a very different mass from their Standard Model counterparts. In fact, this is *the* major difficulty of Supersymmetry. Since it has to be broken it introduces many new parameters, for example, the MSSM breaking produces 105 new masses, phases and angles [27]. It is somewhat hard to believe that a theory that is supposedly more fundamental than the Standard Model has such a high degree of arbitrariness.

The most straight forward way to break Supersymmetry is to introduce terms in the Lagrangian that explicitly break Supersymmetry. To keep Supersymmetry kosher[27], the couplings in these terms have to have positive mass dimension, hence the name soft breaking, they are of the form

$$\mathcal{L}_{soft} = -(\frac{1}{2}M_a\lambda^a\lambda^a + \frac{1}{6}a^{ijk}\phi_i\phi_j\phi_k + \frac{1}{2}b^{ij}\phi_i\phi_j + t^i\phi_i) - (m^2)^i_j\phi^\dagger\phi \tag{1.36}$$

and its conjugate.

The fields in the soft breaking term are the component fields with λ_a the gauginos, ϕ_i the complex scalar fields. The soft breaking terms explicitly introduce masses to the gauginos and the scalar fields. In addition, they provide interactions between the component fields. $\mathcal{L}_{soft}$ clearly breaks Supersymmetry since each component field is not accompanied by its superpartner.

In this age of symmetry supremacy, explicit breaking is heavily frowned upon. It is then believed that Supersymmetry breaking is achieved spontaneously through a hidden sector that becomes the soft breaking terms in the effective Lagrangian, for details see [27].

An important thing to note, Supersymmetry breaking is not to be confused with gauge symmetry breaking, which is the Higgs mechanism.

1.2.3 Minimal Supersymmetric Standard Model (MSSM)

Now we have all the ingredients to construct a Supersymmetric extension of the Standard Model. There are many routes towards constructing an extension, however, in this article we will consider the Minimal Supersymmetric Standard Model (MSSM).

As the name suggests, MSSM only adds superpartners to the already known particles in the Standard Model without introducing any new particles (modulo an extra Higgs field and its superpartner).

The MSSM, just like the Standard Model, is under the SU(3)×SU(2)×U(1) gauge group and consists of seven chiral superfields. And since it is a Supersymmetric theory, all the gauge bosons are accompanied by their gaugino superpartners. The seven chiral fields are given in the Table. 1. Except for the extra Higgs field, MSSM's particle content is the same as that of the Standard Model, although of course that each field is now a superfield.

The superpotential for the MSSM is given by (family indices suppressed)

$$W_{MSSM} = \mu\phi_u\phi_d - y_e\phi_d l\overline{e} + y_u\phi_u q\overline{u} - y_d\phi_d q\overline{d}. \tag{1.37}$$

Each term is gauge invariant as well as supersymmetric invariant. The Yukawa couplings, y_e, y_u, y_d, are understood to be 3×3 matrices in the family space. It is now clear why the MSSM requires two Higgs fields. Since the superpotential can only be a holomorphic function

Table 1: Particle content of the MSSM, name in bracket is the superpartner designation, *e.g.* the superpartner of the Higgs boson is called the Higgsino, the symbol with tilde on top is the conventional symbol used for the superpartner

Name	Symbol	SU(3)×SU(2)×U(1) Rep
Higgs(inos)	ϕ_u ($\widetilde{\phi}_u$)	(1,2,+$\frac{1}{2}$)
	ϕ_d ($\widetilde{\phi}_d$)	(1,2,-$\frac{1}{2}$)
(s)leptons	l ($\widetilde{l}$)	(1,2,-$\frac{1}{2}$)
	$\overline{e}$ ($\widetilde{\overline{e}}$)	(1,2,1)
(s)quarks	q ($\widetilde{q}$)	(3,2,+$\frac{1}{6}$)
	$\overline{u}$ ($\widetilde{\overline{u}}$)	($\overline{3}$,2,-$\frac{2}{3}$)
	$\overline{d}$ ($\widetilde{\overline{d}}$)	($\overline{3}$,2,+$\frac{1}{3}$)

of chiral superfields, one can not use $\phi_d^\dagger$ to make a gauge singlet for the combination of $\overline{u}$ and q like the one in the Standard Model, see Eq. 1.11 for comparison.

The superpotential W_{MSSM} produces the same particle interactions as that of the Standard Model as well as new interactions involving the superpartners like squark-Higgsino-quark, slepton-Higgsino-lepton and Higgs-Higgs-squark-squark vertices.

1.2.4 Softly Breaking the MSSM

We now turn to the subject of soft symmetry breaking terms in the MSSM so as to give different masses to the superpartners. It is given by

$$\begin{aligned}\mathcal{L}_{soft} \quad = \quad & -\tfrac{1}{2}(M_1\widetilde{B}\widetilde{B} + M_2\widetilde{W}\widetilde{W} + M_3\widetilde{g}\widetilde{g}) \\ & +(a_e\phi_d\widetilde{l}\widetilde{\overline{e}} + a_e\phi_d\widetilde{l}\widetilde{\overline{e}} - a_u\phi_u\widetilde{q}\widetilde{\overline{u}} + a_d\phi_d\widetilde{q}\widetilde{\overline{d}}) \\ & -(m_l^2\widetilde{l}^\dagger\widetilde{l} + m_{\overline{e}}^2\widetilde{\overline{e}}^\dagger\widetilde{\overline{e}} + m_q^2\widetilde{q}^\dagger\widetilde{q} + m_{\overline{u}}^2\widetilde{\overline{u}}^\dagger\widetilde{\overline{u}} + m_{\overline{d}}^2\widetilde{\overline{d}}^\dagger\widetilde{\overline{d}}) \\ & +m_{\phi_u}^2\phi_u^\dagger\phi_u + m_{\phi_d}^2\phi_d^\dagger\phi_d + b\phi_u\phi_d\end{aligned} \tag{1.38}$$

and its complex conjugate. Here $W(\widetilde{W})$ denotes the three SU(2) gauge bosons (Winos) while $B(\widetilde{B})$ denotes the U(1) gauge boson (Bino).

M_1, M_2, and M_3 give masses to the Winos, a_e, a_u, and a_d are the ”Yukawa” couplings of the superpartners and they are 3×3 matrices in the family space, $m_{\bar{l}}^2, m_{\bar{e}}^2, m_{\bar{q}}^2, m_{\bar{u}}^2$ and $m_{\bar{d}}^2$ are also 3×3 matrices in the family space and they give rise to the masses of the superpartners.

In a generic soft Supersymmetric breaking scheme, these couplings are free parameters that can be chosen at will, although they should not be much greater than 1000 GeV [27]. In this project, the masses of the superpartners, especially that of the smuons, were chosen to accentuate the efficacy of the antler scheme.

1.2.5 Higgs Mechanism in the MSSM

The electroweak symmetry breaking in the MSSM is more complicated than that of the Standard Model due to the presence of an extra Higgs field. Here, we will not delve much into the details, the interested readers are referred to [27]. The thing to note here is that the condition for a symmetry breaking is not as simple as having a negative mass squared parameter.

The SU(2) components of the Higgs fields are given by

$$\phi_u(x) = \begin{pmatrix} \phi_u^+(x) \\ \phi_u^0(x) \end{pmatrix}, \phi_d(x) = \begin{pmatrix} \phi_d^0(x) \\ \phi_d^-(x) \end{pmatrix} \tag{1.39}$$

The scalar potential (after some gauge transformations, setting ϕ_u^0, ϕ_d^0 real and positive and $|\phi_u^0| = |\phi_d^0|$) is

$$V_\phi = (|\mu|^2 + m_{\phi_u}^2)|\phi_u^0| + (|\mu|^2 + m_{\phi_d}^2)|\phi_d^0|^2 - (b\phi_u^0\phi_d^0 + b(\phi_u^0\phi_d^0)^\dagger). \tag{1.40}$$

For V_ϕ to be bounded from below, $2b < 2|\mu|^2 + m_{\phi_u}^2 + m_{\phi_d}^2$ must be satisfied.

To achieve spontaneous breaking the minimum of the potential has to be away from zero. We then have to make sure that $\phi_u^0 = \phi_d^0 = 0$ is not a stable extremum, *i.e.* $\partial^2 V_\phi/(\partial\phi_{u/d}^0)^2 < 0$. Taking the first partial derivatives gives

$$\begin{aligned} \frac{\partial V_\phi}{\partial \phi_u^0} &= 2(|\mu|^2 + m_{\phi_u}^2)\phi_u^0 - 2b\phi_d^0 = 0 \\ \frac{\partial V_\phi}{\partial \phi_d^0} &= 2(|\mu|^2 + m_{\phi_d}^2)\phi_d^0 - 2b\phi_u^0 = 0 \\ \frac{\partial^2 V_\phi}{(\partial \phi_{u/d}^0)^2} &= 2(|\mu|^2 + m_{\phi_u}^2) - 2\tfrac{b^2}{(|\mu|^2 + m_{\phi_d}^2)} \end{aligned} \tag{1.41}$$

Here we substituted the first equation into the second and then taking a second partial derivative to get the third.

The condition for a spontaneous breaking VEV is easily read off from the last equation $\partial^2 V_\phi/(\partial\phi^0_{u/d})^2 < 0 \rightarrow 2(|\mu|^2 + m^2_{\phi_u})(|\mu|^2 + m^2_{\phi_d}) < b^2$, if this condition is not met then electroweak symmetry breaking is impossible.

We can now set the VEV of ϕ^0_u and ϕ^0_d

$$\begin{aligned} v_u &= \langle\phi^0_u\rangle \\ v_d &= \langle\phi^0_d\rangle \\ v_u^2 + v_d^2 &= \tfrac{1}{2}v^2 \end{aligned} \tag{1.42}$$

The last equation is to make sure that the MSSM is consistent with the Standard Model, v^2 is the VEV of the Standard Model Higgs field, which in terms of the Z boson mass, M_Z, is given by $v^2 = \frac{4M_Z^2}{g_1^2+g_2^2}$, see Eq. 1.7 for comparison.

The ratio of the VEV's is usually denoted by $\tan\beta \equiv \frac{v_u}{v_d}$, it is another somewhat free parameter of the MSSM. The masses of the W and Z bosons can then be expressed in terms of $\tan\beta$.

As a side note, since the two Higgs fields are complex objects there are eight degrees of freedom, after electroweak symmetry breaking, three of them become the longitudinal modes of the W and Z bosons while the other five are given the name A^0, h^0, H^0, H^+ and H^-. Their masses are also given in terms of $\tan\beta$.

1.2.6 Dark Matter in the MSSM

The WIMP candidate in the MSSM is given by the Lightest Supersymmetric Particle (LSP), which is the Neutralinos. The Neutralinos are the combination of the Higgsinos and the neutral gauginos, it is a direct result of the kinetic term of the chiral superfields.

From the last two terms of Eq. 1.30, we can see that in this case z represents the Higgs, λ represents the gaugino and ψ the Higgsino. Once the Higgs acquire a VEV, this term becomes a mixing between the gaugino and the Higgsino while the charged Higgsinos combine with the charged gauginos to form the charginos.

Since the Neutralinos are the mass eigenstates of the neutral Higgsinos and gauginos, their masses are given in terms of M_1, M_2, θ_W, μ and $\tan\beta$.

Even though the charginos are not candidates for WIMP, they are also useful in testing the antler scheme because they have similar decay modes as the smuons.

1.2.7 R-parity

R-parity is needed to ensure that the LSP is stable and hence makes a good WIMP candidate. It is given by

$$P_R = (-1)^{3(B-L)+2s} \tag{1.43}$$

where B is the baryon number, L the lepton number, and s the spin of the particle. It is a multiplicative symmetry and every term in the Lagrangian has to have R-parity equal to one (+1). All Standard Model particles have R-parity +1 and all the superpartners have R-parity -1.

Conservation of R-parity ensures that every interaction vertex must contain even number of odd R-parity particles. This in turns guarantee that the lightest superpartner is stable and makes a desirable WIMP candidate. Furthermore, an odd parity means that the LSP is produced by the decay of a pair of superparticles, making it a perfect case study for the antler scheme.

In summary, we have thus shown the basic mechanism of how Supersymmetry, specifically MSSM, complements the Standard Model by providing a good non-baryonic dark matter candidate. This of course is still a major speculation, specifically since the LHC has *not* found any supporting evidence for Supersymmetry to date. There are many unanswered questions surrounding the validity of Supersymmetry as a fundamental symmetry of nature, in particular the arbitrariness introduced by the requirement of Supersymmetry breaking. However, in this article we will only use MSSM as a platform to exemplify the antler scheme, which is the subject of the next discussion, in determining the mass (and possibly the spin [28]) of dark matter and their intermediate particles.

2.0 REVIEW OF THE ANTLER DECAY

In this chapter we review the anatomy of an antler decay and how it can be used to detect and measure the masses of invisible particles. In the first section we will present the cusps and endpoints of such decay in the framework of MSSM. In the following section we will choose a specific masses for the particles involved in the decay process and in the last section we will discuss the effect of acceptance cuts on these singular points.

2.1 SINGULAR STRUCTURES OF ANTLER DECAY AT THE ILC

A future e^+e^- collider has many virtues, which will be complementary to the LHC in many respects. It has a much cleaner experimental environment which is appropriate for high-precision physics. The initial state is well-defined with a fixed center of mass (c.m.) energy $\sqrt{s}$, unlike the undetermined collision energy of the colliding partons at the LHC. Furthermore, all the measurements are in the e^+e^- c.m. frame, which is the lab frame, unlike the unknown boost of the collision at the LHC.

This leads to several advantages for measuring the cusps and endpoints of the kinematical distributions of “antler” diagrams [22]. The $\cos\Theta$ and E_a variables are unambiguous at the ILC. The invariant mass distribution of the invisible particles $m_{\tilde{\chi}_1^0\tilde{\chi}_1^0}$ can be measured using the recoil energy, which is crucial to the mass measurement and the SM background suppression, as we will see.

The energy of the lepton has well-defined cutoffs. The beam polarization of the e^+e^- collider can be used to suppress the SM background and enhance the sensitivity of the mass measurement.

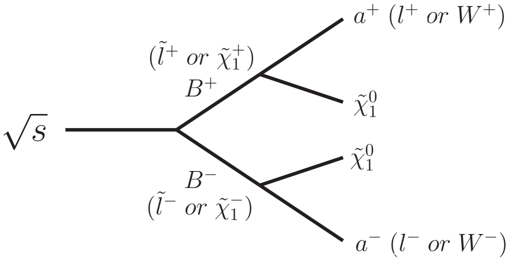

Figure 2: The "antler" diagram at a lepton collider for the MSSM: a known center-of-mass energy produces two on-shell particles $B^\pm$ ($\tilde{l}^\pm$ or $\tilde{\chi}^\pm$) which then decay to $a^\pm$ ($l^\pm$ or $W^\pm$) and two LSP neutralinos ($\tilde{\chi}_1^0$).

To illustrate these strengths, in this article, we will only consider two cases in the MSSM framework, which we refer to as the massless and massive cases (in the energy scale we are interested in). For the massless case, two sleptons, $\tilde{l}$, are pair produced, which then decay to leptons l and the lightest supersymmetric particle (LSP) which we take to be the lightest neutralino ($\tilde{\chi}_1^0$). We consider the process:

$$e^+e^-(\sqrt{s}) \to \tilde{l}^+(p_1) + \tilde{l}^-(p_2) \to l^+(k_1)\tilde{\chi}_1^0(q_1) + l^-(k_2)\tilde{\chi}_1^0(q_2). \tag{2.1}$$

This case is called massless because the leptons are practically massless at the energy scale considered in this study.

For the massive case, two charginos ($\tilde{\chi}_1^\pm$) are pair produced, which then decay to W bosons (which will decay to jets) and again the lightest neutralinos ($\tilde{\chi}_1^0$).

$$e^+e^-(\sqrt{s}) \to \tilde{\chi}_1^+(p_1) + \chi_1^-(p_2) \to W^+(k_1)\tilde{\chi}_1^0(q_1) + W^-(k_2)\tilde{\chi}_1^0(q_2). \tag{2.2}$$

This case is called massive because the W bosons are massive at the energy scale considered in this study.

Since we know the c.m. energy, these processes satisfy the requirements for an antler diagram[22] as seen in Fig. 2. The kinematical distributions of antler diagrams contain singularities known as kinematical cusps and endpoints that depend on the masses of the particles and the c.m. energy. Therefore, if we can measure those cusps and endpoints and we know the c.m. energy, we can determine the masses of the unknown particles. In the present case, the cusps and endpoints can be used to determine the masses of the sleptons ($m_{\tilde{l}}$), charginos ($m_{\tilde{\chi}_1^\pm}$) and the neutralinos ($m_{\tilde{\chi}_1^0}$).

The massless and massive cases share a lot of common attributes. Thus for notational simplicity, we introduce the variable B to represent the intermediate particles, *i.e.* $\tilde{\chi}_1^\pm$ and $\tilde{l}$, and a to represent the leptons l and W bosons. The difference between the massless ($m_a = 0$) and massive ($m_a \neq 0$) case lies in the fact that the singular points are ambiguous in the latter case which will be discussed in detail later in this section.

It is useful to introduce the rapidity of B in the lab frame and the rapidity of $\tilde{\chi}_1^0$ and a in B's rest frame which is given by:

$$\cosh\eta_B^{(\text{c.m.})} = \frac{\sqrt{s}}{2m_B}, \quad \cosh\eta_{\tilde{\chi}_1^0}^{(B)} = \frac{m_B^2 + m_{\tilde{\chi}_1^0}^2 - m_a^2}{2m_{\tilde{\chi}_1^0} m_B}, \quad \cosh\eta_a^{(B)} = \frac{m_B^2 + m_a^2 - m_{\tilde{\chi}_1^0}^2}{2m_a m_B}. \tag{2.3}$$

The derivation of these equations is given in the Appendix.

When a is massless $\cosh\eta_a^{(B)}$ does not make sense because of m_a in the denominator. Thus, in this case we introduce an explicit expression for the energy:

$$E_l^{(B)} = \frac{m_B}{2}\left(1 - \frac{m_{\tilde{\chi}_1^0}^2}{m_B^2}\right) = \lim_{m_a \to 0} m_a \cosh\eta_a. \tag{2.4}$$

It was shown in [22] that the shape of the invariant mass distributions m_{aa} and $m_{\tilde{\chi}_1^0\tilde{\chi}_1^0}$ can be deduced from the symmetry of the antler diagram to be roughly triangles, each with a cusp and two endpoints.

We study the distributions of the following kinematic variables:

$$m_{aa}, \quad m_{\text{rec}}, \quad \cos\Theta, \quad E_a, \quad E_{aa}, \quad E_{\tilde{\chi}_1^0\tilde{\chi}_1^0} \tag{2.5}$$

(*i*) m_{aa} *distribution:* This is the invariant mass of the two visible final particles, which for the massless case, $a = l$ (μ and e), the cusps and endpoints of m_{ll} are given by:

$$\begin{aligned} m_{ll}^{\min} &= 0 \\ m_{ll}^{\text{cusp}} &= 2E_l^{(\tilde{l})} e^{-\eta_{\tilde{l}}} \\ m_{ll}^{\max} &= 2E_l^{(\tilde{l})} e^{\eta_{\tilde{l}}} \end{aligned} \tag{2.6}$$

We defer the discussion of m_{aa} for massive final particles, $a = W$, until after the discussion of $m_{\rm rec}$ since they both share many common characteristics.

(ii) $m_{\rm rec}$ *distribution:* The invariant mass of the two invisible final particles can be inferred from the c.m. energy and the momenta of their visible counterparts:

$$m^2_{\rm rec} \equiv m^2_{\tilde{\chi}^0_1 \tilde{\chi}^0_1} = s - 2\sqrt{s}\,(E_{a_1} + E_{a_2}) + m^2_{aa} \tag{2.7}$$

where $m_{\rm rec}$ is the recoil energy. The initial state radiation (ISR) and beamstrahlung of the electron and positron beams will add a small smearing to s. This will affect our measurement of $m_{\rm rec}$ but we will show that the effect is not significant.

Due to the symmetry of the antler decay topology, the invariant mass distribution for the invisible particles, $m_{\rm rec}$, exhibits the same singular points (two end points and a cusp) as m_{aa} even when a is massive.

On the other hand, the distribution of m_{WW} and $m_{\rm rec} = m_{\tilde{\chi}^0_1 \tilde{\chi}^0_1}$ (collectively denoted by m_{DD} where D is either W or $\tilde{\chi}^0_1$) depends on the c.m. energy and the region of parameter space. There are three regions given by:

$$\mathcal{R}_1 : \eta_B < \frac{\eta_D}{2}, \quad \mathcal{R}_2 : \frac{\eta_D}{2} < \eta_B < \eta_D, \quad \text{and} \quad \mathcal{R}_3 : \eta_D < \eta_B. \tag{2.8}$$

In order to see the characteristic features of $\mathcal{R}_1$, $\mathcal{R}_2$, and $\mathcal{R}_3$, we show in Fig. 3 each region in the parameter space of $m_{\tilde{\chi}^0_1}/\sqrt{s}$ and $m_B/\sqrt{s}$. The lower-right triangle corner of this figure is excluded by our assumption that the intermediate particle is heavier than the LSP neutralino ($m_B > m_{\tilde{\chi}^0_1}$). The region $\mathcal{R}_1$ occurs when the intermediate particle pair is produced near threshold and/or when the intermediate particle is substantially heavier than the LSP. In the region $\mathcal{R}_3$, the c.m. energy is much higher than the intermediate particle pair mass and/or the B mass is similar to the $\tilde{\chi}^0_1$ mass. The region $\mathcal{R}_2$ is in between. The cusps and endpoints in these three regions are given in Table 2. The minimum endpoint is the same for $\mathcal{R}_1$ and $\mathcal{R}_2$ but different for $\mathcal{R}_3$ while the cusp has one value for $\mathcal{R}_1$ but another for $\mathcal{R}_2$ and $\mathcal{R}_3$. The maximum endpoint only depends on the masses and collision energy and is the same for all three regions. Although the maximum of the m_{DD} distribution has a unique dependence on the mass parameters, the absence of *a priori* knowledge of the masses gives us ambiguity among $\mathcal{R}_1$, $\mathcal{R}_2$, and $\mathcal{R}_3$: we do not know whether the measured $m^{\rm min}_{DD}$

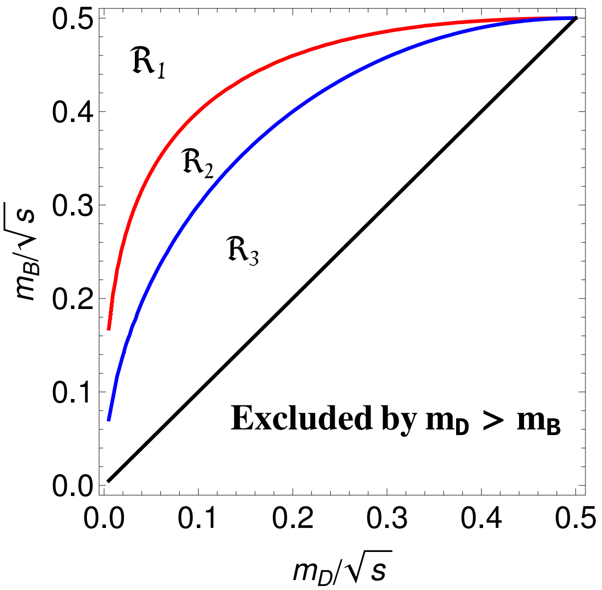

Figure 3: The three regions for $m_{\tilde{\chi}_1^0\tilde{\chi}_1^0}$ ($\mathcal{R}_1$, $\mathcal{R}_2$, and $\mathcal{R}_3$) in the parameter space of $m_{\tilde{\chi}_1^0}/\sqrt{s}$ and $m_B/\sqrt{s}$.

Table 2: The cusp and endpoints of the invariant mass distribution m_{DD} in the three regions of c.m. energy and parameter space

	$\mathcal{R}_1:\ \eta_B < \frac{\eta_D}{2}$	$\mathcal{R}_2:\ \frac{\eta_D}{2} < \eta_B < \eta_D$	$\mathcal{R}_3:\ \eta_D < \eta_B$
$m_{DD}^{\text{min}} =$	$2m_D$		$2m_D\cosh(\eta_B - \eta_D)$
$m_{DD}^{\text{cusp}} =$	$2m_D\cosh(\eta_B - \eta_D)$	$2m_D\cosh\eta_B$	
$m_{DD}^{\text{max}} =$	$2m_D\cosh(\eta_B + \eta_D)$		

is $2m_D$ or $2m_D\cosh(\eta_B - \eta_D)$. However, fortunately, the cusps and endpoints in the other kinematical distributions do not have this ambiguity and are sufficient to determine which region we are in.

(*iii*) $\cos\Theta$ *distribution:* The angular distribution have also been shown to accommodate a pronounced cusp for the massless case $a = l$. The cosine of the angle (Θ) between l_1 or l_2 and the combined momentum of the two leptons ($k_{l_1} + k_{l_2}$) in the rest frame of the two leptons has a pronounced peak where the cusp and the maximum endpoint meet at:

$$|\cos\Theta|_{\max} = \tanh\eta_{\tilde{l}} = \sqrt{1-\frac{4m_{\tilde{l}}^2}{s}}. \tag{2.9}$$

In fact, in Ref. [22], it was shown that the distribution function is remarkably simple, given by

$$\frac{d\Gamma}{d\cos\Theta} \propto \begin{cases} \sin^{-3}\Theta, & \text{if } |\cos\Theta| < \tanh\eta_{\tilde{l}}, \\ 0, & \text{otherwise .} \end{cases} \tag{2.10}$$

This variable gives one way to distinguish between the regions for $m_{\tilde{\chi}_1^0\tilde{\chi}_1^0}$ distribution. As can be seen from Eq. (2.9), the rapidity of the slepton, $\eta_{\tilde{l}}$, is measured by $|\cos\Theta|_{\max}$. With the known $\eta_{\tilde{l}}$, the comparison of the expressions in Table 2 with three measurements of $m^{\min}_{\tilde{\chi}_1^0\tilde{\chi}_1^0}$, $m^{\text{cusp}}_{\tilde{\chi}_1^0\tilde{\chi}_1^0}$, and $m^{\max}_{\tilde{\chi}_1^0\tilde{\chi}_1^0}$ determines to which region the signal belongs.

The end point of $\cos\Theta$ distribution for the massless case does not depend on $m_{\tilde{\chi}_1^0}$ because the momentum of a ($k^{(a1a2)}_{a_{(1,2)}}$) only depends on $m_{\tilde{\chi}_1^0}$ through $E_l^{(B)}$. However, since a is massless its momentum is proportional to $E_l^{(B)}$ and hence the normalized momentum does not depend on $m_{\tilde{\chi}_1^0}$.

It is the same case with the total momentum $k_{12} = k_{a_1} + k_{a_1}$ as well but we need to boost it to the lab frame. Thus, $\cos\Theta = k^{(a1a2)}_{a_{(1,2)}} \cdot k_{12}^{(\text{c.m.})}/|k^{(a1a2)}_{a_{(1,2)}}||k_{12}^{(\text{c.m.})}|$ depends on m_B only.

Unfortunately, for the massive case $\cos\Theta$ does not have a maximum or minimum, it runs through from -1 to +1. Rendering this kinematic distribution not as useful as in the massless case.

(iv) E_a *distribution:* The energy distribution of visible particle a in the lab frame has two end points, E_a^{min} and E_a^{max}. For $B = \tilde{l}$, which is a scalar particle, its decays are isotropic which produces a flat energy spectrum while for $B = \tilde{\chi}_1^{\pm}$, spin correlation causes the energy distribution to be steeply tilted. However, in both cases the energy distribution has sharp edges $E_a^{\min}$ and $E_a^{\max}$. In terms of $\sqrt{s}$, m_B, m_a and $m_{\tilde{\chi}_1^0}$, they are

$$E_a^{\min,\max} = \frac{\sqrt{s}}{4}\left(1-\frac{(m^2_{\tilde{\chi}_1^0}-m_a^2)}{m_B^2}\right)\left(1\pm\beta_B\sqrt{1-\frac{4m_a^2m_B^2}{(m_B^2+m_a^2-m^2_{\tilde{\chi}_1^0})^2}}\right) \tag{2.11}$$

where the β_B is defined by

$$\beta_B = \sqrt{1 - \frac{4m_B^2}{s}}. \tag{2.12}$$

The formula for E_a simplifies drastically for the massless case, $m_a = 0$,

$$E_a^{\text{min,max}} = \frac{\sqrt{s}}{4}\left(1 - \frac{m_{\tilde{\chi}_1^0}^2}{m_B^2}\right)(1 \pm \beta_B). \tag{2.13}$$

In the event where $m_B \ll \sqrt{s}/2$, the min for the massless case can be very low:

$$E_a^{\text{min}}(m_B \ll \sqrt{s}/2) \sim \frac{m_B^2}{2\sqrt{s}}\left(1 - \frac{m_{\tilde{\chi}_1^0}^2}{m_B^2}\right) \tag{2.14}$$

which can be below the threshold for detection. In this case, this parameter alone will not be sufficient to determine both m_B and $m_{\tilde{\chi}_1^0}$.

(v) E_{aa} *distribution:* The distribution of the energy of a_1a_2 system, $E_{aa} \equiv E_{a_1} + E_{a_2}$, is triangular, leading to three singular positions of E_{aa}^{min}, E_{aa}^{cusp}, and E_{aa}^{max}. Note that the E_{aa} cusp shape is always sharp. For the massless case, their positions in terms of masses are

$$\begin{aligned} E_{aa}^{\text{min}} &= \frac{\sqrt{s}}{2}\left(1 - \frac{m_{\tilde{\chi}_1^0}^2}{m_B^2}\right)(1 - \beta_B) \\ E_{aa}^{\text{cusp}} &= \frac{\sqrt{s}}{2}\left(1 - \frac{m_{\tilde{\chi}_1^0}^2}{m_B^2}\right) \\ E_{aa}^{\text{max}} &= \frac{\sqrt{s}}{2}\left(1 - \frac{m_{\tilde{\chi}_1^0}^2}{m_B^2}\right)(1 + \beta_B) \end{aligned} \tag{2.15}$$

where β_B is defined in Eq. (2.12).

(vi) $E_{\tilde{\chi}_1^0\tilde{\chi}_1^0}$ *distribution:* Although the energy of one invisible particle is not possible to measure, the sum of two invisible particle energies can be measured through

$$E_{\tilde{\chi}_1^0\tilde{\chi}_1^0} \equiv E_{(\tilde{\chi}_1^0)_1} + E_{(\tilde{\chi}_1^0)_2} = \sqrt{s} - E_{aa}. \tag{2.16}$$

The distribution of $E_{\tilde{\chi}_1^0\tilde{\chi}_1^0}$ is also triangular and its cusp shape is always sharp. For the massless case the three singular positions are

$$\begin{aligned} E_{\tilde{\chi}_1^0\tilde{\chi}_1^0}^{\text{min}} &= \frac{\sqrt{s}}{2}\left\{1 + \frac{m_{\tilde{\chi}_1^0}^2}{m_B^2} - \beta_B\left(1 - \frac{m_{\tilde{\chi}_1^0}^2}{m_B^2}\right)\right\} \\ E_{\tilde{\chi}_1^0\tilde{\chi}_1^0}^{\text{cusp}} &= \frac{\sqrt{s}}{2}\left(1 + \frac{m_{\tilde{\chi}_1^0}^2}{m_B^2}\right) \\ E_{\tilde{\chi}_1^0\tilde{\chi}_1^0}^{\text{max}} &= \frac{\sqrt{s}}{2}\left\{1 + \frac{m_{\tilde{\chi}_1^0}^2}{m_B^2} + \beta_B\left(1 - \frac{m_{\tilde{\chi}_1^0}^2}{m_B^2}\right)\right\} \end{aligned} \tag{2.17}$$

where β_B is defined in Eq. (2.12). The derivation of the above equations are given in the Appendix.

Four kinematic variables of m_{aa}, $m_{\rm rec}$, E_{aa}, and $E_{\tilde{\chi}_1^0\tilde{\chi}_1^0}$ have common characteristic features in their distribution, a triangular shape leading to three singular points of the minimum, cusp, and maximum. In order to understand this distinctive feature as well as their correlation, we examine four critical points in the parameter space of $(\cos\theta_1, \cos\theta_2)$, where θ_1 and θ_2 are the polar angle of a_1 and a_2, respectively, in the rest frame of their mother particle B_1 and B_2. The correspondence of each corner to a singular point is as follows:

1D configuration	m_{aa}	$m_{\rm rec}$	E_{aa}	$E_{\tilde{\chi}_1^0\tilde{\chi}_1^0}$
$\overset{a_2}{\Longleftarrow}\quad\overset{B_2}{\longleftarrow}\quad\overset{e^+e^-}{\bullet}\quad\overset{B_1}{\longrightarrow}\quad\overset{a_1}{\Longrightarrow}$	max	min	max	min
$\overset{a_2}{\Longrightarrow}\quad\overset{B_2}{\longleftarrow}\quad\overset{e^+e^-}{\bullet}\quad\overset{B_1}{\longrightarrow}\quad\overset{a_1}{\Longleftarrow}$	cusp	max	min	max
$\overset{a_2}{\Longrightarrow}\quad\overset{B_2}{\longleftarrow}\quad\overset{e^+e^-}{\bullet}\quad\overset{B_1}{\longrightarrow}\quad\overset{a_1}{\Longrightarrow}$	min	cusp	cusp	cusp
$\overset{a_2}{\Longleftarrow}\quad\overset{B_2}{\longleftarrow}\quad\overset{e^+e^-}{\bullet}\quad\overset{B_1}{\longrightarrow}\quad\overset{a_1}{\Longleftarrow}$	min	cusp	cusp	cusp

(2.18)

For illustrative purposes, in this article we will choose three different MSSM parameter points, two for the massless $a = l$ case and another for the massive $a = W$ case. The masses of the particles in those parameter points are given in Table 3.

Our couplings are also given by these benchmark points. However, our techniques and conclusions only depend on the general structure of the mass spectrum and not on the specific point.

Since only the right slepton mass is relatively low in our first benchmark point (`IA`), $(2m_{\tilde{l}_R} < \sqrt{s} < 2m_{\tilde{l}_L})$, only the $\tilde{l}_R$ will contribute to the signal. For benchmark point `IB`, both $\tilde{l}_R$ and $\tilde{l}_L$ contribute to the signal.

Note that different c.m. energies $\sqrt{s}$, with the given mass parameters, corresponds to different region. With the chosen mass parameters in Table 3, the c.m. energy determines

Table 3: Illustrative SUSY mass spectrum (in GeV) used for our massless case (`IA` and `IB`) and our chargino decay analysis (`II`).

Label	$\tilde{\mu}_R/\tilde{e}_R$	$\tilde{\mu}_L/\tilde{e}_L$	$\tilde{\chi}_1^0$	$\tilde{\chi}_2^0$	$\tilde{\chi}_3^0$	$\tilde{\chi}_4^0$	$\tilde{\chi}_1^\pm$	$\tilde{\chi}_2^\pm$
`IA`	158	636	141	529	654	679	529	679
`IB`	158	170	141	529	654	679	529	679
`II`	158	337	139	235	504	529	235	515

the region as

$$\begin{array}{c|c|c|c} & \text{For } \tilde{l}_R(\text{GeV}) & \text{For } \tilde{l}_L(\text{GeV}) & \text{For } \tilde{\chi}_1^\pm(\text{GeV}) \\ \hline \mathcal{R}_1 & 316.3 < \sqrt{s} < 316.8 & 340.8 < \sqrt{s} < 342.3 & 470 < \sqrt{s} < 474.9 \\ \mathcal{R}_2 & 316.8 < \sqrt{s} < 318.4 & 342.3 < \sqrt{s} < 347 & 474.9 < \sqrt{s} < 489.8 \\ \mathcal{R}_3 & 318.4 < \sqrt{s} & 347 < \sqrt{s} & 489.8 < \sqrt{s} \end{array} \tag{2.19}$$

The minimum of $\sqrt{s}$ is from the requirement of the on-shell production of an intermediate particle pair. In this article however, we will choose $\sqrt{s} = 500\,\text{GeV}$.

2.2 THE CUSP AND ENDPOINTS OF SLEPTON PAIR PRODUCTION AT THE ILC

In order to focus the basic feature of cusp and endpoints at the ILC, in this section we consider only the smuon pair production (the selectron pair production has similar features). There are two kinds of smuons, $\tilde{\mu}_L$ and $\tilde{\mu}_R$, scalar partners of the left- and right-handed muon respectively. Negligibly small mass of the muon compared with the beam energy suppresses the left-right mixing and thus makes $\tilde{\mu}_L$ and $\tilde{\mu}_R$ the mass-eigenstates. The smuon pair production in e^+e^- collisions is via s-channel diagram mediated by photon and Z boson. Since the exchanged particles are vector bosons, the helicities of e^+ and e^- are opposite to each other, and only two kinds of pairs, $\tilde{\mu}_R^+\tilde{\mu}_R^-$ and and $\tilde{\mu}_L^+\tilde{\mu}_L^-$, are produced. If the lightest neutralino $\tilde{\chi}_1^0$ has a dominant Bino component, $\tilde{\mu}_R$ predominantly decays into $\mu\tilde{\chi}_1^0$. The decay of $\tilde{\mu}_L \to \mu\tilde{\chi}_1^0$ is also sizable. At the ILC, we have substantial rate of $e^+e^- \to \tilde{\mu}_R\tilde{\mu}_R/\tilde{\mu}_L\tilde{\mu}_L \to \mu\tilde{\chi}_1^0 + \mu\tilde{\chi}_1^0$. This is one of the most perfect processes for the antler decay topology.

The final state we observe is

$$e^+e^- \to \mu^+\mu^- + \not{E}. \tag{2.20}$$

There are three major signals with the antler topology type:

- the $\tilde{\mu}_R\tilde{\mu}_R$ production;
- the $\tilde{\mu}_L\tilde{\mu}_L$ production;
- the SM WW production followed by a decay into lepton and neutrino, $W \to \mu\nu$.

In this section and the next we denote the invisible particle X which can be either a neutralino $\tilde{\chi}_1^0$ or a neutrino ν.

The relative rates depend on the particular MSSM parameters in use. Thus the two different MSSM parameter points, called `IA` and `IB`, given in Table 3. In both cases, $\tilde{\chi}_1^0$ is most likely Bino-like while $\tilde{\chi}_2^0$ and $\tilde{\chi}_1^\pm$ are Wino-like. And the lightest chargino is too heavy to be produced in pairs at $\sqrt{s} = 500\,\text{GeV}$ ILC. In the `IA`, there is a big mass gap between $\tilde{\mu}_R$ and $\tilde{\mu}_L$. The $\tilde{\mu}_L\tilde{\mu}_L$ pair production is not kinematically accessible.

Thus we have a very simple situation where the new physics involves only the $\tilde{\mu}_R\tilde{\mu}_R$ pair production. In `IB`, most of the particle masses are the same as `IA`, except for $\tilde{\mu}_L$. Now $\tilde{\mu}_R$ and $\tilde{\mu}_L$ masses are quite close, with the mass gap of about 10 GeV. In this case with $m_{\tilde{\mu}_R} \sim m_{\tilde{\mu}_L}$, the total cross section of $\sigma(e^+e^- \to \tilde{\mu}_R^+\tilde{\mu}_R^-)$ is compatible with $\sigma(e^+e^- \to \tilde{\mu}_L^+\tilde{\mu}_L^-)$. This is because the left- and right-chiral coupling of the smuon with the Z boson, say $g_L^{\tilde{\mu}}$ and $g_R^{\tilde{\mu}}$, are accidentally similar in size like

$$g_L^{\tilde{\mu}} = \frac{-1 + 2\sin^2\theta_W}{2\sin\theta_W\cos\theta_W} \approx -0.64, \quad g_R^{\tilde{\mu}} = \frac{\sin\theta_W}{\cos\theta_W} \approx 0.55, \tag{2.21}$$

here we have entangled signal of antler topology processes from $\tilde{\mu}_R\tilde{\mu}_R$, $\tilde{\mu}_L\tilde{\mu}_L$.

The SM WW process is always there as a background for the two cases mentioned above. How to disentangle the information for the mass measurement of$\tilde{\mu}_R$, $\tilde{\mu}_L$, and $\tilde{\chi}_1^0$ is our main purpose.

Table 4: The values of various kinematic cusps and endpoints for the mass parameters in Table 3. All the masses and energies are in units of GeV. Here X denotes an invisible particle (either a $\tilde{\chi}_1^0$ or a ν).

$\sqrt{s}$	500 GeV		
Production channel	$\tilde{\mu}_R\tilde{\mu}_R$	$\tilde{\mu}_L\tilde{\mu}_L$	WW
(m_B, m_X)	$(158, 141)$	$(170, 141)$	$(m_W, 0)$
$\lvert\cos\Theta\rvert_{\max}$	0.77	0.73	0.95
$(m_{aa}^{\min}, m_{aa}^{\text{cusp}}, m_{aa}^{\max})$	$(0, 12, 91)$	$(0, 21, 137)$	$(0, 13, 487)$
$(m_{\text{rec}}^{\min}, m_{\text{rec}}^{\text{cusp}}, m_{\text{rec}}^{\max})$	$(408, 445, 488)$	$(363, 413, 479)$	$(0, 13, 487)$
$(E_a^{\min}, E_a^{\max})$	$(6, 46)$	$(11, 68)$	$(7, 243)$
$(E_{aa}^{\min}, E_{aa}^{\text{cusp}}, E_{aa}^{\max})$	$(12, 52, 92)$	$(21, 79, 137)$	$(13, 250, 487)$
$(E_{\tilde{\chi}_1^0\tilde{\chi}_1^0}^{\min}, E_{\tilde{\chi}_1^0\tilde{\chi}_1^0}^{\text{cusp}}, E_{\tilde{\chi}_1^0\tilde{\chi}_1^0}^{\max})$	$(408, 448, 488)$	$(363, 421, 479)$	$(13, 250, 487)$

In Table 4, we show the values of various kinematic cusps and endpoints for the mass parameters in Table 3. The c.m. energy is fixed at 500 GeV. The mass spectra of the $\tilde{\mu}_R\tilde{\mu}_R$ antler and the WW antler are applied to both the `IA` and `IB`, while that of the $\tilde{\mu}_L\tilde{\mu}_L$ only to the `IB`. With the given masses, all of the minimum, cusp, and maximum positions are determined, which are considerably different from each other.

In Fig. 4, we show these singular points in the normalized distributions of (a) m_{aa}, (b) m_{rec}, (c) $\cos\Theta$, (d) E_a, (e) E_{aa}, and (f) $E_{\tilde{\chi}_1^0\tilde{\chi}_1^0}$ for the $\tilde{\mu}_R\tilde{\mu}_R$, $\tilde{\mu}_L\tilde{\mu}_L$, and WW productions. The normalization is over the total cross section, which reveals the distribution shape only. Here we have considered only the kinematics. The full results including the spin correlation, the ISR, the beamstrahlung, and the detector smearing effects are to be shown in the next section. First of all, the m_{aa} distributions for the $\tilde{\mu}_R\tilde{\mu}_R$, $\tilde{\mu}_L\tilde{\mu}_L$, and WW productions do not show any cusp but featureless round shape. This is because the c.m. energy is too high

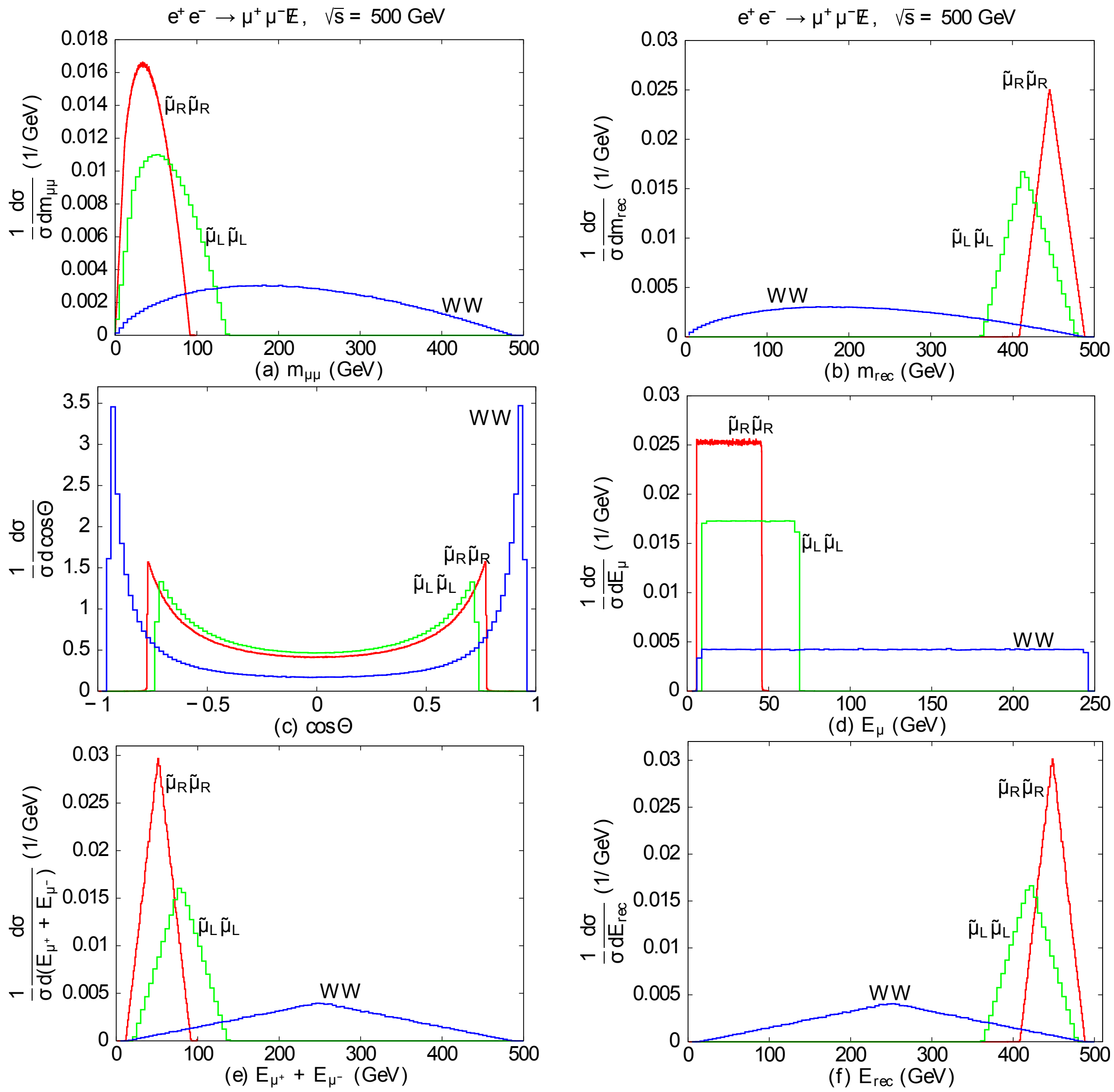

Figure 4: The normalized distributions of m_{aa}, $m_{\rm rec}$, $\cos\Theta$, E_a, E_{aa}, and E_{XX} for three cases in Table 4. Here we consider only the kinematics.

to reveal the m_{aa} cusp, which is pronounced when $m_B > 0.44\sqrt{s}$ [22]. For $B = \tilde{\mu}_R$, for example, a sharp m_{aa} cusp requires $\sqrt{s} \lesssim 360\,\mathrm{GeV}$. On the contrary, the $m_{\rm rec}$ distributions for $\tilde{\mu}_R\tilde{\mu}_R$ and $\tilde{\mu}_L\tilde{\mu}_L$ in Fig. 4(b) are of a sharp triangle. This is attributed to the massive $\tilde{\chi}_1^0$. For the WW production, massless neutrinos lead to the same invariant mass distributions as massless muons.

The $\cos\Theta$ distributions of $\tilde{\mu}_R\tilde{\mu}_R$, $\tilde{\mu}_L\tilde{\mu}_L$, and WW in Fig. 4(c) present the same functional behavior, proportional to $1/\sin^3\Theta$. There are two sharp merging points of cusp and maximum, which correspond to $\pm|\cos\Theta|_{\max}$. The $\tilde{\mu}_R\tilde{\mu}_R$ and $\tilde{\mu}_L\tilde{\mu}_L$ processes have similar values of $|\cos\Theta|_{\max}$, while the WW process has a smaller value.

Figure 4(d) show the energy distribution of one visible particle. Since the spin correlation effects are not included, the distribution is flat, of a box shape. As shall be shown later, this holds true for two scalar particles, but not true for WW. In principle, two measurements of $E_a^{\min}$ and $E_a^{\max}$ can determine two unknown masses m_B and m_X. As the $\tilde{\mu}_R$ case implies ($E_a^{\min} \simeq 5.8\,\mathrm{GeV}$), $E_a^{\min}$ can be very low, like below the detection threshold. We then need another independent observable to determine all the masses. In addition, over-constraints on the involving masses are very useful in establishing new physics model.

The distribution of two energy sum of visible particles in Fig. 4(d), which is of triangular shape, is different from the individual energy distribution. For $\tilde{\mu}_R\tilde{\mu}_R$ and $\tilde{\mu}_L\tilde{\mu}_L$, the E_{aa} distributions are localized so that the pronounced cusp is easy to identify. For WW, instead, the E_{aa} distribution is widely spread out. Finally the energy sum of two missing particles are presented in Fig. 4(f). For WW, the missing particle is neutrino, and thus the distribution is the same as E_{aa}. For $\tilde{\mu}_R\tilde{\mu}_R$ and $\tilde{\mu}_L\tilde{\mu}_L$, the shape is similar to that of E_{aa}, but distributed in high energy region.

Note that the discussed kinematic cusps and endpoints are based on ideal distributions from the whole data without any contamination. In a realistic situation, however, inevitable are some acceptance cuts from the limitation of the detector design or for the control of the SM background. The application of acceptance cuts causes shifts to the locations of the singular points. Initial state radiation (ISR), beamstrahlung and detector smearing effects are also unavoidable. They may smear some sharp cusps. Detailed study on these effects are presented later, which are shown to be under control.

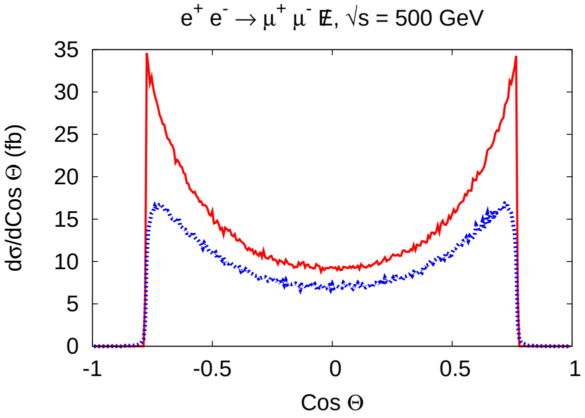

Figure 5: The normalized $\cos\Theta$ distribution with the effects of initial state radiation (ISR), beamstrahlung and detector smearing. We set $\sqrt{s} = 500\,\mathrm{GeV}$, $m_B = 158.2\,\mathrm{GeV}$, $m_X = 140.9\,\mathrm{GeV}$, and $m_a = 0$.

2.3 THE EFFECTS OF ACCEPTANCE CUTS ON THE CUSPS

We now turn to the study of the effects of acceptance cuts as well as other inevitable setup on the kinematic cusp and endpoints. We will show the effect of each one at a time to examine limitations of the antler method in more detail. Following the previous section, here X denotes an invisible particle, either a $\tilde{\chi}_1^0$ or ν.

First we examine the effects from inevitable design factors of the ILC, *i.e.* the effects of ISR, beamstrahlung and detector smearing. We find that the most affected distribution is the $\cos\Theta$ distribution. In Fig. 5, we show the combined effects by using the calculation package Whizard [29]. The red line with two sharp peak is the $\cos\Theta$ distribution from kinematics only. And the blue line includes all three effects. The $\cos\Theta$ cusp is rounded and bent. If we define the cusp position as the highest point, the $\cos\Theta$ cusp position is shifted slightly by about $3-5\%$. Most distortion is from ISR and beamstrahlung. The detector smearing effect is rather minor.

For the acceptance cuts, we consider two kinematic cuts, the missing transverse momentum ($\not{p}_T$) and the energy of the muon. In particular, the lower bound on E_a not only ensures

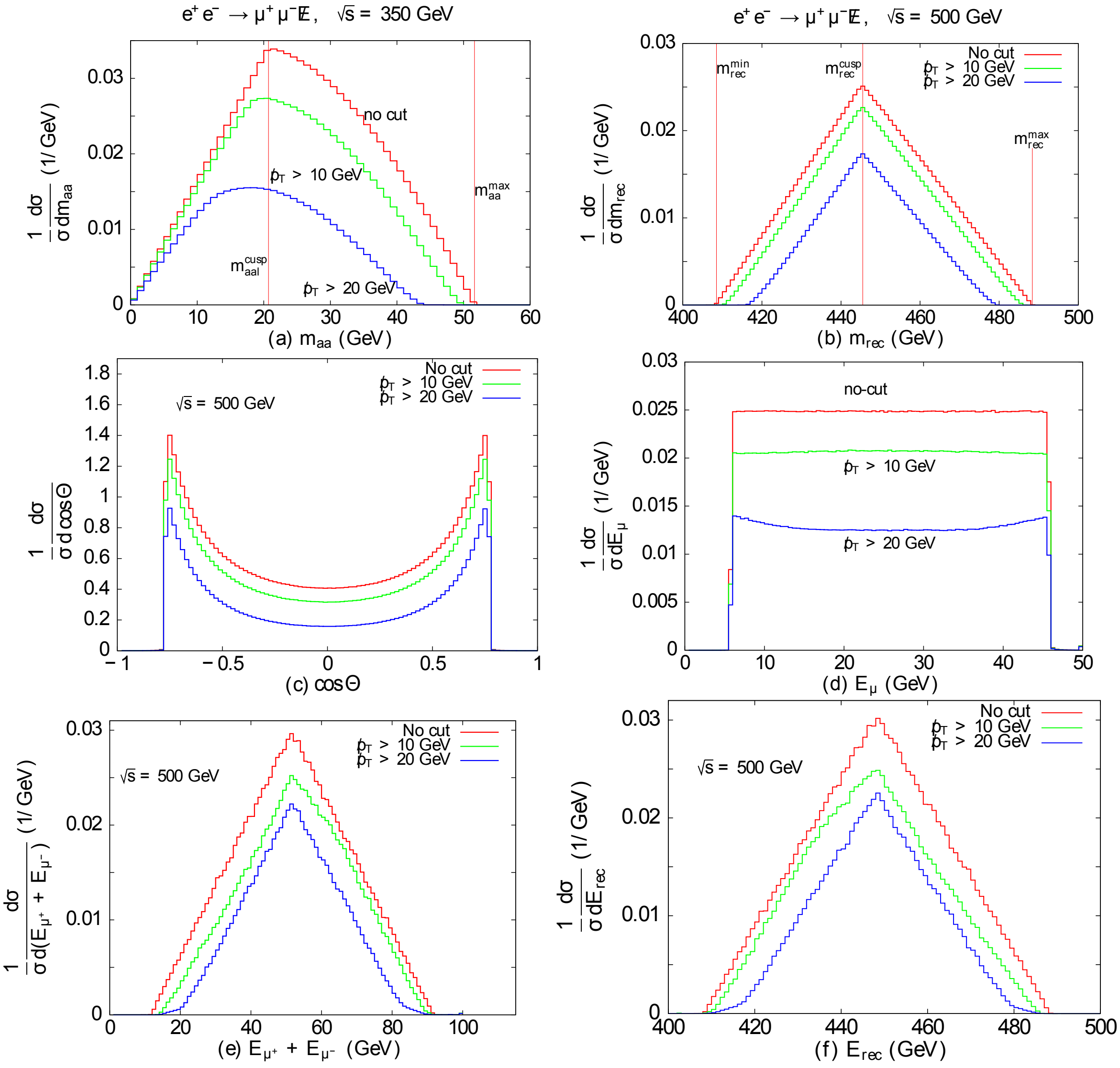

Figure 6: For the mass spectrum of `IA`, the $\not{p}_T$ cut effects on the $m_{\mu\mu}$, $m_{\rm rec}$, $\cos\Theta$, E_μ, $E_{\mu^+}+E_{\mu^-}$, and $E_{\rm rec}=E_{X_1}+E_{X_2}$ distributions for the process $e^+e^-\to\mu^+mu^-+$ missing energy without spin-correlation and other realistic effects. Each distribution is normalized by the total cross section without any acceptance cut. The c.m. energy is set 350 GeV for m_{aa} distribution, and $\sqrt{s}=500\,\text{GeV}$ for the other distributions. .

the perturbativity of tree-level calculation but also suppresses a dominant SM background of $e^+e^- \to e^+e^-\mu^+\mu^-$ with two electrons disappearing into the beam line. Note that the E_a cut is applied to both μ^+ and μ^-. We take the mass parameters in the `IA` (see Table 3) and $\sqrt{s} = 500\,\mathrm{GeV}$ except for m_{aa} distribution. The m_{aa} cusp is too round for $\sqrt{s} = 500\,\mathrm{GeV}$ in `IA`, which does not show the dependence of the kinematic cut clearly, for m_{aa} distribution, we set $\sqrt{s} = 350\,\mathrm{GeV}$.

In Fig. 6, we show the effects of $\not{p}_T$ on the distributions of m_{aa}, $m_{\rm rec}$, $\cos\Theta$, E_a, E_{aa}, and E_{XX}. The $\not{p}_T$ cut is essential to probe the dark matter particle. We normalize each distribution by the total cross section without kinematic cuts. Obviously the $\not{p}_T$ cut takes some events out from the original full distribution, and thus the event rate is reduced. In addition, since the $\not{p}_T$ cut applies unevenly, the positions of the cusp and endpoints can be shifted. First the m_{aa} distribution with various $\not{p}_T$ cut effects are shown in Fig. 6(a). With $\not{p}_T > 10\,\mathrm{GeV}$ cut, the m_{aa} distribution retains its triangular shape, but starts to lose the true cusp and maximum positions. The shift is a few GeV. If $\not{p}_T > 20\,\mathrm{GeV}$, the sharp cusp is smeared out and the $m_{aa}^{\max}$ position is shifted by about $10\,\mathrm{GeV}$. In both cases, the $m_{aa}^{\min}$ stays intact. The $m_{\rm rec}$ distribution Fig. 6(b), on the contrary, keeps its triangular shape even with high $\not{p}_T$ cut. It is interesting to note that the $\not{p}_T$ cut shifts the $m_{\rm rec}^{\min}$ and $m_{\rm rec}^{\max}$ while keeping the $m_{\rm rec}^{\rm cusp}$ position.

The $\cos\Theta$ distribution in Fig. 6(c) keeps the functional behavior to some extent. And the $|\cos\Theta|_{\max}$ positions remain almost the same. The $\not{p}_T$ cut removes the data evenly from the $\cos\Theta$ distribution. Figure 6(d) shows the E_a distribution under the $\not{p}_T$ cut effects.This acceptance cut reduces the whole rate uniformly. The box-shaped distribution is still maintained. Figures 6(e) and (f) present the distributions of the summed energy of two visible and invisible particles, respectively. In both cases, triangular shapes as well as the cusp positions are retained. But the minimum and maximum positions are shifted.

Figure 7 presents the E_a cut effects, which apply quite differently from the $\not{p}_T$ cut effects. The normalzation is applied using the total cross section before the cut. The m_{aa} distribution retains its maximum position from the E_a cut, while its minimum position is stable from the $\not{p}_T$ cut. The m_{aa} cusp position is also shifted by sizable amount, *e.g.* about 10 GeV for $E_a > 10\,\mathrm{GeV}$ cut. This behavior is the same for E_{aa} distribution in Fig. 7(e). The E_{XX}

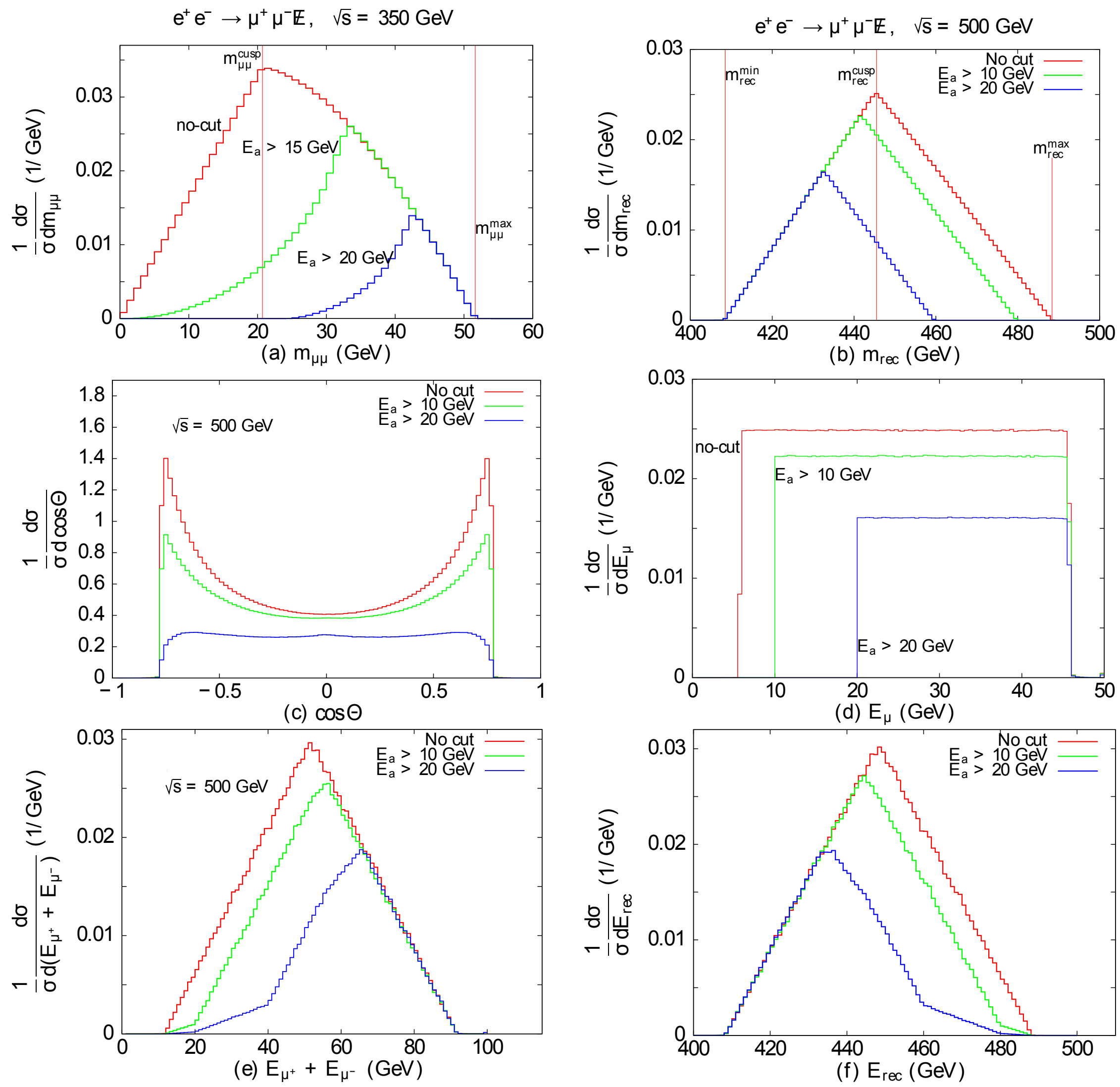

Figure 7: For the mass spectrum of `IA`, the E_a cut effects on the $m_{\mu\mu}$, $m_{\rm rec}$, $\cos\Theta$, E_μ, $E_{\mu^+}+E_{\mu^-}$, and $E_{\rm rec}=E_{X_1}+E_{X_2}$ distributions for the process $e^+e^-\to\mu^+mu^-+$ missing energy without spin-correlation and other realistic effects. The c.m. energy is set 350 GeV for m_{aa} distribution, and $\sqrt{s}=500\,\mathrm{GeV}$ for the other distributions. .

distribution in Fig. 7(f) behaves oppositely: its maximum and cusp positions are shifted while its minimum position is retained. The $m_{\rm rec}$ distribution in Fig. 7(b) shows that the E_a cut holds its minimum position, as in the E_{XX} distribution. The $\cos\Theta$ distribution under the E_a cut shows similar behavior to that under the $\not{p}_T$ cut. The locations of $|\cos\Theta|_{\rm max}$ are the same. The overall distribution is reduced almost evenly. Finally the E_a distribution shows the shift of its minimum into the lower bound on E_a. Note that some data satisfying the $E_a > E_a^{\rm cut}$ are cut off. This is because we have applied the E_a cut to both of final leptons.

In short, the acceptance cut distorts kinematic distributions, and thus shifts the singular position. When we read the mass information from endpoints, these cut effects are to be cautiously considered.

We have thus shown how antler cascade decay provides information about WIMP mass through the singular points of the various kinematical distributions and how realistic considerations alter these distributions. Next we discuss the simulation procedure and result of what these distributions will look like at the ILC by including all realistic factors and backgrounds mentioned above.

3.0 SIMULATION RESULTS AND DISCUSSION

We now present and examine the different kinematic distributions mentioned previously using the chosen parameter points shown in Table 3. We have included realistic collider environment and setup composed of ISR, beamstrahlung and detector smearing effects. Our choice of simulation package is Whizard[29].

3.1 BACKGROUNDS AND SIMULATION PROCEDURE

For our signal of $e^+e^- \to \mu^+\mu^- + \not{E}$, there are substantial SM backgrounds. The main irreducible SM background is W boson pair production, $e^+e^- \to W^+W^- \to \mu^+\nu_\mu\mu^-\bar{\nu}_\mu$. The next dominant mode is ZZ production, $e^+e^- \to ZZ \to \mu^+\mu^-\nu_i\bar{\nu}_i$ where ν_i denotes a neutrino of all three flavors. The W^+W^- background is larger than the ZZ background by a factor of about 20. In the following numerical simulation, we include the full SM processes for the final state $\mu^+\mu^-\nu\bar{\nu}$.

Another substantial SM background is from $e^+e^- \to e^+e^-\mu^+\mu^-$ where the outgoing e^+ and e^- go down the beam pipe and thus are missed by the detectors. It is mainly generated by Bhabha scattering, with the incoming electron and positron through a t-channel diagram. Depending on the angular cut on the outgoing electrons, this background could be a few orders of magnitude larger than the signal. However, a cut on the missing transverse momentum can effectively remove it. The maximum missing transverse momentum in this background comes from the final electron and positron, each of which retains the full energy ($\sqrt{s}/2$ each) and moves within an angle of 1° with respect to the beam pipe (at the edge of the end-cap detector coverage). As a result, most of these background events lie within

$$(\not{p}_T)_{\text{beam line } e^+e^-} \lesssim 3 \times 250\,\text{GeV} \times \sin(1^\circ) \simeq 15\,\text{GeV}. \tag{3.1}$$

We thus design our basic acceptance cuts for the event selection

$$\begin{aligned} \texttt{Basic cuts:} \qquad & E_a \geq 10\,\text{GeV}, \quad \not{p}_T \geq 15\,\text{GeV}, \\ & |\cos\theta_\ell^{\text{cm}}| \leq 0.9962, \quad m_{aa} \geq 1\,\text{GeV}, \quad m_{\text{rec}} \geq 1\,\text{GeV}. \end{aligned} \tag{3.2}$$

The angular cut on θ_ℓ^{cm} requires that the observed lepton lies within 5° from the beam pipe. This angular acceptance and the invariant mass cut on the lepton pair regularize the perturbative singularities.

In principal, the full SUSY backgrounds should be included in addition to the $\tilde{\mu}_R$ and $\tilde{\mu}_L$ signal pair production. There are many types of SUSY backgrounds. The dominant ones are the production of $\tilde{\chi}_1^0\tilde{\chi}_{j\geq 2}^0$ followed by the heavier neutralino decay of $\tilde{\chi}_{j\geq 2}^0 \to l^+l^-\tilde{\chi}_1^0$. However, their contributions are negligible with our mass point and event selection.

At the ILC environment, it is crucial to consider the other realistic factors in order to reliably estimate the accuracy for the mass determination. These include the effects of initial state radiation (ISR), beamstrahlung [30] and detector resolutions. We adopt the commonly used calculational package Whizard [29] for the simulations. For the muon detector effect, we take the Gaussian momentum smearing as

$$\frac{\delta p_T}{p_T^2} = a \oplus \frac{b}{(p_T/\text{TeV})\sqrt{\sin\theta}}, \tag{3.3}$$

with the resolutions $a = 2 \times 10^{-5}$ and $b = 1$ [31].

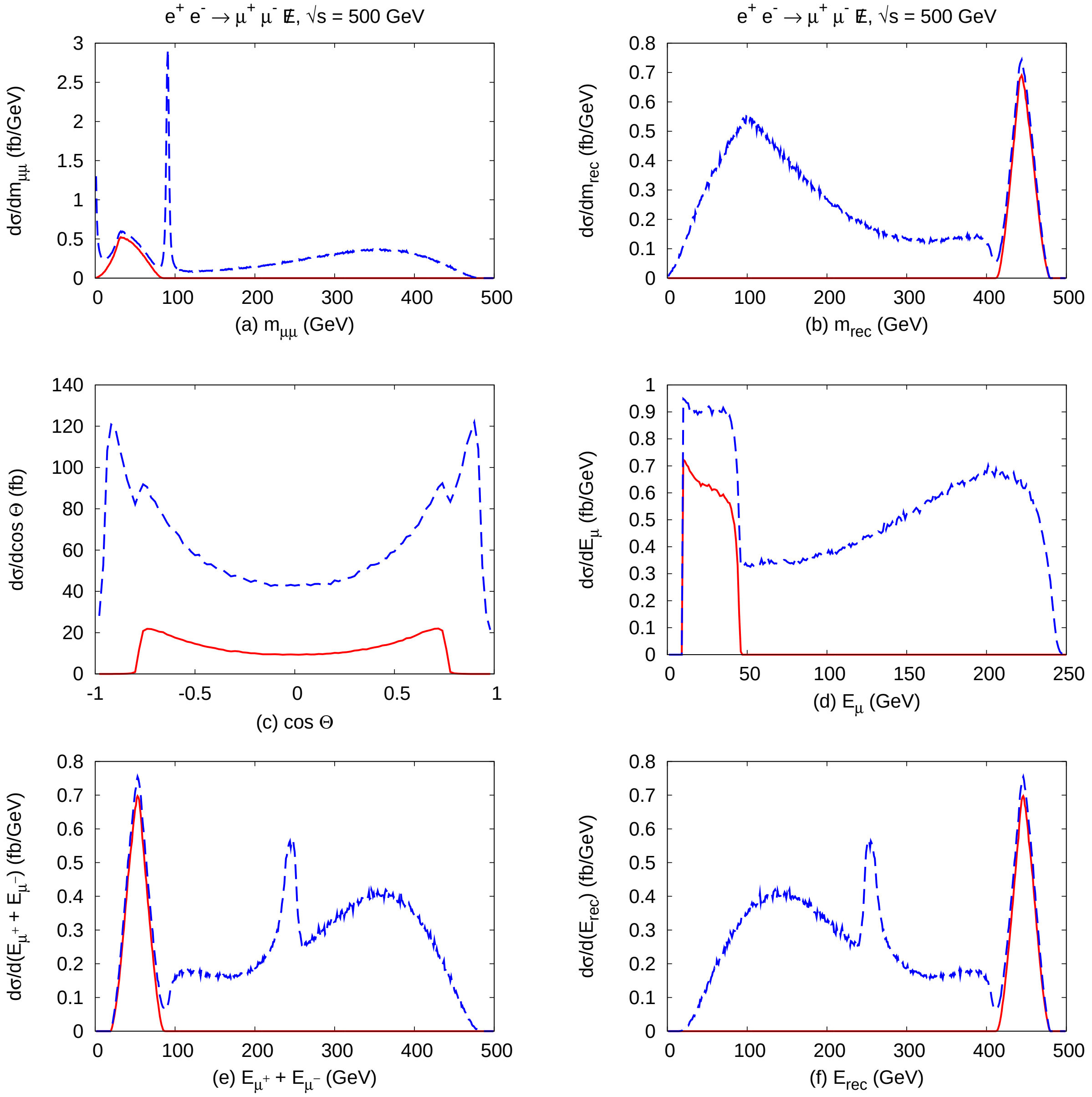

Figure 8: `IA` for $e^+e^- \to \tilde{\mu}_R\tilde{\mu}_R \to \mu^+\mu^-\not{E}$. Basic acceptance cut on the $m_{\mu\mu}$, $m_{\rm rec}$, $\cos\Theta$, E_μ, $E_{\mu^+}+E_{\mu^-}$, and $E_{\rm rec} = E_{X_1}+E_{X_2}$ distributions with spin-correlation and other realistic effects. The c.m. energy is set at $\sqrt{s} = 500\,\text{GeV}$ for all distributions. The solid (red) line denotes our signal of the resonant production of a $\tilde{\mu}_R$ pair. The dashed (blue) line is the total event including our signal and the SM backgrounds.

3.2 `IA`: $\tilde{\mu}_R\tilde{\mu}_R$ PAIR PRODUCTION

For the mass spectrum in `IA`, Fig. 8 presents a full simulation of the six kinematic distributions at $\sqrt{s} = 500\,\text{GeV}$ with the basic cuts in Eq. (3.2). The solid (red) line denotes our signal of the resonant production of a $\tilde{\mu}_R\tilde{\mu}_R$ pair. The dashed (blue) line is the total distribution including our signal and the SM backgrounds.

The $m_{\mu\mu}$ distribution from our signal in Fig. 8(a) does not reveal the best feature of the antler process. Its cusp is not very pronounced and its maximum is submerged under the dominant Z pole. As discussed before, this is because the c.m. energy of 500 GeV is too high compared with the smuon mass. On the contrary, the m_{rec} distribution in Fig. 8(b) separates our signal from the SM backgrounds well: a sharp triangular shape is clearly seen above the SM background tail. This separation is attributed to the weak scale mass of the missing particle X. If X were much lighter, with $M_X \simeq 10\,\text{GeV}$ or so, the cusp position in the m_{rec} distribution of the signal would be shifted downward to a lower value and thus overlap with that of the large W^+W^- continuum background.

Figure 8(c) presents the $\cos\Theta$ distributions, with the the W^+W^- background and the $\tilde{\mu}_R\tilde{\mu}_R$ signal. However, the highest point of $\cos\Theta$ (the cusp location) is shifted from the location of the $|\cos\Theta|_{\text{max}}$ as given in Table 4, by about $2 \sim 3\%$. This is from the kinematical smearing due to ISR and beamstrahlung effects.

Figure 8(d) shows the muon energy distribution, which consists of two previously box-shaped distributions. Our signal distribution, which is expected to be flat for a scalar boson, is distorted by acceptance cuts, event selection criteria and ISR. The SM background, mainly the W^+W^- background, shows a more tilted distribution, which has additional effects from spin correlation. The reason for the tilted distribution toward higher E_μ is that the W^+W^- production has the largest contribution from the production of $W_L^-W_R^+$ mediated by a t-channel neutrino [32]. Here W_L^- (W_R^+) denotes the left-handed (right-handed) negatively (positively) charged W boson. W_L^- has the left-handed coupling of ℓ_L^--$\bar{\nu}_R$-W_L^- so that the decayed ℓ_L^- moves along the parent W^- direction and the $\bar{\nu}$ in the opposite direction. The ℓ^- tends to have higher energy. Even though the E_a distribution is not flat both for the signal and the backgrounds, their maximum positions are the same as predicted in Table 4.

However, the minimum position for the W^+W^- distribution is below the acceptance cut while the minimum for the $\tilde{\mu}_R\tilde{\mu}_R$ signal is approximately the same as the cut making the measurement of these minima problematic. As a result, the other kinematic observables discussed here are essential in the measurement of these masses.

Finally Figures 8(e) and 8(f) present the energy sum of two visible particles and two missing particles, respectively. Both distributions for our signal are triangular. In addition, the signal distributions of E_{aa} and E_{XX} are separated from the SM backgrounds. Even in the full and realistic simulation, the cusps and endpoints of the signal are very visible. In fact, the signal parts of these distributions take a very similar form to that of m_{rec}.

Understanding the six kinematic distributions of our signal is of great use to suppress the SM background. For example, we apply an additional cut of

$$m_{\rm rec} > 350\,{\rm GeV}, \tag{3.4}$$

and present the distributions of the same 6 kinematic variables in Fig. 9. Now our signal, denoted by the solid (red) lines, remains intact since $m_{\rm rec}^{\rm min} = 408\,{\rm GeV}$ for $\tilde{\mu}_R\tilde{\mu}_R$. On the other hand, a large portion of the SM background is excluded. The antler characteristics of our signal emerge in the total distributions. We can identify all of the cusp structures.

3.3 `IB`: PRODUCTION $\tilde{\mu}_R\tilde{\mu}_R$ AND $\tilde{\mu}_L\tilde{\mu}_L$ OF SMUONS

We now consider the more complex `IB`, where three different antler processes, $\tilde{\mu}_R\tilde{\mu}_R$, $\tilde{\mu}_L\tilde{\mu}_L$, and W^+W^-, are simultaneously involved. In Fig. 10, we present 6 distributions for `IB` at $\sqrt{s} = 500\,{\rm GeV}$. Here $m_{\rm rec} > 350\,{\rm GeV}$ cut has been applied to suppress the main SM backgrounds from W^+W^-. The solid (red) line is the $\tilde{\mu}_R\tilde{\mu}_R$ signal, the dotted (purple) line is from $\tilde{\mu}_L\tilde{\mu}_L$. Finally, the dashed (blue) line is the total event including our two signals and the SM backgrounds. Note that the total rate for $\tilde{\mu}_R\tilde{\mu}_R$ is compatible with that for $\tilde{\mu}_L\tilde{\mu}_L$.

In Fig. 10(a), we show the m_{aa} distributions. As expected from the previous analyses, the $\tilde{\mu}_R\tilde{\mu}_R$ signal leads to a cusp structure, while $\tilde{\mu}_L\tilde{\mu}_L$ and W^+W^- do not due to the specific mass and energy relations. On the contrary, the $m_{\rm rec}$ distributions in Fig. 10(b) do show

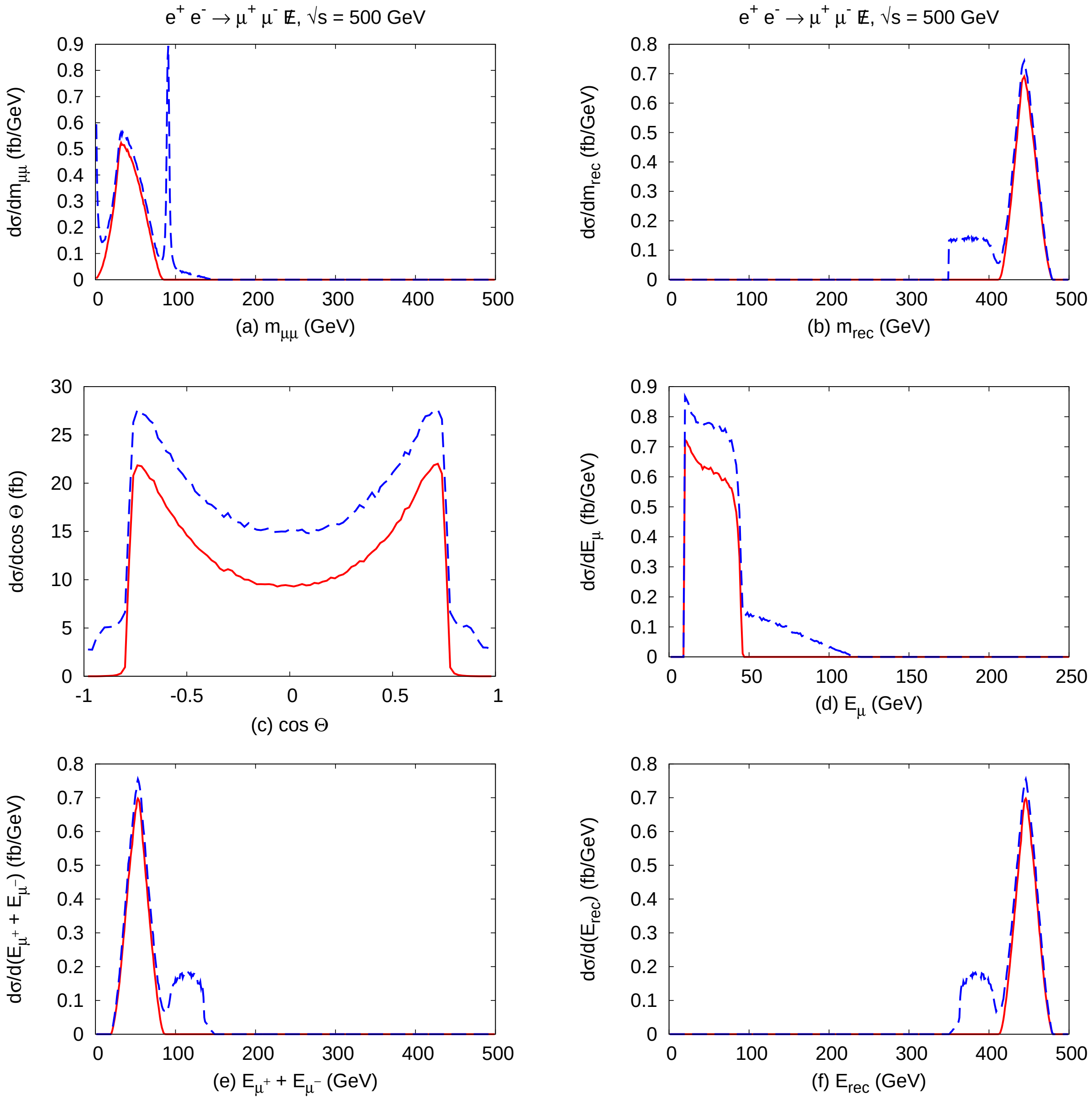

Figure 9: `IA` for $e^+e^- \to \tilde{\mu}_R\tilde{\mu}_R \to \mu^+\mu^-\not{E}$. The effect of an additional cut of $m_{\rm rec} > 350\,{\rm GeV}$ on the $m_{\mu\mu}$, $m_{\rm rec}$, $\cos\Theta$, E_μ, $E_{\mu^+} + E_{\mu^-}$, and $E_{\rm rec} = E_{X_1} + E_{X_2}$ distributions with spin-correlation and other realistic effects. The c.m. energy is set $\sqrt{s} = 500\,{\rm GeV}$ for all distributions. The solid (red) line denotes our signal of the resonant production of a $\tilde{\mu}_R$ pair. The dashed (blue) line is the total event including our signal and the SM backgrounds.

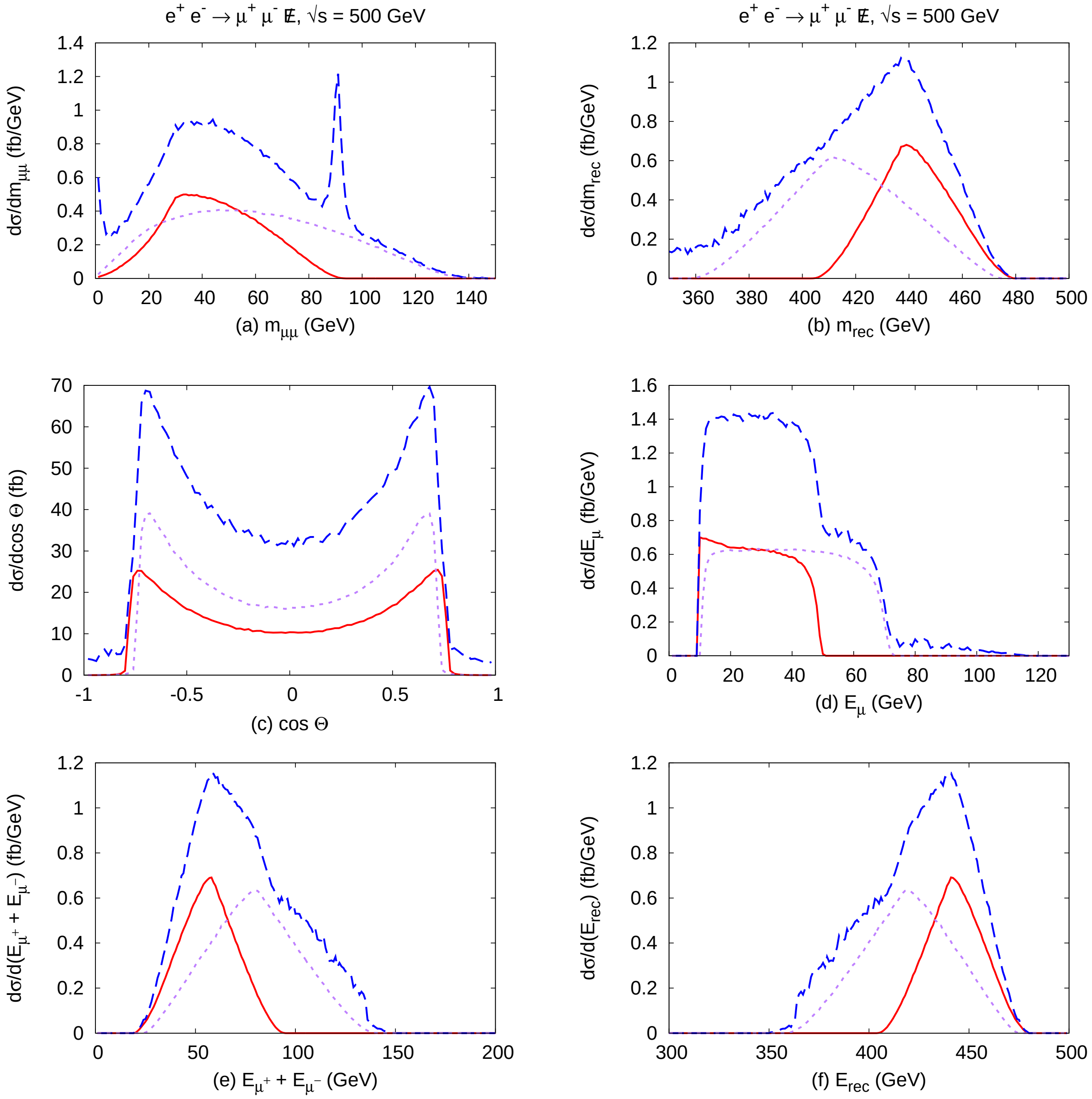

Figure 10: `IB` for $e^+e^- \to \tilde{\mu}_L\tilde{\mu}_L, \tilde{\mu}_R\tilde{\mu}_R \to \mu^+\mu^-\not{E}$. The additional cut of $m_{\rm rec} > 350\,{\rm GeV}$ is included. We show the $m_{\mu\mu}$, $m_{\rm rec}$, $\cos\Theta$, E_μ, $E_{\mu^+}+E_{\mu^-}$, and $E_{\rm rec} = E_{X_1}+E_{X_2}$ distributions with spin-correlation and other realistic effects. The c.m. energy is set $\sqrt{s} = 500\,{\rm GeV}$ for all distributions. The solid (red) line corresponds to $\tilde{\mu}_R^+\tilde{\mu}_R^-$, the dotted (purple) line to $\tilde{\mu}_L^+\tilde{\mu}_L^-$. The dashed (blue) line is the total event including our signal and the SM backgrounds.

two individual triangles, with $\tilde{\mu}_R\tilde{\mu}_R$ by the solid (red) curve, $\tilde{\mu}_L\tilde{\mu}_L$ by the dotted (purple) curve. The SM background is well under-control after the stringent cuts. The challenge is to extract the hidden mass information from the observed overall (blue) curve as a combination of the twin peaks. It is conceivable to achieve this by a fitting procedure based on two triangles. Instead, as done below, we demonstrate another approach by taking advantage of the polarization of the beams.

Figure 10(c) presents the $\cos\Theta$ distribution. The visible $\cos\Theta$ cusp is usually attributed to the lighter intermediate particles ($\tilde{\mu}_R$ in our case): a larger $|\cos\Theta|_{\max}$ comes from a smaller m_B with a given c.m. energy. It appears that, with our parameter choice, the $\tilde{\mu}_R\tilde{\mu}_R$ and $\tilde{\mu}_L\tilde{\mu}_L$ lead to a similar value of $|\cos\Theta|_{\max}$, which differ by about 5%.

The E_a distribution, with the energy end-point in Fig. 10(d), is known to be one of the most robust variables. Two box-shaped distributions are added to create a two-step stair. Although the ISR and beamstrahlung smear the sharp edges, leading to some uncertainty in the $E_a^{\max}$ measurement, the observation of the two maxima should be quite feasible. On the other hand, the determination of $E_a^{\min}$ could be more challenging since the acceptance cut for the lepton lower energy threshold could overwhelm $E_a^{\min}$ for $\tilde{\mu}_R\tilde{\mu}_R$, and make it marginally visible for $\tilde{\mu}_L\tilde{\mu}_L$.

Finally, we present the energy sum distributions of two visible particles and two missing particles in Fig. 10(e) and (f), respectively. The individual distributions from the $\tilde{\mu}_R\tilde{\mu}_R$ and $\tilde{\mu}_L\tilde{\mu}_L$ production lead to impressive sharp triangles, as those in Fig. 10(b). The challenge is, once again, to extract the two unknown masses from the observed summed distribution. We next discuss beam polarization as a way to accomplish this.

All six distributions show that the two entangled new physics signals as well as the SM backgrounds limit the precise measurements of the cusps and endpoints. The polarization of the electron and positron beams can play a critical role in disentangling this information. The current baseline design of the ILC anticipates at least 80% (30%) polarization of the electron (positron) beam. By controlling the beam polarization, we can suppress the SM backgrounds and distinguish the two different signals. For the $\tilde{\mu}_R\tilde{\mu}_R$ signal, our optimal setup is $\mathcal{P}_{e^-} = +80\%$ and $\mathcal{P}_{e^+} = -30\%$, denoted by $e_R^- e_L^+$, while for the $\tilde{\mu}_L\tilde{\mu}_L$ signal we apply $\mathcal{P}_{e^-} = -80\%$ and $\mathcal{P}_{e^+} = +30\%$ denoted by $e_L^- e_R^+$.

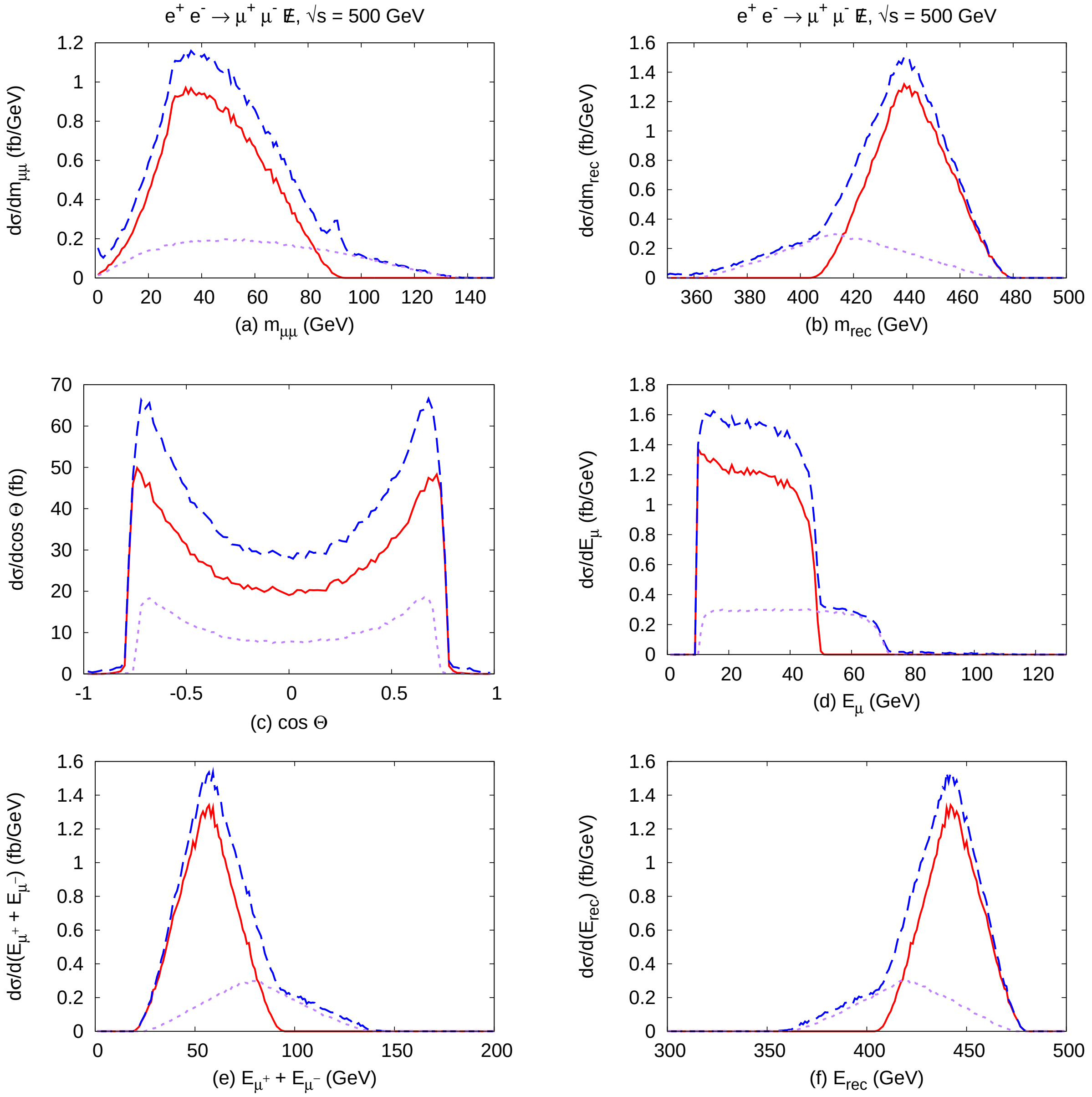

Figure 11: `IB` for $e^+e^- \to \tilde{\mu}_L\tilde{\mu}_L, \tilde{\mu}_R\tilde{\mu}_R \to \mu^+\mu^-\not{E}$. Effects of an additional cut of $m_{\rm rec} > 350\,{\rm GeV}$ and polarizations $\mathcal{P}_{e^-} = +80\%$ and $\mathcal{P}_{e^+} = -30\%$ on the $m_{\mu\mu}$, $m_{\rm rec}$, $\cos\Theta$, E_μ, $E_{\mu^+} + E_{\mu^-}$, and $E_{\rm rec} = E_{X_1} + E_{X_2}$ distributions with spin-correlation and other realistic effects. The c.m. energy is set to $\sqrt{s} = 500\,{\rm GeV}$ for all distributions. The solid (red) line corresponds to $\tilde{\mu}^+_R\tilde{\mu}^-_R$, the dotted (purple) line to $\tilde{\mu}^+_L\tilde{\mu}^-_L$. The dashed (blue) line is the total event including our signal and the SM backgrounds.

Figure 11 shows how efficient the right-handed electron beam is at picking out the $\tilde{\mu}_R\tilde{\mu}_R$ signal. For the suppression of the SM backgrounds, we apply the cut of $m_{\rm rec} \geq 350\,{\rm GeV}$. As before, the solid (red) line corresponds to $\tilde{\mu}_R^+\tilde{\mu}_R^-$, the dotted (purple) line to $\tilde{\mu}_L^+\tilde{\mu}_L^-$. The dashed (blue) line is the total event including our signal and the SM backgrounds. The nearly right-handed electron beam suppresses the SM background as well as the $\tilde{\mu}_L\tilde{\mu}_L$ signal. Only the $\tilde{\mu}_R\tilde{\mu}_R$ signal stands out. The main SM background is through the resonant W^+W^- production: the left-handed coupling of the e-ν_e-W is suppressed by the right-handed electron beam. Another interesting feature is that the Z-pole in the $m_{\mu\mu}$ distribution is also very suppressed. A significant contribution to the Z-pole is from the $e^+e^- \to \nu_e\bar{\nu}_e Z$ process where Z is via WW-fusion. Again the left-handed coupling of the charged current is suppressed by the right-handed electron beam.

The advantage of the cusp is clearly shown here. Its peak structure is not affected. But other endpoints, such as $m_{\rm rec}^{\rm min}$, $E_a^{\rm min}$, $E_{aa}^{\rm max}$, and $E_{\tilde{\chi}_1^0\tilde{\chi}_1^0}^{\rm min}$, are overlapped with other backgrounds, although the right-handed polarization removes a large portion of the SM backgrounds. We also observe that $m_{\rm rec}^{\rm max}$, $E_a^{\rm max}$, $E_{aa}^{\rm min}$, and $E_{\tilde{\chi}_1^0\tilde{\chi}_1^0}^{\rm max}$ are not contaminated. In summary, the mass measurement of $\tilde{\mu}_R$ and $\tilde{\chi}_1^0$ through the cusp and endpoint is well benefited by the right-handed polarization of the electron beam.

The left-handed $\tilde{\mu}_L\tilde{\mu}_L$ signal is more difficult to probe since its left-handed couplings are the same as the SM background. In Fig. 12, we set $\mathcal{P}_{e^-} = -80\%$ and $\mathcal{P}_{e^+} = +30\%$ with the additional cut of $m_{\rm rec} > 350\,{\rm GeV}$.

From the m_{aa} distribution, we see that the Z-pole is still strongly visible and the round $m_{aa}^{\rm cusp}$ for the $\tilde{\mu}_L\tilde{\mu}_L$ signal is very difficult to identify. The total $m_{\rm rec}$ distribution in Fig. 12(b) does not show the sharp triangular shape of the antler decay topology either. The individual triangular shapes of the $\tilde{\mu}_R\tilde{\mu}_R$ and $\tilde{\mu}_L\tilde{\mu}_L$ signals along with the background are combined into a rather featureless bump-shaped distribution. Although there is a peak point, it is hard to claim as a cusp. The $\cos\Theta$ distribution in Fig. 12(c) shows one of the most characteristic features of the antler topology. Two sharp cusps appear, of which the peak position is the same as that of the $\tilde{\mu}_L\tilde{\mu}_L$ signal.

The total E_a distribution in Fig. 12(d) does not provide quite as clean a series of rectangular distributions. The mixture of different contributions from $\tilde{\mu}_R\tilde{\mu}_R$, $\tilde{\mu}_L\tilde{\mu}_L$ and W^+W^-

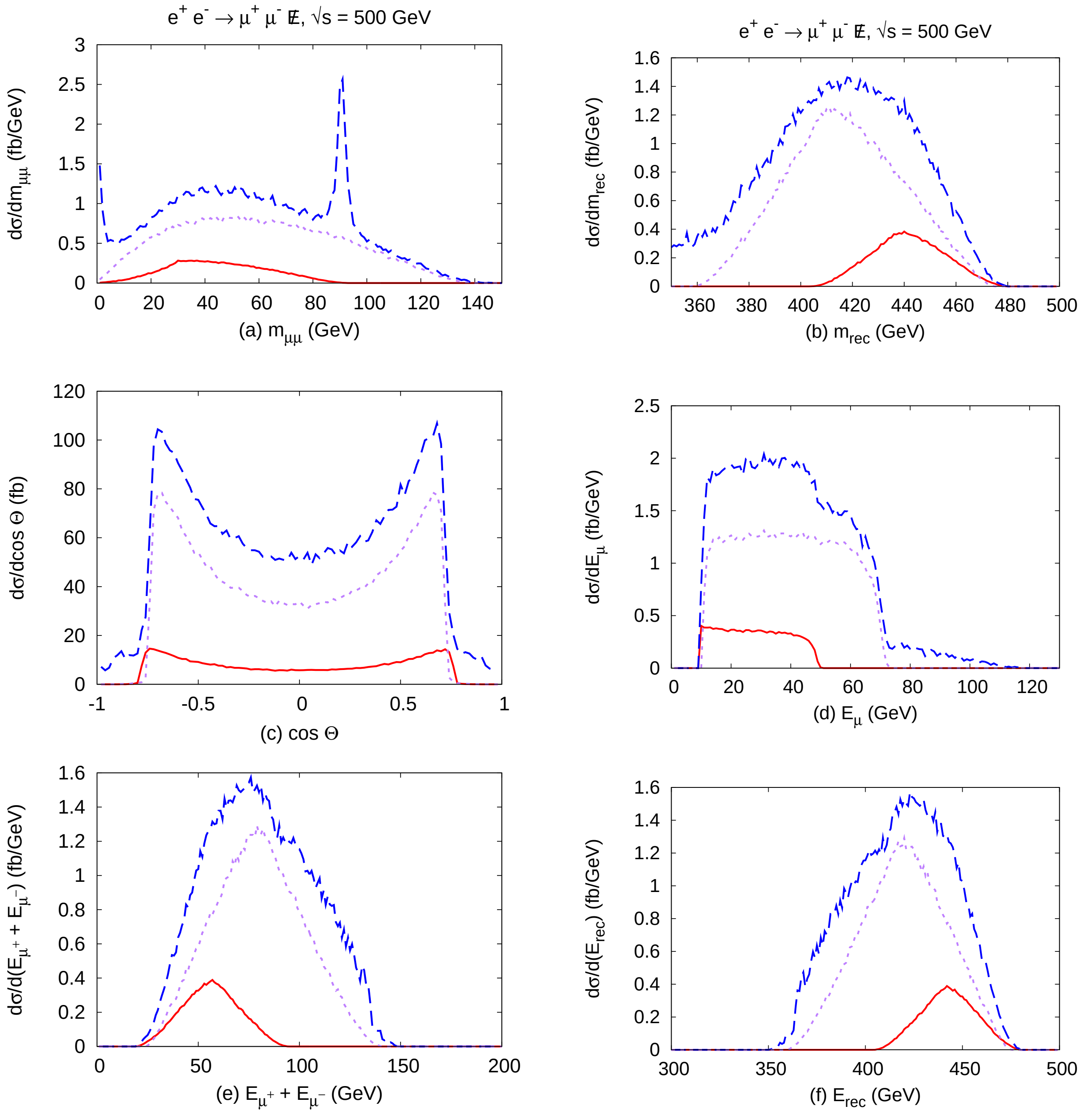

Figure 12: `IB` for $e^+e^- \to \tilde{\mu}_L\tilde{\mu}_L, \tilde{\mu}_R\tilde{\mu}_R \to \mu^+\mu^-\not{E}$. Effects of an additional cut of $m_{\rm rec} > 350\,{\rm GeV}$ and polarizations $\mathcal{P}_{e^-} = -80\%$ and $\mathcal{P}_{e^+} = +30\%$ on the $m_{\mu\mu}$, $m_{\rm rec}$, $\cos\Theta$, E_μ, $E_{\mu^+} + E_{\mu^-}$, and $E_{\rm rec} = E_{X_1} + E_{X_2}$ distributions with spin-correlation and other realistic effects. The c.m. energy is set $\sqrt{s} = 500\,{\rm GeV}$ for all distributions. The solid (red) line corresponds to $\tilde{\mu}_R^+\tilde{\mu}_R^-$, the dotted (purple) line to $\tilde{\mu}_L^+\tilde{\mu}_L^-$. The dashed (blue) line is the total event including our signal and the SM backgrounds.

along with the shorter broader nature of the $\tilde{\mu}_L\tilde{\mu}_L$ rectangle and the smearing makes reading the maximum points more difficult. The $E_a^{\min}$ position of the $\tilde{\mu}_L\tilde{\mu}_L$ signal is mixed with the SM backgrounds and the $\tilde{\mu}_R\tilde{\mu}_R$ signal as well as being near the kinematic cut. Finally, both the total E_{aa} and E_{XX} distributions lose the triangular shape of the $\tilde{\mu}_L\tilde{\mu}_L$ signal: see Fig. 12(e) and (f). Nevertheless the peak position coincides with the cusp position for both energy sum distributions. We can identify them with the cusps.

3.4 MASSIVE VISIBLE PARTICLE CASE: CHARGINO PAIR PRODUCTION

It is quite likely that the DM particles will be accompanied by other massive observable final states in the decay process. Although the nature of the cusps is similar to the previous discussions, the characteristic features and their observability may be rather different. An important example of this type of kinematics is in chargino pair production followed by the chargino's decay into a W and a LSP. This process is a typical antler process, which is different from the smuon pair production in that the visible particle W is massive. In order to fully reconstruct the kinematics of the W, we consider the case where the W boson decays hadronically. Therefore, our signal event selection is

$$e^+e^- \to \tilde{\chi}_1^+\tilde{\chi}_1^- \to W^+W^-\tilde{\chi}_1^0\tilde{\chi}_1^0 \to jj, jj + \tilde{\chi}_1^0\tilde{\chi}_1^0. \tag{3.5}$$

For illustrative purposes, we will choose the masses of the particles as

$$\begin{aligned} m_a &= m_W, \quad m_B = m_{\tilde{\chi}_1^\pm} = 235\,\mathrm{GeV}, \quad m_X = m_{\tilde{\chi}_1^0} = 139\,\mathrm{GeV}, \qquad (3.6) \\ m_{\tilde{\chi}_2^0} &= 235\,\mathrm{GeV}, \quad m_{\tilde{\chi}_3^0} = 504\,\mathrm{GeV}, \quad m_{\tilde{\chi}_4^0} = 529\,\mathrm{GeV}, \\ m_{\tilde{\chi}_2^\pm} &= 515\,\mathrm{GeV}. \end{aligned}$$

This is called `II` and shown in Table 3.

Table 5: The values of various kinematic cusps and endpoints for the mass parameters in Eq. 3.6. All the masses and energies are in units of GeV.

$\sqrt{s}$	Channel	(m_B, m_X, m_a)	$(m_{aa}^{\text{min}}, m_{aa}^{\text{cusp}}, m_{aa}^{\text{max}})$	$(m_{\text{rec}}^{\text{min}}, m_{\text{rec}}^{\text{cusp}}, m_{\text{rec}}^{\text{max}})$
500	$\tilde{\chi}_1^+\tilde{\chi}_1^-$	$(235, 139, m_W)$	$(161, 171, 221)$	$(279, 296, 338)$
		$(E_a^{\text{min}}, E_a^{\text{max}})$	$(E_{aa}^{\text{min}}, E_{aa}^{\text{cusp}}, E_{aa}^{\text{max}})$	$(E_{\tilde{\chi}_1^0\tilde{\chi}_1^0}^{\text{min}}, E_{\tilde{\chi}_1^0\tilde{\chi}_1^0}^{\text{cusp}}, E_{\tilde{\chi}_1^0\tilde{\chi}_1^0}^{\text{max}})$
		$(81, 111)$	$(162, 190, 221)$	$(278, 309, 338)$

The massive visible particle case involves the three rapidities of the intermediate particle B, the missing particle X, and the visible particle W. In order to avoid notational confusion from the massless visible particle case, we denote the rapidities by ξ_B, ξ_X, and ξ_W, given by

$$\cosh\xi_B = \frac{\sqrt{s}}{2m_B}, \quad \cosh\xi_W = \frac{m_B^2 - m_X^2 + m_W^2}{2m_W m_B}, \quad \cosh\xi_X = \frac{m_B^2 - m_W^2 + m_X^2}{2m_X m_B}. \tag{3.7}$$

The distributions of the invariant mass of W^+W^- and $\tilde{\chi}_1^0\tilde{\chi}_1^0$ follow the same characteristic function where now the visible particle W is massive. The cusp and endpoint positions of these distributions are listed in Table 2 where for m_{WW}, we replace $\eta_B \to \xi_B$ and $\eta_X \to \xi_W$ and for m_{rec}, we take $\eta_B \to \xi_B$ and $\eta_X \to \xi_X$. The $\cos\Theta$ distribution for the massive visible particle case does not present a sharp cusp or endpoint in this case. The E_W distribution has a minimum and maximum as in the massless visible particle case, with the generalized expressions

$$E_W^{\text{max,min}} = \frac{\sqrt{s}}{4}\left(1 - \frac{m_X^2 - m_W^2}{m_B^2}\right)\left(1 \pm \beta_B\sqrt{1 - \frac{4m_a^2 m_B^2}{(m_B^2 + m_a^2 - m_X^2)^2}}\right). \tag{3.8}$$

The E_{WW} distribution has minimum, cusp, and maximum positions which are given by

$$\begin{aligned} E_{WW}^{\text{min}} &= 2m_W\cosh(\xi_W - \xi_B), \\ E_{WW}^{\text{cusp}} &= 2m_W\cosh\xi_W\cosh\xi_B, \\ E_{WW}^{\text{max}} &= 2m_W\cosh(\xi_W + \xi_B). \end{aligned} \tag{3.9}$$

The positions of the E_{XX} singular points are obtained through $E_{XX} = \sqrt{s} - E_{WW}$. In Table 5, we present the values of the cusps and endpoints for `II`.

The reconstruction of the variables m_{WW}, $m_{\rm rec}$, E_{WW}, and E_{XX} is straight forward in terms of the jets and the known collision frame. In order to reconstruct E_W and $\cos\Theta$, we split the jets into two pairs which each reconstruct an invariant mass near m_W. We then note that due to the symmetry of the antler decay topology, the E_{W^+} and E_{W^-} distributions are symmetric with respect to each other and the $\cos\Theta$ distribution is symmetric with respect to an interchange of W^+ and W^-. As a result, the E_W and $\cos\Theta$ distributions can be obtained by averaging the distributions for each W.

We show the kinematic distributions for the process $e^+e^- \to jj, jj + \not{E}$ at $\sqrt{s} = 500\,\text{GeV}$ in Fig. 13. In these plots, we have included the full spin correlation as well as the effects of ISR, beamstrahlung and detector smearing. In addition to our basic cuts outlined in Eq. (3.2), we have applied the following cuts

$$\Delta R_{jj} \equiv \sqrt{(\Delta\eta_{jj})^2 + (\Delta\phi_{jj})^2} \geq 0.4 \ , \tag{3.10}$$
$$|m_{jj} - m_W| < 5\Gamma_W \ , \quad m_{\rm rec} > 120\,\text{GeV} \ ,$$

where the jet separation ΔR_{jj} is between all pairs of jets, m_{jj} is only between pairs of jets identified with the W and the $m_{\rm rec} > 120\,\text{GeV}$ cut removes most of the remaining SM background. We have also applied a Gaussian momentum smearing to approximate the detector effect

$$\frac{\delta E}{E} = \frac{a}{\sqrt{E/GeV}} \oplus b \tag{3.11}$$

with the resolutions $a = 0.55$ and $b = 0.075$ [31]. In Fig. 13, the solid (red) lines denote our chargino signal. The dotted (blue) lines give the total differential cross section including our signal and the SM backgrounds. The SM backgrounds are computed through the full two-to-six processes $e^+e^- \to jjjj\nu\bar{\nu}$ which includes the full spin correlation.

Figures 13(a) and (b) show the invariant mass distributions of four jets and two invisible particles, respectively. Realistic effects smear the sharp m_{4j} and $m_{\rm rec}$ distributions significantly. In particular, the locations of $m_{4j}^{\rm min}$ and $m_{\rm rec}^{\rm min}$ are shifted to lower values by about 20 GeV from the expected value from kinematics alone which are shown in Table 5. This is mainly due to detector smearing. The m_{4j}^{cusp} and m_{4j}^{max} are respectively in agreement with the m_{aa}^{cusp} and m_{aa}^{max} values in Table 5 but are significantly smeared. The $m_{\text{rec}}^{\text{cusp}}$ and $m_{\text{rec}}^{\text{max}}$ are larger by about 10 GeV than the expected values. As commented earlier, the $\cos\Theta$ distribution in Fig. 13(c) does not have a sharp cusp even before including realistic effects.

Figure 13(d) presents the E_W distribution which is significantly smeared and the sharp edges are no longer visible due to jet energy resolution effects. The expected values of E_W^{min} and E_W^{max} cannot be read from this distribution. In Figs. 13(e) and (f), we show the distributions of E_{jjjj} and $E_{\text{rec}} \equiv \sqrt{s} - E_{jjjj}$, respectively. The expected triangular shapes can be seen but the sharp features are smeared due to the realistic considerations. Their minimum and maximum positions are moved to approximately 10 GeV lower and higher values, respectively, while the cusp positions identified with the peaks remain near the expected values.

In summary, we have shown how the various kinematical distributions will most probably look like in the future International Linear Collider environment by including the various realistic effects for the two distinct cases, massless and massive final visible particles. We have also seen that in the massive case hadronization of the W bosons into jets affects the energy distribution of the visible particle heavily by smearing the sharp end points into smooth gradients. This and other realistic effects as shown in the previous chapter alter the location of singular points within the distributions that we need in extracting the WIMP mass. Hence we need a way to quantify the uncertainty in our mass measurement which will be the subject of the next chapter.

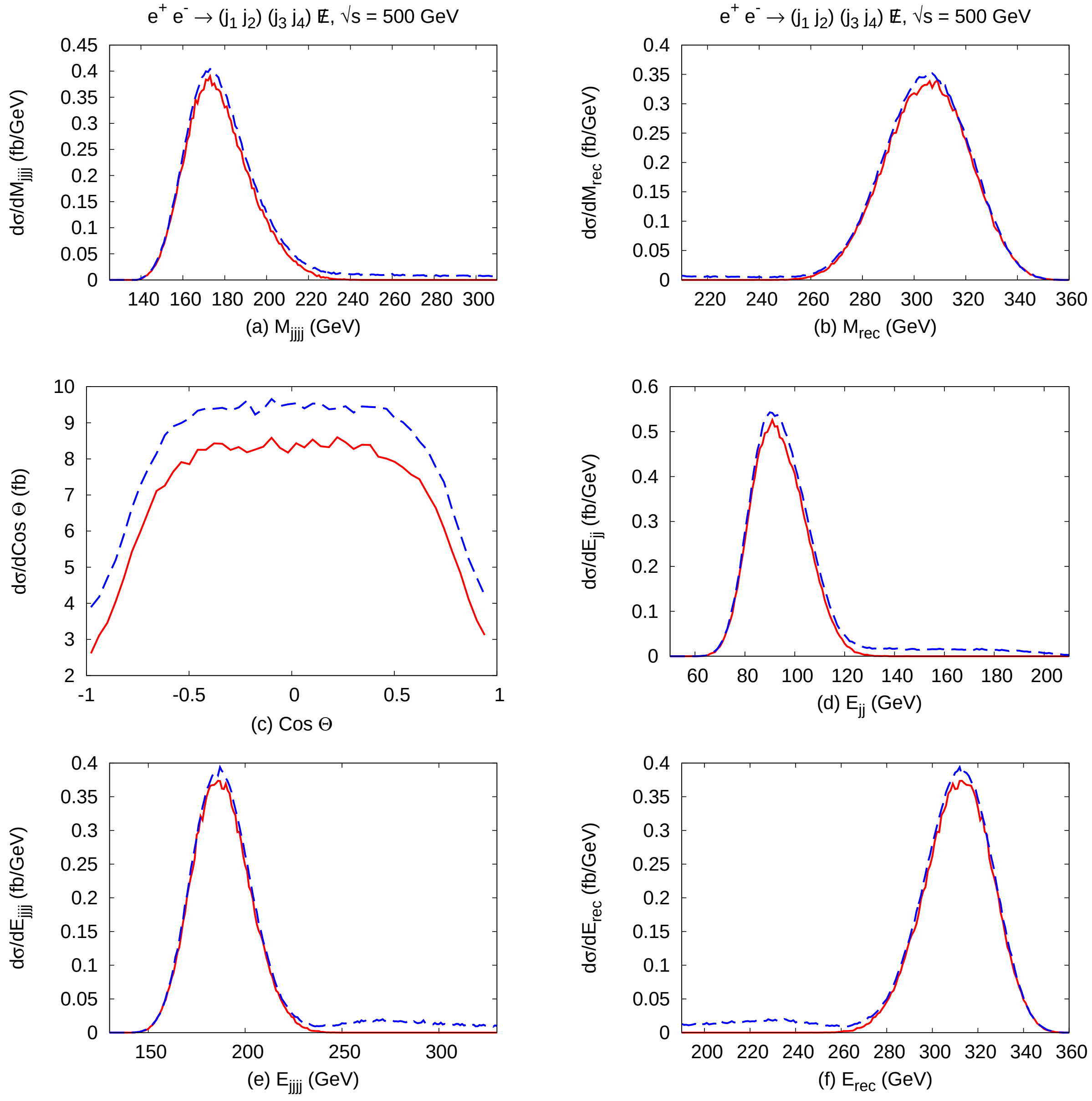

Figure 13: `II` for $e^+e^- \to jj, jj + \not{E}$ with an additional cut of $m_{\rm rec} \geq 120\,{\rm GeV}$ and $|m_{jj} - m_W| < 5\Gamma_W$. We show the m_{jjjj}, $m_{\rm rec}$, $\cos\Theta$, E_{jj}, E_{WW}, and $E_{\rm rec} = E_{X_1} + E_{X_2}$ distributions with spin-correlation and other realistic effects. The c.m. energy is set to $\sqrt{s} = 500\,{\rm GeV}$ for all distributions. The solid (red) line denotes our signal of the resonant production of a chargino pair. The dashed (blue) line is the total event including our signal and the SM backgrounds.

4.0 UNCERTAINTY OF CUSP AND ENDPOINTS MEASUREMENT

In the present chapter we study the uncertainty of the masses of the intermediate and missing particles inferred from the cusp and endpoints of antler decay processes. This is different from the problem of identifying the cusp and endpoints of the distributions. As mentioned in the previous chapter, the minimum endpoint of the E_a distribution is well below the acceptance cut. The masses of the intermediate and missing particles are therefore not deducible from this distribution alone.

This, however, is not the subject of our present discussion. Instead, we would like to derive a quantitative measure of the accuracy of the cusp and endpoints given by a particular model due to the statistical nature of the process, *i.e.* whether models with different parameter points give the same cusp and endpoints within the expected statistical fluctuations. This is important because events of particle scattering and decay are governed by Poisson distribution. The lack of number of events can often pass off one parameter point as a very different one and so we would like to know the minimum number of events to ensure an acceptable level of certainty as well.

In order to estimate the achievable precision of a measurement of the masses in the presence of realistic effects, we analyze the distributions we have discussed here using the log-likelihood method based on Poisson statistics. A benefit of a log-likelihood analysis is that it compares the full shape of the distribution and not just the position of the cusps and endpoints which, as we have seen, can be smeared and even moved due to realistic collider effects.

In the following sections we will discuss the log-likelihood method and how it can be used in evaluating the uncertainty of masses of intermediate and missing particles measured through the antler decay scheme.

4.1 DISTINGUISHING HYPOTHESES USING THE LOG-LIKELIHOOD

In theoretical high energy physics, it is often important to determine how well one hypothesis can be distinguished from another. In the present case, the hypotheses are different masses for the smuons, charginos and neutralinos and we would like to know how well a new kinematical variable distinguishes between these masses. In another context, the hypotheses may be the Standard Model (SM) and a new model beyond the SM and we may want to determine how well we can distinguish the models with a standard kinematical variable such as the invariant mass. In any case, the outcome of a scattering experiment is governed by probability and the tests to determine the degree to which a hypothesis fits the data is governed by statistics. As a result, determining the power of a particular observable to distinguish between different hypotheses is also governed by statistics.

In order to determine how likely a particular measurement agrees with experiment, we need to form a *test statistic* which is a function of a hypothesis and the observation. If the value of the test statistic is in certain ranges, the observation agrees well with the hypothesis while if the test statistic is in other ranges, the agreement is poor. There are many possibilities for the test statistic ranging from a multidimensional vector to a scalar function. Scalar test statistics are often convenient because they are more manageable while still retaining the power to distinguish between hypotheses. Two very popular test statistics in high energy physics are the log-likelihood based on Gaussian statistics and the log-likelihood based on Poisson statistics.

4.1.1 Random Fluctuations Around the Mean

During a scattering experiment, a very large number of collisions occur with each collision being independent of, and uncorrelated with, every other collision. As a result, the random probability of a particular collision or of an observable of particular value is given by the Poisson probability function

$$f_P(n;\nu) = \frac{\nu^n e^{-\nu}}{n!} \ , \tag{4.1}$$

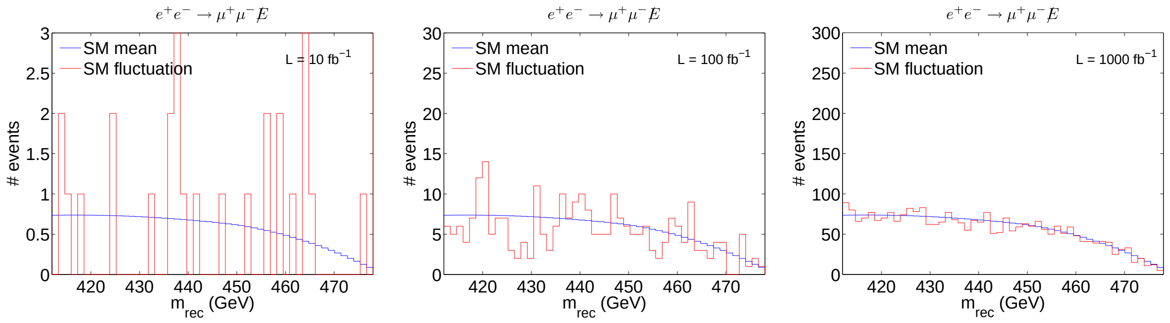

(a) (b) (c)

Figure 14: The SM mean in blue and one particular random fluctuation in red for the m_{rec} distribution for (a) 10 fb^{-1}, (b) 100 fb^{-1}, and (c) 1000 fb^{-1}.

where n is the number of events that actually occur of the type specified and ν is the mean, or the expectation value, for the specific collision or observable. For particle collisions, ν is given by the cross section times the integrated luminosity for the specific collision or observable value. For example, if the cross section for resonant production of a new particle is 1 fb and the integrated luminosity is 100 fb^{-1}, then $\nu = 100$. Or, if the cross section for the invariant mass to be between 600 GeV and 700 GeV in a particular model is 5 fb and the integrated luminosity is 10 fb^{-1}, then $\nu = 50$. The actual number generated during the experiment is random and unknown until measured, but the probability for each n is given by $f_P(n;\nu)$.

As another example, in Fig. 14, we show the m_{rec} distribution discussed in Sec. 2.2 on the discussion for the SM background. There are 50 bins in this distribution. For each bin, the blue curve gives ν, the number of events expected under the assumption of the SM. Its shape does not change with the integrated luminosity. Only its normalization changes and scales with the integrated luminosity. As already mentioned, the actual distribution is random and unknown, a priori. In each bin, the probability of getting n_i events is given by $f_P(n_i;\nu_i)$ where ν_i is the expectation value for that bin. The red curves in Fig. 14 give one particular randomly generated distribution. As the integrated luminosity increases, the relative size of the fluctuations decreases.

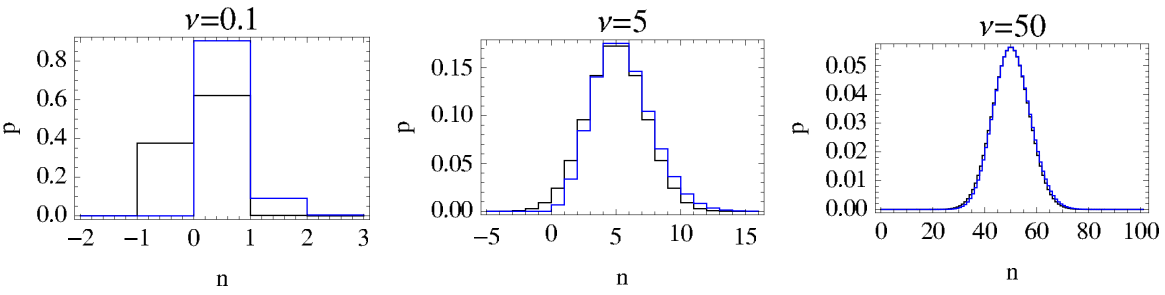

(a) (b) (c)

Figure 15: A comparison of Poisson (blue line) and Gaussian (black line) distributions for three expectation values (a) $\nu = 0.1$, (b) $\nu = 5$, and (c) $\nu = 50$. The Gaussian distribution is integrated for each bin.

In the limit that the expectation value goes to infinity ($\nu \to \infty$), the Poisson probability becomes a Gaussian distribution

$$\lim_{\nu\to\infty} f_P(n;\nu) = f_G\left(n;\nu,\sqrt{\nu}\ \right) = \frac{1}{\sqrt{2\pi\nu}} e^{-(n-\nu)^2/(2\nu)} \tag{4.2}$$

with mean equal to ν and standard deviation equal to $\sqrt{\nu}$. This is one example of the Central Limit Theorem. Even for moderate ν, this is a good approximation. We show the Poisson and Gaussian distributions for three expectation values in Fig. 15. When $\nu = 0.1$, we can see that the two distributions are very different. The Gaussian distribution has nonzero value when $n < 0$ while the Poisson distribution is always zero for negative n. The other bins are also significantly different. By the time $\nu = 5$, the two distributions are already very similar. At $\nu = 50$, they are practically the same.

4.1.2 Log-Likelihood

When multiple measurements are made that are probabilistically independent (such as the bins of a distribution), the total probability is simply the product of the probabilities for each measurement. This product is called the likelihood and is given by

$$L_P(n_i;\nu_i) = \prod_i \frac{\nu_i^{n_i} e^{-\nu_i}}{n_i!} \quad \text{and} \quad L_G(n_i;\mu_i,\sigma_i) = \prod_i \frac{1}{\sqrt{2\pi}\sigma_i} e^{-(n_i-\mu_i)^2/(2\sigma_i^2)} dn_i \tag{4.3}$$

for Poisson and Gaussian probabilities, respectively. Larger values of the likelihood mean the measurements are more likely. Smaller values mean the measurements are less likely.

To get the log-likelihood, we first normalize the likelihoods as in

$$\frac{L_P(n_i;\nu_i)}{L_P(n_i;n_i)} = \prod_i \left(\frac{\nu_i}{n_i}\right)^{n_i} e^{n_i-\nu_i} \quad \text{and} \quad \frac{L_G(n_i;\mu_i,\sigma_i)}{L_G(n_i;n_i,\sigma_i)} = \prod_i e^{-(n_i-\mu_i)^2/(2\sigma_i^2)} \ . \tag{4.4}$$

We next take the natural logarithm and multiply by -2 to give

$$LL_P(n_i;\nu_i) = 2\sum_i \left[n_i \ln\left(\frac{n_i}{\nu_i}\right) + \nu_i - n_i \right] \quad \text{and} \quad LL_G(n_i;\mu_i,\sigma_i) = \sum_i \frac{(n_i-\mu_i)^2}{\sigma_i^2} \ . \tag{4.5}$$

The Gaussian log-likelihood is better known as the χ^2 test statistic because the probability of getting a particular value of LL_G is given by the χ^2 probability which is given by

$$f_{\chi^2}(x;k) = \frac{x^{k/2-1}e^{-x/2}}{2^{k/2}\Gamma\left(\frac{k}{2}\right)} \tag{4.6}$$

where x corresponds with the value of LL_G that was measured and k is the number of degrees of freedom. For LL_G, k is equal to the number of probabilistically independent measurements (or the number of bins in the distribution minus the number of parameters fit by minimizing LL_G).

As was mentioned in Sec. 4.1.1, the number of events in a scattering experiment is distributed according to a Poisson distribution which is not equal to a Gaussian distribution for small statistics but which approaches a Gaussian distribution for large statistics. As a result, $LL_P(n_i;\nu_i)$ and $LL_G(n_i;\nu_i,\sqrt{\nu_i}\ )$, where we have replaced the Gaussian standard deviation with the square root of the mean, do not fit the χ^2 distribution for small statistics, but approach it for large statistics, as shown in Fig. 16 for three different integrated luminosities. For the χ^2 distribution, we have used $k = 50$ degrees of freedom which is equal to the number of bins we used in the calculation of the log-likelihoods. For the log-likelihoods, we generated a random distribution as in Fig. 14 and calculated the log-likelihoods based on that fluctuation. After binning this log-likelihood, we generated a new random distribution and binned it. We followed this procedure 40,000 times to generate the probability distribution for the log-likelihood functions under the assumption of the SM. The resulting normalized log-likelihood distributions are seen in Fig. 16 as the red curve for LL_G and as the blue curve for LL_P. These plots show that the log-likelihood distributions are clearly

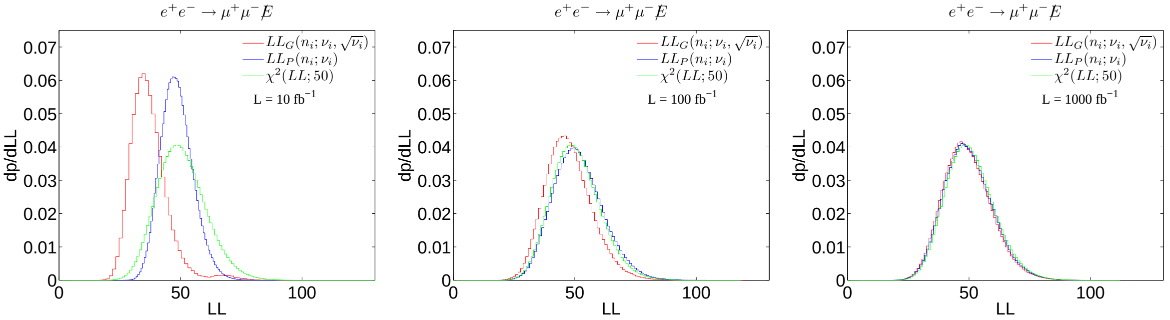

(a) (b) (c)

Figure 16: The log-likelihood and χ^2 distributions for (a) 10 fb^{-1}, (b) 100 fb^{-1}, and (c) 1000 fb^{-1}. For the LL_G distribution in red, the standard deviation was replaced with the square root of the mean. For the χ^2 curve in green, the number of degrees of freedom was taken as 50 which is the number of bins that were used in the calculation of the log-likelihoods. The LL_P distribution is in blue.

different than the χ^2 distributions for low luminosity but approach the χ^2 distribution for large luminosity. We also note that the Poisson based log-likelihood (LL_P) approaches the χ^2 distribution faster.

The χ^2 distribution also satisfies the central limit theorem. For large k, it also approaches a Gaussian distribution with expectation value k and standard deviation $\sigma = \sqrt{2k}$ as shown in Fig. 17.

4.1.3 Test Statistics

As we mentioned, the purpose of a test statistic is to determine how well the experimental data agree or disagree with a hypothesis. Each hypothesis makes a prediction for the expectation value(s) of the experiment. The actual experimental data are random with probability given by the appropriate probability function (Poisson for collider experiments). Each possible random outcome gives a particular value for the test statistic t. Each hypothesis H gives a different probability distribution for the values of the test statistic t. This determines the probability of measuring a particular value of the test statistic t under the assumption of

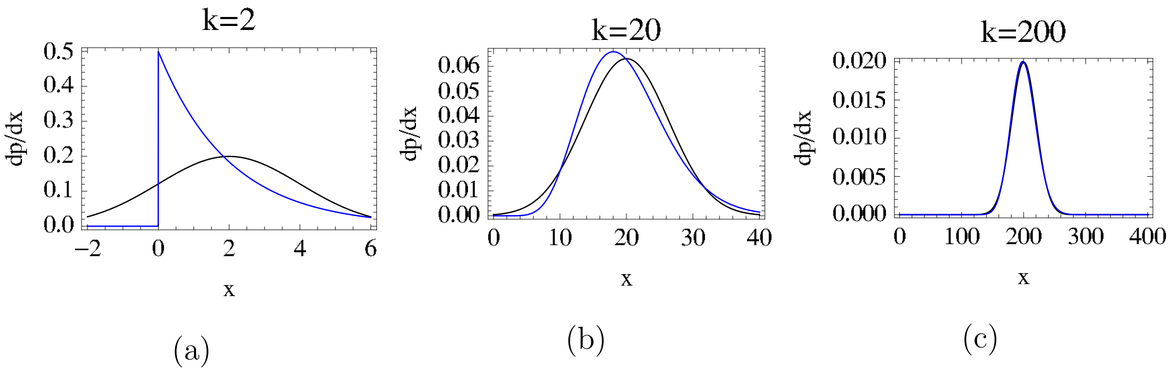

(a) (b) (c)

Figure 17: A comparison of the χ^2 and Gaussian distributions for the three values (a) $k = 2$, (b) $k = 20$, and (c) $k = 200$. The χ^2 distribution is in blue. The Gaussian distribution is in black.

that hypothesis $g(t|H)$.

For example, consider the log-likelihoods of the previous subsection (Eq. (4.5)) as the test statistics where the expectation value is given by the SM mean ν_{SMi} and we replace σ_i by $\sqrt{\nu_{SMi}}$ as in the previous subsection. In other words, we define our log-likelihood test statistics as

$$t_{PSM}(n_i) = 2\sum_i \left[n_i \ln\left(\frac{n_i}{\nu_{SMi}}\right) + \nu_{SMi} - n_i\right] \quad \text{and} \quad t_{GSM}(n_i) = \sum_i \frac{(n_i - \nu_{SMi})^2}{\nu_{SMi}} \ . \quad (4.7)$$

The n_i are randomly distributed according to the hypothesis H. For example, if the hypothesis is the SM, $g(t_{PSM}|SM)$ and $g(t_{GSM}|SM)$ are given by the blue and red curves of Fig. 16, respectively. As we mentioned in the previous sections, these distributions approach a χ^2 distribution for large integrated luminosity. We will call the hypothesis where the test statistic approaches a χ^2 distribution the null hypothesis H_0. For the test statistics $t_{PSM}(n_i)$ and $t_{GSM}(n_i)$, the null hypothesis is $H_0 = SM$.

Using the same test statistics, a different hypothesis will give a different distribution. For example, consider the MSSM parameter point `IA` for the same m_{rec} distribution. In Fig. 18, we have plotted the SM expectation values in green (identical to the blue curve in Fig. 14), the MSSM `IA` expectation values in blue and one particular random fluctuation of the MSSM `IA` in red for three different integrated luminosities. If we calculate the test statistic for the

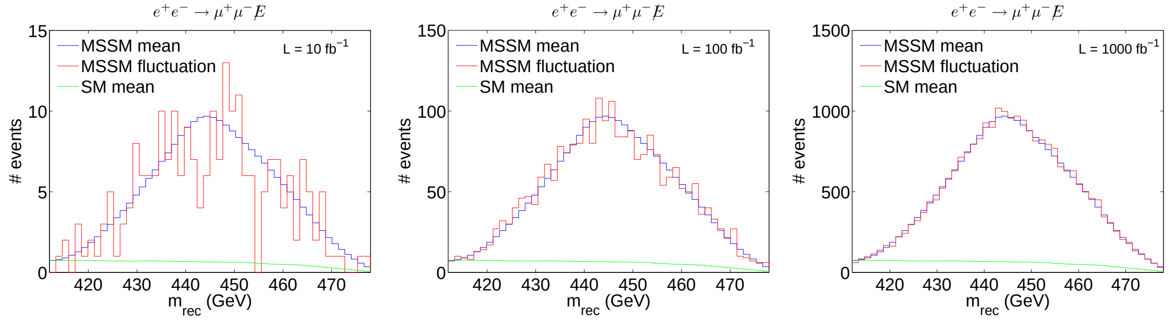

(a) (b) (c)

Figure 18: The SM mean in green, the MSSM IA mean in blue and one particular MSSM IA random fluctuation in red for the m_{rec} distribution for (a) 10 fb^{-1}, (b) 100 fb^{-1}, and (c) 1000 fb^{-1}.

alternate hypothesis MSSM `IA` fluctuations (we still use ν_{SMi} as defined in our test statistic), we can build the distributions $g(t_{PSM}|\text{MSSM IA})$ and $g(t_{GSM}|\text{MSSM IA})$ as in Fig. 19 for three different integrated luminosities. These give the probability of measuring t under the assumption of the MSSM `IA`. The red solid curve gives the probability density function for the Gaussian based statistic under the assumption of the MSSM `IA` while the blue solid curve gives the Poisson based statistic under the same assumption. The dashed red and blue curves give the same statistics under the assumption of $H_0 = SM$. The green curve gives the χ^2 distribution. Both the dashed curves and the green solid curve are the same as in Fig. 16.

We immediately note that, unlike the SM assumption, the test statistic under the assumption of an alternate hypothesis does not approach a χ^2 distribution with k equal to the number of degrees of freedom. Nor do the Poisson and Gaussian based test statistics approach each other. Rather, they grow linearly with the integrated luminosity. This can easily be seen from the definition. If we consider the mean of the alternate hypothesis (currently

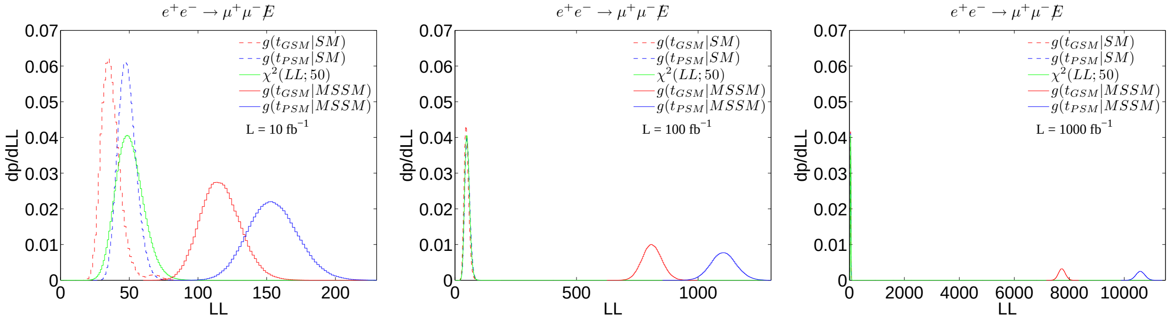

(a) (b) (c)

Figure 19: The test statistic distributions under the null hypothesis of the SM (dashed) and under the hypothesis of the MSSM (solid) for both the Poisson based test statistic (blue) and the Gaussian based tests statistic (red). The χ^2 curve is also shown for reference (green solid). Each of these is shown for (a) 10 fb^{-1}, (b) 100 fb^{-1}, and (c) 1000 fb^{-1}.

H_1=MSSM `IA`), we find

$$\begin{aligned} t_{PH_0}(n_{H_1 i}) &= 2\sum_i \left[\sigma_{H_1 i} L \ln\left(\frac{\sigma_{H_1 i} L}{\sigma_{H_0 i} L}\right) + \sigma_{H_0 i} L - \sigma_{H_1 i} L\right] \\ &= L\ 2\sum_i \left[\sigma_{H_1 i} \ln\left(\frac{\sigma_{H_1 i}}{\sigma_{H_0 i}}\right) + \sigma_{H_0 i} - \sigma_{H_1 i}\right] \end{aligned} \tag{4.8}$$

and

$$\begin{aligned} t_{GH_0}(n_{H_1 i}) &= \sum_i \frac{(\sigma_{H_1 i} L - \sigma_{H_0 i} L)^2}{\sigma_{H_0 i} L} \\ &= L \sum_i \frac{(\sigma_{H_1 i} - \sigma_{H_0 i})^2}{\sigma_{H_0 i}}\ , \end{aligned} \tag{4.9}$$

where L is the integrated luminosity.

As another example, we take the two hypotheses as the MSSM with two different mass points. The first corresponds with our parameter point `IA` and the second is the same except that the neutralino mass is six GeV lower at 135 GeV. We will call this second point `IA-6`. We show the expectation value of the m_{rec} distribution for these two mass points along with one particular fluctuation of `IA` in Fig. 20.

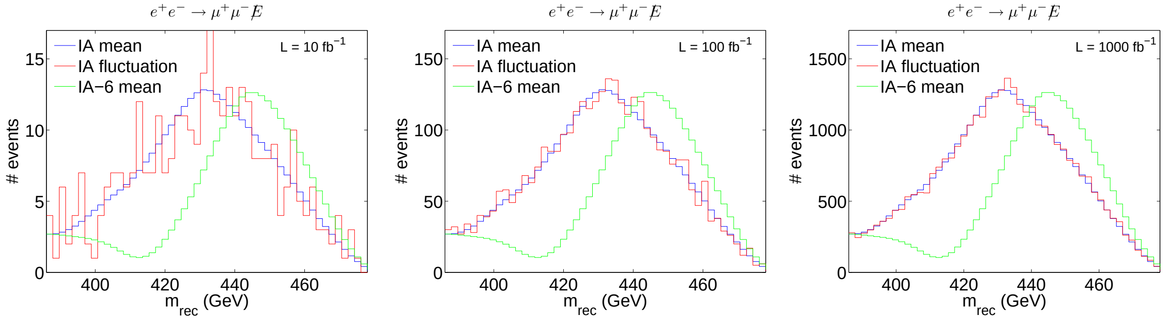

(a) (b) (c)

Figure 20: The MSSM `IA-6` mean in green, the MSSM `IA` mean in blue and one particular MSSM `IA` random fluctuation in red for the m_{rec} distribution for (a) 10 fb^{-1}, (b) 100 fb^{-1}, and (c) 1000 fb^{-1}.

We will now define our test statistics as

$$t_{PIA}(n_i) = 2\sum_i \left[n_i \ln\left(\frac{n_i}{\nu_{IAi}}\right) + \nu_{IAi} - n_i \right] \quad \text{and} \quad t_{GIA}(n_i) = \sum_i \frac{(n_i - \nu_{IAi})^2}{\nu_{IAi}} \ . \qquad (4.10)$$

When we compute the distributions of these test statistics under the assumption of the `IA` point, we get a probability distribution that approaches a χ^2 distribution for large integrated luminosity as seen as the dashed curves in Fig. 21. From this, we see that the null hypothesis for these test statistics is $H_0 =$ `IA`. When we calculate the test statistic distribution under the alternate hypothesis of the `IA-6` point, we get a distribution that moves towards larger values proportional to the integrated luminosity as shown in the solid red and blue curves.

4.1.4 Acceptance Region and Power of Discrimination

The ability of the test statistic to distinguish the two hypotheses (H_0 and H_1) depends on the amount of overlap between the distribution for the test statistic for the two hypotheses ($g(t|H_0)$ and $g(t|H_1)$). Greater overlap diminishes the ability to distinguish the hypotheses while less overlap increases the ability to distinguish. To make our point more clear, we have plotted the probability distributions for the test statistics $t_{GIA}(n_i)$ and $t_{PIA}(n_i)$ for the null

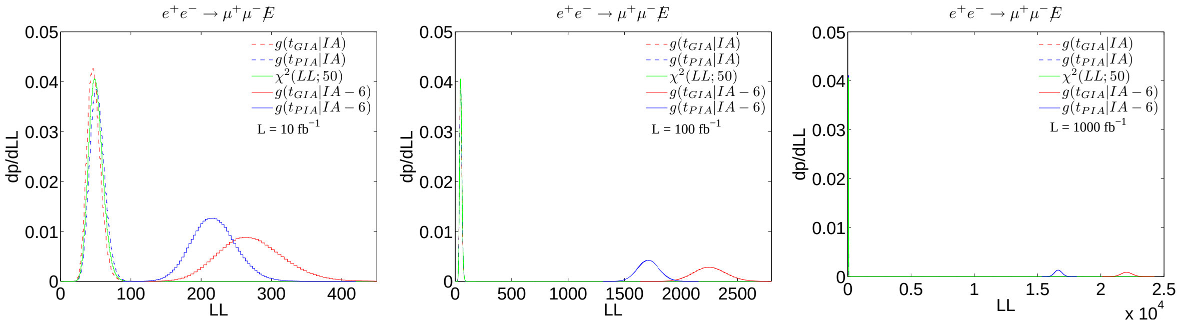

(a) (a) (a)

Figure 21: The test statistic distributions under the null hypothesis of the MSSM `IA` point (dashed) and under the alternate hypothesis of the MSSM `IA-6` point (solid) for both the Poisson based test statistic (blue) and the Gaussian based tests statistic (red). The χ^2 curve is also shown for reference (green solid). Each of these is shown for (a) 10 fb^{-1}, (b) 100 fb^{-1}, and (c) 1000 fb^{-1}.

hypothesis H_0 = `IA` and for the alternate hypothesis H_1 = `IA-6` for a very low integrated luminosity of 1 fb^{-1} where there is a large overlap between the curves in Fig. 22. The red dashed and blue dashed curves are given by $g(t_{GIA}|\text{IA})$ and $g(t_{PIA}|\text{IA})$, respectively, while $g(t_{GIA}|\text{IA-6})$ and $g(t_{PIA}|\text{IA-6})$ are given by the solid black lines.

Suppose the experiment measured the m_{rec} distribution and calculated these test statistics to be 50 and 51 for t_{GIA} and t_{PIA}, respectively. We would like to know how compatible these values are with each hypothesis. If we integrate the area under the $g(t_{GIA}|\text{IA})$ and $g(t_{PIA}|\text{IA})$ curves from 0 to the measured values, we get 0.928 and 0.813, respectively. This means there is a 7.2% and 18.7% chance of mass point `IA` fluctuating to give the measured test statistic or one that is less compatible with the mass point `IA` hypothesis. Apparently, the measured value is in good agreement with hypothesis `IA`. On the other hand, if we integrate the distributions for the alternate hypothesis $g(t_{GIA}|\text{IA-6})$ and $g(t_{PIA}|\text{IA-6})$ from 0 to the measured values, we get 0.213 and 0.112. So, there is a 21.3% and 11.2% chance of the mass point `IA-6` fluctuating down to look like the measured value of the test statistics or a value more like mass point `IA`, which is not insignificant.

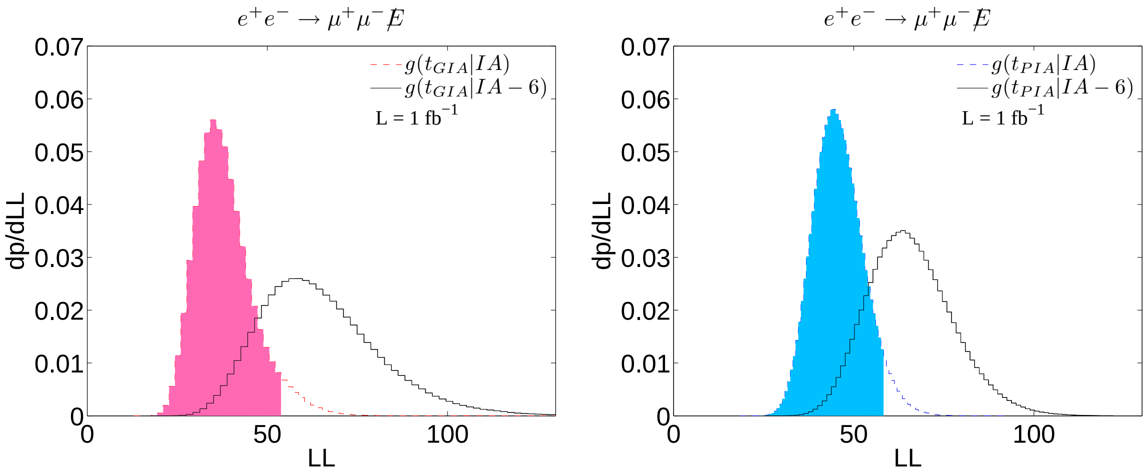

(a) (b)

Figure 22: The test statistic distributions for a low luminosity where there is a large overlap between the distributions for the null and alternate hypothesis. The dashed curve is for the null hypothesis `IA` while the solid curve is for the alternate hypothesis `IA-6`. The Gaussian based test statistic is in (a) while the Poisson based test statistic in in (b). 95% of the null hypothesis distributions are filled in from the left.

We would like to set a criteria ahead of time for acceptance or rejection of the null hypothesis. We will define an acceptance region for the test statistic such that if the test statistic falls below t_c, we will accept the null hypothesis H_0 and if the test statistic falls above t_c, we will reject H_0. We will decide the value of t_c by agreeing on a probability for measuring t_c or higher under the assumption of H_0. We will call this probability the significance level or α. A typical value for α is 5% for a 95% confidence level test. However, α must be even lower to claim "evidence" or "discovery" of new physics. For Fig. 22, the 5% critical region occurs for $t_{GIA} \geq 54$ and $t_{PIA} \geq 58$. We have filled in the acceptance regions of these curves for reference. If we measure a value of the test statistic in the critical region when the hypothesis H_0 is correct, this is an error of the first kind. Therefore, using a 95% confidence level test to determine agreement with H_0 gives a 5% chance of making an error of the first kind if the null hypothesis is correct.

On the other hand, the alternative hypothesis has a probability to fluctuate down to the acceptance region. We call this probability β and it is equal to the area under the distribution for the alternate hypothesis (H_1) from 0 to t_c. For Fig. 22, β is 0.306 and 0.281 for t_{GIA} and t_{PIA}, respectively. If the test statistic falls in the acceptance region but the alternate hypothesis is correct, this is an error of the second kind. Apparently, for these test statistics and for 1 fb^{-1}, there is a 30.6% and 28.1% probability of making an error of the second kind if the alternate hypothesis is correct. As we saw in the previous subsection, increasing the integrated luminosity pushes the alternate hypothesis distribution towards higher values of the test statistic while the null hypothesis distribution converges on a χ^2 distribution with k equal to the number of degrees of freedom. That is to say, increasing the integrated luminosity decreases β. $1 - \beta$ is called the power of the test statistic to discriminate against the alternate hypothesis and increases with greater integrated luminosities. Obviously, higher powers are better and reduces the probability of errors of the second kind under the assumption of the alternate hypothesis.

4.1.5 LL Mean Approximation

In high energy phenomenology, we are often interested in determining the integrated luminosity required to reduce β, the probability of an error of the second kind under the assumption of an alternate hypothesis, to some small value for a given α, the probability of an error of the first kind under the assumption of the null hypothesis. Or, alternatively, we are interested in determining which alternate hypotheses can have a β below a certain value at a fixed integrated luminosities. One way to do this would be to generate the test statistic distributions $g(t|H)$ as we did in the previous section for each distribution, each hypothesis, and each integrated luminosity. However, it is usually possible to estimate the integrated luminosity required by calculating the test statistic for the mean of the alternate hypothesis as in Eqs. (4.8) and (4.9). Although β is relatively high using this method (the test statistic for the mean is near the peak), it has the property that it grows linearly with integrated luminosity. It also has the property that it can be immediately calculated from the means of the null and alternate hypothesis with no need to generate the test statistic distributions.

Since our test statistic distributions under the assumption of the null hypothesis approach a χ^2 distribution for large expectation values, we can estimate the probability of obtaining a value of the test statistic that is greater than or equal to a particular value by integrating the χ^2 distribution

$$P(t > t_0) = \int_{t_0}^{\infty} dt\ \chi^2(t;k)\ =\ 1 - \int_0^{t_0} dt\ \chi^2(t;k)\ , \tag{4.11}$$

where k is the number of degrees of freedom and t_0 is the value of the test statistic for the mean of the alternate hypothesis. This is useful when the integrated luminosity is fixed where we can calculate the test statistic for the mean as in Eqs. (4.8) and (4.9) and determine the probability associated with it. We often like to quote how many "standard deviations" or "sigmas" away from the null hypothesis, the result is. This is based on the intuition physicists have from Gaussian distributions. Although the distribution may not be Gaussian, we can find the number of Gaussian standard deviations that would correspond with the same probability for fluctuating to the mean of the alternate hypothesis or to something more incompatible with the null hypothesis. We do this by equating probabilities as in

$$P(t > t_0) = \int_{t_0}^{\infty} dt \chi^2(t, k) = 2 \int_{S(t_0)}^{\infty} dx \frac{1}{\sqrt{2\pi}} e^{-x^2/2} \tag{4.12}$$

and solve for S (often numerically). If $k = 1$, this equation gives $t_0 = S^2$

$$\int_{t_0}^{\infty} dt \chi^2(t, 1) = 2 \int_{\sqrt{t_0}}^{\infty} dx \frac{1}{\sqrt{2\pi}} e^{-x^2/2} \tag{4.13}$$

In other words, for $k = 1$, the Gaussian "significance" is equal to $\sqrt{t_0}$.

On the other hand, we may wish to estimate the integrated luminosity necessary to achieve a fixed probability of an error of the first kind α under the null hypothesis. In this case, we wish to find the critical value of the test statistic

$$\alpha = \int_{t_c}^{\infty} dt \ \chi^2(t; k) \ = \ 1 - \int_{0}^{t_c} dt \ \chi^2(t; k) \ . \tag{4.14}$$

Once we find t_c (often numerically or by look-up in a table), we can solve for the required integrated luminosity by use of Eqs. (4.8) and (4.9) giving

$$L = \frac{t_c}{2 \sum_i \left[\sigma_{H_1} \ln \left(\frac{\sigma_{H_1}}{\sigma_{H_0}} \right) + \sigma_{H_0} - \sigma_{H_1} \right]} \tag{4.15}$$

or

$$L = \frac{t_c}{\sum_i \frac{\left(\sigma_{H_1} - \sigma_{H_0} \right)^2}{\sigma_{H_0}}} \tag{4.16}$$

depending on whether the Poisson or Gaussian based test statistic, respectively, is being used.

For example, consider the comparison of the MSSM points `IA` and `IA-6` at 100 fb^{-1} using the m_{rec} distribution as in Figs. (20) and (21). As we can see in Fig. 21(b), the test statistic distributions under the null hypothesis are very close to a χ^2 distribution, so this approximation is well justified for this analysis. Since there are 50 degrees of freedom for this test statistic, we find that for an $\alpha = 0.05$, we get a $t_c = 67.5$ (see Eq. (4.14)). Because this χ^2 distribution is close to a Gaussian distribution (see Fig. 17), we could have estimated this as the mean plus two standard deviations or $50 + 2\sqrt{2 \cdot 50} = 70$. If we calculate the test statistics $t_{PIA}(n_{IA-6})$ and $t_{GIA}(n_{IA-6})$, we get 1707 and 2248, respectively. These are much greater than the critical value t_c which means there is much smaller than a 5% chance of the point `IA` fluctuating to give the test statistic this high or higher. In Sec. 4.2, we scanned over the masses calculating this probability for each mass point and drew a contour for the mass points where this probability was 5%. We did this individually for each distribution.

4.1.6 Joint Test Statistic

We typically have more than one distribution to compare between the null and alternate hypothesis. By comparing all of them at the same time, we can increase the power to discriminate between the hypotheses. However, when the same data is used to construct the distributions, they are typically correlated. As a result, we need to determine the properties of this correlation and the effect on the resulting discrimination power. We do this by creating a new test statistic that combines the properties of the individual test statistics. One nice choice is the sum of the test statistics as in

$$t = t_0 + t_1 + \cdots \ . \tag{4.17}$$

However, even for the null hypothesis, in the presence of correlation, the distribution for this new test statistic will *not* asymptotically approach a χ^2 distribution with $k = k_0 + k_1 + \cdots$.

As an example, we begin by considering a maximally correlated pair of kinematical variables. The first is the energy sum of the observable particles discussed in Sec. 2.1, namely $E_{\mu^+} + E_{\mu^-}$. We have plotted the expectation value for this distribution for 100 fb^{-1} for the mass point `IA` and `IA-6` along with one random fluctuation of `IA` in Fig. 23(a). In Fig. 23(b), we have plotted the test statistic distribution based on this observable for both the null hypothesis ($H_0 =$ `IA`) and the alternate hypothesis ($H_1 =$ `IA-6`). The second kinematical observable is the energy sum of the missing particles, $E_{\tilde{\chi}_1^0} + E_{\tilde{\chi}_1^0}$. We have plotted the expectation values for this kinematical observable in Fig. 23(c) along with the test statistic based on this observable in Fig. 23(d). These two observables are related to each other by

$$E_{\mathrm{rec}} \equiv E_{\tilde{\chi}_1^0} + E_{\tilde{\chi}_1^0} = \sqrt{s}/2 - (E_{\mu^+} + E_{\mu^-}) \ . \tag{4.18}$$

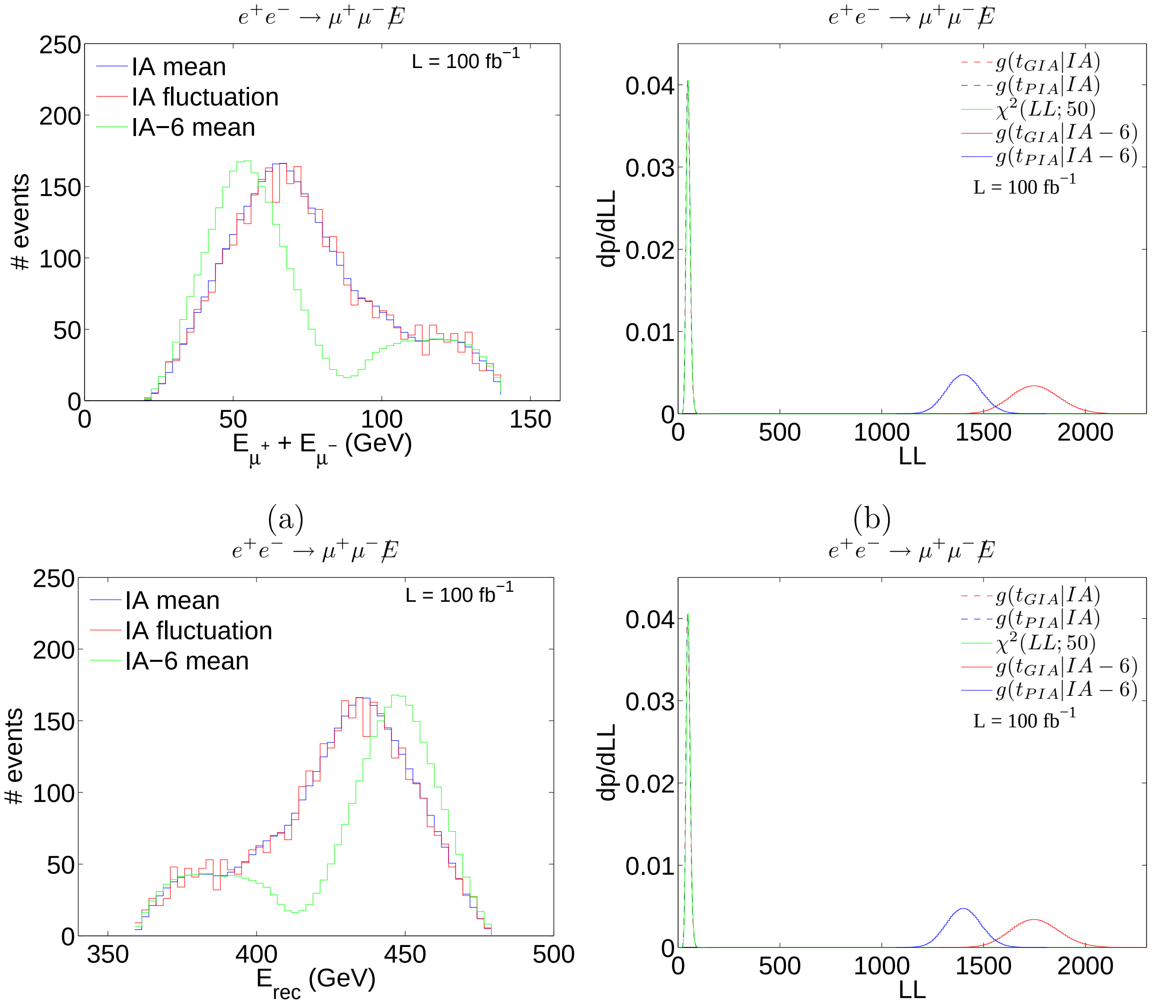

(a) (b)

(c) (d)

Figure 23: The $E_{\mu^+} + E_{\mu^-}$ distribution in (a), the $E_{\rm rec}$ distribution in (b) and the resulting test statistic distribution, respectively, for these kinematical distributions in (b) and (d). All are for 100 fb^{-1}. The color coding is the same as in Figs. 20 and 21.

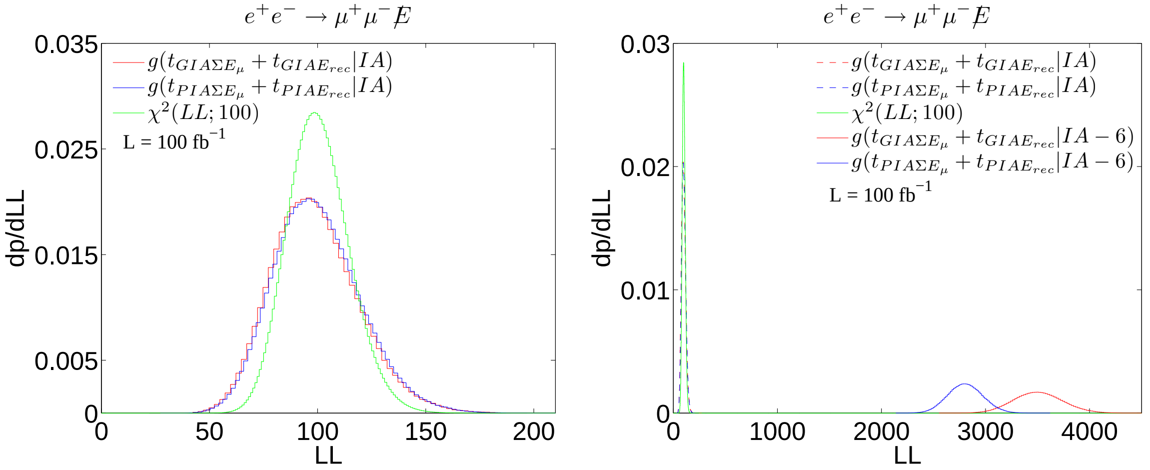

(a) (b)

Figure 24: The joint test statistic distributions based on the Gaussian log-likelihood (red) and Poisson log-likelihood (blue) for the null hypothesis in (a) and for the alternate hypothesis in (b).

Consequently, their expectation values (the blue and green curves of Fig. 23(a) and (c)) and even any particular random fluctuation (the red curves of Fig. 23(a) and (c)) are mirror images of each other. If we use the same number of bins in our log-likelihood test statistics spread over the same areas of the curves for each observable, then their test statistic distributions will also be the same. This is what we have done for Fig. 23(b) and (d). For our joint test statistic, we will add the two test statistics together as in

$$\begin{aligned} t_{PSM}(n_i) &= 2\sum_i \left[n_{E_{2\mu}i} \ln\left(\frac{n_{E_{2\mu}i}}{\nu_{IAE_{2\mu}i}}\right) + \nu_{IAE_{2\mu}i} - n_{E_{2\mu}i} \right] \\ &\quad +2\sum_i \left[n_{E_{\mathrm{rec}}i} \ln\left(\frac{n_{E_{\mathrm{rec}}i}}{\nu_{IAE_{\mathrm{rec}}i}}\right) + \nu_{IAE_{\mathrm{rec}}i} - n_{E_{\mathrm{rec}}i} \right] \end{aligned} \tag{4.19}$$

$$t_{GSM}(n_i) = \sum_i \frac{\left(n_{E_{2\mu}i} - \nu_{IAE_{2\mu}i}\right)^2}{\nu_{IAE_{2\mu}i}} + \sum_i \frac{\left(n_{E_{\mathrm{rec}}i} - \nu_{IAE_{\mathrm{rec}}i}\right)^2}{\nu_{IAE_{\mathrm{rec}}i}} . \tag{4.20}$$

We have plotted these joint test statistics in Fig. 24(a) in solid red and blue. For reference, we have also plotted the χ^2 distribution in dashed green where the number of degrees of freedom was taken to be the sum of the number of degrees of freedom of each individual test statistic. If the two distributions were completely independent of each other, this χ^2 curve would be a very good approximation of the joint test statistic. However, as we can see from the plots, they are significantly different. The peaks of these curves are close to each other, but the variances are very different. The χ^2 curve has standard deviation $\sigma = \sqrt{2k} = \sqrt{2(50+50)} = 14$. To estimate the standard deviation of the joint test statistic, we fit it with a Gaussian to obtain $\sigma = 19.9$ for the Gaussian based test statistic and $\sigma = 19.8$ for the Poisson based test statistic which we see is very close to twice the standard deviation of the individual test statistic distributions $2\sqrt{2 \cdot 50} = 20$.

On the other hand, in Fig. 24(b), we have plotted the same test statistic distributions for the alternate hypothesis $H_1 =$ `IA-6`. If we compare this to the test statistic distributions for the alternate hypothesis in Fig. 23, we see that the distributions have simply moved up to twice the value. In other words, as defined, the test statistic for the alternate hypothesis is simply the sum as we expect. Now, suppose that for some integrated luminosity, the expected test statistic (or the test statistic measured at an experiment) is exactly twice the standard deviation of the individual test statistics $t_1 - \mu_1 = t_2 - \mu_2 = 20$. The joint test statistic is given by the sum $t - \mu = t_1 - \mu_1 + t_2 - \mu_2 = 40$. Since the new standard deviation is $\sigma = 20$, we find that the new test statistic is still exactly two standard deviations from the mean. That is to say, the significance has not changed by combining these two measurements, as a consequence of these kinematical variables being fully correlated. If, on the other hand, these two kinematical observables were completely independent, we would have had $\sigma = 14$ as described above and the joint test statistic would have been $20/14 = 1.4$ or $2\sqrt{2}$ standard deviations above the mean.

We now consider another, less correlated, example. We take the m_{rec} distribution discussed in the beginning of this appendix and combine it with the E_μ measurement. We have already plotted the means for the m_{rec} distribution in Fig. 20 and its resulting test statistic distribution in Fig. 21. We combine this with a measurement of the E_μ distribution whose mean and one particular random fluctuation in Fig. 25(a) and the test statistic distributions based on E_μ in Fig. 25(b). Although these kinematical variables are related to each other by

$$m_{\text{rec}}^2 \equiv m_{\tilde{\chi}_1^0 \tilde{\chi}_1^0}^2 = s - 2\sqrt{s}\,(E_{\mu^+} + E_{\mu^-}) + m_{\mu\mu}^2 \tag{4.21}$$

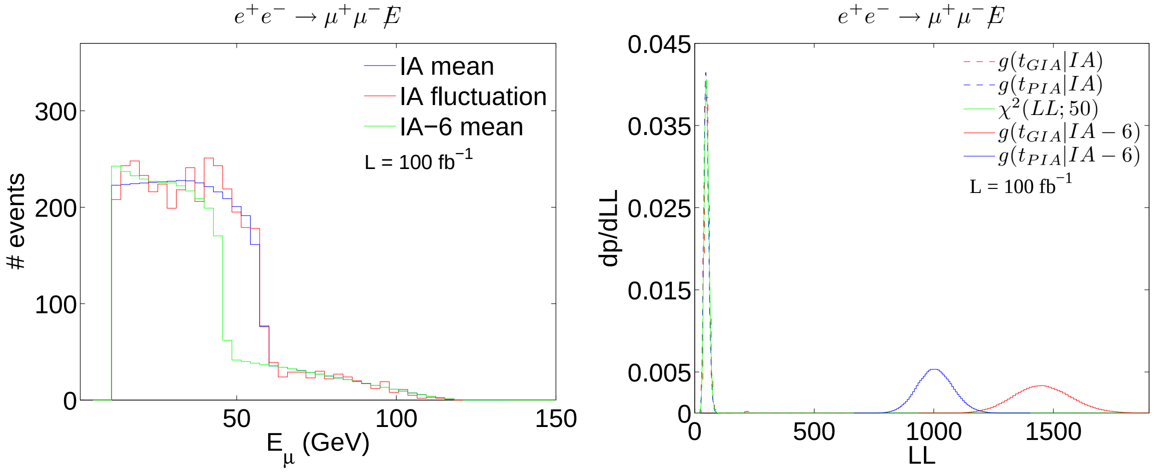

(a) (b)

Figure 25: The MSSM `IA-6` mean in green, the MSSM `IA` mean in blue and one particular MSSM `IA` random fluctuation in red for the E_μ distribution in (a). The joint test statistic distributions of E_μ based on the Gaussian log-likelihood (red) and Poisson log-likelihood (blue) for the alternate hypothesis in (b).

where E_μ is one of E_{μ^+} or E_{μ^-}, the energy of the other muon and $m_{\mu\mu}$ are still free. As a result, we will see that the sum of the test statistics for these distributions add to give a more constraining test statistic.

We define the test statistics as

$$\begin{aligned} t_{PSM}(n_i) &= 2\sum_i \left[n_{m_{\rm rec}i} \ln\left(\frac{n_{m_{\rm rec}i}}{\nu_{IAm_{\rm rec}i}}\right) + \nu_{IAm_{\rm rec}i} - n_{m_{\rm rec}i} \right] \qquad (4.22) \\ & \quad +2\sum_i \left[n_{E_\mu i} \ln\left(\frac{n_{E_\mu i}}{\nu_{IAE_\mu i}}\right) + \nu_{IAE_\mu i} - n_{E_\mu i} \right] \\ t_{GSM}(n_i) &= \sum_i \frac{\left(n_{m_{\rm rec}i} - \nu_{IAm_{\rm rec}i}\right)^2}{\nu_{IAm_{\rm rec}i}} + \sum_i \frac{\left(n_{E_\mu i} - \nu_{IAE_\mu i}\right)^2}{\nu_{IAE_\mu i}} \,. \qquad (4.23) \end{aligned}$$

We have plotted these combined test statistics in Fig. 26. This time, we see a very different result. The combined test statistic is almost indistinguishable from the χ^2 distribution where we have taken the number of degrees of freedom as the sum $k = 50 + 50 = 100$. As a result, the power of this joint statistic to discriminate against the alternate hypothesis is greatly

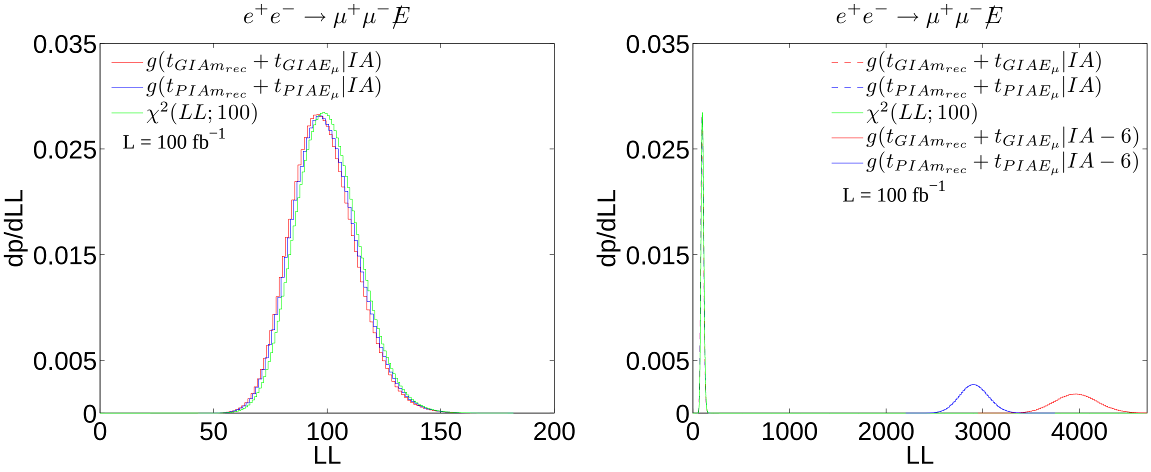

(a) (b)

Figure 26: The joint test statistic distributions based on the Gaussian log-likelihood (red) and Poisson log-likelihood (blue) for the null hypothesis in (a) and for the alternate hypothesis in (b).

increased from the individual test statistics. The standard deviation is $\sigma = \sqrt{2 \cdot 100} = 14$, which is much smaller than the fully correlated $\sqrt{2 \cdot 50} + \sqrt{2 \cdot 50} = 20$.

4.1.7 Covariance Matrix

In the last section, we described how to generate the distribution for the joint test statistics and how correlation affected their properties with emphasis on their standard deviations. In principle, we could calculate these distributions for each kinematical variable, each integrated luminosity and each hypothesis under question. We will now discuss the use of the covariance matrix to approximate the resulting standard deviation from the individual standard deviations.

Our joint test statistic is a sum of the individual test statistics

$$t = \sum_i t_i \tag{4.24}$$

The expectation value of this is given by

$$\begin{aligned}
\mu = E(t) &= \int_0^\infty \prod_k dt_k \sum_i t_i \; f(t_0, t_1, t_2, \cdots) \\
&= \sum_i \int_0^\infty dt_i \; t_i \; f(t_i) \\
&= \sum_i E(t_i) = \sum_i \mu_i
\end{aligned} \tag{4.25}$$

which is to say, the expectation of the test statistic sum is simply the sum of the expectation values in our case. If the combination were more complicated than a linear sum, there would be higher order corrections. The variance is given by

$$\begin{aligned}
V(t) = E\left[(t-\mu)^2\right] &= \int_0^\infty \prod_k dt_k \left(\sum_i (t_i - \mu_i) \right)^2 \; f(t_0, t_1, t_2, \cdots) \\
&= \sum_{i,j} \int_0^\infty dt_i dt_j (t_i - \mu_i)(t_j - \mu_j) \; f(t_i, t_j) \\
&= \sum_{i,j} V_{i,j} \; .
\end{aligned} \tag{4.26}$$

Again, if our function were not a linear sum over the t_i, there would be higher order corrections to this formula. $V_{i,j}$ is called the covariance matrix. The diagonal terms are simply the variances of the individual distributions

$$V_{i,i} = V(t_i) = E\left[(t_i - \mu_i)^2\right] \tag{4.27}$$

which we already know. The off-diagonal terms are new and must be computed.

In order to calculate the covariance matrix, we must calculate the joint probability distribution function for all pairs of our test statistics. We do this by generating random distributions for each of our observables and calculating each of our test statistics on it and binning on a two-dimensional histogram for the test statistics. For example, for the m_{rec} and E_μ test statistics, we present this joint distribution in Fig. 27(a). This distribution is nearly rotationally symmetric, which is the sign of nearly independent variables. From this, we calculated the covariance matrix. For the off-diagonal term, we got $V_{m_{\text{rec}},E_\mu} = 2.3$. Since

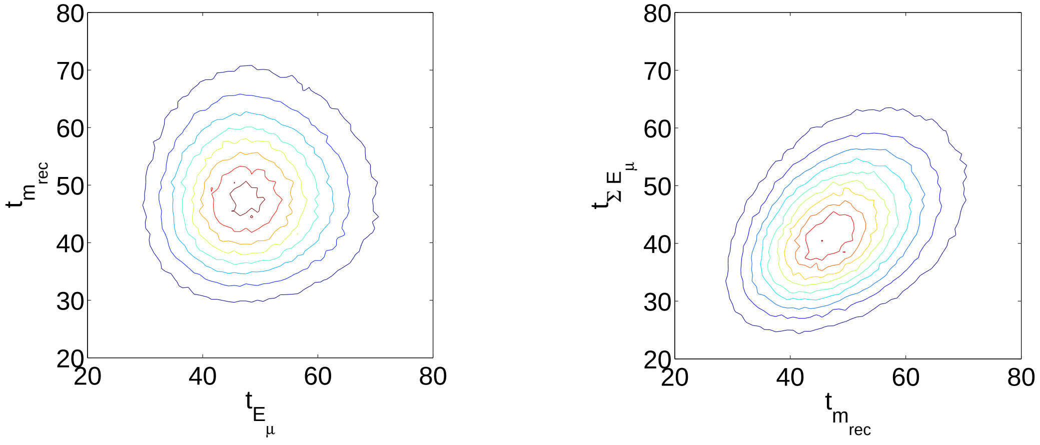

(a)

(b)

Figure 27: The joint distributions for the test statistics of (a) m_{rec} vs E_μ and (b) $E_{\mu^+} + E_{\mu^-}$ vs m_{rec}.

this is very small compared to the individual variances ($2 \cdot 50 = 100$), the correlation is very weak and the resulting standard deviation is given by

$$\sigma = \sqrt{\sigma^2_{m_{\text{rec}}} + \sigma^2_{E_\mu} + 2V_{m_{\text{rec}},E_\mu}} = \sqrt{(2 \cdot 50) + (2 \cdot 50) + 2 \cdot 2.3} = 14.3 \tag{4.28}$$

as we found in the previous subsection. The standard deviation is very close to that of two independent variables.

In Fig. 27(b), we plot the joint test statistic distribution between m_{rec} and $\sum E_\mu$. Because these two variables are more strongly correlated, we see that the distribution is more oblong along the diagonal direction. We find that in general for these test statistics, the more correlated the two variables are, the more oblong their joint test statistic distributions are along the diagonal. We calculated the off-diagonal term of the covariance matrix between these two test statistics and found it to be $V_{m_{\text{rec}},\sum E_\mu} = 37$. As a result, the standard deviation of the combination of these two variables is

$$\sigma = \sqrt{\sigma^2_{m_{\text{rec}}} + \sigma^2_{\sum E_\mu} + 2V_{m_{\text{rec}},\sum E_\mu}} = \sqrt{(2 \cdot 50) + (2 \cdot 50) + 2 \cdot 37} = 16.6 \tag{4.29}$$

which is larger than in the case of m_{rec} and E_μ.

Finally, we also calculated the joint distribution for the two energy sum distributions. Because these two distributions are fully correlated, their test statistics are equal for all randomly generated distributions. As a result, their joint test statistic distribution consisted of zero everywhere except the diagonal. We then use this to calculate the covariance matrix and get the off-diagonal piece as $V_{\sum E_\mu, E_{\text{rec}}} = 99$, which is the same order as the diagonal terms. As a result, the standard deviation of the sum of these test statistics is

$$\sigma = \sqrt{\sigma^2_{\sum E} + \sigma^2_{E_{\text{rec}}} + 2V_{\sum E_\mu, E_{\text{rec}}}} = \sqrt{(2 \cdot 50) + (2 \cdot 50) + 2 \cdot 99} = 20 \tag{4.30}$$

as we found in the last subsection.

Our final test statistic is the sum of the test statistics for our four kinematical variables

$$t = t_{E_\mu} + t_{m_{\text{rec}}} + t_{m_{\mu\mu}} + t_{\cos\theta}. \tag{4.31}$$

We calculated the full covariance matrix for this set of variables. It is

$$V = \begin{pmatrix} 99.9 & 2.28 & 1.74 & 1.27 \\ 2.28 & 98.7 & 7.9 & 0.88 \\ 1.74 & 7.9 & 99.4 & 0.78 \\ 1.27 & 0.88 & 0.78 & 99.1 \end{pmatrix}. \tag{4.32}$$

We note that the diagonal terms correspond with the expected individual variances ($\sqrt{2 \cdot 50} = 100$). The off-diagonal terms are all small compared to the diagonal terms, showing that these variables are not significantly correlated. The largest correlation is between m_{rec} and $m_{\mu\mu}$. Its off-diagonal term is 10% of the diagonal terms. We further calculated this covariance matrix at 3 other mass points without any significant difference. As a result, we find that this covariance matrix is a good approximation for our range of parameters. Finally, we use this covariance matrix to estimate our final standard deviation in order to determine the significance of our results. We get

$$\sigma = 20.65 \tag{4.33}$$

where a totally independent set of variables would have given $\sqrt{4 \cdot 2 \cdot 50} = 20$. A totally correlated set of variables would have given us $4 \cdot \sqrt{2 \cdot 50} = 40$. As a result, we can double our significance by combining the test statistics of these four variables in this way.

4.1.8 Multivariate Limit for Log-Likelihood

In practice, the amount of improvement is limited when combining log-likelihood test statistics in this way. In Fig. 28, we show the effect of combining the log-likelihood test statistics for the E_μ and m_{rec} variables as a function of the mass difference with a fixed luminosity (a) and as a function of the luminosity for a fixed mass difference (b). We see that although the 95% CL points are very near each other for the two variables, their combined 95% CL point is not any better than the E_μ 95% CL point.

In Fig. 28(c) and (d), we show an ideal case where the log-likelihood is a quadratic function of the mass difference (c) and a linear function of the luminosity (d). We took the coefficients in each case to give the same order of magnitude as in (a) and (b), but did not try to match them exactly. We will see that these coefficients do not affect the relative improvement of the measurement. We will assume for this subsection that both the individual test statistics and the combined test statistics are well approximated by Gaussian distributions. For cases where this approximation is not valid, there will be corrections. We will note where this is likely important.

Let us assume that we have a number of variables that are fully independent and all have the same functional form for the test statistic as a function of the mass difference and the luminosity. This is the scenario where combining the test statistics will have the maximal effect. Any other case will have less benefit from combining. We will take the form of these individual test statistics to be

$$t_{\Delta M} = \alpha_{\Delta M} \left(\Delta M\right)^2 \quad \text{and} \quad t_L = \alpha_L L \tag{4.34}$$

where α determines the slope of these curves. These individual test statistics are given by the solid blue lines in Fig. 28(c) and (d). If we combine N of these test statistics in a sum, the combined test statistic will be given by

$$\bar{t}_{\Delta M} = N t_{\Delta M} = N \alpha_{\Delta M} \left(\Delta M\right)^2 \quad \text{and} \quad \bar{t}_L = N t_L = N \alpha_L L \; . \tag{4.35}$$

These test statistics are given by the solid black lines in Fig. 28(c) and (d) for $N = 2, 3,$ and 4. The expectation value for these combined test statistics is given by the sum of the

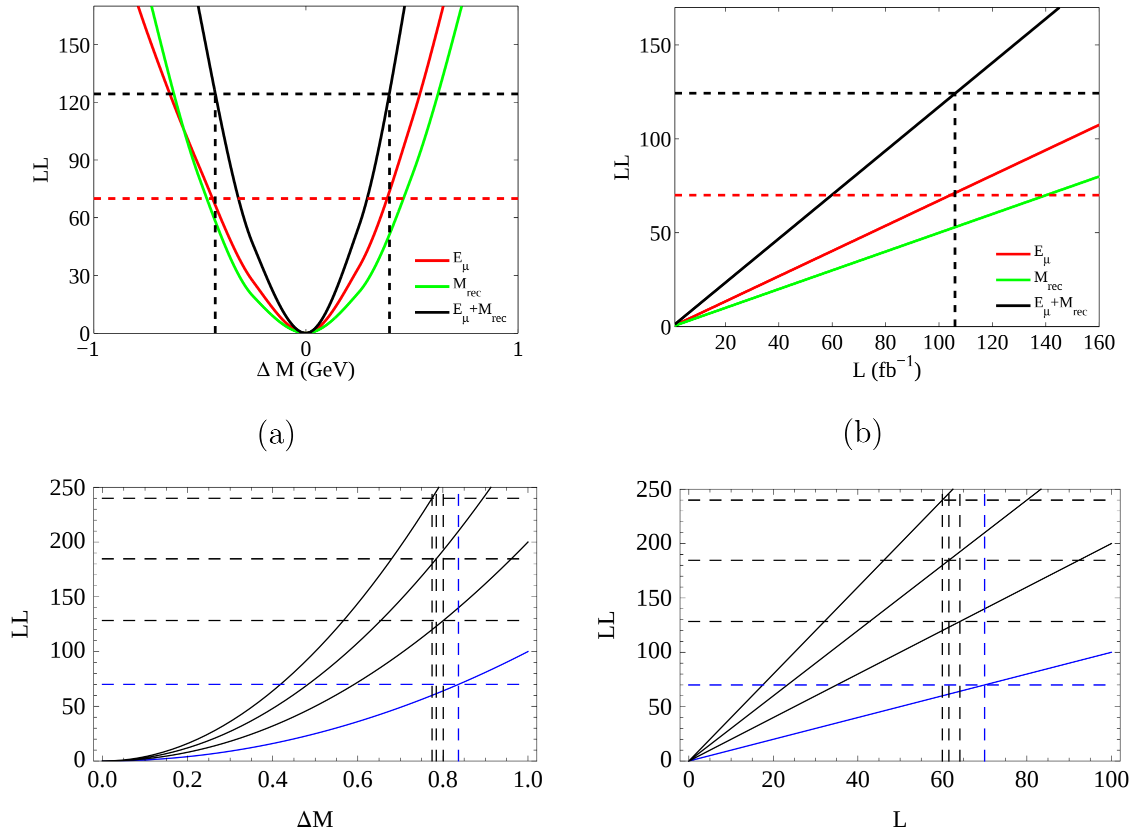

(a)
(b)
(c)
(d)

Figure 28: Ideal combination of two, three, and four test statistics. The individual test statistics are given by the solid blue lines while the combined test statistics are given by the solid black lines. The horizontal dashed lines give the 95% CL for the individual test statistics (blue) and the combined test statistics (black). The horizontal lines show the value of the mass difference (a,c) and the luminosity (b,d) at 95% CL.

expectation values. Since we are taking these test statistics to be well fit by Gaussians related to χ^2 distributions, this is $\overline{\mu} = Nn$, where n is the number of degrees of freedom (or the number of bins in this study). For small n, the Gaussian approximation breaks down, where for large n, it is a good approximation. Since we are assuming these variables to all be independent, the standard deviation is the sum in quadrature of the others, or $\overline{\sigma} = \sqrt{N \cdot 2n}$. As a result, the 95% CL value for the combined test statistic is at

$$\overline{\mu} + 2\overline{\sigma} = nN + 2\sqrt{2nN}. \tag{4.36}$$

This is plotted as the horizontal dashed blue line for the individual test statistics ($N = 1$) and in horizontal dashed black line for the combined statistics for $N = 2, 3$, and 4 in Fig. 28(c) and (d). The point at which these two cross gives the 95% CL point for the mass difference in Fig. 28(c) and for the luminosity in Fig. 28(d) as vertical dashed lines. These vertical lines are blue for the individual test statistics ($N = 1$) and in black for $N = 2, 3$, and 4. The values for these cross over points is given by

$$\bar{t}_{\Delta M} = N\alpha_{\Delta M}\left(\Delta M\right)^2 = nN + 2\sqrt{2nN} \quad \text{and} \quad \bar{t}_L = N\alpha_L L = nN + 2\sqrt{2nN}\ . \tag{4.37}$$

Solving these for the value of the mass difference and luminosity where this occurs gives

$$\Delta M_N = \sqrt{\frac{n}{\alpha_{\Delta M}} + \frac{2}{\alpha_{\Delta M}}\sqrt{\frac{2n}{N}}} \quad \text{and} \quad L_N = \frac{n}{\alpha_L} + \frac{2}{\alpha_L}\sqrt{\frac{2n}{N}}. \tag{4.38}$$

As we can see this is a function the coefficient α as well as the number of bins and the number of variables combined. In the limit of a very large number of variables combined, this approaches a limit as we saw in Fig. 28(c) and (d). This limit is

$$\lim_{N\to\infty} \Delta M_N = \sqrt{\frac{n}{\alpha_{\Delta M}}} \quad \text{and} \quad \lim_{N\to\infty} L_N = \frac{n}{\alpha_L}. \tag{4.39}$$

The relative improvement over using one individual variable is given by the ratio

$$\frac{\Delta M_N}{\Delta M_1} = \sqrt{\frac{n + 2\sqrt{2n/N}}{n + 2\sqrt{2n}}} \quad \text{and} \quad \frac{L_N}{L_1} = \frac{n + 2\sqrt{2n/N}}{n + 2\sqrt{2n}}. \tag{4.40}$$

We see that the relative improvement does not depend on the coefficients $\alpha_{\Delta M}$ and α_L. It does however depend on the number of degrees of freedom in each individual test statistic

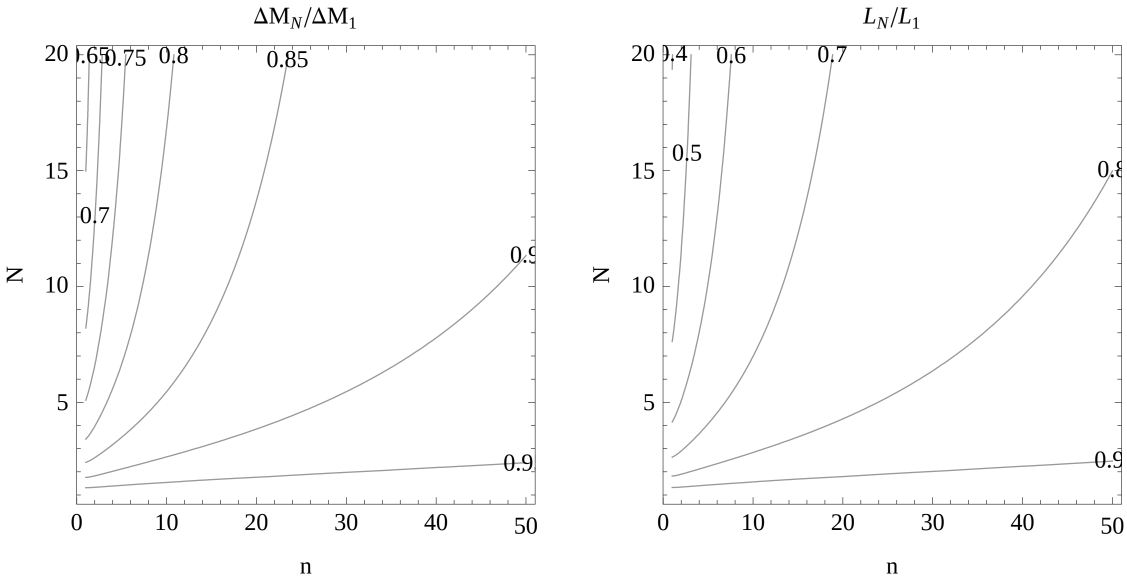

(a) (b)

Figure 29: The relative improvement in the 95% CL measurement as a function of the number of degrees of freedom n and the number of independent variables maximally combined N.

(n) and on the number of combined test statistics (N). We have plotted these ratios in Fig. 29. However, we have used the full χ^2 analysis rather than the Gaussian approximation in the figure to cover a larger region more accurately. For small N, the dependence on the number of bins is rather weak. However, as the number of independent variables combined increases, the potential relative improvement is increased substantially by decreasing the number of degrees of freedom. Furthermore, we find that if the number of independent variables measured is small, the potential improvement by combining in this way is very small. If the variables are not independent and if they are not equal, the improvement is much less and in fact, the result may not be better.

4.2 UNCERTAINTY OF THE MASSES OF LSP AND THE INTERMEDIATE PARTICLE

For our log-likelihood calculation, since we have shown that the background can be almost totally removed by appropriate cuts, we focus on comparing one signal with full collider effects to another. We calculate the log-likelihood as

$$LL(N;\nu) = 2\sum_i \left[N_i \ln\left(\frac{N_i}{\nu_i}\right) + \nu_i - N_i \right] \tag{4.41}$$

where ν_i is the expected number of events in bin i with the masses set according to `IA` and N_i is the number of events expected in bin i for the alternate mass point. For each distribution, we use 50 bins. We take the integrated luminosity to be 100 fb^{-1} and find that the number of signal events is sufficiently large that the log-likelihood approximates well a χ^2 distribution. We then find that the 95% confidence level value for each log-likelihood is $LL_{95\%} = 67.5$. We scan over the masses of the smuons and neutralinos in steps of 0.25 GeV, calculating the log-likelihood for each mass point and plot the contour where it is equal to 67.5 in Fig. 30 for four kinematical variables assuming `IA`. These are the 95% confidence lines for each kinematical variable considered separately.

We find that the E_μ (red dot-dashed lines) and $m_{\rm rec}$ (blue dashed lines) variables are roughly equally good at measuring these masses, leading to an accuracy of approximately ± 1 GeV. We also find that the $E_{\mu\mu}$ and E_{rec} variables give equally good accuracy but were left off the figure for clarity. These are followed by the $M_{\mu\mu}$ variable (blue dotted lines) which has roughly 0.5 GeV less sensitivity. We also find that our kinematical variables are very sensitive if we vary one mass parameter at a time. However, the determination for the two masses is correlated, as seen from Fig. 30 with a linear band rather than a closed ellipse. This is due to the fact that the cusps and endpoints depend on the masses mainly as a ratio rather than independently, as can be seen in Eqs.(2.6), (2.13), (2.15) and (2.17). As a side remark, this degeneracy in the uncertainties of the smuon and muon masses can be broken by using two different center of mass energies. This can be seen from the fact that the formulae for the singular points, Eq. (2.13) (for energy of the muons) and Table. 2 (for the recoil mass) involve c.m. energy through the factor β_B and η_B respectively.

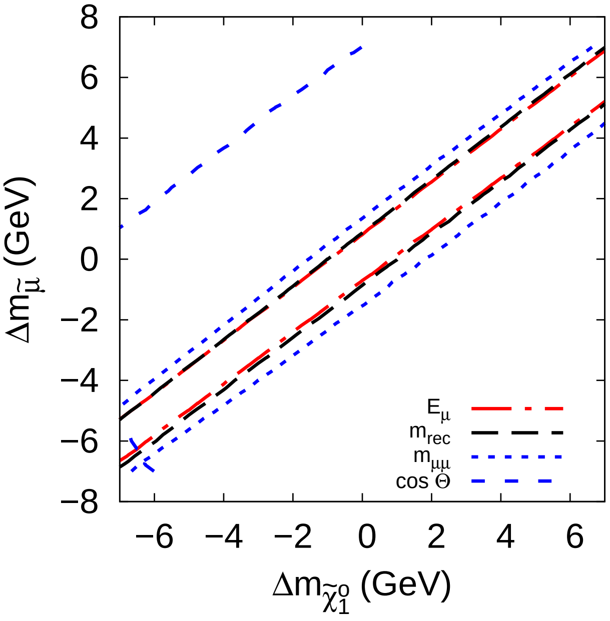

Figure 30: `IA` for $e^+e^- \rightarrow \tilde{\mu}_R\tilde{\mu}_R \rightarrow \mu^+\mu^-\not{E}$, the 95% C.L. contours for the precision of the mass measurement in the parameter space of $(\Delta m_{\tilde{\chi}_1^0}, \Delta m_{\tilde{\mu}_R})$. An additional cut of $m_{\rm rec} > 350\,{\rm GeV}$ on the distributions with spin-correlation and other realistic effects are included. The c.m. energy is set to $\sqrt{s} = 500\,{\rm GeV}$ for all distributions and the integrated luminosity is $100\,{\rm fb}^{-1}$.

We have also considered the effect of combining these measurements in a joint test-statistic including a calculation of the correlation between these variables. We found that the correlation between m_{rec}, E_μ and $\cos\Theta$ was negligible (the off-diagonal terms of the covariance matrix was a few percent or smaller compared to the diagonal terms), the correlation between m_{rec} and $E_{\mu\mu}$ was small but non-negligible (the off-diagonal term was approximately 8% of the diagonal terms), and $E_{\mu\mu}$ and E_{rec} were fully correlated as expected (the off-diagonal term was the same size as the diagonal term). However, we did not find appreciable improvement in the uncertainty of the mass measurements when the log-likelihoods were combined. This is due partly to the correlation between these variables, partly to the differences in how the log-likelihood depends on each of these variables, and partly to the properties of the χ^2 distribution when test statistics with a large number of degrees of freedom are combined as we previously explained.

We perform a log-likelihood analysis for the massive visible particle case and present the 95% C.L. contours for the mass measurement of $\tilde{\chi}_1^0$ and $\tilde{\chi}_1^\pm$ in Fig. 31. It is clear that the $m_{\rm rec}$ distribution (or the E_{jjjj} or E_{rec} distribution) leads to the most precise mass measurement, in comparison with the well-known variable E_W. This is due to the fact that the cusp peak position is more stable with respect to the smearing effects compared with the sharp energy endpoint. The accuracy can reach about 5 GeV. Nevertheless, the mass measurement precision is not as good as that of the smuon pair final state, because of hadronic uncertainties in the four jet measurement.

There have been other recent attempts to measure masses of invisible non-SM particles, most notably by [33, 34] and references therein. Their approach can be taken to complement ours, especially [33] where the main thrust is to distinguish different stabilization symmetries of dark matter particles rather than mass measurement of the invisible particles themselves. On the other hand, the mass measurement proposed in [34] depends solely on the energy distribution of the massless visible particle, namely the peak location. Their proposal depends on accurately measuring the location of the peak by fitting an analytic function as an ansatz.

This is vaguely similar to our approach where we need to fit the triangular distribution to extract the cusp (not necessarily the maximum point) and endpoints of the distribution,

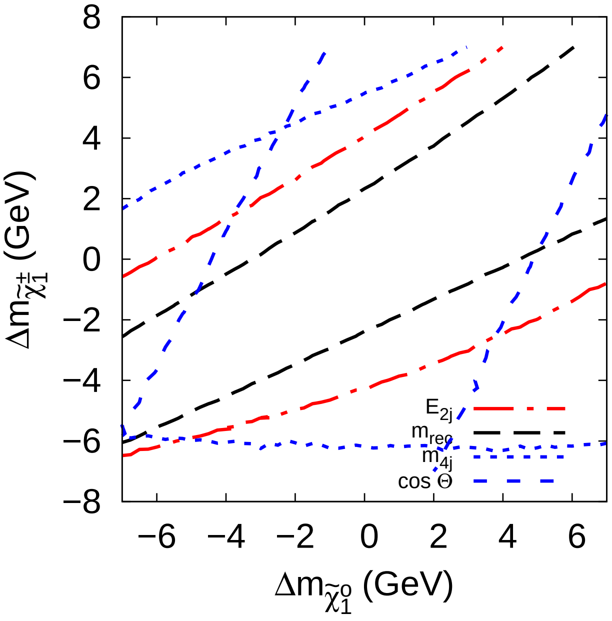

Figure 31: `II` for $e^+e^- \to jj, jj + \not{E}$, the 95% C.L. contours for the precision of the mass measurement in the parameter space of $(\Delta m_{\tilde{\chi}_1^0}, \Delta m_{\tilde{\chi}_1^\pm})$. The additional cuts of $m_{\rm rec} \geq 120\,{\rm GeV}$ and $|m_{jj} - m_W| < 5\Gamma_W$ are included inn the distributions as well as spin-correlation and other realistic effects. The c.m. energy is set to $\sqrt{s} = 500\,{\rm GeV}$ for all distributions and the integrated luminosity is $100\,{\rm fb}^{-1}$.

albeit through a log-likelihood analysis. However, in our approach we utilize several kinematical variables instead of just the energy of the visible SM particle. There are other similarities between the two approaches as well, for example the avoidance of the use of transverse mass. One advantage of [34] is the fact that it can be used for non symmetric decay processes, for example $t\bar{t} \to b\bar{b}\mu^- e^+ \nu_e \overline{\nu}_\mu$, thus pair production is not required.

If the pair-produced particles at the $2 \to 2$ production undergo longer decay chains, so that there are more intermediate on-shell states before ending up with the missing particles, then there may be enough kinematical constraints to determine the masses of the missing particle and the intermediate states, as proposed in [35]. The main strength of this approach is that it does not rely on any specific shape of the kinematical observables. A major drawback of this approach is the ambiguity in the combinatorics of the decay particles. In light of this, they also propose a procedure that potentially minimizes the number of combinations.

As it stands, our approach can be used to improve their direct calculation of the masses. This can be achieved by first measuring the masses of the particles through cusps and endpoints and subsequently using this information to eliminate wrong combinations.

As a final remark, we have also compared with the standard "mono-photon" signal, $e^+e^- \to \gamma \not{E}$ [36, 13]. Although this is the most model-independent channel, the measurement of the endpoint in a slowly-varying E_γ spectrum results in rather poor sensitivity. In addition, we find that the background $e^+e^- \to \gamma\nu\bar{\nu}$ in the benchmark point of Ref. [13] is about 100 times larger than the signal. We have performed the log-likelihood analysis and find that the best accuracy for the lightest neutralino mass determination would be no better than about 50 GeV.

In short, the antler decay topology of the smuon or chargino pair production benefits the mass measurement even in the statistical approach.

5.0 SUMMARY AND CONCLUSION

WIMP dark matter below or near the TeV scale remains a highly motivated option. To convincingly establish a WIMP DM candidate, it is ultimately important to reach consistency between direct searches and collider signals for the common parameters of mass, spin and coupling strength.

Through the processes of antler decay topology at a lepton collider, $e^+e^- \to B\overline{B} \to Xa + \overline{X}\bar{a}$, we studied a new method for measuring the missing particle mass (m_X) and the intermediate particle mass (m_B): the cusp method. With this special and yet common topology, we explored six kinematic experimentally accessible observables, m_{aa}, $m_{\rm rec} \equiv m_{XX}$, $\cos\Theta$, E_a, E_{aa} and $E_{\rm rec} \equiv E_{XX}$. Each of these distributions accommodates singular structures: a minimum, a cusp and a maximum. Their positions are determined by the kinematics only, *i.e.* the masses of B, a, X and $\sqrt{s}$, providing a powerful method to measure the particle masses m_B and m_X. We presented the analytic expressions for the minimum, cusp, and maximum positions in terms of their masses in Sec. 2. We chose to study the accuracy for the mass determination at a lepton collider with three benchmark scenarios in the framework of the MSSM, as listed in Table 3, and named `IA`, `IB`, and `II`.

`IA` is the simplest illustration where only a right-handed smuon ($\tilde{\mu}_R$) pair is kinematically accessible. `IB` is slightly more complicated since both right-handed and left-handed ($\tilde{\mu}_L$) smuon pairs can be produced. We consider the clean leptonic final state of $\mu^+\mu^-\not{E}$ from the smuon decays. By presenting the signal kinematics, we first confirmed the analytic expressions numerically in Fig. 4. We showed that, except for m_{aa}, due to an anticipated kinematical reason, all the other variables yield the pronounced features of a cusp distribution. Although the SM background $e^+e^- \to W^+W^- \to \mu^+\nu_\mu\mu^-\bar{\nu}_\mu$ also results in the antler topology, the positions of the cusps are significantly different due to the massless missing particles, the neutrinos. This difference is used to separate the SM background very efficiently. Furthermore, we pointed out that the experimental acceptance cuts on the observable leptons may change the positions and the shapes of the cusps in a systematic and predictable way, as seen in Figs. 6 and 7.

Through a full simulation including spin correlation, the SM backgrounds, and other realistic effects, we studied how much of the idealistic features of the cusps and endpoints survive, and how well the cusp method determines the missing particle mass for a 500 GeV ILC. We found that the inevitable experimental effects of ISR, beamstrahlung and detector resolutions not only distort the characteristic distributions but also shift the cusp and endpoint positions, as seen in Figs. 8, 9 and 10. The beam polarization may be used to effectively separate the final state $\tilde{\mu}_R\tilde{\mu}_R$ and $\tilde{\mu}_L\tilde{\mu}_L$, as shown in Figs. 11 and 12. To optimize our statistical treatment, we exploited the log-likelihood method based on the Poisson probability function. The precisions for the mass measurement with various variables in `IA` were shown in Fig. 30. The accuracy could reach approximately 1 GeV for smuon pair production, and was comparable for the energy endpoint E_μ and the cusp in $m_{\rm rec}$, $E_{\mu\mu}$ or E_{XX}.

In `II`, we studied the chargino pair production with $\tilde{\chi}_1^\pm \to W^\pm\tilde{\chi}_1^0$. We focused on the hadronic decay $W \to jj$ in order to effectively reconstruct the kinematics, and to explore the detector effects on the hadronic final state. The poor energy resolution for the hadronic final state of the W decay smears the cusp and endpoint quite significantly, as shown in Fig. 13. We found that the $m_{\rm rec}$, E_{jjjj} and $E_{\rm rec}$ cusps are more stable than the energy endpoint E_{jj} against realistic experimental effects, and thus provided a more robust mass determination reaching approximately 5 GeV.

Under the clean experimental environment and well-defined kinematics, a future high energy lepton collider may take advantage of the antler decay topology and provide an accurate determination for the missing particle mass consistent with the WIMP DM candidate.

6.0 SEARCH FOR CONFORMAL INVARIANCE IN TWO-DIMENSIONAL TURBULENCE

Strong turbulence is fiercely difficult to understand because it is dominated by nonlinear effects, and because many degrees of freedom of fluid flow are excited [37]. Complicating the issue further is the fact that there is no fully satisfying description of what turbulence is or what causes it, although the success of Direct Numerical Simulation (DNS) has put a lot of confidence that it is most likely governed by Navier-Stokes equation. Another difficulty is that despite the many specific characteristics of turbulence, not all of them are shared among the various types of turbulent flow [38]. It is important to note that amid these challenges there are fruitful approaches in studying turbulence, conventional ones include statistical, structural and deterministic studies [38], while a recent and an unorthodox point of view involves extracting the information content of turbulence [39]. Here we propose another novel and unconventional way to study turbulence through the lens of conformal invariance.

Some of the main features of turbulence can be understood from dimensional arguments based on a classical formulation of turbulence called the eddy cascade theory (although this point of view is somewhat contradictory to the Galerkin approximation [38]). There is a range of eddy sizes over which the system exhibits approximate self-similarity or scale invariance. Most efforts have been focused on this self-similar range, often called the inertial range. It can span length scales ranging from many meters down to eddy sizes of tens of microns in the atmosphere, in the ocean, and in large wind tunnels.

Though most endeavors are focused on understanding three-dimensional (3D) turbulence (an extreme school of thought suggests that only three dimensions possess turbulent flows), (effective) two dimensional (2D) flows are important from a practical and fundamental point of view. The depth of oceans (L) and the thickness of the atmosphere is very small compared to the earth's radius R. Large-scale velocity variations $R >> L$ are properly viewed as two-dimensional.

Two dimensional turbulence displays striking differences from its 3D counterpart. In 2D, smaller eddies combine to form bigger ones while the reverse happens in three dimensions. This so-called "inverse cascade" in 2D turbulence characterizes hurricane growth in the troposphere [40].

The theory of two-dimensional (2D) turbulence brings new complications and simplifications at the same time. Between the large eddies in 2D turbulence are thin regions where the vorticity of the flow is very large, even though these regions contain only a small fraction of the turbulent energy. In two dimensions, the vorticity is, of course, perpendicular to the plane of the 2D flow and is hence a scalar. In 3D, the vorticity is amplified by velocity gradients, whereas in 2D, its mean square vorticity is a constant, viscous damping aside. As for this damping, it occurs at small scales and is almost absent in the self-similar range of interest here.

It is obviously important if 2D turbulence should turn out to exhibit invariance features that go beyond self-similarity. Recent theoretical and numerical work suggests that this is so. This evidence comes from the study of contours of zero vorticity in an incompressible flow [41] (to be called BBCF) . In that important paper, the authors focus on the geometry of (contorted) paths through the fluid where the vorticity ω is zero at each instant of time τ. Their simulations reveal a new type of conformal invariance. The conformal invariance discussed here , and by BBCF, is unrelated to the usual conformal mapping technique applied to electric potential functions. Rather, it is about the growth of a random curve where each incremental length is produced by a conformal map characterized by a Brownian function.

A path in the x, y plane, written as $z = (x, iy)$, is conformally invariant (in this sense [42]), if there is a function $g(z) = (u, iv)$ that can map the path back to the real axis in the u, v plane while preserving all the angles (See Fig. 32).

The present work is an experimental study of the contours of constant vorticity in a *compressible* flow. We know of no published experiments for incompressible systems. The present laboratory observations display approximate conformal invariance for the contours of zero vorticity measured at hundreds of instants of time τ. Contours of nonzero vorticity paths were also examined. Larger deviations from conformal invariance are observed.

It was noted by BBCF that with present technology, it is technically not possible to search for conformal invariance in *incompressible* 2D flow experiments. However, in the compressible flow experiments to be described here, it was possible to accumulate data over a sufficiently wide parameter range to make such a test. In this work, we use an overhead fast camera to track the motion of particles that float on a turbulent tank of water. These particles have a density that is a fourth of the density of water, so their motion is confined to the surface of the underlying turbulent flow, which is, of course three-dimensional. The flow of the turbulent water underneath the floaters is incompressible, assuring that the two-dimensional divergence of the velocity of the floaters is not zero. The particles are small enough to be almost inertia-free. Thus they sample the velocity of the flow $\mathbf{v}(x, y, z)$ in the surface plane $z = 0$, as discussed below. The present experiments are performed at a moderately high Reynolds number where the inertial range is appreciably large.

This system of floaters is very different from conventional two-dimensional turbulence and also from those studied by BBCF. It is not merely that the surface on which the floaters move is rippled (their amplitude is small [43]), it is that the floaters do not form a separate system; they can exchange energy with those water particles beneath them. In principle, at least, they can take and return their kinetic energy to the underlying fluid on all spatial scales. Thus there is no reason to expect an energy cascade which implies dissipation only at small scales or at the boundaries of the container. Nevertheless, the squared velocity difference $\langle \delta v(\mathbf{r})^2 \rangle \equiv D_2(r)$ between pairs of points separated by distances r, closely conform to that of 3D turbulence, $D_2(r) \propto r^{2/3}$. This scaling is seen in experiments as well as simulations [43].

The present study hinges on the measurement of a random variable $U(t)$, yet to be defined, whose average mean square must be Brownian in character. In that case

$$\langle (U(t) - U(0))^2 \rangle = \kappa t^a. \tag{6.1}$$

The exponent a and the value of κ are measured in the experiments discussed here.

The parameter t is a dimensionless length and not time, and the exponent a must be unity, as in Brownian motion, a requirement that must be met if conformal invariance is realized. The dimensionless "diffusivity" κ is a very important parameter in the theory being tested here. One may think of κ as the dimensionless diffusivity, but only if $a = 1$. For a self-avoiding random walk κ =8/3, and for critical percolation $\kappa = 6$ [42]. This last value is deduced in the simulations of BBCF. In the present experiments, the value of κ for the zero-vorticity contours was extracted from measurements made at many instants of time. At each instant of time τ, there are many constant vorticity lines. The parameter t increases along each line.

6.1 THE SEARCH FOR $U(T)$

The analysis of the experimental data, to be discussed below, requires that the above-defined $g(z)$ be uniquely determined by the function $U(t)$ (usually referred to as the *driving function*), which is related to the experimental observations. Thus, $g(z)$ also depends on t and hence will be written as $g_t(z)$. Roughly speaking, the dimensionless parameter t is proportional to the "length" of the 2D curve, which is being mapped by $g_t(z)$. This dependence on t is what is usually referred to as the *Löwner differential equation*,

$$\frac{\partial g_t(z)}{\partial t} = \frac{2}{g_t(z) - U(t)}. \tag{6.2}$$

It was O. Schramm who first discovered that for a conformally invariant random curve in a 2D plane, $U(t)$ is a one-dimensional Brownian motion obeying Eq. 6.1 [44]. In this case, the random curve is referred to as a Schramm-Löwner Evolution (SLE) trace. For a more formal and complete discussion of SLE, see [42].

One of the most effective ways to identify this type of conformal invariance is to measure $U(t)$, defined by the above differential equation, and see if its mean square average obeys Eq. 6.1. In the next two sections, the experiment and the procedure to calculate $\langle(\delta U(t))^2\rangle \equiv \langle(U(t) - U(0))^2\rangle$ is described.

A typical SLE trace is shown in Fig. 32. Such traces are both self-similar and self-avoiding. After the conformal transformation, the grid in the u, v plane is rectangular; the transformation under $g_t(z)$ is conformal, as all the angles are preserved.

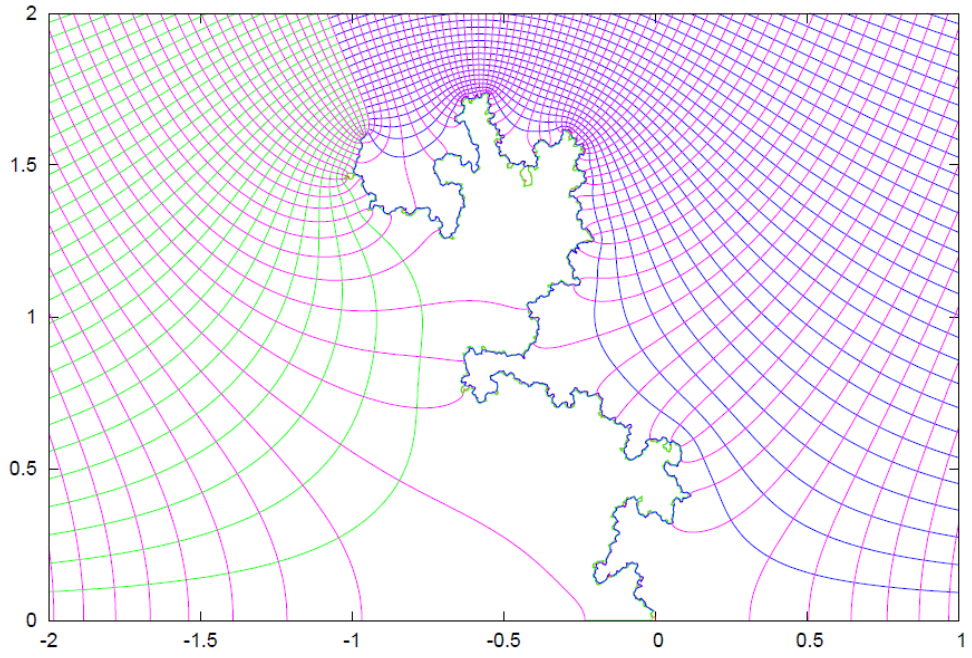

Figure 32: A typical SLE trace with $\kappa = 2$ is shown in Fig. 1. Writing $g_t(z) = u + iv, z = x + iy$, the horizontal and vertical axes in this figure are x and iy respectively. The solid irregular line, which corresponds to a particular value the parameter t, separates a pair of regions where $g(z)$ is analytic. It is called a trace. The traces are self-similar and also self-avoiding. In the experiments to be discussed below, the traces were measured at many of instants of (dimensionless) time τ. (With permission from T. Kennedy. See T. Kennedy, http://www.math.arizona.edu/∼tgk/rtg_2011/sle2.0.pdf, 2011 for original graph.)

6.2 AN ABRIDGED INTRO TO SLE

This section borrows heavily from [45] and gives a heuristic introduction to SLE which closely resembles its numerical algorithm implementation [45]. First, we would like to construct a toy model that does not use the Löwner equation at all. Imagine a conformal mapping function $f_+(z)$ which takes $\mathbb{H}$ (the upper complex plane) onto $\mathbb{H}$ minus a line segment $re^{i\theta}$. To make $f_+(z)$ unique we require $f_+(\infty) = \infty, f'_+(\infty) = 1, f_+(0) = re^{i\theta}$. The first two conditions mean $f_+(z) = z + c_0 + \frac{c_1}{z} + \frac{c_2}{z^2} + ...$ for z about ∞. Now consider another map $f_-(z)$ that takes $\mathbb{H}$ onto $\mathbb{H}$ minus a line segment $re^{i(\pi-\theta)}$, a reflection of $re^{i\theta}$.

Composing the two maps, $f_+(z) \circ f_-(z)$, the second map will push the line segment produced by the first map into the upper plane and bend it. Since the maps take the origin to the tip of the segment $re^{i\theta}$ or $re^{i(\pi-\theta)}$, the end point the of first segment will become the tip of the second line segment, thus the image of $f_+(z) \circ f_-(z)$ will be $\mathbb{H}$ with a curved removed.

Now consider a map $F_n = f_{X_1} \circ f_{X_2} \circ ... \circ f_{X_n}$ where $X_n = \pm 1$ is a random variable with probability 1/2. F_n will map $\mathbb{H}$ onto $\mathbb{H}$ minus a curve γ_n. By taking $n \to \infty$ we can get an infinite curve γ. The SLE curve is then obtained by taking the limit $r \to 0$ for the length of each of the line segment.

How does this relate to Löwner evolution? Let $\gamma(t)$ be a parametrized simple curve in the upper complex plane which starts at the origin. There is a conformal map g_t from $\mathbb{H}$ minus $\gamma[0,t]$ to $\mathbb{H}$. We choose a map that satisfies $g_t(z) = z + \frac{C(t)}{z} + O\left(\frac{1}{z^2}\right), z \to \infty$. Then g_t satisfies Löwner's equation $\frac{\partial g_t(z)}{\partial t} = \frac{2}{g_t(z)-U_t}, g_0(z) = z$ with a suitable choice of curve parametrization $C(t) = 2t$. U_t is usually called the driving function. Note that g_t does the opposite of F_n, it maps $\mathbb{H}$ minus a curve back to $\mathbb{H}$.

The mapping function g_t can be decomposed to $g_{t_k} = \overline{g}_k \circ \overline{g}_{k-1} \circ \overline{g}_{k-2} \circ ... \circ \overline{g}_2 \circ \overline{g}_1, 0 = t_0 < t_1 < t_2... < t_k$, while each $\overline{g}_k$ satisfies Löwner's equation $\frac{d}{dt}\overline{g}_k(z) = \frac{2}{\overline{g}_t(z)-U_{t_{k-1}+t}}$ and takes $\mathbb{H}$ minus a small cut starting $U_{t_{k-1}}$ onto $\mathbb{H}$. Thus g_t maps $\mathbb{H}$ minus a curve back to $\mathbb{H}$ by swallowing a small cut at a time. Each $\overline{g}_k(z)$ represents the inverse of $f_\pm(z)$ with the exception that $\overline{g}_k(z)$ does not start from the origin as $f_\pm(z)$ does.

6.3 EXPERIMENTAL SLE

The 1m × 1m tank is filled with water to a height of 30 cm. The tank is large compared to the camera's field of view. The turbulence is generated by a large pump connected to a network of rotating jets in a plane 10 cm above the tank floor. See Fig. 33 for a schematic of the experimental setup. The arrangement creates uniform turbulence in the center of the tank and also moves the source of turbulent injection far from the fluid surface where the measurements are made [43]. With this scheme, surface waves, which cannot be avoided, do not exceed an amplitude of ~ 1 mm [43]. It is necessary that the surface of the tank be freshly cleaned before each set of measurements. Otherwise, amphiphiles form a continuous layer on the surface and prevents the floaters from moving freely under the action of the turbulence [43].

The hydrophilic particles chosen here are subject to capillary forces which are very small compared to forces coming from the turbulence, and do not affect the results as they do in [46, 47]. The non-inertial character of the particles is minimal because the Stokes number St is small: $St \simeq 0.01$ [48].

During an experimental run, the floating particles (50 μm diameter and specific gravity of 0.25) are constantly seeded into the fluid from the tank floor, where they undergo turbulent mixing as they rise due to buoyancy and are uniformly dispersed by the time they rise to the surface. Once at the free-surface, their motion is constrained to the two-dimensional surface plane. Their motion is tracked with a high-speed camera (Phantom v.5) situated above the tank. The camera field-of-view is a square area of side length L = 9 cm. The constant particle injection is necessary to replace floaters that stick to the tank walls. The sources and sinks at the surface fluctuate in both time and space, which can cause particles to leave the camera's field of view.

Instantaneous velocity fields are measured using an in-house developed particle imaging velocimetry (PIV) program which processes the recorded images of the floaters. The constant injection of particles ensures that surface sources and sinks receive an adequate coverage of particles on the surface. The local particle density at the surface determines the average spacing of the velocity vector fields produced by the PIV program. The resulting velocity

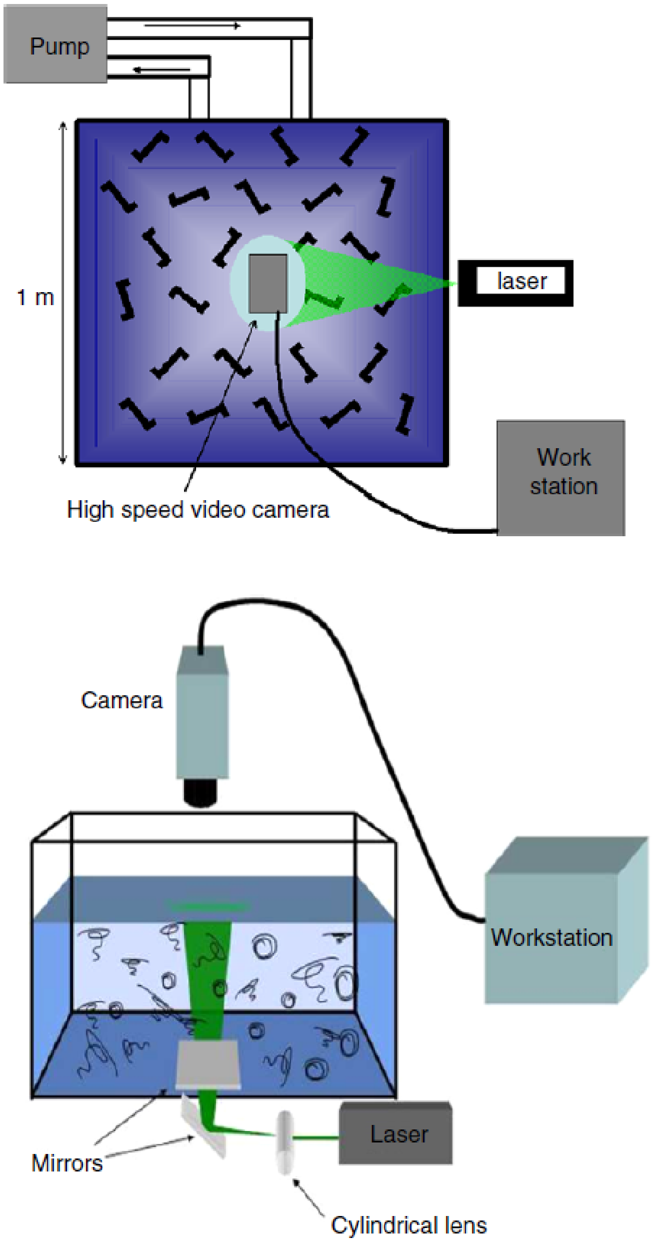

Figure 33: Schematic of the top-view (top panel) and side-view (bottom panel) of the experimental setup. 36 rotating capped jets are placed horizontally on the tank floor (shown as randomly oriented Z-shaped patterns) that pump water into the tank recirculated by an 8 hp pump. The region in the lateral center of the tank and at the surface (z=0) is illuminated by a laser-sheet. A high-speed digital camera suspended vertically above this central region captures images of the light scattered by buoyant particles (50 μm hollow glass spheres of specific gravity 0.25).

vectors are spaced (on average) by $\delta x \simeq 2.7\eta$ over both sources and sinks, where η is the size of the smallest eddies in the inertial range [49].

This vector grid spacing is important for the Lagrangian particle evolution scheme, which is discussed below. The camera's height above the water surface was chosen so that a pixel size is roughly 0.1 mm, comparable to the dissipative scale of the turbulence.

The measured velocity field was then used to solve the equation of motion for Lagrangian particles:

$$\frac{d\mathbf{x}_i}{dt} = \mathbf{v}(\mathbf{x}_i(t), t), \tag{6.3}$$

where $\mathbf{v}(\mathbf{x}_i(t), t)$ is the velocity field and $\mathbf{x}_i = (x_i, y_i)$ are the individual particle positions. To achieve accurate results for the Lagrangian particle evolution, the vector fields used in Eq. 6.3 were interpolated from the experimentally determined velocity vectors via a bi-cubic interpolation scheme developed for numerical simulations, as discussed in [50] and implemented in [43]. This scheme uses the smooth flow between grid points separated by length scales comparable to η to interpolate the velocity field between measured velocity grid points. To use this scheme it is necessary for the measured velocity grid spacing to satisfy the criterion $\delta x < \pi\eta$, where δx is the above mentioned average measured velocity grid spacing. We have tested to ensure that the results do not depend on the velocity grid spacing by varying the spacing from $\delta x = 2.5\eta$ to $\delta x = 4\eta$.

The Lagrangian particle tracks evolved by Eq. 6.3 are then used for the measurements presented in this work. This is the method used to achieve a uniform distribution of floaters at t = 0. The experimental setup is discussed in more detail in [43].

Data were taken for several values of $Re_\lambda \simeq 150 - 170$ with an average $Re_\lambda \simeq 160$. Turbulent parameters measured at the surface are listed in Table 6. All of the statistics presented below were obtained by evolving $\sim 10^5$ Lagrangian particles in each frame.

6.4 RESULTS AND DISCUSSION

The vorticity field at each point, and at each instant of time τ, is extracted from a measurement of the velocity field at equally spaced points separated by $\simeq 2.7\eta = 0.54$ mm over the 9

Table 6: Turbulent parameters measured at the surface. Measurements are made at several values of Re_λ with an average $Re_\lambda \simeq 160$. The parameters listed are averages, with deviations less than 10%.

Parameter	Symbol used in text	Measured value
Taylor microscale λ (cm)	$\lambda = \sqrt{\frac{v_{rms}^2}{\langle(\partial v_x/\partial x)^2\rangle}}$	0.37
Taylor Re_λ	$Re_\lambda = \frac{v_{rms}\lambda}{\nu}$	160
Integral scale l_0 (cm)	$l_0 = \int dr \frac{\langle v_\parallel(x+r)v_\parallel(x)\rangle}{\langle(v_\parallel(x))^2\rangle}$	1.42
Large Eddy Turnover Time (LETT) τ_0 (s)	$\tau_0 = \frac{l_0}{v_{rms}}$	0.43
Dissipation rate ε_{diss} ($\mathrm{cm}^2/\mathrm{s}^3$)	$\varepsilon_{diss} = 10\nu\langle(\frac{\partial v_x}{\partial x})^2\rangle$	6.05
Kolmogorov scale η (cm)	$\eta = (\frac{\nu^3}{\varepsilon})^{1/4}$	0.02
RMS velocity v_{rms}(cm/s)	$v_{rms} = \sqrt{\langle v^2\rangle - \langle v\rangle^2}$	3.3
Compressibility $\mathcal{C}$	$\mathcal{C} = \frac{\langle(\vec{\nabla}_2\cdot\vec{v})^2\rangle}{\langle(\vec{\nabla}_2\vec{v})^2\rangle}$	0.49 ± 2%

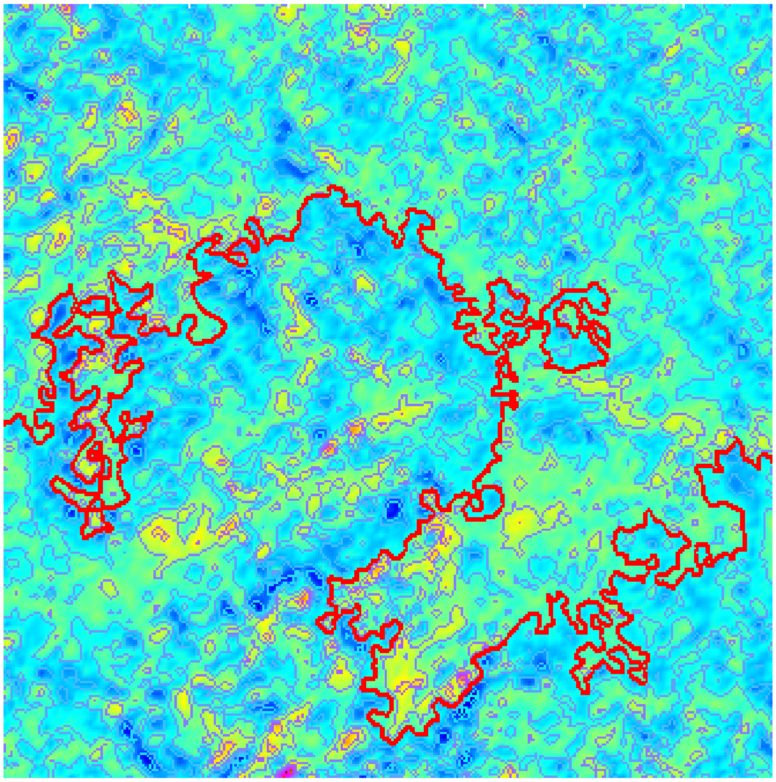

Figure 34: A typical vorticity field displayed with the isolines. The image is of a square 9 cm by 9 cm. The thick solid line is the longest zero isoline in this particular field.

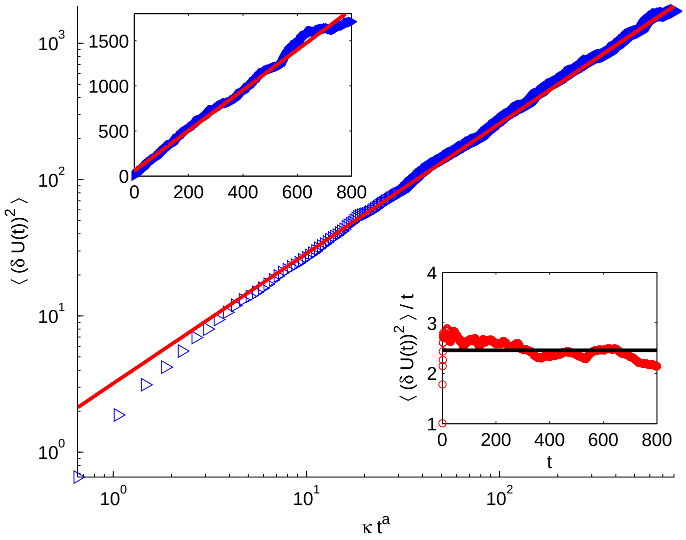

Figure 35: Main frame: a typical log-log plot of $\langle (U(t+t_0) - U(t_0))^2 \rangle$ showing its linearity with respect to t. Upper-left inset: a typical linear plot of $\langle (U(t+t_0) - U(t_0))^2 \rangle$ showing the value of κ as its slope. Lower-right inset: the distribution of $\kappa = \langle (\delta U(t))^2 \rangle / t$

cm × 9 cm field of view of the camera, giving a resolution of 160 × 160 points. The camera captures the images at a rate of 133 Hz. The total number of frames that were analyzed is 833.

In each frame there are roughly 1000 vorticity isolines and 400 zero-vorticity lines, see Fig. 34. The vorticity field is approximated using Stoke's Theorem $\omega = \frac{\oint \mathbf{v} \cdot \mathbf{dl}}{A}$, where A is an area of size $\simeq (2.7\eta)^2$. Although for a fractal object the concept of length is not clearly specified, the average length of the longest zero isoline of each frame is roughly 1000 steps, where the step size is 1.35η.

From each frame, the longest zero and non-zero vorticity lines are extracted. An x-y axis is chosen for each isoline in each frame. The lowest point of the isoline is taken as the origin of the complex plane, $x = y = 0$ because $g_t(z)$ only concerns the upper complex plane, $y > 0$. Next, we calculate the driving function $U(t)$ of each of the vorticity isolines using an algorithm implemented by T. Kennedy [45].

Stated briefly, the algorithm goes by decomposing $g_{s+t}(z) = \overline{g}_t \circ g_s(z)$, where $g_s(z)$ maps the curve from 0 to s back to the real axis and $\overline{g}_t(z)$ maps the image of the curve from s to t under $g_s(z)$ back to the real axis. By recursively decomposing $g_s(z)$, we get $g_{t_k} = \overline{g}_k \circ \overline{g}_{k-1} \circ \overline{g}_{k-2} \circ ... \circ \overline{g}_2 \circ \overline{g}_1, 0 = t_0 < t_1 < t_2 ... < t_k$. Each $\overline{g}_k$ maps one small segment Δt of the curve to the real axis, where $\overline{g}_k$ has to satisfy Löwner equation (Eq. 6.2) within each Δt. In principle, we take $\Delta t \to 0$ but in the experiments the smallest Δt is the spatial interval of the two closest points with the same vorticity ($\Delta t \simeq 2.7\eta$). Each incremental map $\overline{g}_k(z)$ is approximated by a Laurent series around $z \to \infty$, $\overline{g}_k(z) = z + \frac{\Delta t}{z} + U_k + O(\frac{1}{z^2})$. This produces a sequence of discrete U_k that approximates the true driving functions $U(t)$.

There are two ways of calculating $\langle(\delta U(t))^2\rangle$ (Eq. 6.1). One way is to do self-averaging along t followed by an ensemble average over the 833 runs, another way is to calculate the ensemble average over t directly as done by BBCF. If $U(t)$ is Brownian, as expected of SLE traces, the two methods should yield the same result for κ and the exponent a. The resulting values of κ and a from the two different methods will be denoted κ_t and a_t for the self-average and κ_e and a_e for the ensemble average.

The self-averaging is done by calculating $\langle(U(t+t_0) - U(t_0))^2\rangle$, where $\langle \cdots \rangle$ is an average over t_0 for each fixed value of t. The exponent a in Eq. 6.1 is calculated by taking the log of both sides of the equation, *i.e.* $\log\langle (U(t+t_0)-U(t_0))^2\rangle = a\log(t)+\log(\kappa)$ for each curve and fitting it to a straight line (Fig. 35). The slope of the line is the value of the exponent a for that particular curve. The ensemble average over the 833 values of κ and a are then taken to be the value for κ_t and a_t for the system.

For SLE, as for Brownian motion, these two methods of averaging should produce the same results. Therefore, an easy way to distinguish vorticity data from effects of random noise follows from comparing results obtained by these two different averaging methods. To illustrate, we simulated SLE traces, and performed this particular test on those traces for a range of κ-values from 1 to 8 with increments of 0.5. In this simulation, there are 1000 SLE traces for each value of κ; each trace contains 4000 points. We compare the results of $\langle(\delta U(t))^2\rangle$ of the two averaging methods and find that they yield the same values of κ within 2 %.

We also extracted isolines from purely random fields. These fields were produced by generating uniformly distributed vorticity amplitude at each site and have the same resolution as the measured velocity fields. The isolines of the random fields satisfy other tests of SLE (as described below) but fail the ensemble vs self average comparison test. Thus, comparing the results of the two averaging methods proves to be a very useful tool for differentiating noise effects from real SLE traces.

Turning now to our experimental data, as seen in Table 7, the values produced by the two averaging procedures differ by approximately two standard deviations for both κ and a. Since a_t and a_e are measurably different from unity, the meaning of the κ's in this case is ambiguous. We defer discussion of other parameters in the table.

Two stringent tests of SLE, namely χ_a^2 and χ_b^2 as described by Kennedy [51], were also performed on the isolines. The experimental data failed this test, and so did a simulated SLE at a similar resolution. Clearly a more refined resolution is required to produce a conclusive result.

The function $U(t)$ is a random variable, and we have measured its probability distribution function (PDF, see Fig. 36) to determine if it is Gaussian for all values of t as required for a Brownian process. If so, the PDF of $U(t)/(\kappa_e t)^{1/2}$ should collapse onto a standard Gaussian PDF with mean $\mu = 0$ and standard deviation $\sigma = 1$ (Fig. 36). Here, only κ_e is meaningful,

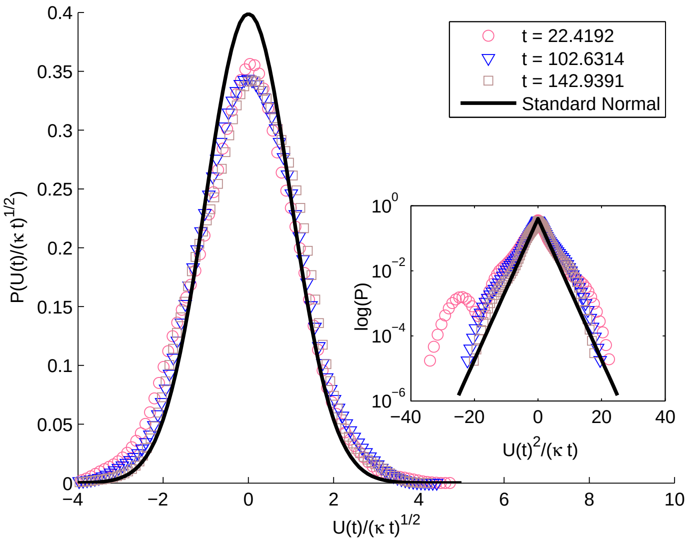

Figure 36: Main frame: the probability distribution function of $U(t)/(\kappa t)^{1/2}$ for the zero-vorticity isolines for three different values of t. Lower-right inset: the log-linear plot of the PDF for 3 different values of t.

Table 7: Results of different tests of conformal invariance for zero isolines. For the non-zero isolines the results show that they are not conformally invariant

Test	t Avg (833 runs)	Ensemble Avg (833 runs)	SLE_κ
Exponent a	a_t=1.2 ± 0.1	a_e=0.97	a_t=a_e=1
κ	κ_t =3.9 ± 1	κ_e =2.45 ± 0.2	$\kappa_t = \kappa_e$
$P(U(t)/\sqrt{\kappa t})$		Not Gaussian see Fig. 36 and text	$\propto e^{-x^2/2}$ $\langle x \rangle = 0$
$P(\theta)$ Eq. 6.4 see dotted line in Fig. 37	No	Yes	see text
D_q independent of q, q=0 to 10 see Fig. 38	see text	No	Yes

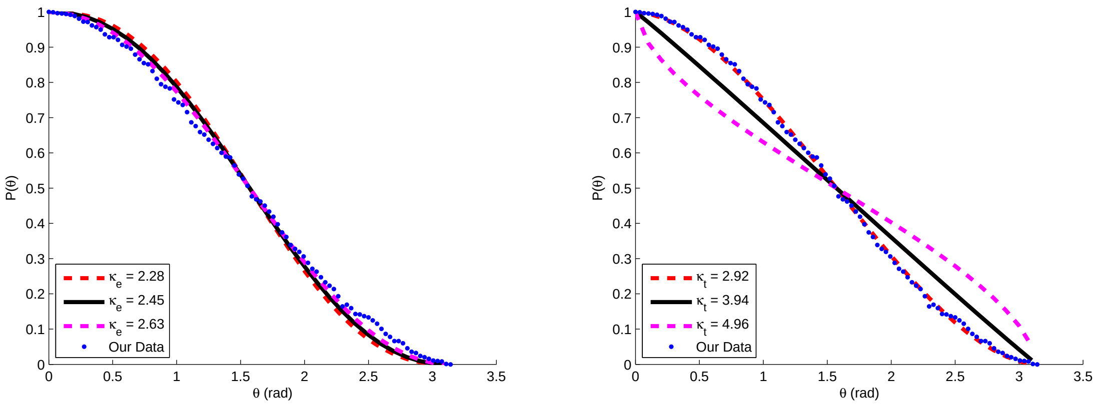

Figure 37: Probability that an isoline keeps a given $z = \rho e^{i\theta}$ to its right. The horizontal axis is θ in radians with respect to the x axis. The probability distribution for zero isolines compared to the expected values for κ_e (Left) and κ_t (Right). Solid lines are predicted distribution based on mean of κ and dashed lines are based on the value of $\kappa\pm$ one standard deviation.

since the PDF of $U(t)$ is produced by the values of $U(t)$ for a fixed t in the ensemble. The inset of Fig. 36 shows that the PDF's of $U(t)$ for three different values of t do not conform to a Gaussian distribution. That is, all data points do not lie on an inverted V. For the non-zero isolines the PDF of $U(t)/(\kappa_e t)^{1/2}$ has non-zero mean and is strongly skewed, ruling out conformal invariance (mean and skewness of the zero isolines are 0.04 and -0.0006 respectively while for the non-zero isolines they are 0.6 and -0.2 respectively).

We apply another test to validate the Brownian characteristic of $U(t)$ (Eq. 6.1). If the vorticity isolines are characterized by Brownian $U(t)$, they must be identified by a particular probability distribution for keeping a point $z = \rho e^{i\theta}$ to the right of each isoline. Here θ is defined with respect to the x axis. It is given by [52]

$$P(\theta) = \frac{1}{2} + \left(\frac{\Gamma\left(\frac{4}{\kappa}\right)}{\sqrt{\pi}\Gamma\left(\frac{8-\kappa}{2\kappa}\right)} \right) {}_2F_1\left(\frac{1}{2}, \frac{4}{\kappa}; \frac{3}{2}; -\cot^2\theta\right) \cot(\theta), \tag{6.4}$$

where Γ is the ordinary Gamma function with κ as a parameter, and ${}_2F_1$ is the gauss hypergeometric function.

The probability distribution for the zero isolines is shown in Fig. 37. The solid lines represent the distributions based on the mean values of κ; the dashed lines denote ± one standard deviation. The dots are the measured distribution. The left panel of this figure shows better agreement with our measurements. Equivalently, the measured angular distribution fits better to the expected distribution for κ_e. We are puzzled by this finding.

It has been argued that Eq. 6.4 is a unique property of SLE traces [52]. One may ask if this equations is satisfied by a vorticity field that is purely random, *i.e.* of zero correlation length. To answer this question, the distribution $P(\theta)$ was calculated for isolines extracted from random fields as explained previously. For a completely random field, one might naively expect that $P(\theta)$ is a constant for all values of θ; this corresponds to SLE traces with the value of κ=8. However, this is not observed in our simulation. Rather, the simulation demonstrates that $P(\theta)$ for isolines of random fields favors small angles, $0 \leq \theta < \pi/2$, corresponding to SLE traces with $\kappa \simeq 2.8$. This result shows that SLE traces indeed form a unique class of symmetry.

It is obvious that the measured angular distribution of the zero-vorticity isolines behave more like the predicted probability distribution (Eq. 6.4). It lies well within one standard deviation of the expected distribution (Fig. 37 Left). We also calculated the distribution function in the case where the starting point of the curve is chosen at random.The result again shows that the distribution of zero vorticity lines fit better than their non-zero counterparts.

Our last test to see whether the system exhibits conformal invariance is calculating the multifractal spectrum of the isolines (Fig. 38), since conformal invariance requires scale invariance. The multifractal spectrum D_q of the longest zero and non-zero vorticity isoline of each frame is then computed using [53]

$$D_q = \lim_{q \to 0} \frac{1}{q-1} \frac{d \log(C_q(r))}{d \log r} \tag{6.5}$$

$$C_q(r) = \frac{1}{N} \sum_{i}^{N} \left[\frac{1}{N-1} \sum_{j \neq i}^{N-1} H(r - r_{ij}) \right]^{q-1} \tag{6.6}$$

Here N are the total number of points in the isoline, H is the heaviside step function, and r_{ij} is the distance between points i and j. This algorithm for determining the spectrum of fractal dimensions is given by Hentschel and Procaccia [54].

To calculate D_q, the log of the correlation sum (Eq. 6.6) is plotted versus the log of r. The range of r over which the plot is a straight line is the scale-free (or scaling) region. The slope of the line $d\log(C_q(r))/d\log(r)$ is the value of D_q.

There are three lines in each graph in Fig. 38. They are the fractal dimensions given by $D_\kappa = 1 + \frac{\kappa}{8}, \kappa < 8$ [55, 56]. The middle horizontal line in each graph represents D_κ using the measured mean value of κ (taking a to be unity); the upper and lower dashed horizontal lines show D_κ using one standard deviation from the mean value of κ. The dots represent the measured mean fractal dimension for each q. The vertical error bars show the uncertainty in the measured values of D_q. The scaling region of $C_q(r)$, of which slope determines the value of D_q, is shown in Fig. 39. The scaling region typically extends 7/10 of a decade in r for both $q = 2$ and $q = 10$.

The multifractal spectrum of the zero isolines is then compared to that of the expected value of D_κ. Fig. 38 shows that the multifractal spectrum of the zero isolines conforms better to the value of D_κ given by κ_t. It is interesting to note that $P(\theta)$ fits better to the distribution given by κ_e. Strictly speaking, a conformally invariant curve should have a constant multifractal spectrum which is independent of q.

In light of the error bars in this figure, we are forced to conclude that departures from homogeneous fractal behavior are not clearly present. At the same time, the secular decrease in D_q with increasing q, suggest that D_q may not be a homogeneous fractal.

6.5 SUMMARY

The goal of this experiment is to determine if the vorticity isolines of the compressible system of floaters meet all the imposed tests for SLE. The floaters exhibit a measurable departure from SLE for the zero vorticity isolines and a much larger departure for lines of nonzero vorticity. The departures are clearly evident in Fig. 36. The interest of this study may be that the floaters display approximate SLE, as Fig. 35 and Table 7 show. One intriguing question, borrowing ideas from Quantum Field Theory, is whether or not compressible turbulence in general a manifestation of a ”spontaneous” broken conformal symmetry. If this is indeed the

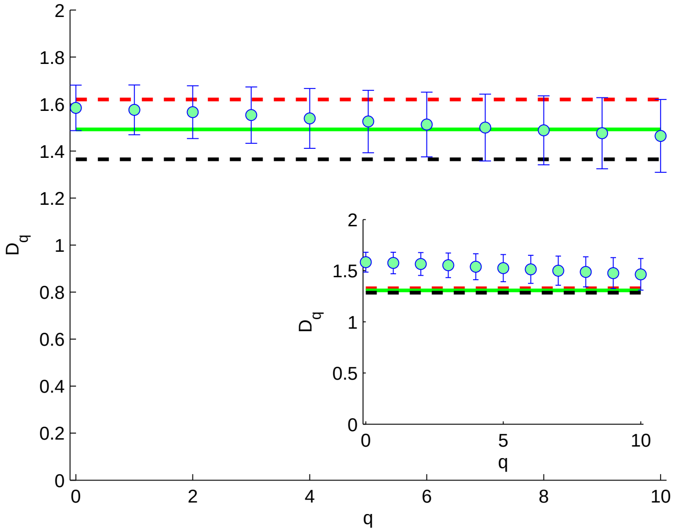

Figure 38: Main frame: multifractal spectrum of the zero vorticity isolines compared to the value of D_q based on κ_t. Lower-right inset: multifractal spectrum of the zero vorticity isolines compared to the value of D_q based on κ_e

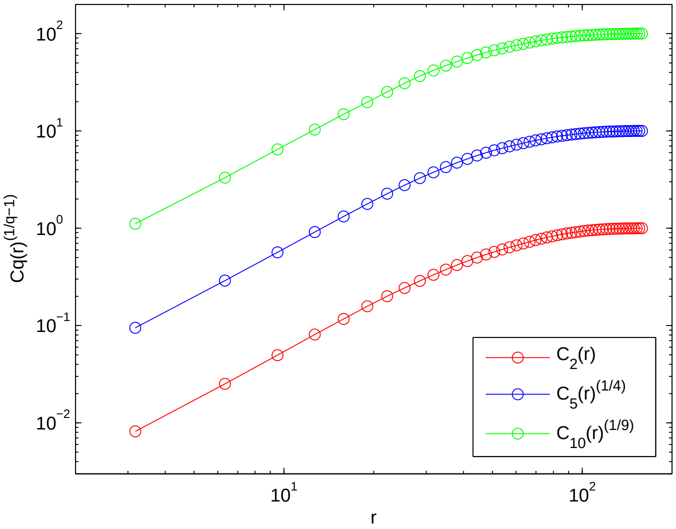

Figure 39: Log-log plot of typical $C_q(r)^{1/q-1}$ versus r for q=2, 5, and 10. The scaling region (straight portion) of $C_q(r)$ typically extends 0.7 decades in r as depicted in the plot. From top to bottom, the curves are C_{10}, C_5, and C_2

case, the study of how the symmetry is broken will be a very interesting endeavor (though not guaranteed to be fruitful).

7.0 DIRECT MEASUREMENT OF TURBULENT SHEAR

Fluids dissipate energy as they flow through pipes or past any smooth or rough surface. Examples include river flow or wind blowing across the land. This energy dissipation is proportional to the velocity gradient, or shear rate, of the flow at the bounding surface. This frictional energy loss, and its dependence on the Reynolds number of the flow [57, 58], is not yet fully understood a century after the first explanation was advanced by L. Prandtl [59].

Here we introduce a new scheme for measuring the shear rate near a bounding surface. It also might be applicable in the interior of a fluid. Unlike some widely-used methods [57], the shear rate s is recorded at a single "point" of size w. The motivation for developing this technique was to improve the usual method for measuring the shear rate in turbulent flows [58, 60].

The scheme introduced here is that of photon correlation spectroscopy (PCS) [61]. It is a variant of that used by Fuller and Leal to study laminar flows [62]. For turbulence, the shear rate s is a random variable. The PCS method enables determination of the time-averaged shear rate $\overline{s}$, its standard deviation σ, and the Gaussian transform of the probability density function (PDF) $P(s)$ itself. Because the method has not been used before, the values of the mean shear $\overline{s}$ obtained by PCS are compared with those measured by laser Doppler velocimetry (LDV) [63].

The PCS scheme has the advantage of improved signal-to-noise, short data-collection times, and also the compactness of the apparatus. The PCS scheme can be used when the mean flow rate is absent or present. Hence it may be useful outside of the domain of turbulence studies. With the PCS scheme, a single beam illuminates a group of moving particles that scatter light into a photodetector at some scattering angle θ. The inset of

Fig. 40 (a) shows the incident and scattered laser beam of momentum $\mathbf{k}_0$ and $\mathbf{k}_s$, respectively and the scattering vector $\mathbf{k} = \mathbf{k}_s - \mathbf{k}_0$. At a point in the flowing soap film, an incident beam is focused to a bright spot of size w. The intensity I_0 of the incident beam is taken to be Gaussian form, $I_0(r) = I(0)e^{-(r^2/w^2)}$. Figure 40b, a side view of the setup, will be discussed below.

The velocity at any point r can then be written as the velocity at the center of the spot r=0 plus a term proportional to the shear rate tensor $\tilde{S}$, which is the quantity of interest. The dominant component of $\tilde{S}$ near a wall in this experiment is $s \equiv \partial_y u(y,t)$, where u is in the flow direction x while y is in the transverse direction in the film plane. Note that s is a scalar quantity. Let $u(t)$ be the velocity of an illuminated particle at a horizontal distance y from the center of the incident beam ($y = 0$). Then

$$u(y,t) = u(0,t) + s\,y(t) + ..., \tag{7.1}$$

where the higher order terms have been neglected.

Within a multiplicative constant, the scattered electric field from N particles within the incident beam at time t is

$$E(t) = \sum_{j=1}^{N} E_0(\mathbf{r}_j)e^{i\mathbf{k}\cdot\mathbf{r}_j(t)} \propto \sum_{j=1}^{N} E_0(\mathbf{r}_j)e^{is(\mathbf{k}\cdot\mathbf{r}_j)t}. \tag{7.2}$$

Here $E_0(\mathbf{r}_j)$ is the incident Gaussian field at the position of the j^{th} particle. Because the scattering from micron-size particles is almost perfectly elastic, $k = (4\pi n/\lambda)\sin(\theta/2)$ where λ is the vacuum wavelength of the incident light beam (633 nm) and n is the refractive index of the soap film, which is 99 % water.

It will first be assumed that the flow is laminar, so that $\tilde{S}$ is time-independent, that is to say, the PDF of the shear tensor is a delta function centered at the mean value of $\tilde{S}$. Then the intensity correlation function which is simply related to the electric field autocorrelation function through the Bloch-Siegert theorem [61] (which is applicable to any Gaussian PDF, including a delta function) is $g(\tau) \equiv \langle I(t)I(t+\tau)\rangle / \langle I(t)\rangle^2 = 1 + G(\tau)$, where

$$G(\tau) = |\langle E(t)E^*(t+\tau)\rangle|^2 / \langle I(t)\rangle^2. \tag{7.3}$$

Evaluating (7.3), using (7.1)-(7.2) and averaging over t gives a result previously obtained by Fuller et al. [62] for laminar flow, as opposed to a turbulent one. They evaluated $G(\tau)$ rather than $g(\tau)$. In the experiments described below, the turbulent soap film flows in the x direction with mean velocity U, where this average is over the width W of the soap film. Then $G(\tau) = e^{-k^2w^2s_t^2\tau^2/2}$, where s_t is an average over time. Use has been made here of the Gaussian form of the incident beam.

Because s is a random function for turbulent flows, an additional average over s is needed, giving

$$G(\tau) = \int e^{-k^2s^2w^2\tau^2/2} P(s)ds, \tag{7.4}$$

(with $P(s)$ having its maximum near $\overline{s}$); $G(\tau)$ is the Gaussian transform of $P(s)$.

Two important parameters, in addition to w, are W and the Reynolds number, $Re = UW/\nu$, where ν is the kinematic viscosity of the soap solution.

If the supporting walls that bound the film flow are not smooth, their roughness R^* is another important control parameter. As in three dimensions one expects [64, 65, 66] the dimensionless frictional drag $f \equiv \nu s/U^2$ to be independent of Re when it is sufficiently large. It now depends on the ratio R^*/W [57]. At intermediate values of Re, experiment [58] and theory [66] support the result $f = CRe^{-1/2}$, where C is just a number, and in 3D flows, $f = CRe^{-1/4}$.

If the shear tensor has more than one component [62]

$$G(\tau) = e^{-2Dk^2\tau - U^2\tau^2/2w^2} \int e^{-(\tilde{S}\cdot\mathbf{k})^2w^2\tau^2/2} P(s)ds, \tag{7.5}$$

with $\tilde{S}_{ij} = \tilde{S}_{ji}$ when the fluid is incompressible, as in this experiment [57]. The factors to the left of the integral take into account the extraneous effects of particle diffusion ($e^{-2Dk^2\tau}$) and transit time broadening ($e^{-U^2\tau^2/2w^2}$); they are discussed later in the text. In the next section we will take a quick detour and present a quick and intuitive derivation apt for experimentalists of the correlation function including the transit time broadening term.

7.1 A QUICK DERIVATION OF INTENSITY CORRELATION AND TRANSIT TIME BROADENING

The derivation of the diffusion term ($e^{-2Dk^2\tau}$) is readily available in many articles on dynamic light scattering, one that is particularly useful is [67], as it also explains a lot of the assumptions made in this derivation. The main purpose of this derivation is to show that a simple "*physical*" idea can go a long way. It was also the first derivation I did as a graduate student which was experimentally tested.

We now focus our attention to the other two terms $e^{-U^2\tau^2/2w^2}$ and $e^{-k^2w^2s_t^2\tau^2/2}$. First, the setup is that the flow is going down in positive x direction while the horizontal direction is parallel to the y axis, see Fig. 40 for reference. A very helpful way of thinking about this is to break up the flow to strands, where each strand is just a line of constant y, *i.e.* a vertical line. The intensity correlation within each strand is easily derived because in laminar flow each particle scatters light the same way. Once we have the intensity correlation within each strand, we will average all the different strands using the beam intensity profile, which is Gaussian. The main thing in this derivation is separating the effect that is experimentally/physically important from the irrelevant ones, a very memorable lesson I learned from my fluid dynamics mentor.

The total electric field scattered by the spot illuminated by the laser beam is given by

$$\begin{aligned} E_s(t) &= \sum_{i=1}^{N} E_i(t) \propto \sum_{i=1}^{N} A_i(r_i(t))e^{ikr_i(t)+i\omega t} \\ r_i(t) \to x_i(t) &= v_{x_i}(y)t \\ v_{x_i}(y) &= v_{0_i} + sy, \quad s = \left.\frac{\partial v_{x_i}(y)}{\partial y}\right|_{y=0} \end{aligned} \tag{7.6}$$

where $E_i(t)$ is electric field scattered by particle i, $A_i(r_i(t))$ its magnitude, $x_i(t)$ the location of the scatterer as a function of time t, $v_{x_i}(y)$ the velocity of the particle as a function of its horizontal position y, and finally s is the shear rate that we are interested in, evaluated at $y = 0$, since within the laser spot the shear is approximately constant.

The intensity of the incoming laser beam is given by a Gaussian profile in both x and y directions, here we choose the center of the laser spot to be at $x = 0,\ y = 0$ and normalize the peak magnitude of the laser beam to one

$$\begin{array}{rcl} I_0(x,y) & = & \exp\left(-\frac{x^2+y^2}{w^2}\right) \\ A_i(r_i(t)) \;\rightarrow\; A_i(x_i(t)) & = & \exp\left(-\frac{(v_{0_i}t+syt)^2+y^2}{2w^2}\right) \end{array} \tag{7.7}$$

the intensity auto-correlation function is given by

$$\begin{array}{rcl} \langle I(t)I(t+\tau)\rangle & = & \sum_{i,j,k,l}^{N} \langle E_i(t)E_j^*(t)E_k(t+\tau)E_l^*(t+\tau)\rangle \\ & = & \sum_{i=j,k=l}^{N} \langle E_i(t)E_i^*(t)E_k(t+\tau)E_k^*(t+\tau)\rangle + \\ & & \sum_{i=l,j=k}^{N} \langle E_i(t)E_i^*(t+\tau)\rangle\langle E_j^*(t)E_j^(t+\tau)\rangle \\ & = & N^2|\langle I_0(t,y)\rangle|^2 + N\sum_{i}^{N} |\langle E_i(t)E_i^*(t+\tau)\rangle|^2 \\ & = & \widetilde{G}(0) + \widetilde{G}(\tau) \end{array} \tag{7.8}$$

where we have defined $\widetilde{G}(0) \equiv N^2|\langle I_0(t,y)\rangle|^2$, $\widetilde{G}(\tau) \equiv N\sum_{i}^{N} |\langle E_i(t)E_i^*(t+\tau)\rangle|^2$. Notice that we have thrown away some of the summation products because their average is negligible, see [67]. The electric field product term is given by

$$\begin{array}{rcl} E_i(t)E_i^*(t+\tau) & = & A_i(x_i(t))A_i(x_i(t+\tau))e^{ikr_i(t)+i\omega t}e^{-(ikr_i(t+\tau)+i\omega(t+\tau))} \\ & = & I_{0_i}(t,\tau,y)e^{ik(v_{0_i}+sy)t-ik(v_{0_i}+sy)(t+\tau)}e^{i\omega t-i\omega(t+\tau)} \\ & = & I_{0_i}(t,\tau,y)e^{-ik(v_{0_i}+sy)\tau}e^{-i\omega\tau} \end{array} \tag{7.9}$$

The fact that in our experiments the Gaussian intensity falls off faster than the rate of change of the velocity within the laser spot means that we can approximate the velocity inside the spot, v_x, by its average value, $\overline{v}_x$

$$I_{0_i}(t,\tau,y) \;\simeq\; \exp\left(-\frac{(\overline{v}_x t)^2+(\overline{v}_x(t+\tau))^2+2y^2}{2w^2}\right). \tag{7.10}$$

We can now take the average in both time and horizontal direction (the limits of the integral can be taken to infinity because the Gaussian falls off quickly enough that the correction is small)

$$\begin{array}{rcl} \langle E_i(t)E_i^*(t+\tau)\rangle & = & e^{-ikv_{0_i}\tau}e^{-i\omega\tau}\int_{-\infty}^{\infty} dt\;\exp\left(-\frac{(\overline{v}_x t)^2+(\overline{v}_x(t+\tau))^2}{2w^2}\right)\times \\ & & \int_{-\infty}^{\infty} dy\;\exp\left(-\frac{y^2}{w^2}-iksy\tau\right) \\ & = & (e^{-ikv_{0_i}\tau-i\omega\tau})\left(\frac{\pi w^2}{\overline{v}_x}\right)e^{-\overline{v}_x{}^2\tau^2/4w^2}e^{-k^2s^2w^2\tau^2/4} \end{array} \tag{7.11}$$

the electric field correlation, $\widetilde{G}(\tau)$, is then

$$\begin{aligned}
|\langle E_i(t)E_i^*(t+\tau)\rangle|^2 &= \left(\frac{\pi^2 w^4}{\overline{v}_x^2}\right) e^{-\overline{v}_x{}^2\tau^2/2w^2} e^{-k^2 s^2 w^2 \tau^2/2} \\
\sum_i^N |\langle E_i(t)E_i^*(t+\tau)\rangle|^2 &= N\left(\frac{\pi^2 w^4}{\overline{v}_x^2}\right) e^{-\overline{v}_x{}^2\tau^2/2w^2} e^{-k^2 s^2 w^2 \tau^2/2} \\
\widetilde{G}(\tau) &= N\sum_i^N |\langle E_i(t)E_i^*(t+\tau)\rangle|^2 \\
&= N^2\left(\frac{\pi^2 w^4}{\overline{v}_x^2}\right) e^{-\overline{v}_x{}^2\tau^2/2w^2} e^{-k^2 s^2 w^2 \tau^2/2}
\end{aligned} \tag{7.12}$$

while $\widetilde{G}(0)$ is given directly by

$$\begin{aligned}
\langle I_0(t,y)\rangle &= \textstyle\int_{-\infty}^{\infty} dt\ e^{-\overline{v}_x^2 t^2/w^2} \int_{-\infty}^{\infty} dy\ e^{-y^2/w^2} \\
&= \left(\frac{\pi w^2}{\overline{v}_x}\right) \\
\widetilde{G}(0) &= N^2 |\langle I_0(t,y)\rangle|^2 \\
\widetilde{G}(0) &= N^2\left(\frac{\pi^2 w^4}{\overline{v}_x^2}\right)
\end{aligned} \tag{7.13}$$

and finally, the complete intensity correlation function, $g(\tau)$, is

$$\begin{aligned}
g(\tau) &= (\widetilde{G}(0) + \widetilde{G}(\tau))/\widetilde{G}(0) \\
&= 1 + \widetilde{G}(\tau)/\widetilde{G}(0) \\
&= 1 + e^{-\overline{v}_x{}^2\tau^2/2w^2} e^{-k^2 s^2 w^2 \tau^2/2} \\
g(\tau) &= 1 + e^{-U^2\tau^2/2w^2} e^{-k^2 s^2 w^2 \tau^2/2}
\end{aligned} \tag{7.14}$$

where the first exponential is the transit time broadening term and the second is the shear dependent correlation function which is the main topic of this study.

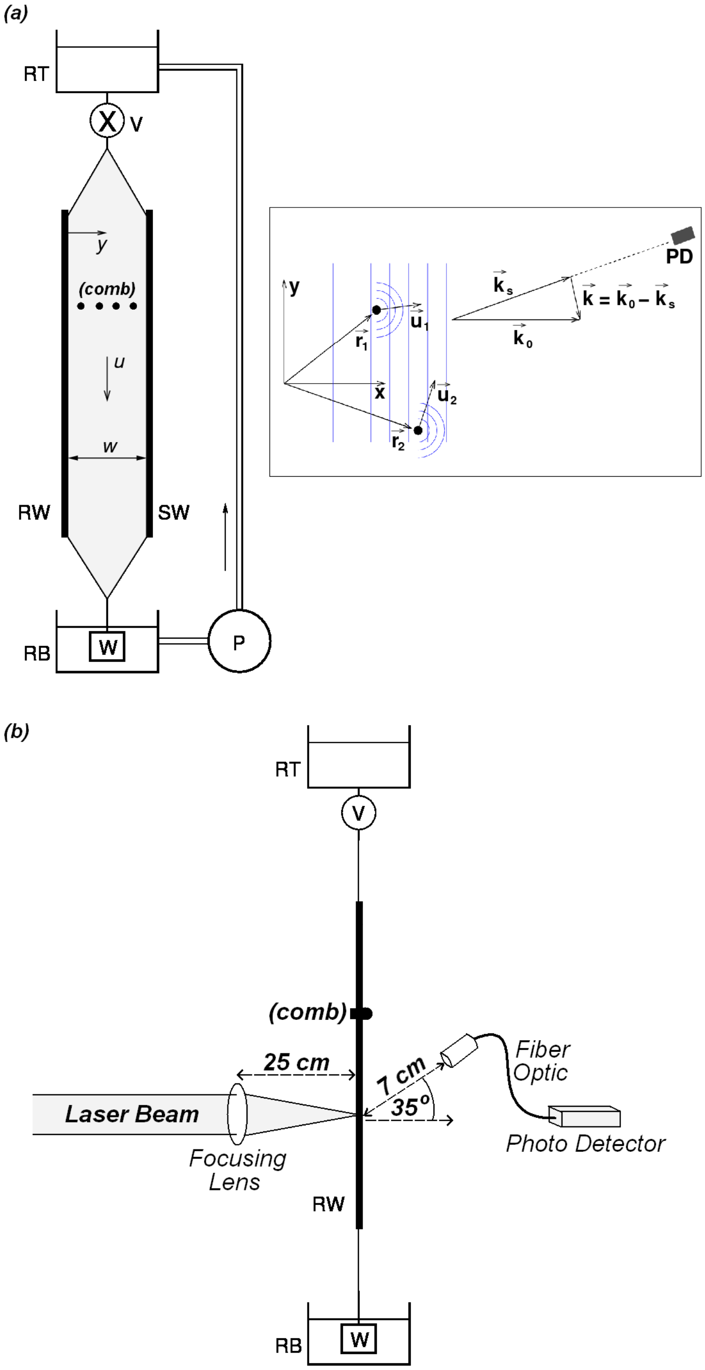

Figure 40: (a): Setup for vertically flowing soap film. The film flows down from reservoir RT through valve V between strips RW and SW, separated by width W. The weight W keeps the the nylon wires taut. Inset shows scattering diagram. (b): Side view of the setup, showing laser source, focusing lens and photodetector

7.2 THE EXPERIMENTS

The experiments were performed on a soap film channel, shown in Fig. 40 with W=2 cm. The flow is driven by gravity, but there is an appreciable opposing force from air friction. However, near the vertical plastic strips that support the film, the viscous force from the wires dominates [58].

These strips are glued to thin plastic wires 0.5 mm in diameter that join to form an inverted V at the top and at the bottom, as indicated in Fig. 40. At the apex, a small tube connects the reservoir to a valve V that controls the flow rate. The wires at the bottom connect and deliver the spent soap solution to reservoir RB, where it is pumped back to the top reservoir RT to keep the flow rate steady. Typical flow rates of the soap solution are $\sim$ 0.2 ml/s.

The soap solution is 1% Dawn dishwashing detergent in water. It is loaded with neutrally buoyant polystyrene particles which scatter the incident beam from a 5 mW 633 nm He-Ne laser into the photodetector, a Perkin Elmer SPCM-AQR-12-FC. The laser source is located behind the soap film while the photodetector is located in front of it as shown in Fig. 40b. The laser beam is focused onto the soap film with a lens of focal length 25 cm. The photon stream is delivered to the photodetector through an optical fiber, where the fiber tip is located 7 cm from the illuminated spot on the film.

In these experiments, w is limited by the wavelength of visible light, focal length of the focusing lens and the diameter of the incident beam and has a value of w = 100 μm. The scattering vector $\mathbf{k}$ is in the vertical (x) direction and the dominant component of the shear rate is $s \equiv \partial_y u(y,t)$. The diameter ϕ of the seed particles (0.4 μm) is sufficiently small that their Stokes number in the strongest turbulence is less than 0.1 [58]. Hence the particle velocities are adequately close to that of the fluid. The refractive index of the soap solution is roughly 1.3. Typically, the scattering angle $\theta = 35°$, $k = 6\times10^6$ m^{-1}. Using a seed-particle density of 1.5 gm/l yields an average photon counting rate of 10^6 Hz.

Experiments were performed with a horizontally oriented comb penetrating the soap film at a point above the measuring point and with the comb absent. Only with the comb present is the turbulence reasonably developed and the energy spectrum is of scaling form,

$E(k) \propto k^{-b}$, with $b \simeq 3$ [58, 68, 69]. This is the *enstrophy range*, defined as the interval where vorticity of larger size fluctuations cascade to smaller scales. In two dimensions there is also a cascade of energy fluctuations to larger scales, where $b = 5/3$, as in three dimensions. However, it is not accessible for decaying turbulence, as in this experiment [69]. By making the bounding walls rough, so that turbulence is constantly being generated there, the inverse energy cascade can also be seen [70]. The teeth of the comb as well as their spacing is 2 mm.

To further test the PCS technique, measurements are also made with the comb absent. In this case, there is no well-defined energy spectrum decaying as a power law. Nevertheless the flow is far from laminar, so that $\overline{s}$ can be measured by both PCS and LDV.

To first order, $e^{-k^2w^2s^2\tau^2/2} \simeq 1 - k^2w^2s^2\tau^2/2$ and $G(\tau) \rightarrow 1 - k^2w^2\overline{s^2}\tau^2/2$. However, experimentally $G(\tau)$ is found to be a non-Gaussian function. If $P(s) \propto e^{-(s-\overline{s})^2/2\sigma^2}$,

$$G(\tau) = \frac{1}{\sqrt{k^2w^2\sigma^2\tau^2 + 1}} e^{-k^2w^2\overline{s^2}\tau^2/(2k^2w^2\sigma^2\tau^2+2)}, \tag{7.15}$$

which is clearly non-Gaussian in τ. Both panels of Fig. 41 show that while $P(s)$ is close to Gaussian form, the Gaussian fit (solid lines) is not perfect. These "good" fits to Gaussian form were unexpected.

There are two other effects that can contribute to the decay of $G(\tau)$: thermal diffusion of the seed particles and transit time broadening, which can be dominant for large U/w. Both of these contributions are small in these experiments but are easy to correct for [71]. To take diffusion into account, one multiplies Eq. 7.4 by the factor, $G_D = e^{-2Dk^2\tau}$, where D is the diffusion constant, which, for spherical particles of diameter ϕ is $k_BT/3\pi\eta\phi$, where k_B is Boltzmann's constant and η is viscosity.

As for the transit time effect, particles passing through a beam of size w produce a burst of light intensity that temporally modulates the scattered light. The multiplicative correction factor here is $G_{tt}(\tau) = e^{-(U^2\tau^2/2w^2)}$[71].

The decay times for both of these effects is long compared to the viscous decay time of interest so these multiplicative time factors can be dropped. For example, with a spot size $w = 100\mu$m and a typical mean velocity of $U = 1$ m/sec, the transit time τ_{tt} associated with the effect is or order $a/U \simeq 0.1$ ms. This is fifty times longer than typically measured τ_c.

Diffusion times are much longer than this and hence contribute insignificantly to the decay of $G(\tau)$.

Fig. 41 shows $G(\tau)$ for measurements made with the comb absent (a) and present (b), respectively. Here $U \simeq 2$ m/s in both experiments, W=2 cm, and $w = 100$ μm. The vertical axis is linear, but the horizontal axis is $\log \tau$, so as to display several decades of lag time. The insets to both figures show $\log G(\tau)$ vs τ^2, so that a Gaussian decay of $G(\tau)$ appears as a straight line. The straight lines in the lower insets indicate that $G(\tau)$ is indeed of Gaussian form for very small τ. They are a best fit to the experimental curves and correspond $\overline{s} =$ 1600 s^{-1} and 1000 s^{-1} for the experiments with and without the comb.

The solid lines in the upper insets to Fig. 41 are best fits under the assumption of a Gaussian $P(s)$. A good fit clearly extends beyond the small-τ limit and enables the determination of the standard deviations σ of the mean shear as well as $\overline{s}$ itself. The mean shear $\overline{s}$ is calculated from the definition of variance, $\sigma^2 = \overline{s^2} - \overline{s}^2, \overline{s} = \sqrt{\overline{s^2} - \sigma^2}$. The results are $\overline{s} = 950$ Hz $\sigma = 300$ Hz with the comb absent and $\overline{s} = 1620$ Hz $\sigma = 500$ Hz with the comb present. The ratio of σ to $\overline{s}$ is near 20 %.

The shear measurement is done in the viscosity-dominated layer of width $\delta(x)$, where x is the distance from the comb. Ideally the spot size w should be much smaller than $\delta(x)$. The function $u(y)$ is proportional to y within $\delta(x)$. Prior experiments have established that at $x = 20$ cm below the comb, where the measurements were made, δ is roughly 200 μm [58]. Thus the beam size w is small enough to correctly measure the viscous shear rate.

The single-point PCS measurements of $\overline{s}$ are now compared with those of LDV, made in the traditional way; the vertical velocity component u is measured at two nearby horizontally-spaced points in the viscosity-dominated interval.

The LDV measurements were made 2.5 cm below the PCS beam spot, which is 80 cm below point P in Fig. 40 and 20 cm below the comb. The LDV measurement point is advanced in 50 μm steps starting at y=0. The minimum useful value of y is dictated by the necessity of avoiding strong light scattering from the supporting plastic strip with its edge at y=0.

The LDV laser source is 514 nm line from a Coherent argon-ion laser operating at a power of 500 mW, roughly one hundred times that used in the PCS device. The data collection

(a) Normalized Correlation Function Near Wall (No Comb)

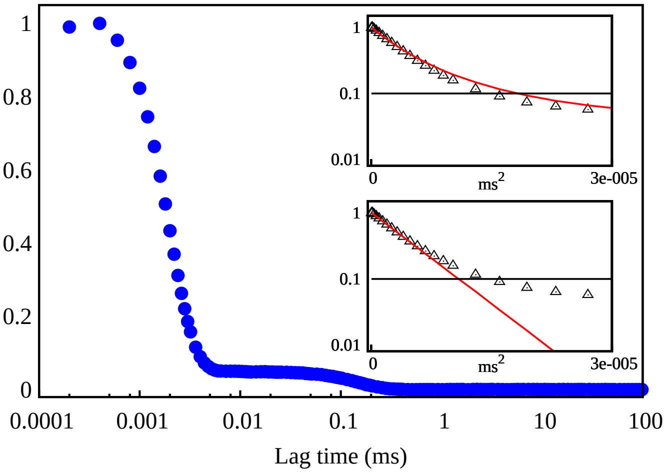

(b) Normalized Correlation Function Near Wall (Comb)

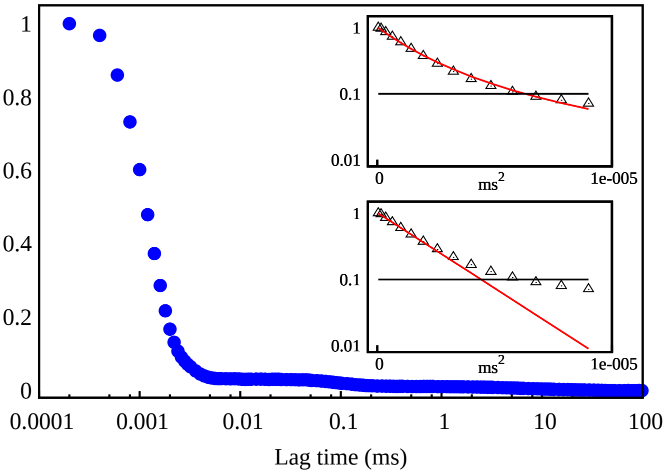

Figure 41: Panel (a) and (b) are semilog plots of typical correlation functions $G(\tau)$ obtained with the comb absent and present. The conditions of these measurements are described in the text. The first data point in panel (a) should be ignored; it is instrumental in origin. The curved solid lines are a best fit to the data using a Gaussian $P(s)$. The straight solid lines are first order approximation of $G(\tau)$ and valid only for $k^2w^2\overline{s^2}\tau^2 << 1$. However, a Gaussian $P(s)$ fits $G(\tau)$ reasonably well for more than a decade. This fit has no theoretical basis.

time for each measurement of $u(y)$ is roughly 20 s. Because the correlation time is of the order of microseconds, and the counting rate is of the order of MHz the function form of $G(\tau)$ emerges after only a few seconds of data collection with the correlator.

7.3 RESULTS

The mean shear rate $\overline{s}$ in the viscous region obtained by LDV and PCS agree to within one standard deviation, as seen in Table 8. The uncertainties are deduced from seven measurements made at the indicated values of U. From an individual run, one cannot extract σ from the LDV data, because noise fluctuations can change even the sign of $\partial_y u(y,t)$.

The LDV and PCS measurements span the range 29000 $< Re <$45000 and from 40000 $< Re <$57000, with and without comb respectively. With the comb in place, the Taylor microscale Reynolds number $Re_\lambda \equiv u_{rms}\lambda/\nu = 130$, where $\lambda = u_{rms}/\sqrt{\langle(\partial u/\partial x)^2\rangle} = 1$ mm.

The errors from one run to another are *not* statistical in origin. Rather, the source is variations in the flow speed through the valve and the motion of the film plane caused by velocity fluctuations of the surrounding air which could be only partially suppressed by placing the entire apparatus in a tent.

Fig. 42 shows measurements of $\overline{s}$ as a function of y in units of 50 μm obtained using PCS (circles) and LDV (triangles) in the range out to y =1.50 mm with the comb present. Here U = 2.16 m/s, W=2 cm and the kinematic viscosity of the soap solution is close to that of water (ν =0.01 cm^2/s), Re=45,000.

The main messages conveyed by this graph are (a) the two schemes give roughly the same results for $\overline{s}(y)$, (b) near one of the walls, the LDV measurements are noisier (for reasons already discussed), and (c) $\overline{s}$ decreases with increasing y. Even in the absence of air friction, this decrease is expected and is well-studied in 3D flows [57]. In soap film flows, air friction slows the flow far from the walls, making analysis of the data there difficult.

This experiment indicates it should be possible to measure $\overline{s}$ near the wall and in the interior of 3D flows, though care must be taken to collect scattered photons from only a small volume in the fluid. Far from a bounding wall in 3D turbulence, the PCS method will

Table 8: Mean shear rate $\overline{s}$ as measured by LDV and PCS in a narrow range of mean flow speeds (comb inserted).

U **(m/s)**	LDV $\overline{s}$ (Hz)	PCS $\overline{s}$ (Hz)
1.4	1500	1660
1.6	1120	1030
1.7	1760	1830
1.8	1880	1430
1.9	1230	1200
2.2	1760	1700
2.2	1860	1640
Average	1590	1500
Std. Dev.	300 (20%)	300 (20%)

suffer from the limitation that w should be smaller than the smallest eddy size [72], defined as $\eta = (\nu^3/\epsilon)^{1/4}$. Even in these soap film experiments, η is estimated to be comparable to or smaller than w. Yet, as Fig. 42 shows, the LDV measurements of $\overline{s}$ agree with the PCS result up to $y = 1.5$ mm from a wall, well outside the viscous region.

7.4 SUMMARY

Though the photon correlation scheme has been used here to measure properties of the shear rate in a two-dimensional soap film, it can be used in three dimensional flows as well. The PCS method has good signal-to-noise, is compact, and uses a laser in the mW range. The method yields the variance of the shear rate as well as its mean value. The correlation function itself is the Gaussian transform of the probability density function, $P(s)$.

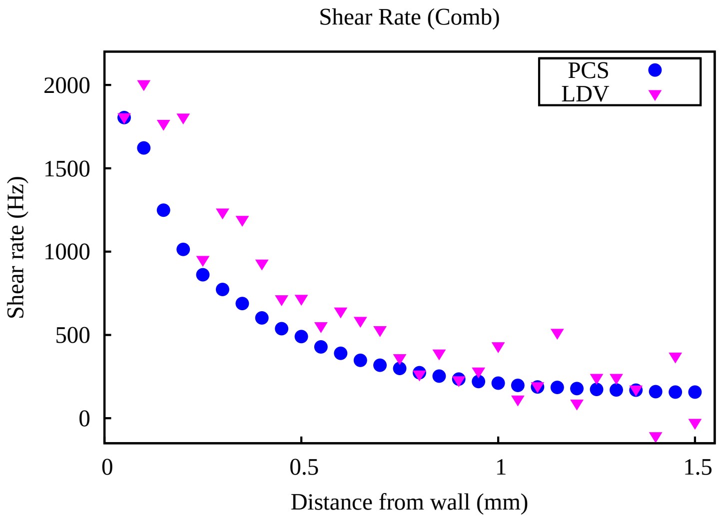

Figure 42: Plot of mean shear rate $\overline{s}$ as a function of distance from the wall (in mm) with a comb in place to strengthen the turbulence. The mean flow speed $U = 2.16$ m/s, Re=45,000.

8.0 GALILEO

8.1 INTRODUCTION

Physics has come a long way since the days of Galileo. While most classical mechanics calculations can be done with pen and paper, the same thing cannot be said about particle physics. The mathematical formulation and machinery to produce numerical prediction is far too complicated for manual calculations. This is especially true for models with massive symmetry groups like supersymmetric ones. Tools are available, however, they are cumbersome to learn and use and contains certain disadvantages.

The most common disadvantage is the fact that they are fragmented. Fragmented, because one has to use different packages for different stages of the calculation. For example, the first step in testing a model would be to generate its Feynman rules. A very popular tool to do this particular job is FeynRules [73]. One then needs to feed the rules to a monte carlo event generator like calcHEP [74] or Whizard [29], which then can be complemented by supplementary hadronization packages like Pythia [75]. Another popular package for building and analyzing Supersymmetric models is SARAH [76].

However, this is not the main impediment in exploring and testing new particle physics models. Exploring a new model usually requires implementing new symmetries into the Lagrangian, be it super or otherwise. To date there is no tool that can automatically generate Lagrangians based on the symmetry groups under which they must be invariant.

These obstacles mean that it will take a very long time for a theorist to get a numerical physical prediction from the time a new model is proposed. The grand vision of our computer algebra package, codenamed Galileo, is to streamline the available packages and introduce a new core element for automatic Lagrangian generations that will enable theorists to come up with new models with ease. In this way, the time taken from the creation of new models to the calculation of physical predictions can be cut down significantly. Another advantage will be the enablement of the classification of classes of various particle physics models under different symmetries. As Galileo's telescope was the breakthrough apparatus in astronomy, our vision is for Galileo to play the same role in theoretical particle physics.

In this article, we concentrate only on the computer algebra system that automatically generates Lagrangians, especially its singlet generator. In modern particle physics, the Lagrangian is usually characterized by the symmetry under certain gauge groups. To make sure that the symmetry is not broken, each term in the Lagrangian has be singlet under the gauge groups. The ability to form singlets depend on the representations chosen for the fields. The computer algebra package has to then be able to generate various representations and form singlets using those representations. The details of this singlet generation is the focus of the next section.

8.2 SINGLET GENERATION ALGORITHM

The gauge groups we are interested in and the ones proven to be physically viable so far are the Lie groups. Galileo has the ability to generate all semisimple compact Lie groups' representations. In the following discussion I will show how the algorithm generates singlets using a concrete example of SU(2) representations.

Given say two representations (reps for short) of SU(2), *e.g.* isospin-1 representations of the SU(2) group, we would like to find the singlet combination of these two reps. For concreteness we will label the first representation $|j_1, m_1\rangle,\ j_1 = 1,\ m_1 = -1, 0, 1$ and the second $|j_2, m_2\rangle,\ j_2 = 1,\ m_2 = -1, 0, 1$. Here, $j_{1,2}$ label the representations and $m_{1,2}$ denote the weight of a specific state in the corresponding representation.

- The first step in calculating the singlet between j_1 and j_2 is to generate the most generic tensor product of the two representations that has zero weight. A tensor product of the two will be denoted $|j_1, m_1\rangle_1 \otimes |j_2, m_2\rangle_2$ and its weight is $m_1 + m_2$.

The most generic zero weight tensor product of $j_1 \otimes j_2$ is then $A|1,1\rangle_1 \otimes |1,-1\rangle_2 + B|1,0\rangle_1 \otimes |1,0\rangle_2 + C|1,-1\rangle_1 \otimes |1,1\rangle_2$ (to reduce clutter, the tensor product symbol $\otimes$ will be dropped in the following discussion). Note that in certain cases such combination might not exist, for example if $j_1 = 1$ and $j_2 = \frac{1}{2}$, $m_1 + m_2 \neq 0$ for any combinations of $m_1 = -1, 0, 1$ and $m_2 = \pm\frac{1}{2}$. In this case the algorithm will return an error.

- Next, we utilize the fact that applications of raising or lowering operators [77] on a singlet state annihilate the state $J_\pm|0,0\rangle = 0$. For isospins of SU(2), the raising and lowering operators are $J_\pm|j,m\rangle = \sqrt{(j \mp m)(j \pm m + 1)}|j, m \pm 1\rangle$. For a tensor product, they are simply given by $J_{1\otimes2\pm} = J_{1\pm} + J_{2\pm}$. Here we have the freedom to choose between the raising and lowering operators. Our strategy will be to use one to calculate the singlet and the other to verify the result. For this example we use the lowering operator to calculate the singlet

$$(J_{1-} + J_{2-})(A|1,1\rangle_1|1,-1\rangle_2 + B|1,0\rangle_1|1,0\rangle_2 + C|1,-1\rangle_1|1,1\rangle_2) \;=\; 0. \tag{8.1}$$

The first term gives

$$\begin{aligned}(J_{1-} + J_{2-})(A|1,1\rangle_1|1,-1\rangle_2) &= (J_{1-}A|1,1\rangle_1)|1,-1\rangle_2 + A|1,1\rangle_1(J_{2-}|1,-1\rangle_2) \\ &= \sqrt{2}A|1,0\rangle_1|1,-1\rangle_2 + A|1,1\rangle_1(0) \\ (J_{1-} + J_{2-})(A|1,1\rangle_1|1,-1\rangle_2) &= \sqrt{2}A|1,0\rangle_1|1,-1\rangle_2\end{aligned} \tag{8.2}$$

The second term gives

$$\begin{aligned}(J_{1-} + J_{2-})(B|1,0\rangle_1|1,0\rangle_2) &= (J_{1-}B|1,0\rangle_1)|1,0\rangle_2 + B|1,0\rangle_1(J_{2-}|1,0\rangle_2) \\ &= \sqrt{2}B|1,-1\rangle_1|1,0\rangle_2 + \sqrt{2}B|1,0\rangle_1|1,-1\rangle_2\end{aligned} \tag{8.3}$$

While the third gives

$$\begin{aligned}(J_{1-} + J_{2-})(C|1,-1\rangle_1|1,1\rangle_2) &= (J_{1-}C|1,-1\rangle_1)|1,1\rangle_2 + C|1,-1\rangle_1(J_{2-}|1,1\rangle_2) \\ &= C(0)|1,-1\rangle_2 + \sqrt{2}C|1,-1\rangle_1|1,0\rangle_2 \\ (J_{1-} + J_{2-})(A|1,1\rangle_1|1,-1\rangle_2) &= \sqrt{2}C|1,-1\rangle_1|1,0\rangle_2\end{aligned} \tag{8.4}$$

Combining everything together results in

$$\begin{aligned}\sqrt{2}A|1,0\rangle_1|1,-1\rangle_2 + \sqrt{2}B|1,-1\rangle_1|1,0\rangle_2 & \\ +\sqrt{2}B|1,0\rangle_1|1,-1\rangle_2 + \sqrt{2}C|1,-1\rangle_1|1,0\rangle_2 &= 0\end{aligned} \tag{8.5}$$

- Now comes the punchline, $|1,0\rangle_1|1,-1\rangle_2$ is linearly independent of $|1,-1\rangle_1|1,0\rangle_2$, thus we can collect the coefficients based on these two states. In this way we will get two *linear* equations, one for $|1,0\rangle_1|1,-1\rangle_2$ and another for $|1,-1\rangle_1|1,0\rangle_2$ with three unknowns A, B, and C. However, we can reduce the number independent coefficients by realizing that one of them (either A, B, or C) determines the overall normalization. Therefore we will scale the coefficients by $A \to \tilde{B} = B/A,\ \tilde{C} = C/A$. The system of linear equations we need to solve is then

$$\begin{aligned} A(\sqrt{2}+\sqrt{2}\tilde{B})|1,0\rangle_1|1,-1\rangle_2 &= 0 \\ A(\sqrt{2}\tilde{B}+\sqrt{2}\tilde{C})|1,-1\rangle_1|1,0\rangle_2 &= 0 \\ \to 1+\tilde{B} &= 0,\ \tilde{B}=-1 \\ \tilde{B}+\tilde{C} &= 0,\ \tilde{C}=-B=1 \end{aligned} \tag{8.6}$$

- Finally, the singlet combination is given by

$$A\left(|1,1\rangle_1|1,-1\rangle_2 - |1,0\rangle_1|1,0\rangle_2 + |1,-1\rangle_1|1,1\rangle_2\right) \tag{8.7}$$

  requiring the overall normalization to be 1 sets $A = \frac{1}{\sqrt{3}}$.

To verify the result we apply the raising operator $J_{1\otimes 2+} = J_{1+} + J_{2+}$ on the singlet state and see if we get zero

$$(J_{1+}+J_{2+})(|1,1\rangle_1|1,-1\rangle_2 - |1,0\rangle_1|1,0\rangle_2 + |1,-1\rangle_1|1,1\rangle_2) \overset{?}{=} 0. \tag{8.8}$$

The first term gives

$$\begin{aligned} (J_{1+}+J_{2+})|1,1\rangle_1|1,-1\rangle_2 &= (J_{1+}|1,1\rangle_1)|1,-1\rangle_2 + |1,1\rangle_1(J_{2+}|1,-1\rangle_2) \\ &= (0)|1,-1\rangle_2 + \sqrt{2}|1,1\rangle_1|1,0\rangle_2 \\ (J_{1+}+J_{2+})|1,1\rangle_1|1,-1\rangle_2 &= \sqrt{2}|1,1\rangle_1|1,0\rangle_2 \end{aligned} \tag{8.9}$$

The second gives

$$\begin{aligned} -(J_{1+}+J_{2+})|1,0\rangle_1|1,0\rangle_2 &= -(J_{1+}|1,0\rangle_1)|1,0\rangle_2 - |1,0\rangle_1(J_{2+}|1,0\rangle_2) \\ &= -\sqrt{2}|1,1\rangle_1|1,0\rangle_2 - \sqrt{2}|1,0\rangle_1|1,1\rangle_2 \end{aligned} \tag{8.10}$$

While the last is

$$\begin{aligned}(J_{1+}+J_{2+})|1,-1\rangle_1|1,1\rangle_2 &= (J_{1+}|1,-1\rangle_1)|1,1\rangle_2+|1,-1\rangle_1(J_{2+}|1,1\rangle_2)\\ &= \sqrt{2}|1,0\rangle_1|1,1\rangle_2+|1,-1\rangle_2(0)\\ (J_{1+}+J_{2+})|1,0\rangle_1|1,1\rangle_2 &= \sqrt{2}|1,0\rangle_1|1,1\rangle_2\end{aligned} \tag{8.11}$$

Combining all three terms we get

$$\begin{aligned}\sqrt{2}|1,1\rangle_1|1,0\rangle_2-\sqrt{2}|1,1\rangle_1|1,0\rangle_2&\\ -\sqrt{2}|1,0\rangle_1|1,1\rangle_2+\sqrt{2}|1,0\rangle_1|1,1\rangle_2 &= 0\end{aligned} \tag{8.12}$$

Thus the coefficients $A=\frac{1}{\sqrt{3}},\ \tilde{B}=-1,\ \tilde{C}=1$ do give a singlet combination.

For this particular example, we will get the exact same system of linear equations had we used the raising operator to calculate the singlet. This is not always the case, as will be shown later. Applying the raising operator on the zero weight state gives

$$(J_{1+}+J_{2+})(A|1,1\rangle_1|1,-1\rangle_2+B|1,0\rangle_1|1,0\rangle_2+C|1,-1\rangle_1|1,1\rangle_2) = 0 \tag{8.13}$$

The calculation of each term is similar

$$\begin{aligned}(J_{1+}+J_{2+})(A|1,1\rangle_1|1,-1\rangle_2) &= (J_{1+}A|1,1\rangle_1)|1,-1\rangle_2+A|1,1\rangle_1(J_{2+}|1,-1\rangle_2)\\ &= \sqrt{2}A|1,1\rangle_1|1,0\rangle_2\\ (J_{1+}+J_{2+})(B|1,0\rangle_1|1,0\rangle_2) &= (J_{1+}B|1,0\rangle_1)|1,0\rangle_2+B|1,0\rangle_1(J_{2+}|1,0\rangle_2)\\ &= \sqrt{2}B|1,1\rangle_1|1,0\rangle_2+\sqrt{2}B|1,0\rangle_1|1,1\rangle_2\\ (J_{1+}+J_{2+})(C|1,-1\rangle_1|1,1\rangle_2) &= (J_{1+}C|1,-1\rangle_1)|1,1\rangle_2+C|1,-1\rangle_1(J_{2+}|1,1\rangle_2)\\ &= \sqrt{2}C|1,0\rangle_1|1,1\rangle_2\end{aligned} \tag{8.14}$$

Producing the following linear equations

$$\begin{aligned}A(\sqrt{2}+\sqrt{2}\tilde{B})|1,1\rangle_1|1,0\rangle_2 &= 0\\ A(\sqrt{2}\tilde{B}+\sqrt{2}\tilde{C})|1,0\rangle_1|1,1\rangle_2 &= 0\end{aligned} \tag{8.15}$$

which is the exact same system of linear equations as Eq. 8.6 and thus gives the same values of $A=\frac{1}{\sqrt{3}},\ \tilde{B}=-1,\ \tilde{C}=1$. Note that the raising operator produces different states than the lowering one but they both give the same system of linear equations, and that is what we are after, the solution of which determines the coefficients.

Another example to further illustrate the singlet generating algorithm will be that of $j_1 = 1,\ j_2 = \frac{1}{2},\ j_3 = \frac{1}{2}$. For simplicity, I will denote the tensor product state as $|m_1, m_2, m_3\rangle,\ m_1 = -1, 0, 1,\ m_2 = \pm\frac{1}{2},\ m_3 = \pm\frac{1}{2}$ and its weight is $m_1 + m_2 + m_3$.

The most generic combination with zero weight is given by

$$A|1, -\tfrac{1}{2}, -\tfrac{1}{2}\rangle + B|0, -\tfrac{1}{2}, \tfrac{1}{2}\rangle + C|0, \tfrac{1}{2}, -\tfrac{1}{2}\rangle + D| - 1, \tfrac{1}{2}, \tfrac{1}{2}\rangle. \tag{8.16}$$

The system of linear equations induced by the application of the lowering operator is

$$\begin{aligned}(\sqrt{2}A + B + C)|0, -\tfrac{1}{2}, -\tfrac{1}{2}\rangle &= 0\\ (\sqrt{2}B + D)| - 1, \tfrac{1}{2}, -\tfrac{1}{2}\rangle &= 0\\ (\sqrt{2}C + D)| - 1, -\tfrac{1}{2}, \tfrac{1}{2}\rangle &= 0\end{aligned} \tag{8.17}$$

while the raising operator will produce

$$\begin{aligned}(\sqrt{2}D + B + C)|0, \tfrac{1}{2}, \tfrac{1}{2}\rangle &= 0\\ (\sqrt{2}C + A)|1, \tfrac{1}{2}, -\tfrac{1}{2}\rangle &= 0\\ (\sqrt{2}B + A)|1, -\tfrac{1}{2}, \tfrac{1}{2}\rangle &= 0\end{aligned} \tag{8.18}$$

In this case, the raising operator generates a seemingly different system of linear equations. However, we will need to check whether they produce different solutions.

We will again pull out A as the overall normalization $\tilde{B} = B/A,\ \tilde{C} = C/A,\ \tilde{D} = D/A$, for the first system of linear equations we get

$$\begin{aligned}\sqrt{2} + \tilde{B} + \tilde{C} &= 0\\ \sqrt{2}\tilde{B} + \tilde{D} &= 0\\ \sqrt{2}\tilde{C} + \tilde{D} &= 0\\ \rightarrow \tilde{B} &= -\tfrac{1}{\sqrt{2}},\ \tilde{C} = -\tfrac{1}{\sqrt{2}},\ \tilde{D} = 1\end{aligned} \tag{8.19}$$

while for the second one we get

$$\begin{aligned}\sqrt{2}\tilde{D} + \tilde{B} + \tilde{C} &= 0\\ \sqrt{2}\tilde{C} + 1 &= 0\\ \sqrt{2}\tilde{B} + 1 &= 0\\ \rightarrow \tilde{B} &= -\tfrac{1}{\sqrt{2}},\ \tilde{C} = -\tfrac{1}{\sqrt{2}},\ \tilde{D} = 1\end{aligned} \tag{8.20}$$

Here we see that despite the apparent difference of the system of linear equations, the solutions are the same. The singlet state (normalized to 1) is thus given by

$$\tfrac{1}{\sqrt{3}}(|1,-\tfrac{1}{2},-\tfrac{1}{2}\rangle - \tfrac{1}{\sqrt{2}}|0,-\tfrac{1}{2},\tfrac{1}{2}\rangle - \tfrac{1}{\sqrt{2}}|0,\tfrac{1}{2},-\tfrac{1}{2}\rangle + |-1,\tfrac{1}{2},\tfrac{1}{2}\rangle). \tag{8.21}$$

In this case the algorithm will return $A = \frac{1}{\sqrt{3}}$, $\tilde{B} = \tilde{C} = -\frac{1}{\sqrt{2}}$, $\tilde{D} = 1$. This example shows that the choice of raising or lowering operator makes no difference in the solution, which is generally true.

For groups other than the SU(2), the weight is represented by a tuplet instead of just a single number, *e.g.* for SU(3) the weight of a state is characterized by two numbers (w_1, w_2) and for E6, the weight is a tuplet of six numbers. A tensor product of two SU(3) reps therefore will look like $|(u_1, u_2)_1, (w_1, w_2)_2\rangle$, its corresponding weight is $(u_1 + w_1, u_2 + w_2)$. An SU(3) zero weight state then has both $u_1 + w_1 = 0$ *and* $u_2 + w_2 = 0$. In spite of this extra complication, the algorithm for generating singlets stays the same.

In both examples shown above, there was only one singlet combination. However, there are many cases where a tensor product of representations result in multiple singlets. An instructive example of this would be the combination of four isospin-$\frac{1}{2}$ representations of the SU(2) group, $j_1 = j_2 = j_3 = j_4 = \frac{1}{2}$. For simplicity, the tensor product state of these representations will be denoted by $|m_1 m_2 m_3 m_4\rangle$ with $m_{1,2,3,4} = \pm$, where $\pm$ stand for $\pm\frac{1}{2}$. The most generic zero weight tensor product state is then

$$C_0|{+}{+}{-}{-}\rangle + C_1|{+}{-}{+}{-}\rangle + C_2|{+}{-}{-}{+}\rangle + C_3|{-}{+}{+}{-}\rangle + C_4|{-}{+}{-}{+}\rangle + C_5|{-}{-}{+}{+}\rangle. \tag{8.22}$$

Application of the lowering operator generates the following system of linear equations

$$(C_0 + C_3 + C_4)|-+--\rangle = 0 \tag{8.23}$$

$$(C_0 + C_1 + C_2)|+---\rangle = 0 \tag{8.24}$$

$$(C_1 + C_3 + C_5)|--+-\rangle = 0 \tag{8.25}$$

$$(C_2 + C_4 + C_5)|---+\rangle = 0 \tag{8.26}$$

or in matrix form

$$\begin{pmatrix} 1 & 0 & 0 & 1 & 1 & 0 \\ 1 & 1 & 1 & 0 & 0 & 0 \\ 0 & 1 & 0 & 1 & 0 & 1 \\ 0 & 0 & 1 & 0 & 1 & 1 \end{pmatrix} \begin{pmatrix} C_0 \\ C_1 \\ C_2 \\ C_3 \\ C_4 \\ C_5 \end{pmatrix} = 0. \tag{8.27}$$

The first step is to make the matrix into an upper triangular form

$$\begin{pmatrix} 1 & 0 & 0 & 0 & 0 & -1 \\ 0 & 1 & 0 & 0 & -1 & 0 \\ 0 & 0 & 1 & 0 & 1 & 1 \\ 0 & 0 & 0 & 1 & 1 & 1 \end{pmatrix}. \tag{8.28}$$

At first this looks like a complete disaster as there are only four equations with six unknowns. However, the fact that there are more than one nonzero elements in the last row actually betokens the existence of more than one system of linear equations. In this particular example, three non zero elements in the last row translate to *two* unique systems of linear equations (which is consistent with results from SU(2) recoupling theory [78]). This example is crucial, as many other zero weight combinations produce a similar system of equations. To disentangle them we need to remove the last two columns one at a time

$$S_1 \rightarrow \begin{pmatrix} 1 & 0 & 0 & 0 & -1 \\ 0 & 1 & 0 & 0 & 0 \\ 0 & 0 & 1 & 0 & 1 \\ 0 & 0 & 0 & 1 & 1 \end{pmatrix} \begin{pmatrix} C_0 \\ C_1 \\ C_2 \\ C_3 \\ C_5 \end{pmatrix} = 0 \quad S_2 \rightarrow \begin{pmatrix} 1 & 0 & 0 & 0 & 0 \\ 0 & 1 & 0 & 0 & -1 \\ 0 & 0 & 1 & 0 & 1 \\ 0 & 0 & 0 & 1 & 1 \end{pmatrix} \begin{pmatrix} C_0 \\ C_1 \\ C_2 \\ C_3 \\ C_4 \end{pmatrix} = 0 \tag{8.29}$$

Removing a column equals to setting the coefficient associated with it to zero, *e.g.* removing the sixth column sets $C_5 = 0$. We denote the first system of equations S_1 and the second S_2. Both S_1 and S_2 exhibit the same structure as our first example of two isospin-1 representations. In each, there are five unknowns and four equations. One of the unknowns can be used to set the overall normalization. For simplicity, instead of pulling out a coefficient, we will just set one coefficient to 1 and normalize the singlet at the end of the calculation. For S_1 we set $C_5 = 1$ while in S_2 we set $C_4 = 1$. Remember that the removal of one of the columns already set $C_4 = 0$ for S_1 and $C_5 = 0$ for S_2. The systems of equations then become

$$S_1 \rightarrow \begin{array}{rcl} C_0 - 1 & = & 0 \\ C_1 & = & 0 \\ C_2 + 1 & = & 0 \\ C_3 + 1 & = & 0 \end{array} \qquad S_2 \rightarrow \begin{array}{rcl} C_0 & = & 0 \\ C_1 - 1 & = & 0 \\ C_2 + 1 & = & 0 \\ C_3 + 1 & = & 0 \end{array} \tag{8.30}$$

which yield the following sets of solutions, $C_0 = 1,\ C_1 = 0,\ C_2 = -1,\ C_3 = -1,\ C_4 = 0,\ C_5 = 1$ for S_1 and $C_0 = 0,\ C_1 = 1,\ C_2 = -1,\ C_3 = -1,\ C_4 = 1,\ C_5 = 0$ for S_2. Thus, the (unnormalized) singlet combinations are

$$\begin{aligned} S_1 &\rightarrow |++--\rangle - |+--+\rangle - |-++-\rangle + |--++\rangle \\ S_2 &\rightarrow |+-+-\rangle - |+--+\rangle - |-++-\rangle + |-+-+\rangle \end{aligned} \tag{8.31}$$

However, since each solution sets the original linear equations to zero, *i.e.*

$$S_1 \rightarrow \begin{pmatrix} 1 & 0 & 0 & 1 & 1 & 0 \\ 1 & 1 & 1 & 0 & 0 & 0 \\ 0 & 1 & 0 & 1 & 0 & 1 \\ 0 & 0 & 1 & 0 & 1 & 1 \end{pmatrix} \begin{pmatrix} 1 \\ 0 \\ -1 \\ -1 \\ 0 \\ 1 \end{pmatrix} = 0 \qquad S_2 \rightarrow \begin{pmatrix} 1 & 0 & 0 & 1 & 1 & 0 \\ 1 & 1 & 1 & 0 & 0 & 0 \\ 0 & 1 & 0 & 1 & 0 & 1 \\ 0 & 0 & 1 & 0 & 1 & 1 \end{pmatrix} \begin{pmatrix} 0 \\ 1 \\ -1 \\ -1 \\ 1 \\ 0 \end{pmatrix} = 0 \tag{8.32}$$

we can always add the solution of S_1 to that of S_2 to get another solution that we will denote S_{12}. The actual singlets that are generated by Galileo are those of S_1 and S_{12}, the normalized singlets combinations are then

$$\begin{aligned} S_1 &\rightarrow \frac{1}{2}(|++--\rangle - |+--+\rangle - |-++-\rangle + |--++\rangle) \\ S_{12} &\rightarrow \frac{1}{2\sqrt{3}}(|++--\rangle + |+-+-\rangle - 2|+--+\rangle \\ &\qquad - 2|-++-\rangle + |-+-+\rangle + |--++\rangle) \end{aligned} \tag{8.33}$$

The reason for this choice of solutions is solely to maximize computational efficiency.

Another example of multiple singlet combinations is that of three adjoint reps of SU(3). In this case there are two singlets. The tensor product of the three reps that has zero weight possesses fifty five different coefficients, too many to use as a complete example. The first few terms of the first singlet state are as follows

$$\begin{aligned}&\tfrac{1+\sqrt{3}}{\sqrt{3}}|(1,1)_1,(0,0)_2,(-1,-1)_3\rangle-\sqrt{2}|(1,1)_1,(1,-2)_2,(-2,1)_3\rangle\\&-\tfrac{1}{\sqrt{2}}|(1,1)_1,(-2,1)_2,(1,-2)_3\rangle+|(1,1)_1,(-1,-1)_2,(0,0)_3\rangle+...\end{aligned}\tag{8.34}$$

while the first few terms of the second singlet state are as follows

$$\begin{aligned}&\tfrac{5+\sqrt{3}}{2\sqrt{3}}|(1,1)_1,(0,0)_2,(-1,-1)_3\rangle-\sqrt{2}|(1,1)_1,(1,-2)_2,(-2,1)_3\rangle\\&-\tfrac{1+\sqrt{3}}{\sqrt{2}}|(1,1)_1,(-2,1)_2,(1,-2)_3\rangle+2|(1,1)_1,(-1,-1)_2,(0,0)_3\rangle+...\end{aligned}\tag{8.35}$$

In summary, the algorithm to calculate singlet states is as follows

- From m representations input by the user, the singlet algorithm generates the most generic tensor product that has zero weight. In general, it has the form

$$\sum_{i=1}^{k} C_i|(u_{11},...,u_{n1}),...,(u_{1m},...,u_{nm})\rangle_i \tag{8.36}$$

  where $(u_{m1},...,u_{mn})$ is the weight of a state in the mth rep, $|(u_{11},...),...,(u_{1m},...)\rangle_i$ is the ith tensor product that has zero weight ($\sum\limits_{l=1}^{m} u_{jl}=0$, for each $j=1...n$) and C_i is its coefficient. For the two isospin-1 rep example shown above, $n=1$, $m=2$, $i=1,2,3$, and $C_1=A,\ C_2=B,\ C_3=C$. However, if a zero weight tensor product is not found, the algorithm will return an error.

- Next, apply the lowering operator (for a generic group we denote it E_- instead of J_-) on the zero weight tensor product and equate it to zero

$$E_-\left(\sum_{i=1}^{k} C_i|(u_{11},...,u_{n1}),...,(u_{1m},...,u_{nm})\rangle_i\right)=0. \tag{8.37}$$

- The above procedure generates, in general, systems of linear equations

$$f_p^{(q)}(C_1,C_2,...,C_k)(E_-|(u_{11},...,u_{n1}),...,(u_{1m},...,u_{nm})\rangle_i)_p=0 \tag{8.38}$$

  where each $f_p^{(q)}$ is a linear function of C_i, $p=1,..,k-1$ and $q=1,..,r$ if there are r distinct systems of linear equations.

- The solution $(C_1^{(q)}, C_2^{(q)}, ..., C_k^{(q)})$ of each system of linear equations $f_p^{(q)}(C_1^{(q)}, ..., C_k^{(q)}) = 0$ determines a unique singlet

  $$|0\rangle^{(q)} = \sum_{i=1}^{k} C_i^{(q)} |(u_{11}, ..., u_{n1}), ..., (u_{1m}, ..., u_{nm})\rangle_i, \tag{8.39}$$

  there are thus q different singlets.
- Lastly, each singlet is verified by applying the raising operator $E_+|0\rangle^{(q)} = 0$.

8.3 MODEL BUILDING

We have now come to the core of Galileo, automated Lagrangian generation. The singlet algorithm discussed above is its main component in generating the interaction terms. However, there is an additional ingredient needed. For a Lagrangian to be invariant, each term has to be a singlet under all of its symmetry groups be it local or global. The essential symmetry group in quantum field theory is obviously the Lorentz group.

As of now Galileo employs a different mechanism to generate the Lorentz singlets from those of the gauge groups even though the Lorentz group can be identified as SU(2) × SU(2). One of the reasons for this is speed, another is the fact that most Lorentz singlets can be identified immediately, for example, for a product of tensor fields to be invariant, all Lorentz indices must be contracted. There is also a Z_2 discrete symmetry group incorporated in Galileo.

As for now, the symmetry groups supported by Galileo are

1. Supersymmetry, $N = 1$.
2. Compact semisimple Lie groups, they are U(1), AN:SU(N), BN:SO(2N+1), CN:SP(2N), DN:SO(2N), G2, F4, E6, E7, E8.
3. Lorentz group.
4. Z_2 discrete group under fundamental representation.

To build a model, users need to input the maximum number of mass dimensions of the interaction terms, the local and global symmetry groups (continuous, discrete or super), the number of fields and their representations as well as their spins (and handedness for spin-$\frac{1}{2}$ fermions). Lorentz invariance is always assumed. Galileo would then used the information provided to generate the most generic Lagrangian that is invariant under the specified symmetries. Four, five, and six maximum mass dimensions for the interaction terms are supported to accommodate the construction of effective Lagrangians.

The terms of the Lagrangian fall into two distinct categories, kinetic and interaction terms. The construction of the kinetic terms is as follow

1. If supersymmetry is specified, the kinetic terms are generated using the superfield formalism through chiral and vector superfields, *i.e.* $\int d^2\theta d^2\overline{\theta}\ \Phi^\dagger e^V \Phi$.
2. If there is any local gauge group specified by the user, then spacetime derivatives will be promoted to covariant derivatives, $\partial_\mu \to D_\mu$.
3. Kinetic terms of gauge bosons are given by the standard formulae $\text{Tr}(F_{\mu\nu}F^{\mu\nu})$ and $\text{Tr}(F_{\mu\nu}\widetilde{F}^{\mu\nu})$, $\widetilde{F}^{\mu\nu} = \epsilon^{\mu\nu\rho\sigma}F_{\rho\sigma}$.
4. Fermionic kinetic terms are also given by the standard formula $\overline{\Psi}\gamma^\mu D_\mu \Psi$.
5. Scalar field kinetic terms are $(D_\mu\phi)^\dagger(D^\mu\phi)$.
6. Kinetic terms must be invariant under global symmetry if any is specified.

Interaction terms are produced by generating all possible combinations of the fields up to the maximum mass dimension provided by the user. The next immediate step is to make sure that the interaction terms are Lorentz invariant. The following steps are employed to ensure Lorentz invariance

1. If a term is made purely of bosons, all of its Lorentz indices must be fully contracted among themselves.
2. Galileo handles spin-$\frac{1}{2}$ fermions using 4-component Dirac spinors. They are categorized by their chirality, *i.e.* a spinor is either left or right handed. Furthermore, only bilinears of spinors are allowed in the Lagrangian, since the chirality is explicitly specified, pseudo bilinears are automatically included. The rules for bilinears are as follows
    - One of the two spinors in a bilinear must be conjugated, $\overline{\Psi}\Psi$, $\overline{\Psi} = \Psi^\dagger\gamma^0$.

- Gamma matrices can be inserted in a bilinear, *e.g.* $\overline{\Psi}\gamma^\mu\Psi$. We limit the maximum number of gamma matrices in a bilinear to three. The only combinations of gamma matrices in a bilinear used by Galileo are $\sigma^{\mu\nu} = \frac{i}{4}[\gamma^\mu, \gamma^\nu]$, $\gamma^\mu\gamma^\nu$, and $\sigma^{\mu\nu}\gamma^\rho$.
- Derivatives can also be inserted inside a bilinear as long as the Lorentz indices of the derivatives are contracted, *e.g.* $\overline{\Psi}\gamma^\mu D_\mu\Psi$.
- A bilinear with an even number of gamma matrices can only be formed by a right and left handed spinors, *e.g.* $\overline{L}R$, $\overline{R}L$ or a spinor and a charge conjugated spinor of the same handedness, *e.g.* $\overline{L}^c L$, $\overline{R}^c R$.
- A bilinear with an odd number of gamma matrices must be formed by spinors of the same handedness, *e.g.* $\overline{L}\gamma^\mu L$, $\overline{R}\gamma^\mu R$ or a spinor and a charge conjugated spinor of the opposite handedness, *e.g.* $\overline{L}^c\gamma^\mu R$, $\overline{R}^c\gamma^\mu L$, $\overline{L}^c\gamma^\mu D_\mu R$, $\overline{R}^c\gamma^\mu D_\mu L$. The complete list of bilinears is shown in Table. 9.

3. Terms made purely of fermions must be formed only by bilinears and there must be no free Lorentz index.
4. Terms with combinations of bosons and fermions must be formed using bilinears explained above and all of its Lorentz indices must be contracted among the bosons and the bilinears.

Once all Lorentz invariant terms are produced, they are filtered using the local, global, super and discrete symmetries. Any term that is not invariant under any of the symmetries provided by the user is thrown away. For Lie groups (local and global), Galileo uses the singlet algorithm discussed in details in the previous section to check whether or not an interaction term is invariant. For the Z_2 discrete group, the filtering is trivial, any interaction term must have a parity of $+1$. For supersymmetry, Galileo employs the superfield formalism. Thus any holomorphic function of chiral superfields are automatically supersymmetric invariant.

8.4 EXAMPLES

In this section we will present a few examples of Lagrangians that were automatically generated by Galileo. First is the Standard Model with terms up to four mass dimensions for

Table 9: The list of all bilinears generated by Galileo.

Term	Bilinear Type
$\overline{L}R$, $\overline{L}^c L$	scalar
$\overline{R}L$, $\overline{R}^c R$	scalar
$\overline{L}\gamma^\mu L$, $\overline{L}^c\gamma^\mu R$	vector
$\overline{R}\gamma^\mu R$, $\overline{R}^c\gamma^\mu L$	vector
$\overline{L}\gamma^\mu D_\mu L$, $\overline{L}\gamma^\mu D_\mu R^c$	scalar
$\overline{R}\gamma^\mu D_\mu R$, $\overline{R}\gamma^\mu D_\mu L^c$	scalar
$\overline{L}\sigma^{\mu\nu} R$, $\overline{L}^c\sigma^{\mu\nu} L$	tensor
$\overline{R}\sigma^{\mu\nu} L$, $\overline{R}^c\sigma^{\mu\nu} R$	tensor
$\overline{L}\gamma^\nu\gamma^\mu D_\mu R$, $\overline{L}\gamma^\nu\gamma^\mu D_\mu L^c$	vector
$\overline{R}\gamma^\nu\gamma^\mu D_\mu L$, $\overline{R}\gamma^\nu\gamma^\mu D_\mu R^c$	vector
$\overline{L}\sigma^{\mu\nu}\gamma^\rho D_\rho L$, $\overline{L}\sigma^{\mu\nu}\gamma^\rho D_\rho R^c$	tensor
$\overline{R}\sigma^{\mu\nu}\gamma^\rho D_\rho R$, $\overline{R}\sigma^{\mu\nu}\gamma^\rho D_\rho L^c$	tensor

a single family of quarks and leptons before the spontaneous symmetry breaking. Fig. 43 shows the web interface and the Lagrangian produced by Galileo. At the top of the page is a box with the local Lie groups, SU(3) × SU(2) × U(1) which characterize the standard model. Below it is the matter content, S stands for scalar fields, F fermions and V vector fields. The bottom and biggest box contains the Lagrangian. The Lagrangian shown in Fig. 43 also includes the dual field strength tensors as well. Fig. 44 shows the Lagrangian for a standard model with two higgs bosons with interaction terms up to four spacetime dimensions.

Fig. 45 shows a Lagrangian of MSSM in 4 spacetime dimensions with 2 Higgs scalar fields produced by Galileo. It has the same gauge symmetry as the standard model. The Lagrangian are defined using the superfields formalism, Φ denotes chiral superfields.

8.5 CONCLUSION

Galileo is a computer algebra package that aims to simplify the generation and testing of new particle physics model, *i.e.* it is the ultimate model builder package. Simply by specifying the symmetry groups and matter content, all interaction terms are automatically generated, including effective Lagrangian ones. This is of great help since for example Lorentz invariant terms built up out of vectors, fermions and scalars contain 193 distinct combinations.

A graphical user interface (GUI) accessible through the web has also been developed by Daniel Salmon. There are still things that need to be implemented. One is a pipeline to Feynrules, a package that automatically generates the Feynman rules of a Lagrangian, two, a very important element that is still missing is spontaneous symmetry breaking.

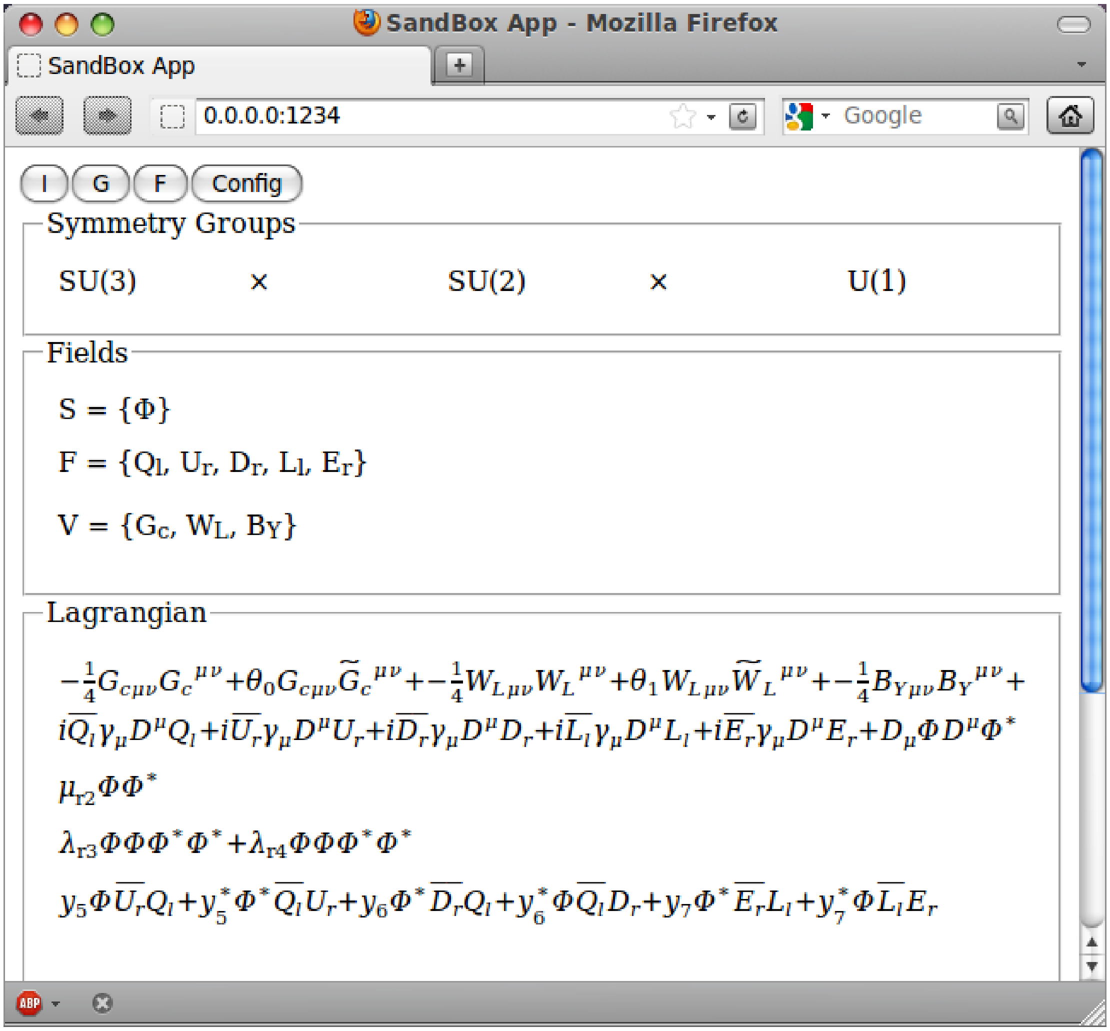

Symmetry Groups

SU(3) × SU(2) × U(1)

Fields

S = {Φ}

F = {Q_l, U_r, D_r, L_l, E_r}

V = {G_c, W_L, B_Y}

Lagrangian

$$-\tfrac{1}{4}G_{c\mu\nu}G_c{}^{\mu\nu}+\theta_0 G_{c\mu\nu}\widetilde{G}_c{}^{\mu\nu}+-\tfrac{1}{4}W_{L\mu\nu}W_L{}^{\mu\nu}+\theta_1 W_{L\mu\nu}\widetilde{W}_L{}^{\mu\nu}+-\tfrac{1}{4}B_{Y\mu\nu}B_Y{}^{\mu\nu}+$$

$$i\overline{Q_l}\gamma_\mu D^\mu Q_l+i\overline{U_r}\gamma_\mu D^\mu U_r+i\overline{D_r}\gamma_\mu D^\mu D_r+i\overline{L_l}\gamma_\mu D^\mu L_l+i\overline{E_r}\gamma_\mu D^\mu E_r+D_\mu\Phi D^\mu\Phi^*$$

$$\mu_{\mathrm{r}2}\Phi\Phi^*$$

$$\lambda_{\mathrm{r}3}\Phi\Phi\Phi^*\Phi^*+\lambda_{\mathrm{r}4}\Phi\Phi\Phi^*\Phi^*$$

$$y_5\Phi\overline{U_r}Q_l+y_5^*\Phi^*\overline{Q_l}U_r+y_6\Phi^*\overline{D_r}Q_l+y_6^*\Phi\overline{Q_l}D_r+y_7\Phi^*\overline{E_r}L_l+y_7^*\Phi\overline{L_l}E_r$$

Figure 43: GUI and the standard model Lagrangian with one Higgs field produced by Galileo.

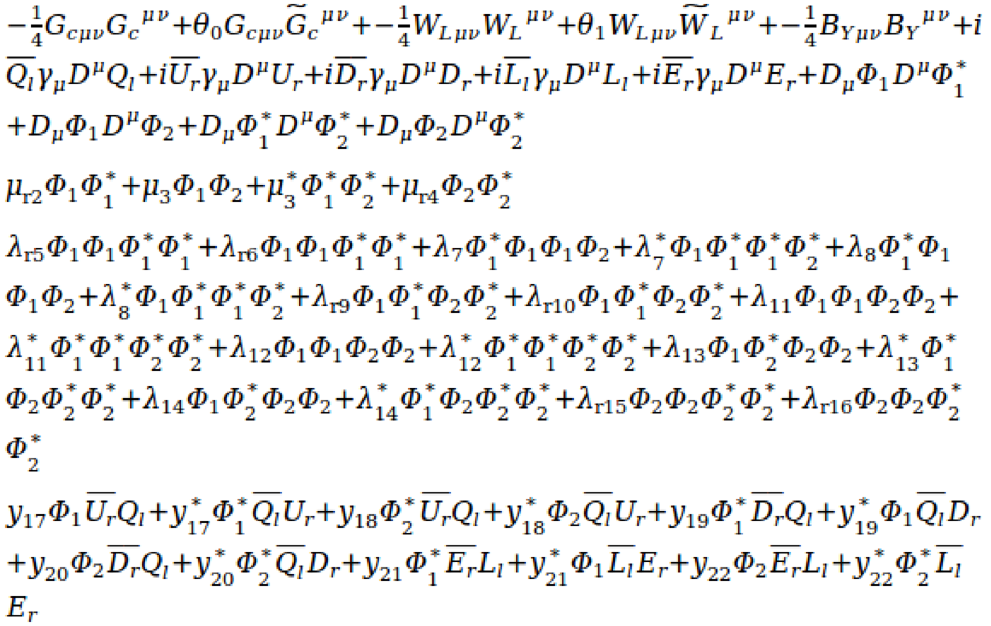

$$-\tfrac{1}{4}G_{c\mu\nu}{G_c}^{\mu\nu}+\theta_0 G_{c\mu\nu}{\widetilde{G}_c}^{\mu\nu}+-\tfrac{1}{4}W_{L\mu\nu}{W_L}^{\mu\nu}+\theta_1 W_{L\mu\nu}{\widetilde{W}_L}^{\mu\nu}+-\tfrac{1}{4}B_{Y\mu\nu}{B_Y}^{\mu\nu}+i$$
$$\overline{Q_l}\gamma_\mu D^\mu Q_l+i\overline{U_r}\gamma_\mu D^\mu U_r+i\overline{D_r}\gamma_\mu D^\mu D_r+i\overline{L_l}\gamma_\mu D^\mu L_l+i\overline{E_r}\gamma_\mu D^\mu E_r+D_\mu\Phi_1 D^\mu\Phi^*_1$$
$$+D_\mu\Phi_1 D^\mu\Phi_2+D_\mu\Phi^*_1 D^\mu\Phi^*_2+D_\mu\Phi_2 D^\mu\Phi^*_2$$

$$\mu_{\mathrm{r}2}\Phi_1\Phi^*_1+\mu_3\Phi_1\Phi_2+\mu^*_3\Phi^*_1\Phi^*_2+\mu_{\mathrm{r}4}\Phi_2\Phi^*_2$$

$$\lambda_{\mathrm{r}5}\Phi_1\Phi_1\Phi^*_1\Phi^*_1+\lambda_{\mathrm{r}6}\Phi_1\Phi_1\Phi^*_1\Phi^*_1+\lambda_7\Phi^*_1\Phi_1\Phi_1\Phi_2+\lambda^*_7\Phi_1\Phi^*_1\Phi^*_1\Phi^*_2+\lambda_8\Phi^*_1\Phi_1$$
$$\Phi_1\Phi_2+\lambda^*_8\Phi_1\Phi^*_1\Phi^*_1\Phi^*_2+\lambda_{\mathrm{r}9}\Phi_1\Phi^*_1\Phi_2\Phi^*_2+\lambda_{\mathrm{r}10}\Phi_1\Phi^*_1\Phi_2\Phi^*_2+\lambda_{11}\Phi_1\Phi_1\Phi_2\Phi_2+$$
$$\lambda^*_{11}\Phi^*_1\Phi^*_1\Phi^*_2\Phi^*_2+\lambda_{12}\Phi_1\Phi_1\Phi_2\Phi_2+\lambda^*_{12}\Phi^*_1\Phi^*_1\Phi^*_2\Phi^*_2+\lambda_{13}\Phi_1\Phi^*_2\Phi_2\Phi_2+\lambda^*_{13}\Phi^*_1$$
$$\Phi_2\Phi^*_2\Phi^*_2+\lambda_{14}\Phi_1\Phi^*_2\Phi_2\Phi_2+\lambda^*_{14}\Phi^*_1\Phi_2\Phi^*_2\Phi^*_2+\lambda_{\mathrm{r}15}\Phi_2\Phi_2\Phi^*_2\Phi^*_2+\lambda_{\mathrm{r}16}\Phi_2\Phi_2\Phi^*_2$$
$$\Phi^*_2$$

$$y_{17}\Phi_1\overline{U_r}Q_l+y^*_{17}\Phi^*_1\overline{Q_l}U_r+y_{18}\Phi^*_2\overline{U_r}Q_l+y^*_{18}\Phi_2\overline{Q_l}U_r+y_{19}\Phi^*_1\overline{D_r}Q_l+y^*_{19}\Phi_1\overline{Q_l}D_r$$
$$+y_{20}\Phi_2\overline{D_r}Q_l+y^*_{20}\Phi^*_2\overline{Q_l}D_r+y_{21}\Phi^*_1\overline{E_r}L_l+y^*_{21}\Phi_1\overline{L_l}E_r+y_{22}\Phi_2\overline{E_r}L_l+y^*_{22}\Phi^*_2\overline{L_l}$$
$$E_r$$

Figure 44: GUI and the standard model Lagrangian with two Higgs fields produced by Galileo.

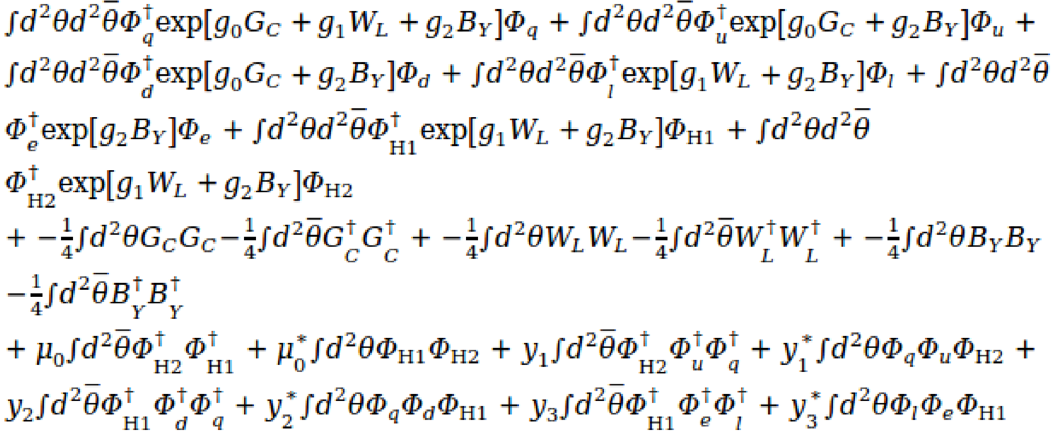

$$\int d^2\theta d^2\bar{\theta}\Phi^\dagger_q\exp[g_0G_C+g_1W_L+g_2B_Y]\Phi_q+\int d^2\theta d^2\bar{\theta}\Phi^\dagger_u\exp[g_0G_C+g_2B_Y]\Phi_u+$$
$$\int d^2\theta d^2\bar{\theta}\Phi^\dagger_d\exp[g_0G_C+g_2B_Y]\Phi_d+\int d^2\theta d^2\bar{\theta}\Phi^\dagger_l\exp[g_1W_L+g_2B_Y]\Phi_l+\int d^2\theta d^2\bar{\theta}$$
$$\Phi^\dagger_e\exp[g_2B_Y]\Phi_e+\int d^2\theta d^2\bar{\theta}\Phi^\dagger_{\mathrm{H1}}\exp[g_1W_L+g_2B_Y]\Phi_{\mathrm{H1}}+\int d^2\theta d^2\bar{\theta}$$
$$\Phi^\dagger_{\mathrm{H2}}\exp[g_1W_L+g_2B_Y]\Phi_{\mathrm{H2}}$$
$$+-\tfrac{1}{4}\int d^2\theta G_CG_C-\tfrac{1}{4}\int d^2\bar{\theta}G^\dagger_CG^\dagger_C+-\tfrac{1}{4}\int d^2\theta W_LW_L-\tfrac{1}{4}\int d^2\bar{\theta}W^\dagger_LW^\dagger_L+-\tfrac{1}{4}\int d^2\theta B_YB_Y$$
$$-\tfrac{1}{4}\int d^2\bar{\theta}B^\dagger_YB^\dagger_Y$$
$$+\mu_0\int d^2\bar{\theta}\Phi^\dagger_{\mathrm{H2}}\Phi^\dagger_{\mathrm{H1}}+\mu^*_0\int d^2\theta\Phi_{\mathrm{H1}}\Phi_{\mathrm{H2}}+y_1\int d^2\bar{\theta}\Phi^\dagger_{\mathrm{H2}}\Phi^\dagger_u\Phi^\dagger_q+y^*_1\int d^2\theta\Phi_q\Phi_u\Phi_{\mathrm{H2}}+$$
$$y_2\int d^2\bar{\theta}\Phi^\dagger_{\mathrm{H1}}\Phi^\dagger_d\Phi^\dagger_q+y^*_2\int d^2\theta\Phi_q\Phi_d\Phi_{\mathrm{H1}}+y_3\int d^2\bar{\theta}\Phi^\dagger_{\mathrm{H1}}\Phi^\dagger_e\Phi^\dagger_l+y^*_3\int d^2\theta\Phi_l\Phi_e\Phi_{\mathrm{H1}}$$

Figure 45: Minimal Supersymmetric Lagrangian up to 4 mass dimensions with 2 Higgs fields produced by Galileo.

APPENDIX

DERIVATION OF ANTLER KINEMATICAL VARIABLES

(i) $\cosh\eta_B^{(\text{c.m.})}$ *derivation:* A mother particle D which is at rest in the lab (and c.m.) frame decays to two daughters B. From conservation of momentum we get

$$\begin{aligned}
\begin{pmatrix}\sqrt{s}\\ \vec{0}\end{pmatrix} &= \begin{pmatrix}E_B\\ \vec{p}_B\end{pmatrix} + \begin{pmatrix}E_B\\ -\vec{p}_B\end{pmatrix}\\
\begin{pmatrix}\sqrt{s}\\ \vec{0}\end{pmatrix} &= \begin{pmatrix}2E_B\\ \vec{0}\end{pmatrix}\\
\rightarrow E_B &= \frac{\sqrt{s}}{2}
\end{aligned} \tag{A.1}$$

where $m_D = \sqrt{s}$.

In B's rest frame, its 4-momentum is just $p_B = (m_B, \vec{0})$. Boosting this 4-momentum into the lab's frame which is also D's rest frame yields

$$\begin{aligned}
\begin{pmatrix}E_B\\ p_B\end{pmatrix} &= \begin{pmatrix}\cosh\eta_B^{(\text{c.m.})} & -\sinh\eta_B^{(\text{c.m.})}\\ -\sinh\eta_B^{(\text{c.m.})} & \cosh\eta_B^{(\text{c.m.})}\end{pmatrix}\begin{pmatrix}m_B\\ 0\end{pmatrix}\\
\begin{pmatrix}E_B\\ p_B\end{pmatrix} &= \begin{pmatrix}m_B\cosh\eta_B^{(\text{c.m.})}\\ -m_B\sinh\eta_B^{(\text{c.m.})}\end{pmatrix}\\
\rightarrow \cosh\eta_B^{(\text{c.m.})} &= \frac{E_B}{m_B} = \frac{\sqrt{s}}{2m_B}
\end{aligned} \tag{A.2}$$

(*ii*) $\cosh\eta^{(B)}_{\tilde{\chi}^0_1}$, $\cosh\eta^{(B)}_a$ *derivation:* Each particle B then decays into a visible particle a and $\tilde{\chi}^0_1$. In B's rest frame this constitutes the following conservation of 4-momentum

$$\begin{aligned}\begin{pmatrix} m_B \\ \vec{0} \end{pmatrix} &= \begin{pmatrix} E_{\tilde{\chi}^0_1} \\ \vec{p}_{\tilde{\chi}^0_1} \end{pmatrix} + \begin{pmatrix} E_a \\ \vec{p}_a \end{pmatrix} \\ \rightarrow m_B &= E_{\tilde{\chi}^0_1} + E_a \\ |\vec{p}_{\tilde{\chi}^0_1}| &= |\vec{p}_a| \end{aligned} \tag{A.3}$$

From the on-shell condition

$$\begin{aligned} E^2_{\tilde{\chi}^0_1} &= |\vec{p}_{\tilde{\chi}^0_1}|^2 + m^2_{\tilde{\chi}^0_1} \rightarrow E_{\tilde{\chi}^0_1} = \sqrt{|\vec{p}_{\tilde{\chi}^0_1}|^2 + m^2_{\tilde{\chi}^0_1}} \\ E^2_a &= |\vec{p}_a|^2 + m^2_a \rightarrow E_a = \sqrt{|\vec{p}_a|^2 + m^2_a} \end{aligned} \tag{A.4}$$

we get

$$\begin{aligned} m_B &= E_{\tilde{\chi}^0_1} + E_a \\ E_a &= -E_{\tilde{\chi}^0_1} + m_B \\ \sqrt{|\vec{p}_a|^2 + m^2_a} &= -\sqrt{|\vec{p}_{\tilde{\chi}^0_1}|^2 + m^2_{\tilde{\chi}^0_1}} + m_B, \quad |\vec{p}_{\tilde{\chi}^0_1}| = |\vec{p}_a| \\ \left(\sqrt{|\vec{p}_a|^2 + m^2_a}\right)^2 &= \left(-\sqrt{|\vec{p}_a|^2 + m^2_{\tilde{\chi}^0_1}} + m_B\right)^2 \\ |\vec{p}_a|^2 + m^2_a &= |\vec{p}_a|^2 + m^2_{\tilde{\chi}^0_1} - 2m_B\sqrt{|\vec{p}_a|^2 + m^2_{\tilde{\chi}^0_1}} + m^2_B \\ m^2_a &= m^2_{\tilde{\chi}^0_1} - 2m_B\sqrt{|\vec{p}_a|^2 + m^2_{\tilde{\chi}^0_1}} + m^2_B \\ 2m_B\sqrt{|\vec{p}_a|^2 + m^2_{\tilde{\chi}^0_1}} &= m^2_{\tilde{\chi}^0_1} - m^2_a + m^2_B, \quad |\vec{p}_a| = |\vec{p}_{\tilde{\chi}^0_1}| \\ 2m_B\sqrt{|\vec{p}_{\tilde{\chi}^0_1}|^2 + m^2_{\tilde{\chi}^0_1}} &= m^2_{\tilde{\chi}^0_1} - m^2_a + m^2_B \\ 2m_B E_{\tilde{\chi}^0_1} &= m^2_{\tilde{\chi}^0_1} - m^2_a + m^2_B \\ E_{\tilde{\chi}^0_1} &= \frac{m^2_B + m^2_{\tilde{\chi}^0_1} - m^2_a}{2m_B} \end{aligned} \tag{A.5}$$

Similarly for E_a, by switching $\tilde{\chi}^0_1 \leftrightarrow a$ we get

$$E_a = \frac{m^2_B + m^2_a - m^2_{\tilde{\chi}^0_1}}{2m_B}. \tag{A.6}$$

In $\tilde{\chi}_1^0$'s rest frame, its 4-momentum is given by $(m_{\tilde{\chi}_1^0}, \vec{0})$, boosting it to B's rest frame we get

$$\begin{aligned}
\begin{pmatrix} E^{(B)}_{\tilde{\chi}_1^0} \\ p^{(B)}_{\tilde{\chi}_1^0} \end{pmatrix} &= \begin{pmatrix} \cosh\eta^{(B)}_{\tilde{\chi}_1^0} & -\sinh\eta^{(B)}_{\tilde{\chi}_1^0} \\ -\sinh\eta^{(B)}_{\tilde{\chi}_1^0} & \cosh\eta^{(B)}_{\tilde{\chi}_1^0} \end{pmatrix} \begin{pmatrix} m_{\tilde{\chi}_1^0} \\ 0 \end{pmatrix} \\
E^{(B)}_{\tilde{\chi}_1^0} &= m_{\tilde{\chi}_1^0} \cosh\eta^{(B)}_{\tilde{\chi}_1^0} \\
\frac{m_B^2 + m_{\tilde{\chi}_1^0}^2 - m_a^2}{2m_B} &= m_{\tilde{\chi}_1^0} \cosh\eta^{(B)}_{\tilde{\chi}_1^0} \\
\rightarrow \cosh\eta^{(B)}_{\tilde{\chi}_1^0} &= \frac{m_B^2 + m_{\tilde{\chi}_1^0}^2 - m_a^2}{2m_B m_{\tilde{\chi}_1^0}} \qquad \text{(A.7)}
\end{aligned}$$

Following the same procedure we get

$$\cosh\eta^{(B)}_a = \frac{m_B^2 + m_a^2 - m_{\tilde{\chi}_1^0}^2}{2m_B m_a}. \qquad \text{(A.8)}$$

(iii) $m_{\text{rec}} \equiv m^2_{XX}(m^2_{\tilde{\chi}_1^0\tilde{\chi}_1^0})$ *derivation:* To avoid clutter I will use the symbol X instead of $\tilde{\chi}_1^0$ for the dark matter particle. The visible final particle will still be denoted a.

From the conservation of 4-momenta we get

$$\begin{aligned}
\begin{pmatrix} \sqrt{s} \\ \vec{0} \end{pmatrix} &= \begin{pmatrix} E_{a_1} + E_{a_2} \\ \vec{p}_{a_1} + \vec{p}_{a_2} \end{pmatrix} + \begin{pmatrix} E_{X_1} + E_{X_2} \\ \vec{p}_{X_1} + \vec{p}_{X_2} \end{pmatrix} \\
\rightarrow E_{X_1} + E_{X_2} &= \sqrt{s} - (E_{a_1} + E_{a_2}) \\
|\vec{p}_{X_1} + \vec{p}_{X_2}| &= |\vec{p}_{a_1} + \vec{p}_{a_2}| \qquad \text{(A.9)}
\end{aligned}$$

The recoil mass, m^2_{rec}, which is equivalent to the recoil mass m^2_{XX} in the absence of ISR, beamstrahlung and detector smearing, is given by

$$\begin{aligned}
m^2_{XX} &= (E_{X_1} + E_{X_2})^2 - |\vec{p}_{X_1} + \vec{p}_{X_2}|^2 \\
&= (\sqrt{s} - (E_{a_1} + E_{a_2}))^2 - |\vec{p}_{a_1} + \vec{p}_{a_2}|^2 \\
&= s - 2\sqrt{s}(E_{a_1} + E_{a_2}) + (E_{a_1} + E_{a_2})^2 - |\vec{p}_{a_1} + \vec{p}_{a_2}|^2 \\
m^2_{\text{rec}} \equiv m^2_{XX} &= s - 2\sqrt{s}(E_{a_1} + E_{a_2}) + m^2_{aa} \qquad \text{(A.10)}
\end{aligned}$$

(iv) $E^{\text{min,max}}_{a/\tilde{\chi}_1^0}$ *derivation:* In a's rest frame, its 4-momentum is given by $(m_a, \vec{0})$, boosting it to B's rest frame we get

$$\begin{aligned}
\begin{pmatrix} E_a^{(B)} \\ p_a^{(B)} \end{pmatrix} &= \begin{pmatrix} \cosh\eta_a^{(B)} & -\sinh\eta_a^{(B)} \\ -\sinh\eta_a^{(B)} & \cosh\eta_a^{(B)} \end{pmatrix} \begin{pmatrix} m_a \\ 0 \end{pmatrix} \\
\to E_a^{(B)} &= m_a \cosh\eta_a^{(B)} \\
p_a^{(B)} &= -m_a \sinh\eta_a^{(B)}
\end{aligned} \tag{A.11}$$

Boosting it one more time to the lab's frame

$$\begin{aligned}
\begin{pmatrix} E_a^{(\text{c.m.})} \\ p_a^{(\text{c.m.})} \end{pmatrix} &= \begin{pmatrix} \cosh\eta_B^{(\text{c.m.})} & \pm\sinh\eta_B^{(\text{c.m.})} \\ \pm\sinh\eta_B^{(\text{c.m.})} & \cosh\eta_B^{(\text{c.m.})} \end{pmatrix} \begin{pmatrix} E_a^{(B)} \\ p_a^{(B)} \end{pmatrix} \\
E_a^{(c.m.)} &= E_a^{(B)} \cosh\eta_B^{(\text{c.m.})} \pm \vec{p}_a^{(B)} \sinh\eta_B^{(\text{c.m.})} \\
&= m_a \cosh\eta_a^{(B)} \cosh\eta_B^{(\text{c.m.})} \mp m_a \sinh\eta_a^{(B)} \sinh\eta_B^{(\text{c.m.})}
\end{aligned} \tag{A.12}$$

Using our results on the rapidities and the fact that $1 = \cosh^2 - \sinh^2$ we get

$$\begin{aligned}
E_a^{(\text{c.m.})} &= m_a \left(\frac{m_B^2 + m_a^2 - m_{\tilde{\chi}_1^0}^2}{2m_B m_a}\right)\left(\frac{\sqrt{s}}{2m_B}\right) \mp m_a \left(\sqrt{\frac{(m_B^2 + m_a^2 - m_{\tilde{\chi}_1^0})^2}{2m_B m_a} - 1}\right)\left(\sqrt{\frac{s}{4m_B^2} - 1}\right) \\
&= \frac{\sqrt{s}}{2m_B}\left[\frac{m_B^2 + m_a^2 - m_{\tilde{\chi}_1^0}^2}{2m_B}\right]\left(1 \mp \sqrt{1 - \frac{4m_B^2}{s}}\sqrt{1 - \frac{4m_B^2 m_a^2}{m_B^2 + m_a^2 - m_{\tilde{\chi}_1^0}^2}}\right) \\
&= \frac{\sqrt{s}}{4}\left[1 - \left(\frac{m_{\tilde{\chi}_1^0}^2 - m_a^2}{m_B^2}\right)\right]\left(1 \mp \sqrt{1 - \frac{4m_B^2}{s}}\sqrt{1 - \frac{4m_B^2 m_a^2}{m_B^2 + m_a^2 - m_{\tilde{\chi}_1^0}^2}}\right)
\end{aligned} \tag{A.13}$$

The minus plus sign is due to whether a travels parallel or anti-parallel to B. The minus indicates E_a^{min} while the plus E_a^{max}.

Following the same exact procedure (or just by exchanging $a \leftrightarrow \tilde{\chi}_1^0$), we get

$$E_{\tilde{\chi}_1^0}^{(\text{c.m.})} = \frac{\sqrt{s}}{4}\left[1 - \left(\frac{m_a^2 - m_{\tilde{\chi}_1^0}^2}{m_B^2}\right)\right]\left(1 \mp \sqrt{1 - \frac{4m_B^2}{s}}\sqrt{1 - \frac{4m_B^2 m_{\tilde{\chi}_1^0}^2}{m_B^2 + m_{\tilde{\chi}_1^0}^2 - m_a^2}}\right). \tag{A.14}$$

(*v*) $E_{aa}^{\rm min}, E_{aa}^{\rm cusp}, E_{aa}^{\rm max}$, $E_{\tilde{\chi}_1^0\tilde{\chi}_1^0}^{\rm min}, E_{\tilde{\chi}_1^0\tilde{\chi}_1^0}^{\rm cusp}, E_{\tilde{\chi}_1^0\tilde{\chi}_1^0}^{\rm max}$ *derivation:* For this derivation, we will regard a to be massless ($m_a = 0$) and set $\beta_B \equiv \sqrt{1 - \frac{4m_B^2}{s}}$. $E_{aa}^{\rm min}$ is given by

$$\begin{aligned}
E_{aa}^{\rm min} &= E_{a_1}^{\rm min} + E_{a_2}^{\rm min} \\
&= \frac{\sqrt{s}}{4}\left[1 - \frac{m_{\tilde{\chi}_1^0}^2}{m_B^2}\right]\left(1 - \beta_B\sqrt{1-0}\right) + \frac{\sqrt{s}}{4}\left[1 - \frac{m_{\tilde{\chi}_1^0}^2}{m_B^2}\right]\left(1 - \beta_B\sqrt{1-0}\right) \\
&= \frac{\sqrt{s}}{2}\left[1 - \frac{m_{\tilde{\chi}_1^0}^2}{m_B^2}\right](1 - \beta_B) \qquad \text{(A.15)}
\end{aligned}$$

Meanwhile $E_{aa}^{\rm cusp}$ is given by

$$\begin{aligned}
E_{aa}^{\rm min} &= E_{a_1}^{\rm min} + E_{a_2}^{\rm max} = E_{a_1}^{\rm max} + E_{a_2}^{\rm min} \\
&= \frac{\sqrt{s}}{4}\left[1 - \frac{m_{\tilde{\chi}_1^0}^2}{m_B^2}\right](1 - \beta_B) + \frac{\sqrt{s}}{4}\left[1 - \frac{m_{\tilde{\chi}_1^0}^2}{m_B^2}\right](1 + \beta_B) \\
&= \frac{\sqrt{s}}{4}\left[1 - \frac{m_{\tilde{\chi}_1^0}^2}{m_B^2}\right](1 - \beta_B + 1 + \beta_B) \\
&= \frac{\sqrt{s}}{2}\left[1 - \frac{m_{\tilde{\chi}_1^0}^2}{m_B^2}\right] \qquad \text{(A.16)}
\end{aligned}$$

And finally $E_{aa}^{\rm max}$ is given by

$$\begin{aligned}
E_{aa}^{\rm max} &= E_{a_1}^{\rm max} + E_{a_2}^{\rm max} \\
&= \frac{\sqrt{s}}{4}\left[1 - \frac{m_{\tilde{\chi}_1^0}^2}{m_B^2}\right](1 + \beta_B) + \frac{\sqrt{s}}{4}\left[1 - \frac{m_{\tilde{\chi}_1^0}^2}{m_B^2}\right](1 + \beta_B) \\
&= \frac{\sqrt{s}}{2}\left[1 - \frac{m_{\tilde{\chi}_1^0}^2}{m_B^2}\right](1 + \beta_B) \qquad \text{(A.17)}
\end{aligned}$$

Before continuing on with $E_{\tilde{\chi}_1^0\tilde{\chi}_1^0}^{\rm min}$, we will simplify $E_{\tilde{\chi}_1^0}$ by using the fact that $m_a = 0$

$$\begin{aligned}
E_{\tilde{\chi}_1^0} &= \frac{\sqrt{s}}{4}\left[1 + \frac{m_{\tilde{\chi}_1^0}^2}{m_B^2}\right]\left(1 \mp \beta_B\sqrt{1 - \frac{4m_B^2 m_{\tilde{\chi}_1^0}^2}{m_B^2 + m_{\tilde{\chi}_1^0}^2}}\right) \\
&= \frac{\sqrt{s}}{4}\left(1 + \frac{m_{\tilde{\chi}_1^0}^2}{m_B^2} \mp \beta_B\sqrt{\left(1 + \frac{m_{\tilde{\chi}_1^0}^2}{m_B^2}\right)^2 - \frac{4m_B^2 m_{\tilde{\chi}_1^0}^2}{m_B^4}}\right) \\
&= \frac{\sqrt{s}}{4}\left(1 + \frac{m_{\tilde{\chi}_1^0}^2}{m_B^2} \mp \beta_B\sqrt{\frac{(m_B^2 - m_{\tilde{\chi}_1^0}^2)^2}{m_B^4}}\right) \\
&= \frac{\sqrt{s}}{4}\left(1 + \frac{m_{\tilde{\chi}_1^0}^2}{m_B^2} \mp \beta_B\left(1 - \frac{m_{\tilde{\chi}_1^0}^2}{m_B^2}\right)\right) \qquad \text{(A.18)}
\end{aligned}$$

Therefore, $E^{\min}_{\tilde{\chi}^0_1\tilde{\chi}^0_1}$ is given by

$$\begin{aligned} E^{\min}_{\tilde{\chi}^0_1\tilde{\chi}^0_1} &= E^{\min}_{X_1} + E^{\min}_{X_2} \\ &= \frac{\sqrt{s}}{4}\left(1 + \frac{m^2_{\tilde{\chi}^0_1}}{m^2_B} - \beta_B\left(1 - \frac{m^2_{\tilde{\chi}^0_1}}{m^2_B}\right)\right) + \frac{\sqrt{s}}{4}\left(1 + \frac{m^2_{\tilde{\chi}^0_1}}{m^2_B} - \beta_B\left(1 - \frac{m^2_{\tilde{\chi}^0_1}}{m^2_B}\right)\right) \\ &= \frac{\sqrt{s}}{2}\left(1 + \frac{m^2_{\tilde{\chi}^0_1}}{m^2_B} - \beta_B\left(1 - \frac{m^2_{\tilde{\chi}^0_1}}{m^2_B}\right)\right) \end{aligned} \tag{A.19}$$

Meanwhile $E^{\text{cusp}}_{\tilde{\chi}^0_1\tilde{\chi}^0_1}$ is given by

$$\begin{aligned} E^{\min}_{\tilde{\chi}^0_1\tilde{\chi}^0_1} &= E^{\min}_{X_1} + E^{\max}_{X_2} = E^{\max}_{X_1} + E^{\min}_{X_2} \\ &= \frac{\sqrt{s}}{4}\left(1 + \frac{m^2_{\tilde{\chi}^0_1}}{m^2_B} - \beta_B\left(1 - \frac{m^2_{\tilde{\chi}^0_1}}{m^2_B}\right)\right) + \frac{\sqrt{s}}{4}\left(1 + \frac{m^2_{\tilde{\chi}^0_1}}{m^2_B} + \beta_B\left(1 - \frac{m^2_{\tilde{\chi}^0_1}}{m^2_B}\right)\right) \\ &= \frac{\sqrt{s}}{2}\left(1 + \frac{m^2_{\tilde{\chi}^0_1}}{m^2_B}\right) \end{aligned} \tag{A.20}$$

And finally $E^{\max}_{\tilde{\chi}^0_1\tilde{\chi}^0_1}$ is given by

$$\begin{aligned} E^{\min}_{\tilde{\chi}^0_1\tilde{\chi}^0_1} &= E^{\max}_{X_1} + E^{\max}_{X_2} \\ &= \frac{\sqrt{s}}{4}\left(1 + \frac{m^2_{\tilde{\chi}^0_1}}{m^2_B} + \beta_B\left(1 - \frac{m^2_{\tilde{\chi}^0_1}}{m^2_B}\right)\right) + \frac{\sqrt{s}}{4}\left(1 + \frac{m^2_{\tilde{\chi}^0_1}}{m^2_B} + \beta_B\left(1 - \frac{m^2_{\tilde{\chi}^0_1}}{m^2_B}\right)\right) \\ &= \frac{\sqrt{s}}{2}\left(1 + \frac{m^2_{\tilde{\chi}^0_1}}{m^2_B} + \beta_B\left(1 - \frac{m^2_{\tilde{\chi}^0_1}}{m^2_B}\right)\right) \end{aligned} \tag{A.21}$$

(v) $\cos\Theta$ *derivation:* The angle Θ is defined to be the angle between one of the visible particle in the two visible particle rest frame with respect to the direction of the rest frame of the two particle, *i.e.* $\vec{p}^{\,(12)}_1 \cdot p^{(\text{c.m.})}_{12}/|\vec{p}^{\,(12)}_1||p^{(\text{c.m.})}_{12}|$, where for simplicity I have omitted the subscript/superscript a since we are talking about a.

The total momentum $p^{(\text{c.m.})}_{12}$ is simply given by

$$\begin{aligned} \vec{p}^{\,(\text{c.m.})}_{12} \equiv \vec{p}_{12} &= \vec{p}_1 + \vec{p}_2 \\ \rightarrow \hat{z} &= \frac{\vec{p}_{12}}{|\vec{p}_{12}|} \\ \vec{p}_{12} &= |\vec{p}_{12}|\hat{z} \end{aligned} \tag{A.22}$$

where I have omitted the superscript $^{(\mathrm{c.m.})}$ to avoid clutter. We now use the direction of $\vec{p}_{12}$ as our z axis and decompose p_1 into this new coordinate system

$$\begin{aligned}
\vec{p}_{1\parallel} &= (\vec{p}_1 \cdot \hat{z})\hat{z} = \frac{(\vec{p}_1 \cdot \vec{p}_{12})}{|\vec{p}_{12}|}\hat{z} \\
\vec{p}_{1\perp} &= \vec{p}_1 - \vec{p}_{1\parallel} = \vec{p}_1 - (\vec{p}_1 \cdot \hat{z})\hat{z} \\
\vec{p}_1 &= \vec{p}_{1\parallel} + \vec{p}_{1\perp}
\end{aligned} \tag{A.23}$$

We now need to boost $\vec{p}_1$ into the $\vec{p}_{12}$ rest frame, to do this we need the rapidity of $\vec{p}_{12}$ frame

$$\begin{aligned}
\begin{pmatrix} E_{12} \\ p_{12} \end{pmatrix} &= \begin{pmatrix} \cosh\eta^{(\mathrm{c.m.})} & -\sinh\eta^{(\mathrm{c.m.})} \\ -\sinh\eta^{(\mathrm{c.m.})} & \cosh\eta^{(\mathrm{c.m.})} \end{pmatrix} \begin{pmatrix} m_{12} \\ 0 \end{pmatrix} \\
\rightarrow E_{12} &= m_{12}\cosh\eta^{(\mathrm{c.m.})} \\
\cosh\eta^{(\mathrm{c.m.})} &= \frac{E_{12}}{m_{12}}, \quad \sinh\eta^{(\mathrm{c.m.})} = \sqrt{\frac{E_{12}^2 - m_{12}^2}{m_{12}^2}} = \frac{|\vec{p}_{12}|}{m_{12}}
\end{aligned} \tag{A.24}$$

The only component of $\vec{p}_1$ that is boosted into the 12 c.m. frame will be the parallel component $\vec{p}_{1\parallel}$

$$\begin{aligned}
\begin{pmatrix} E_1^{(12)} \\ p_{1\parallel}^{(12)} \end{pmatrix} &= \begin{pmatrix} \cosh\eta^{(\mathrm{c.m.})} & -\sinh\eta^{(\mathrm{c.m.})} \\ -\sinh\eta^{(\mathrm{c.m.})} & \cosh\eta^{(\mathrm{c.m.})} \end{pmatrix} \begin{pmatrix} E_1 \\ p_{1\parallel} \end{pmatrix} \\
\rightarrow p_{1\parallel}^{(12)} &= -E_1\sinh\eta^{(\mathrm{c.m.})} + p_{1\parallel}\cosh\eta^{(\mathrm{c.m.})}
\end{aligned} \tag{A.25}$$

The magnitude of the boosted $\vec{p}_1^{(12)}$ is given by

$$\begin{aligned}
|\vec{p}_1^{(12)}| &= |\vec{p}_{1\parallel}^{(12)} + \vec{p}_{1\perp}^{(12)}| \\
&= |\vec{p}_{1\parallel}^{(12)} + \vec{p}_{1\perp}| \\
&= \sqrt{|\vec{p}_{1\parallel}^{(12)}|^2 + |\vec{p}_{1\perp}|^2}
\end{aligned} \tag{A.26}$$

where the amplitude of the perpendicular component is given by

$$\begin{aligned}
|\vec{p}_{1\perp}|^2 &= (\vec{p}_1 - (\vec{p}_1 \cdot \hat{z})\hat{z}) \cdot (\vec{p}_1 - (\vec{p}_1 \cdot \hat{z})\hat{z}) \\
&= (\vec{p}_1 \cdot \vec{p}_1) + (\vec{p}_1 \cdot \hat{z})^2 - 2(\vec{p}_1 \cdot \hat{z})^2 \\
&= |\vec{p}_1|^2 - |\vec{p}_{1\parallel}|^2 = p_1^2 - p_{1\parallel}^2
\end{aligned} \tag{A.27}$$

while the amplitude of the boosted parallel component is simply

$$\begin{aligned}
|\vec{p}_{1\|}^{(12)}|^2 &= (-E_1 \sinh \eta^{(\mathrm{c.m.})} + p_{1\|} \cosh \eta^{(\mathrm{c.m.})})^2 \\
&= E_1^2 \sinh^2 \eta^{(\mathrm{c.m.})} + p_{1\|}^2 \cosh^2 \eta^{(\mathrm{c.m.})} - 2E_1 p_{1\|} \sinh \eta^{(\mathrm{c.m.})} \cosh \eta^{(\mathrm{c.m.})} \qquad \text{(A.28)}
\end{aligned}$$

Combining the two components we get

$$\begin{aligned}
|\vec{p}_{1\|}^{(12)}|^2 + |\vec{p}_{1\perp}|^2 &= E_1^2 \sinh^2 \eta^{(\mathrm{c.m.})} + p_{1\|}^2 \cosh^2 \eta^{(\mathrm{c.m.})} - 2E_1 p_{1\|} \sinh \eta^{(\mathrm{c.m.})} \cosh \eta^{(\mathrm{c.m.})} \\
&\quad + p_1^2 - p_{1\|}^2 \\
&= E_1^2 \frac{p_{12}^2}{m_{12}^2} + p_{1\|}^2 \frac{E_{12}^2}{m_{12}^2} - 2E_1 p_{1\|} \frac{p_{12} E_{12}}{m_{12}^2} + p_1^2 - p_{1\|}^2 \\
&= E_1^2 \frac{p_{12}^2}{m_{12}^2} + p_{1\|}^2 \left(\frac{E_{12}^2}{m_{12}^2} - 1 \right) - 2E_1 p_{1\|} \frac{p_{12} E_{12}}{m_{12}^2} + p_1^2 \\
&= E_1^2 \frac{p_{12}^2}{m_{12}^2} + p_{1\|}^2 \frac{p_{12}^2}{m_{12}^2} - 2E_1 p_{1\|} \frac{p_{12} E_{12}}{m_{12}^2} + p_1^2 \\
&= E_1^2 \frac{p_{12}^2}{m_{12}^2} + \frac{(\vec{p}_1 \cdot \vec{p}_{12})^2}{|\vec{p}_{12}|^2} \frac{p_{12}^2}{m_{12}^2} - 2E_1 \frac{(\vec{p}_1 \cdot \vec{p}_{12})}{|\vec{p}_{12}|} \frac{p_{12} E_{12}}{m_{12}^2} + p_1^2 \\
&= E_1^2 \frac{p_{12}^2}{m_{12}^2} + \frac{(\vec{p}_1 \cdot \vec{p}_{12})^2}{m_{12}^2} - 2E_1 E_{12} \frac{(\vec{p}_1 \cdot \vec{p}_{12})}{m_{12}^2} + p_1^2 \qquad \text{(A.29)}
\end{aligned}$$

where the cross term is given by

$$\begin{aligned}
\vec{p}_1 \cdot \vec{p}_{12} &= -\frac{(\vec{p}_{12} - \vec{p}_1)^2 - p_{12}^2 - p_1^2}{2} \\
&= -\frac{(\vec{p}_2)^2 - p_{12}^2 - p_1^2}{2} \\
&= -\frac{p_2^2 - p_1^2 - p_{12}^2}{2}
\end{aligned} \qquad \text{(A.30)}$$

and m_{12} is simply $(E_1 + E_2)^2 - |\vec{p}_1 + \vec{p}_2|^2$.

The dot product of $\vec{p}_1^{(12)}$ and $\vec{p}_{12}$ is

$$\begin{aligned}
\vec{p}_1^{(12)} \cdot \vec{p}_{12} &= \vec{p}_{1\|}^{(12)} \cdot \vec{p}_{12} = |\vec{p}_{1\|}^{(12)}| \times |\vec{p}_{12}| \\
&= -|\vec{p}_{12}| E_1 \sinh \eta^{(\mathrm{c.m.})} + |\vec{p}_{12}||\vec{p}_{1\|}| \cosh \eta^{(\mathrm{c.m.})} \\
&= -|\vec{p}_{12}| E_1 \sinh \eta^{(\mathrm{c.m.})} + |\vec{p}_{12}| \frac{(\vec{p}_1 \cdot \vec{p}_{12})}{|\vec{p}_{12}|} \cosh \eta^{(\mathrm{c.m.})} \\
&= -|\vec{p}_{12}| E_1 \sinh \eta^{(\mathrm{c.m.})} + (\vec{p}_1 \cdot \vec{p}_{12}) \cosh \eta^{(\mathrm{c.m.})} \\
&= -|\vec{p}_{12}| E_1 \frac{|\vec{p}_{12}|}{m_{12}} + (\vec{p}_1 \cdot \vec{p}_{12}) \frac{E_{12}}{m_{12}} \\
&= \frac{(\vec{p}_1 \cdot \vec{p}_{12}) E_{12} - |\vec{p}_{12}|^2 E_1}{m_{12}} \qquad \text{(A.31)}
\end{aligned}$$

Finally $\cos\Theta$ is

$$\cos\Theta \equiv \frac{\vec{p}_1^{(12)} \cdot p_{12}^{(\mathrm{c.m.})}}{\vec{p}_1^{(12)}||p_{12}^{(\mathrm{c.m.})}|} = \frac{(\vec{p}_1 \cdot \vec{p}_{12}) E_{12} - |\vec{p}_{12}|^2 E_1}{|\vec{p}_1^{(12)}||\vec{p}_{12}| m_{12}} \qquad \text{(A.32)}$$

and everything is now in terms of the lab frame variables.

BIBLIOGRAPHY

[1] G. Aad *et al.* [ATLAS Collaboration]. Observation of a new particle in the search for the Standard Model Higgs boson with the ATLAS detector at the LHC, *Phys. Lett. B*, 716:1, 2012.

[2] F. Zwicky. Spectral displacement of extra galactic nebulae. *Helv. Phys. Acta.*, 6:110, 1933.

[3] V. C. Rubin and W. K. Ford, Jr.. Rotation of the Andromeda nebula from a spectroscopic survey of emission regions. *Astrophys. J.*, 159:379, 1970.

[4] V. C. Rubin, N. Thonnard and W. K. Ford, Jr.. Rotational properties of 21 SC galaxies with a large range of luminosities and radii, from NGC 4605 /R = 4kpc/ to UGC 2885 /R = 122 kpc/. *Astrophys. J.*, 238:471, 1980.

[5] A. Bosma. The distribution and kinematics of neutral hydrogen in spiral galaxies of various morphological types. *Astron. J.*, 86:1825, 1981.

[6] A. Refregier. Weak gravitational lensing by large scale structure. *Ann. Rev. Astron. Astrophys.*, 41:645, 2003.

[7] J. A. Tyson, G. P. Kochanski and I. P. Dell'Antonio. Detailed mass map of CL0024+1654 from strong lensing. *Astrophys. J.*, 498:L107, 1998.

[8] B. D. Fields and S. Sarkar. Big-Bang nucleosynthesis. *J. Phys.*, G33:1, 2006.

[9] E. Komatsu *et al.* Seven-year Wilkinson Microwave Anisotropy Probe (WMAP) observations: Cosmological interpretation. *Astrophys. J. Suppl.*, 192:18, 2011.

[10] D. Clowe, M. Bradac, A. H. Gonzalez, M. Markevitch, S. W. Randall, C. Jones, and D. Zaritsky. A direct empirical proof of the existence of dark matter. *Astrophys. J.*, 648:L109, 2006.

[11] R. Bernabei *et al.* First results from DAMA/LIBRA and the combined results with DAMA/NaI. *Eur. Phys. J. C*, 56:333, 2008.

[12] J. L. Feng. Dark matter candidates from particle physics and methods of detection. *Ann. Rev. Astron. Astrophys.*, 48:495, 2010.

[13] P. Konar *et al.* Shedding light on the dark sector with direct WIMP production. *New. J. Phys. C*, 11:1105004, 2009.

[14] I. Hinchliffe, F. E. Paige, M. D. Shapiro, J. Soderqvist and W. Yao. Precision SUSY measurements at LHC. *Phys. Rev. D*, 55:5520, 1997.

[15] H. Bachacou, I. Hinchliffe and F. E. Paige. Measurements of masses in SUGRA models at LHC. *Phys. Rev. D*, 62:015009, 2000.

[16] I. Hinchliffe and F. E. Paige. Measurements in SUGRA models with large tan(beta) at LHC, *Phys. Rev. D* 61:095011, 2000.

[17] B. C. Allanach, C. G. Lester, M. A. Parker and B. R. Webber. Measuring sparticle masses in non-universal string inspired models at the LHC. *JHEP*, 0009:004, 2000.

[18] B. K. Gjelsten, D. J. Miller and P. Osland. Measurement of SUSY masses via cascade decays for SPS 1a. *JHEP* 0412:003, 2004.

[19] B. K. Gjelsten, D. J. Miller and P. Osland. Measurement of the gluino mass via cascade decays for SPS 1a. *JHEP* 0506:015, 2005.

[20] B. K. Gjelsten, D. J. Miller, P. Osland and A. R. Raklev. Mass determination in cascade decays using shape formulas. *AIP Conf. Proc.* 903:257, 2007.

[21] T. Han, I. W. Kim and J. Song. Kinematic cusps with two missing particles I: Antler decay topology. *Phys. Rev. D*, 87:035003, 2013.

[22] T. Han, I. W. Kim and J. Song. Kinematic cusps: Determining the missing particle mass at the LHC. *Phys. Lett. B*, 693:575, 2010.

[23] M. Srednicki. *Quantum Field Theory.* Cambridge University Press, Cambridge, 2007.

[24] A. H. G. Peter. Dark Matter: A brief review. *arXiv:1201.3942 [astro-ph.CO]*, January 2012.

[25] P. Ramond. Dual theory for free fermions. *Phys. Rev. D*, 3:2415, 1971.

[26] A. Bilal. Introduction to Supersymmetry. *arXiv:hep-th/0101055*, January 2001.

[27] S. P. Martin. A Supersymmetry primer. *arXiv:hep-ph/9709356*, September 2011.

[28] N. D. Christensen and D. Salmon. A new method for the spin determination of dark matter. *arXiv:1311.6465 [hep-ph]*, November 2013.

[29] W. Kilian, T. Ohl, and J. Reuter. WHIZARD: Simulating multi-particle processes at LHC and ILC. *Eur. Phys. J. C*, 71:1742, 2011.

[30] T. Abe *et al.* Linear collider physics resource book for Snowmass 2001. 1: Introduction. *arXiv:hep-ex/0106055*, June 2001.

[31] J. E. Brau *et al.* International Linear Collider physics and detectors: 2011 status report. *CERN-LCD-NOTE-2011-038*, 2011.

[32] K. Hagiwara, R. D. Peccei, D. Zeppenfeld, and K. Hikasa. Probing the weak boson sector in e+ e- → W+ W-. *Nucl. Phys. B*, 282:253, 1987.

[33] K. Agashe, D. Kim, M. Toharia and D. G. E. Walker. Distinguishing dark matter stabilization symmetries using multiple kinematic edges and cusps. *Phys. Rev. D*, 82:015007, 2010.

[34] K. Agashe, R. Franceschini and D. Kim. Using energy peaks to measure new particle masses. *arXiv:hep-ph/1309.4776*, September 2013.

[35] H-C. Cheng *et al.* Accurate mass determinations in decay chains with missing energy. *Phys. Rev. Lett.*, 100:252001, 2008.

[36] P. Konar *et al.* Shedding light on the dark sector with direct WIMP production. *New J. Phys.*, 11:105004, 2009.

[37] L. D. Landau and E. M. Lifshitz. *Fluid Mechanics,* 2^{nd} *ed.*. Elsevier, Oxford, 1987.

[38] J. M. McDonough. ME634: Introduction to Turbulence. *Lecture Notes, University of Kentucky*, 2007.

[39] R. T. Cerbus and W. I. Goldburg. Information content of turbulence. *Phys. Rev. E*, 88:053012, 2013.

[40] J. Pedlosky. *Geophysical Fluid Dynamics*. Springer, Berlin, 1986.

[41] D. Bernard, G. Boffetta, A. Celani, and G. Falkovich. Conformal invariance in two-dimensional turbulence. *Nature Physics*, 2:124, 2006.

[42] J. L. Cardy. SLE for theoretical physicists. *Annals. Phys.*, 318:81, 2005.

[43] J. R. Cressman, J. Davoudi, W.I. Goldburg, and J. Schumacer. Eulerian and Lagrangian studies in surface flow turbulence. *New J. Phys.*, 6:53, 2004.

[44] O. Schramm. Scaling limits of loop-erased random walks and uniform spanning trees. *Israel J. Math.*, 118:221, 2000.

[45] T. Kennedy. Numerical computations for the Schramm-Loewner Evolution. *J. Stat. Phys.*, 137:839, 2009.

[46] P. Denissenko, G. Falkovich, and S. Lukaschuk. How waves affect the distribution of particles that float on a liquid surface. *Phys. Rev. Lett.*, 97:244501, 2006.

[47] G. Falkovich, A. Weinberg, P. Denissenko, and S. Lukaschuk. Surface Tension: Floater clustering in a standing wave. *Nature*, 435:1045, 2005.

[48] M. M. Bandi, J. R. Cressman, and W. I. Goldburg. Test of the fluctuation relation in Lagrangian turbulence on a free surface. *J. Stat. Phys.*, 130:27, 2008.

[49] J. Larkin, W. I. Goldburg, and M. M. Bandi. Time evolution of a fractal distribution: Particle concentrations in free-surface turbulence. *Physica D*, 239:1264, 2010.

[50] P. K. Yeung and S.B. Pope. An algorithm for tracking fluid particles in numerical simulations of homogeneous turbulence. *J. Comput. Phys.*, 79:373, 1988.

[51] T. Kennedy. Computing the Loewner driving process of random curves in the half plane. *J. Stat. Phys.*, 131:803, 2008.

[52] W. Kager and B. Nienhuis. A guide to stochastic Lowner evolution and its applications. *J. Stat. Phys.*, 115:1149, 2004.

[53] R. C. Hilborn. *Chaos and Nonlinear Dynamics,* 2^{nd} *ed.*. Oxford University Press, Oxford, 2000.

[54] H. G. E. Hentschel and I. Procaccia. The infinite number of generalized dimensions of fractals and strange attractors. *Physica D*, 8:435, 1983.

[55] H. Saleur and B. Duplantier. Exact determination of the percolation hull exponent in two dimensions. *Phys. Rev. Lett.*, 58:2325, 1987.

[56] V. Beffara. The dimension of the SLE curves. *Annals. Prob.*, 36:1421, 2008.

[57] S. B. Pope. *Turbulent Flows*. Cambridge University Press, Cambridge, 2000.

[58] T. Tuan *et al.* Macroscopic effects of the spectral structure in turbulent flows. *Nature Physics*, 6:436, 2010.

[59] H. Slichting and K. Gersten. *Boundary Layer Theory*. Springer, Berlin, 2000.

[60] N. S. Berman and J. W. Dunning. Pipe flow measurements of turbulence and ambiguity using laser-Doppler velocimetry. *J. Fluid. Mech.*, 61:289, 1973.

[61] B. Chu. *Laser light scattering: Basic principles and practice,* 2^{nd} *ed.*. Academic, New York, 1991.

[62] G. Fuller *et al.* The measurement of velocity gradients in laminar flow by homodyne light-scattering spectroscopy. *J. Fluid Mech.*, 100:555, 1980.

[63] L. E. Drain. *The Laser Doppler Technique*. John Wiley, New York, 1980.

[64] N. Goldenfeld. Roughness induced critical phenomena in a turbulent flow. *Phys. Rev. Lett.*, 96:044503, 2006.

[65] G. Gioia and P. Chakraborty. Turbulent friction in rough pipes and the energy spectrum of the phenomenological theory. *Phys. Rev. Lett.*, 96:044502, 2006.

[66] N. Guttenberg and N. Goldenfeld. Friction factor of two dimensional rough boundary soap film flows. *Phys. Rev. E*, 79:065306, 2009.

[67] W. I. Goldburg. Dynamic light scattering. *Am. J. Phys.*, 67:12, 1999.

[68] R. H. Kraichnan and D. Montgomery. Two-dimensional turbulence. *Rep. Prog. Phys.*, 43:547, 1980.

[69] H. Kellay and W. I. Goldburg. Two-dimensional turbulence: A review of some recent experiments. *Rep. Prog. Phys.*, 65:845, 2002.

[70] M. A. Rutgers. Forced 2D Turbulence: experimental evidence of simultaneous inverse energy and forward enstrophy cascades. *Phys. Rev. Lett.*, 81:2244, 1998.

[71] D. P. Chowdhury *et al.* Application of photon correlation spectroscopy to flowing Brownian motion systems. *Applied Optics*, 23:4149, 1984.

[72] U. Frisch. *Turbulence: The Legacy of A. N. Kolmogorov.* Cambridge University Press, New York, 1995.

[73] A. Alloul *et al.* FeynRules 2.0 - A complete toolbox for tree-level phenomenology. *arXiv:hep-ph/1310.1921*, May 2014.

[74] A. Belyaev, N. D. Christensen, and A. Pukhov. CalcHEP 3.4 for collider physics within and beyond the Standard Model. *Comput. Phys. Commun.*, 184:1729, 2013.

[75] T. Sjostrand, S. Mrenna, and P. Z. Skands. PYTHIA 6.4 Physics and Manual. *JHEP*, 0605:026, 2006.

[76] F. Staub. Sarah. *arXiv:hep-ph/0806.0538*, Jun 2008.

[77] H. Georgi. *Lie Lagebras in Particle Physics: From Isospin to Unified Theories.* Westview Press, Boulder, 1999.

[78] C. Rovelli. *Quantum Gravity.* Cambridge University Press, Cambridge, 2004.